University of Pennsylvania
ScholarlyCommons

Publicly Accessible Penn Dissertations

1-1-2015

MRI Evaluation of Injectable Hyaluronic Acid Hydrogel Therapy to Attenuate Myocardial Infarct Remodeling

Shauna Marie Dorsey
University of Pennsylvania, shauna.dorsey@gmail.com

Follow this and additional works at: http://repository.upenn.edu/edissertations

 Part of the Biomedical Commons, and the Radiology Commons

Recommended Citation
Dorsey, Shauna Marie, "MRI Evaluation of Injectable Hyaluronic Acid Hydrogel Therapy to Attenuate Myocardial Infarct Remodeling" (2015). *Publicly Accessible Penn Dissertations*. 1046.
http://repository.upenn.edu/edissertations/1046

This paper is posted at ScholarlyCommons. http://repository.upenn.edu/edissertations/1046
For more information, please contact libraryrepository@pobox.upenn.edu.

MRI Evaluation of Injectable Hyaluronic Acid Hydrogel Therapy to Attenuate Myocardial Infarct Remodeling

Abstract
Left ventricular (LV) remodeling following myocardial infarction (MI) leads to maladaptive processes that often progress to heart failure. Injectable biomaterials can alter the mechanical signaling post-MI to limit this progression. To design optimal therapies, noninvasive techniques are needed to elucidate the reciprocal interaction between the injected material and the surrounding myocardial tissue. Towards this goal, the general hypothesis of this dissertation was that magnetic resonance imaging (MRI) can be used to characterize the properties of injectable materials once delivered to the myocardium and evaluate the temporal effects of injectable materials on myocardial tissue properties post-MI. To test this hypothesis, injectable hyaluronic acid (HA) hydrogels were developed with a range of gelation, degradation and mechanical properties by altering the initiator concentration, macromer modification, and macromer concentration, respectively. Non-contrast MRI was then used to characterize the properties (e.g., distribution, chemical composition) of injectable HA hydrogels in myocardial explants. Altering hydrogel gelation led to differences in distribution in myocardial tissue, as quantified by T2-weighted MRI. As an alternative to conventional (i.e.T2-weighted) MRI where contrast depends on differences in MR properties and thus, is non-specific for the material, chemical exchange saturation transfer (CEST) MRI was used to specifically image hydrogels based on their functional (i.e. exchangeable proton) groups. CEST contrast correlated with changes in material properties, specifically macromer concentration. Furthermore, CEST MRI was shown to simultaneously visualize and discriminate between different injectable materials based on their unique chemistry. Finally, the effect of injectable HA hydrogels on myocardial tissue properties was temporally evaluated in a porcine infarct model up to 12 weeks post-MI. Outcome assessment using MRI (e.g. cine, late-gadolinium enhancement, and spatial modulation of magnetization MRI) and finite element (FE) modeling demonstrated that hydrogel therapy led to improved global LV structure and function, increased wall thickness, preserved borderzone contractility, and increased infarct stiffness, respectively. This work demonstrates that MRI can be used to simultaneously study hydrogel properties after injection into the myocardium and evaluate the ability of injectable hydrogels to alter myocardial tissue properties to ultimately improve cardiac outcomes and enable future optimization of biomaterial therapies to attenuate adverse remodeling post-MI.

Degree Type
Dissertation

Degree Name
Doctor of Philosophy (PhD)

Graduate Group
Bioengineering

First Advisor
Jason A. Burdick

This dissertation is available at ScholarlyCommons: http://repository.upenn.edu/edissertations/1046

Keywords
Hyaluronic Acid, Hydrogel, Left Ventricular Remodeling, Magnetic Resonance Imaging

Subject Categories
Biomedical | Radiology

This dissertation is available at ScholarlyCommons: http://repository.upenn.edu/edissertations/1046

MRI EVALUATION OF INJECTABLE HYALURONIC ACID HYDROGEL THERAPY TO ATTENUATE MYOCARDIAL INFARCT REMODELING

Shauna M. Dorsey

A DISSERTATION

In Bioengineering

Presented to the Faculties of the University of Pennsylvania

In Partial Fulfillment of the Requirements for the

Degree of Doctor of Philosophy

2015

_____

Supervisor of Dissertation
Jason A. Burdick, Ph.D.
Professor of Bioengineering

_____

Graduate Group Chairperson
Jason A. Burdick, Ph.D.
Professor of Bioengineering

Dissertation Committee
Hee Kwon Song, Ph.D. (Chair), Associate Professor of Radiology
Robert C. Gorman, M.D., Professor of Surgery
Andrew Tsourkas, Ph.D., Associate Professor of Bioengineering

DEDICATION

I would like to dedicate my dissertation to my grandfather, Joseph H. Gainer, D.V.M, who first inspired my interests in science and encouraged me to pursue a career in scientific research.

ACKNOWLEDGEMENTS

I would first like to sincerely thank my thesis advisor, Jason A. Burdick, Ph.D., for giving me the amazing opportunity to work in his lab for the past several years and for his support and guidance throughout my dissertation research. I am truly grateful for the counsel, patience, and help from such an incredible mentor that has both encouraged me to grow as a scientific researcher as well as to pursue my interests in a career in engineering education throughout my time at the University of Pennsylvania. In addition to the mentorship I have received from my thesis advisor, I would also like to thank my dissertation committee, Hee Kwon Song, Ph.D. (Chair), Robert C. Gorman, M.D., and Andrew Tsourkas, Ph.D., who have provided valuable insight into the direction of my project at critical stages throughout my dissertation.

I would also like to acknowledge that this work could not have been possible without several collaborations, both at the University of Pennsylvania and at other universities. I would like to thank Robert C. Gorman, M.D., and members of his lab, especially Jeremy McGarvey, M.D., for their work in our large animal studies. I would also like to thank Ravinder Reddy, Ph.D., and members of his lab, especially Mohammad Haris, Ph.D., Anup Singh, Ph.D., and Feliks Kogan, Ph.D., for their help in our chemical exchange saturation transfer (CEST) MRI studies. In addition, I would like to thanks Jonathan Wenk, Ph.D. at the University of Kentucky for his work on our finite element (FE) modeling. Especially, I would like to thank Walter Witschey, Ph.D. for his assistance on both the large animal imaging as well as the CEST MRI work.

In addition to the research collaborations that made this work possible, I would also like to acknowledge the support of the past and current members of the Polymer Biomaterials Laboratory (under the direction of Jason A. Burdick, Ph.D.). The students and postdocs in my lab have been integral in every stage of my research. In particular, I would like to thank Elena Tous Kichula, Ph.D. for her mentorship during the initial stages of my dissertation research and Christopher B. Rodell for his assistance in the later stages of my research as he continues on our cardiac biomaterial collaboration with the Gorman laboratory. I would also like to thank Vanessa

Chou and Leron Arama, both of whom were students I had the pleasure of mentoring during their masters and undergraduate levels of study, respectively.

Finally, I would like to thank my family for their encouragement throughout my dissertation, especially my parents, Arthur J. Dorsey, Ph.D. and Lisa G. Dorsey. They have given me the drive and focus to face any challenge with determination and enthusiasm. My academic success throughout both my undergraduate and graduate careers would not be possible without their continuous love and support and I could not be the person I am today without them.

ABSTRACT

MRI EVALUATION OF INJECTABLE HYALURONIC ACID HYDROGEL THERAPY TO ATTENUATE MYOCARDIAL INFARCT REMODELING

Shauna M. Dorsey

Jason A. Burdick, Ph.D.

Left ventricular (LV) remodeling following myocardial infarction (MI) leads to maladaptive processes that often progress to heart failure. Injectable biomaterials can alter the mechanical signaling post-MI to limit this progression. To design optimal therapies, noninvasive techniques are needed to elucidate the reciprocal interaction between the injected material and the surrounding myocardial tissue. Towards this goal, the general hypothesis of this dissertation was that magnetic resonance imaging (MRI) can be used to characterize the properties of injectable materials once delivered to the myocardium and evaluate the temporal effects of injectable materials on myocardial tissue properties post-MI.

To test this hypothesis, injectable hyaluronic acid (HA) hydrogels were developed with a range of gelation, degradation and mechanical properties by altering the initiator concentration, macromer modification, and macromer concentration, respectively. Non-contrast MRI was then used to characterize the properties (e.g., distribution, chemical composition) of injectable HA hydrogels in myocardial explants. Altering hydrogel gelation led to differences in distribution in myocardial tissue, as quantified by T_2-weighted MRI. As an alternative to conventional (i.e.T_2-weighted) MRI where contrast depends on differences in MR properties and thus, is non-specific for the material, chemical exchange saturation transfer (CEST) MRI was used to specifically image hydrogels based on their functional (i.e. exchangeable proton) groups. CEST contrast

correlated with changes in material properties, specifically macromer concentration. Furthermore, CEST MRI was shown to simultaneously visualize and discriminate between different injectable materials based on their unique chemistry. Finally, the effect of injectable HA hydrogels on myocardial tissue properties was temporally evaluated in a porcine infarct model up to 12 weeks post-MI. Outcome assessment using MRI (e.g. cine, late-gadolinium enhancement, and spatial modulation of magnetization MRI) and finite element (FE) modeling demonstrated that hydrogel therapy led to improved global LV structure and function, increased wall thickness, preserved borderzone contractility, and increased infarct stiffness, respectively.

This work demonstrates that MRI can be used to simultaneously study hydrogel properties after injection into the myocardium and evaluate the ability of injectable hydrogels to alter myocardial tissue properties to ultimately improve cardiac outcomes and enable future optimization of biomaterial therapies to attenuate adverse remodeling post-MI.

TABLE OF CONTENTS

DEDICATION ..... **II**

ACKNOWLEDGEMENTS ..... **III**

ABSTRACT ..... **V**

LIST OF TABLES ..... **XIV**

LIST OF FIGURES ..... **XV**

CHAPTER 1 ..... **1**

Introduction **1**

1.1. Significance 1

1.2. LV Remodeling Post-MI 1

1.3. Strategies for the Treatment of MI 3

1.4. Principles of MRI 4

1.5. Cardiac MRI 6

1.6. Summary 8

1.7. References 9

CHAPTER 2 ..... **17**

Research Overview **17**

2.1. Objectives 17

2.2. Specific Aims and Hypotheses 18

2.3. Chapter Outline 20

CHAPTER 3 ..... **22**

A Review of Hydrogels in Cardiac Tissue Engineering 22

3.1. Introduction 22

3.2. Acellular Approaches 23

3.2.1. LV Restraints 23

3.2.2. Injectable Hydrogels as Bulking Agents 25

3.2.2.1. Natural Acellular Hydrogels 26

3.2.2.2. Synthetic Acellular Hydrogels 33

3.3. Cellular Approaches 37

3.3.1. Cell Delivery 37

3.3.2. Cardiac Patches 39

3.3.3. Injectable Hydrogels for Cell Delivery 40

3.3.3.1. Natural Hydrogels for Cell Delivery 41

3.3.3.2. Synthetic Hydrogels for Cell Delivery 46

3.4. Injectable Hydrogels for Molecule Delivery 49

3.4.1. Anti-Apoptotic Factors 50

3.4.2. Angiogenic Factors 51

3.4.3. Chemoattractants 53

3.5. Combined Hydrogel Delivery of Cells and Molecules 54

3.6. Future Directions and Conclusions 57

3.7. References 59

CHAPTER 4 80

***In Vitro* Characterization of Hydrolytically Degradable Hyaluronic Acid Hydrogels 80**

4.1. Introduction 80

4.2. Materials and Methods 83

4.2.1. Synthesis of Hydroxyethyl Methacrylated HA (HeMA-HA) Macromer 83

4.2.2. Synthesis of Methacrylated HA (MeHA) Macromer 84

4.2.3. HA Hydrogel Formation 85

4.2.4. *In Vitro* Hydrogel Characterization 86

4.2.5. Statistical Analysis 89

4.3. Results 89

4.3.1. HA Macromer Synthesis and Characterization 89

4.3.2. *In Vitro* Characterization of HeMA-HA Hydrogels 89

4.3.3. Characterization of HeMA-HA/MeHA Copolymer Hydrogel Properties 99

4.4. Discussion 103

4.5. Conclusions 106

4.6. References 107

4.7. Appendix 4.1. Statistical comparisons for selected *in vitro* characterization figures. 112

CHAPTER 5 117

Using MRI to Visualize and Quantify Hyaluronic Acid Hydrogel Distribution in Cardiac Tissue 117

5.1. Introduction 117

5.2. Materials and Methods 121

5.2.1. Synthesis and Gelation of MeHA Macromers 121

5.2.2. Synthesis and Gelation of Guest-Host HA Macromers 122

5.2.3. Synthesis and Gelation of HeMA-HA Macromers 123

5.2.4. MRI of MeHA in Myocardial Explants 124

5.2.5. MRI of Guest-Host Hydrogels in Myocardium 126

5.2.6. *Ex Vivo* MRI of HeMA-HA Hydrogels from *In Vivo* Injections 128

5.2.7. Statistical Analysis 130

5.3. Results 130

5.3.1. MRI Visualization and Quantification of *Ex Vivo* MeHA Hydrogel Distribution 130

5.3.2. Guest-Host HA Hydrogel Distribution in Explants from MRI Assessment 135

5.3.3. MRI Evaluation of HeMA-HA Hydrogel Distribution *Ex Vivo* from *In Vivo* Delivery ... 140

5.4. Discussion 140

5.5. Conclusions 144

5.6. References 146

CHAPTER 6 151

Visualization of Injectable Hyaluronic Acid Hydrogels using Chemical Exchange Saturation Transfer MRI 151

6.1. Introduction 151

6.2. Materials and Methods 155

6.2.1. HeMA-HA Macromer Synthesis 155

6.2.2. Peptide Coupling to HeMA-HA and Characterization 155

6.2.3. Hydrogel Formation and Characterization 156

6.2.4. CEST Imaging Principles 156

6.2.5. MR Imaging of Phantoms at 3 T and 7 T 159

6.2.6. MR Imaging of *Ex Vivo* Tissue at 3 T 159

6.2.7. Processing CEST MRI Data 160

6.2.8. Statistical Analysis 162

6.3. Results 162

6.3.1. Characterization of CEST Effect of Hydrogel Phantoms 163

6.3.2. *Ex Vivo* Imaging of Injectable Hydrogels 169

6.3.3. Alteration of CEST Effect with Peptide Coupling 172

6.4. Discussion 176

6.5. Conclusions 181

6.6. References 182

CHAPTER 7 188

Investigation of Injectable Hyaluronic Acid Hydrogel Therapy to Alter Myocardial Tissue Properties for Infarct Repair using MRI and FE Modeling 188

7.1. Introduction 188

7.2. Materials and methods 190

7.2.1. Synthesis of HeMA-HA Macromer 190

7.2.2. Hydrogel Formation and Characterization 191

7.2.3. *In Vivo* Evaluation in Porcine Infarct Model 191

7.2.4. MRI Acquisition 193

7.2.5. MR Image Post-Processing 194

7.2.5.1. LV Volume Measurement 194

7.2.5.2. Infarct Assessment 195

7.2.5.3. Myocardial Strain Analysis 196

7.2.6. *In Vivo* Diastolic Material Property Estimation 197

7.2.7. Statistical Analysis 199

7.3. Results 200

7.3.1. *In Vitro* Characterization of Selected Hydrogel Formulation 200

7.3.2. Histological Evaluation and *Ex Vivo* Infarct Thickness 202

7.3.3. Global LV Structure and Function 203

7.3.4. *In Vivo* Infarct Thickness and Expansion over Time 204

7.3.5. Myocardial Systolic Strain as an Estimate of Contractility 207

7.3.6. Estimation of *In Vivo* Diastolic Myocardial Properties using FE Modeling 208

7.4. Discussion 214

7.5. Conclusions 219

7.6. References 220

CHAPTER 8 229

Conclusions, Limitations, and Future Directions 229

8.1. Conclusions 229

8.2. Limitations 232

8.2.1. Limitations in *In Vitro* Characterization Studies 232

8.2.2. Limitations in T_2-Weighted Imaging 233

8.2.3. Limitations in CEST Imaging 234

8.2.4. Limitations in *In Vivo* Study 237

8.2.5. Limitations in FE Model 238

8.3. Future Directions 239

8.3.1. *In Vivo* Hydrogel Imaging 239

8.3.2. Small Molecule Release from Injectable HA Hydrogels 242

8.3.3. Improved *In Vivo* Study Design 243

8.4. Summary 244

8.5. References 245

LIST OF TABLES

Table 3.1. Summary of acellular hydrogel systems and their assessment in animal MI models. . 36

Table 3.2. Summary of cellular hydrogel systems and their assessment in animal MI models. ... 42

Table 3.3. Summary of hydrogels for molecule delivery and their evaluation in animal MI models. 49

Table 3.4. Summary of hydrogels for cell and molecule delivery and their *in vivo* assessment. .. 56

Table 4.1. *In vitro* characterization studies of pure HeMA-HA hydrogels. 87

Table 4.2. *In vitro* characterization studies of HeMA-HA and MeHA copolymer hydrogels. 88

Table 6.1. MRI scan parameters optimized for each study. 158

Table 7.1. FE model optimization results for infarct region. 209

Table 7.2. FE model optimization results for remote region. 209

LIST OF FIGURES

Figure 1.1. Schematic of LV remodeling following MI, highlighting the infarct expansion and global geometric changes that occur over time. 2

Figure 1.2. Delivery of injectable hydrogels as bulking therapy to stabilize the LV wall and alter the local myocardial wall stresses post-MI..... 4

Figure 3.1. Schematic of injectable hydrogel strategies for MI repair. 23

Figure 3.2. Finite element (FE) model of simulated polymer injections. 26

Figure 3.3. Natural, injectable hydrogel for acellular cardiac repair. 31

Figure 3.4. Synthetic hydrogel for cell delivery post-MI. 47

Figure 3.5. Molecule release from injectable, natural hydrogels.. 52

Figure 3.6. Percutaneous catheter delivery of decellularized ventricular ECM to healthy rats..... 58

Figure 4.1. Chemical structures of HeMA-HA (A) and MeHA (B) macromers. 82

Figure 4.2. HeMA-HA macromer synthesis..... 84

Figure 4.3. MeHA macromer synthesis. 85

Figure 4.4. Mechanism of hydrogel formation. 86

Figure 4.5. Tunability of mechanical properties of HeMA-HA hydrogels. 90

Figure 4.6. Initial *in vitro* characterization studies of pure HeMA-HA hydrogels at various macromer modifications and concentrations.. 91

Figure 4.7. Effect of initiator concentration on HeMA-HA hydrogel gelation and mechanics 92

Figure 4.8. Extensive analysis of the effect of macromer modification and concentration on HeMA-HA hydrogel properties.. 94

Figure 4.9. Tuning HeMA-HA hydrogel degradation by altering the macromer modification and concentration.. 95

Figure 4.10. *In vitro* characterization of selected HeMA-HA hydrogel formulations with similar gelation and initial mechanics but different rates of degradation.. 96

Figure 4.11. Effect of combining non-degradable MeHA and degradable HeMA-HA into a single copolymer hydrogel system at various macromer concentrations. 97

Figure 4.12. Tuning hydrogel degradation by altering the ratio of HeMA-HA to MeHA at various macromer concentrations..... 100

Figure 4.13. *In vitro* characterization of selected HeMA-HA/MeHA copolymer hydrogels. 102

Figure 5.1. Formation of self-assembling, guest-host HA hydrogels with shear-thinning properties. 123

Figure 5.2. Selection and gelation of MeHA hydrogel formulations applied for *ex vivo* MRI assessment.. 131

Figure 5.3. Optimization of MR imaging parameters for MeHA hydrogels in explants at 9.4 T.. 132

Figure 5.4. Determination of optimal day for imaging MeHA hydrogels in myocardial explants. 133

Figure 5.5. Visualization and quantification of MeHA hydrogel distribution volumes in myocardial explants at 9.4 T..... 134

Figure 5.6. Visualization and quantification of guest-host HA hydrogel distribution in myocardial explants at 9.4 T..... 136

Figure 5.7. Optimization of MR parameters for imaging HA hydrogels in explants at 3 T.. 137

Figure 5.8. Examination of guest-host HA hydrogel distribution in whole heart explant at 3 T. . 138

Figure 5.9. Assessment of HeMA-HA hydrogel distribution in myocardial explant from *in vivo* injections at 3 T.. 139

Figure 6.1. Principles of CEST for imaging hydrogels. 153

Figure 6.2. Chemical structure of HeMA-HA, indicating the exchangeable protons targeted for CEST imaging. 154

Figure 6.3. Processing of CEST data..... 161

Figure 6.4. HeMA-HA as a CEST imaging agent.. 162

Figure 6.5. Characterization of the CEST effect of HeMA-HA hydrogels.. 163

Figure 6.6. Saturation pulse dependence of CEST effect at 7T. 164

Figure 6.7. Effect of hydrogel pH and temperature on the CEST effect at 7T 165

Figure 6.8. CEST effect of HeMA-HA hydrogel phantoms at varying field strengths. 166

Figure 6.9. Saturation pulse amplitude dependence of CEST effect at 3T..... 167

Figure 6.10. Saturation pulse duration dependence of CEST effect at 3T. 168

Figure 6.11. Effect of hydrogel pH and temperature on the CEST effect at 3T.. 169

Figure 6.12. *Ex vivo* CEST effect of HeMA-HA hydrogels at varying field strengths..... 170

Figure 6.13. Chemical shift dependence of the CEST effect. 171

Figure 6.14. Comparison of CEST effect with traditional MRI based on relaxation properties... 172

Figure 6.15. Synthesis of HeMA-HA-Peptide. 173

Figure 6.16. Spectroscopy characterization of HeMA-HA-Peptide. 174

Figure 6.17. Characterization of the CEST effect of HeMA-HA-Peptide hydrogels.. 175

Figure 6.18. Altering the CEST effect by changing the chemistry and saturation frequency. 176

Figure 6.19. CEST effect of HeMA-HA hydrogels tracks with degradation at both field strengths. 177

Figure 7.1. MRI analysis of *in vivo* porcine infarct model. 192

Figure 7.2. Development of finite element models from MRI-based animal specific data.. 197

Figure 7.3. *In vitro* characterization of hydrogel selected for use *in vivo*. 200

Figure 7.4. Histological assessment of infarcts. 201

Figure 7.5. Global cardiac structural and functional outcomes.. 202

Figure 7.6. Myocardial wall thicknesses measured *ex vivo* and *in vivo*.. 204

Figure 7.7. Infarct area assessment from late-gadolinium enhancement (LGE) MRI..... 205

Figure 7.8. Contributions of infarct thinning and expansion from *in vivo* assessment. 206

Figure 7.9. Regional wall function assessed in terms of contractility using systolic strain.. 207

Figure 7.10. Quantification of regional systolic strain as an estimate of myocardial contractility208

Figure 7.11. Finite element model to assess passive myocardial properties.. 210

Figure 7.12. Short-axis view of the diastolic principal strain generated from FE model simulations.. 211

Figure 7.13. Simulated equi-biaxial extension tests using FE model optimization parameters.. 212

Figure 7.14. Quantification of moduli in the infarct region from simulated equi-biaxial tests..... 213

Figure 8.1. Tuning HeMA-HA hydrogel properties to alter degradation and small molecule release..... 241

CHAPTER 1

Introduction

1.1. Significance

Cardiovascular disease (CVD) remains to be the leading cause of death in the United States. Although there has been a dramatic reduction in the death rate due to CVD over the past four decades, CVD still accounts for nearly 1 of every 3 deaths in the U.S.[1] Of these deaths, about half are due to coronary heart disease (CHD), which causes myocardial infarction (MI). Each year, approximately 600,000 Americans suffer their first MI and another 300,000 have a recurrent attack, with an additional 150,000 silent MIs estimated.[1] Advances in the treatment of acute MI have reduced hospital mortality to about 6%.[1] However, in spite of this success, or perhaps because of it, MI has become a major cause of heart failure with approximately 20% of patients developing heart failure within 5 years of their first MI.[1] MI initiates a dynamic process of left ventricular (LV) remodeling, which includes both maladaptive biological and mechanical changes that may lead to altered contractile properties and ultimately, heart failure. Despite current standard of treatment, LV remodeling caused by a MI is responsible for 70% of the 5.1 million cases of heart failure present in the U.S.[2]

1.2. LV Remodeling Post-MI

MI occurs following coronary artery occlusion, resulting in depletion of nutrients and oxygen to the myocardium and subsequent cardiomyocyte death. This cardiomyocyte necrosis leads to an influx of inflammatory cells (i.e., macrophages, monocytes, and neutrophils) into the infarcted area to remove the necrotic debris.[3] Fibroblasts also infiltrating the infarct region secrete bioactive molecules, such matrix metalloproteinases (MMPs).[4,5] Although initially essential to provide the necessary substructure for subsequent scar formation, MMP upregulation is not met

by a concomitant upregulation of their endogenous inhibitors (TIMPs), leading to a substantial increase in the breakdown of cardiomyocyte extracellular matrix (ECM) and collagen.[6] To counteract the ECM breakdown, fibroblasts and myofibroblasts secrete collagen which leads to the formation of a fibrotic scar that is non-contractile and maladaptive.[3,5,7,8] Furthermore, since cardiomyocytes are tethered together with collagen, this leads to continuous stretch and slippage of cardiomyocytes from one another, which weakens the myocardial wall and makes it susceptible to global geometric changes, including thinning and dilatation.[9,10]

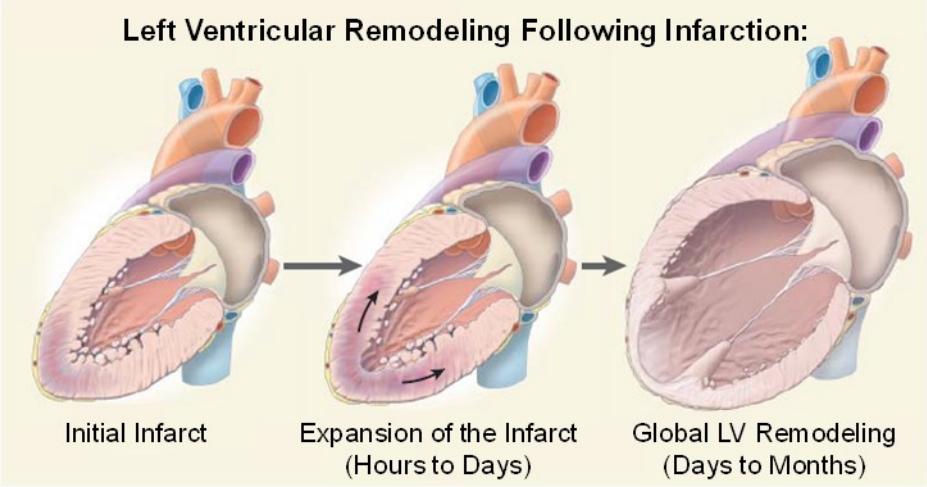

Figure 1.1. Schematic of LV remodeling following MI, highlighting the infarct expansion and global geometric changes that occur over time. Figure adapted from [11].

The mechanical phenomenon that both initiates and sustains the entire adverse LV remodeling process is the initial infarct expansion (**Figure 1.1**).[12-15] From a structural perspective, early infarct expansion results from thinning of the ventricular wall and increased compliance. However, it is a progressive pathologic process that eventually causes abnormal stress distributions in the borderzone (BZ) regions surrounding the infarct. As part of this self-perpetuating process, increased regional BZ stresses lead to maladaptive cellular and enzymatic processes, such as additional cardiomyocyte apoptosis and MMP activation.[13-15] Once initiated,

these biological processes are difficult to reverse by medical or surgical means and ultimately lead to altered contractile properties and heart failure.[4]

1.3. Strategies for the Treatment of MI

Clinical approaches to MI focus on the acute setting, yet few therapies have been developed to prevent the progression from MI to eventual heart failure, at which point heart transplantation remains the only definitive treatment. Current treatments focus on two main approaches: 1) restoring blood flow to the occluded vessel to reperfuse the ischemic tissue through the use of bypass surgery, balloon angioplasty, or coronary stents or 2) replacing the damaged heart tissue using ventricular assist devices, artificial hearts, or ideally, heart transplants. Pharmacological therapies, such as angiotensin-converting enzyme (ACE) inhibitors and beta-blockers, help by either reducing the blood volume to decrease demands on the heart or minimizing arrhythmias to limit recurrent MI attacks, respectively.[11,16] Whereas reperfusion and pharmacologics have been shown to delay the onset of heart failure post infarction, they do little to address the changes in the myocardial tissue properties that occur during remodeling.

As suggested above, limiting initial infarct expansion has been identified as a potential therapy to alter myocardial properties post-MI and reduce the morbidity associated with LV remodeling that leads to heart failure.[17] Previous strategies to limit infarct expansion include surgical reconstruction of the dilated LV and physical restraint of the ventricle or infarct region using polymeric meshed materials to prevent dilation.[18-21] Injectable biomaterials have been explored to circumvent the surgical placement of LV restraining devices or cardiac patches. Injectable biomaterials offer the potential for minimally invasive delivery, which decreases damage to the target and surrounding tissues and enables more rapid clinical translation. Recently, injectable hydrogels have been used to mechanically stabilize the myocardial wall and modulate maladaptive biological processes post-MI through delivery of therapies, such as cells and growth factors (**Figure 1.2**),[22,23] as will be discussed more in depth in Chapter 3. Hydrogels are water-swollen networks of polymer chains with a high degree of flexibility, similar to natural

tissue[24] and can be formed through numerous mechanisms, including *in situ* formation.[25] Due to their high tissue-like water content, structural similarity to native macromolecular components, and mechanical properties resembling those of soft tissues, they have been used for numerous applications in tissue engineering and drug delivery.[26]

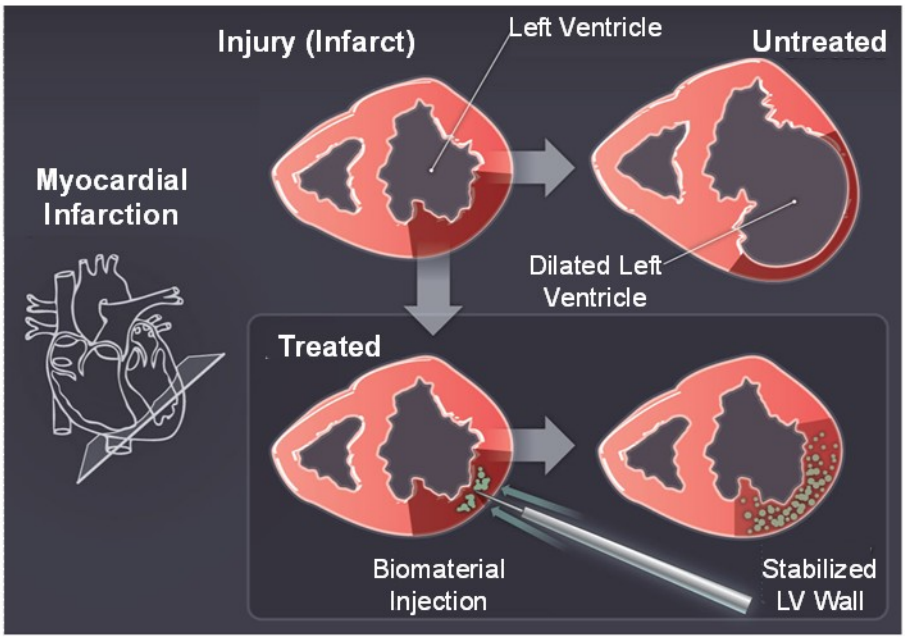

Figure 1.2. Delivery of injectable hydrogels as bulking therapy to stabilize the LV wall and alter the local myocardial wall stresses post-MI. Figure adapted from [27].

1.4. Principles of MRI

In addition to developing therapies to attenuate LV remodeling, noninvasive techniques are also needed to assess the effects of these therapies once delivered to the myocardium. Imaging can noninvasively provide mechanistic information over time regarding the presence and distribution of hydrogels throughout the tissue and simultaneously investigate the impact of injectable materials on myocardial properties post-MI, which may lead to better design principles for future material optimization. Magnetic resonance imaging (MRI) offers advantages over other imaging modalities, such as optical[28-31] or x-ray imaging,[32-35] due to its high spatial and temporal

resolution at any tissue depth without the use of ionizing radiation,[36,37] and thus, has been widely used in the clinic and applied to evaluate cardiac outcomes following MI.[38-40] To understand the ability of MRI to assess injectable hydrogel properties, as will be discussed in Chapters 5 and 6, and evaluate the alterations in myocardial tissue properties with hydrogel therapy, as will be discussed in Chapter 7, an exploration of the basic principles of MRI is needed.

A MRI signal is generated from manipulating the water protons in materials or tissues using oscillating magnetic fields. Any nucleus with an odd number of protons or neutrons can be exploited for MRI but the protons in water are primarily targeted since biological tissues have a high water content. Due to their charge and intrinsic spin property, water protons have a magnetic dipole moment causing them to act like a bar magnet.[41] In the absence of a magnetic field, water protons are randomly oriented and precessing (i.e., spinning) at their natural frequency. To image a material or tissue, the dipole moment property of water protons is manipulated using magnetic fields.[36] When placed in an external, static magnetic field of strength B (referred to as B_0), the protons align themselves with and begin precessing around the magnetic field. Approximately half of the protons point in the direction of the field and half point in the opposite direction. Over time, slightly more protons align with the B_0 field (about one in a million), creating a macroscopic magnetic moment referred to as the net magnetization (M) vector.[41] As a reference, the conventional MRI coordinate system specifies that both the B_0 field and the magnetization vector M are aligned along the z-axis at equilibrium. The maximum signal is obtained when the net magnetization is perpendicular to the B_0 field (i.e., in the x-y plane).

Therefore, to acquire a signal and subsequently generate an image, the protons must be further manipulated. To do so, the MR scanner contains a radiofrequency (RF) coil situated within the larger main (B_0) magnet. The RF coil is selectively tuned to the resonance frequency of water protons and creates a secondary magnetic field (B_1) which rotates the net magnetization of the protons away from their alignment with B_0. The degree of rotation (e.g. 90^o, 180^o) is specified in the pulse sequence, which describes the series of RF pulses.[37,41] For instance, application of a

90^{o} RF pulse causes the protons to become perpendicular to the B_0 field. Whereas the B_0 field is always present, the B_1 field can be turned on and off. When the B_1 magnetic field is removed, the protons relax back to their equilibrium state and realign so that their net magnetization M is again parallel with B_0. During this relaxation process, protons emit energy in the form of an free-induction decay (FID) that can then be detected by the RF coil and processed (by Fourier transformation) to generate an image.[36,41] Gradient coils also embedded within the main magnet are applied during the RF pulse train to produce gradients in the B_0 magnetic field and encode slice, phase and frequency information.[41] This encoding process enables extraction of three-dimensional information and, once reconstructed, results in images with high spatial resolution.

Image contrast between tissues or materials is generated based on differences in composition, specifically proton density and relaxation properties. The relaxation properties describe the manner by which protons respond to RF pulse manipulation. During a RF pulse, interactions between protons cause them to precess at slightly different rates, leading them to dephase (or spread out) from one another, which results in signal decay. Transverse (T_2) relaxation describes this rate of proton dephasing and magnetization decay in the transverse plane.[37] When the RF pulse is turned off, the protons first rephrase rapidly and then recover back to equilibrium along the longitudinal axis (i.e., z-axis) by the process of longitudinal (T_1) relaxation.[41] In terms of the magnetization, the M_{xy} component of the magnetization vector decays rapidly and the M_z component slowly recovers along the z-axis; these are independent but simultaneous processes.[36,37,41] These MR properties (i.e., T_1/T_2 relaxation times, proton density) are intrinsic to the material or tissue of interest but can be manipulated to enhance differences in endogenous image contrast, as will be discussed further in Chapters 5 and 6 in references to visualizing injectable hydrogels in the myocardium.

1.5. Cardiac MRI

Noninvasive imaging techniques are needed not only to visualize the injected material once delivered to the myocardium but also to assess cardiac outcomes to determine the impact

of injectable hydrogel therapies on the heart. The evaluation of cardiac disease and therapeutic interventions with noninvasive imaging techniques has assumed increasing importance over the past few decades, with the goal of defining anatomic abnormalities in the heart and coronary arteries to provide insight to the pathophysiology of cardiac diseases. Advances in rapid MRI acquisition techniques and its application to cardiac imaging have shown its tremendous potential for evaluation of cardiac diseases and the efficacy therapeutic interventions.[42-49] When compared with other well-established cardiac imaging modalities, such as echocardiography, single-photon emission computed tomography (*S*PECT), or positron-emission tomography (PET), cardiac MRI offers an excellent depiction of myocardial wall motion, high image contrast, and high spatial resolution without using ionizing radiation. Its efficacy, together with its excellent safety profile and increasing availability, makes cardiac MRI an important and sophisticated tool for noninvasive 3D evaluation of cardiovascular structure, function and viability.

The most accurate method for evaluating the morphology and function of the heart has become cine MRI. Cine MRI enables noninvasive assessment of global morphology and altered regional wall motion in all segments of the LV, with high spatial and temporal resolution.[50,51] Direct imaging of non-viable myocardial regions can be performed using myocardial late-gadolinium enhancement (LGE) MRI. LGE is exclusively related to irreversible injury, irrespective of contractile function or age of injury and hence, can be used to detect regions of infarction.[52] Using gadolinium-based contrast agents, this technique visualizes MI as regions of bright signal compared to normal myocardium. Finally, myocardial tagging with MRI can be used to directly visualize the contractility of the ventricles. Using pre-saturation pulses, a grid of dark lines or “tags” is produced immediately following the R-wave trigger and then, as the tissue moves and deforms through the cardiac cycle, the tagging pattern moves correspondingly.[50,53-55] By acquiring images perpendicular to the tagging planes, the tags can be used to track the motion of the heart. The power of myocardial tagging lies in the ability to perform quantitative myocardial strain analysis with great accuracy and precision.[36,43] Using MRI tagging data, theoretical finite element (FE) models can compute myocardial stress and strain distributions in the LV post-MI.[56-59]

Recently, FE models have been developed to investigate the effects of injectable biomaterials on attenuating adverse LV remodeling post-MI.[56,60-62] In one study, simulations indicated that injection of a noncontractile material to an infarcted LV has the potential to reduce elevated myofiber stresses.[60,61] However, the use of *in vivo*-derived MRI data as an input to a FE model has yet to be explored prior to this dissertation (as will be addressed in Chapter 7).

1.6. Summary

Motivated by the clinical burden of heart failure, injectable biomaterials are a promising therapy to target the tissue remodeling process that is known to cause progression from MI to heart failure. Despite experimental successes in animal models, only one injectable material has progressed to clinical trials.[63,64] Therefore, to more efficiently develop injectable systems with optimal materials properties to attenuate cardiac remodeling post-MI, noninvasive tools are needed to simultaneously investigate materials properties and cardiac outcomes. To address this need, this dissertation will focus on the use of MRI to both examine material properties once delivered to the myocardium as well as assess the impact of injectable materials on myocardial remodeling post-MI. The imaging techniques explored can be applied to a wide range of injectable materials to better understand the material-myocardial interactions and facilitate selection of injectable systems with higher translational potential for MI repair.

1.7. References

1. Go AS, Mozaffarian D, Roger VL, Benjamin EJ, Berry JD, Blaha MJ, et al. Heart disease and stroke statistics-2014 update: A report from the American Heart Association. Circulation 2014;129(3):e28-e292.

2. Gheorghiade M, Bonow RO. Chronic heart failure in the United States: A manifestation of coronary artery disease. Circulation 1998;97(3):282-289.

3. Cleutjens JP, Creemers EE. Integration of concepts: cardiac extracellular matrix remodeling after myocardial infarction. J Card Fail 2002;8(6 Suppl):S344-S348.

4. Holmes JW, Borg TK, Covell JW. Structure and mechanics of healing myocardial infarcts. Annu Rev Biomed Eng 2005;7:223-253.

5. Dobaczewski M, Gonzalez-Quesada C, Frangogiannis NG. The extracellular matrix as a modulator of the inflammatory and reparative response following myocardial infarction. J Mol Cell Cardiol 2010;48(3):504-511.

6. Spinale FG. Myocardial matrix remodeling and the matrix metalloproteinases: Influence on cardiac form and function. Physiol Rev 2007;87(4):1285-1342.

7. Gu Y, Yu J, Lum LG, Lee RJ. Tissue engineering and stem cell therapy for myocardial repair. Front Biosci 2007;12:5157-5165.

8. Dobaczewski M, Bujak M, Zymek P, Ren G, Entman ML, Frangogiannis NG. Extracellular matrix remodeling in canine and mouse myocardial infarcts. Cell Tissue Res 2006;324(3):475-488.

9. Buckberg GD. Architecture must document functional evidence to explain the living rhythm. Eur J Cardiothorac Surg 2005;27(2):202-209.

10. Nahrendorf M. Imaging of infarct healing predicts left ventricular remodeling and evolution of heart failure: Focus on protease activity. Circ Cardiovasc Imaging 2011;4(4):351-353.

11. Jessup M, Brozena S. Medical progress: Heart failure. N Engl J Med 2003;348(20):2007-2018.

12. Kramer CM, Lima JA, Reichek N, Ferrari VA, Llaneras MR, Palmon LC, et al. Regional differences in function within noninfarcted myocardium during left ventricular remodeling. Circulation 1993;88(3):1279-1288.

13. Jackson BM, Gorman JH,3rd, Salgo IS, Moainie SL, Plappert T, St John-Sutton M, et al. Border zone geometry increases wall stress after myocardial infarction: Contrast echocardiographic assessment. Am J Physiol Heart Circ Physiol 2003;284(2):H475-H479.

14. Epstein FH, Yang Z, Gilson WD, Berr SS, Kramer CM, French BA. MR tagging early after myocardial infarction in mice demonstrates contractile dysfunction in adjacent and remote regions. Magn Reson Med 2002;48(2):399-403.

15. Pilla JJ, Blom AS, Gorman JH,3rd, Brockman DJ, Affuso J, Parish LM, et al. Early postinfarction ventricular restraint improves borderzone wall thickening dynamics during remodeling. Ann Thorac Surg 2005;80(6):2257-2262.

16. Bui AL, Horwich TB, Fonarow GC. Epidemiology and risk profile of heart failure. Nat Rev Cardiol 2011;8(1):30-41.

17. Blom A, Mukherjee R, Pilla J, Lowry A, Yarbrough W, Mingoia J, et al. Cardiac support device modifies left ventricular geometry and myocardial structure after myocardial infarction. Circulation 2005;112(9):1274-1283.

18. Batista R. Partial left ventriculectomy--the Batista procedure. Eur J Cardiothorac Surg 1999;15 Suppl 1:S12-9; discussion S39-43.

19. Kelley ST, Malekan R, Gorman JH,3rd, Jackson BM, Gorman RC, Suzuki Y, et al. Restraining infarct expansion preserves left ventricular geometry and function after acute anteroapical infarction. Circulation 1999;99(1):135-142.

20. Klodell CT,Jr, Aranda JM,Jr, McGiffin DC, Rayburn BK, Sun B, Abraham WT, et al. Worldwide surgical experience with the Paracor HeartNet cardiac restraint device. J Thorac Cardiovasc Surg 2008;135(1):188-195.

21. Starling RC, Jessup M, Oh JK, Sabbah HN, Acker MA, Mann DL, et al. Sustained benefits of the CorCap Cardiac Support Device on left ventricular remodeling: Three year follow-up results from the Acorn clinical trial. Ann Thorac Surg 2007;84(4):1236-1242.

22. Nelson DM, Ma Z, Fujimoto KL, Hashizume R, Wagner WR. Intra-myocardial biomaterial injection therapy in the treatment of heart failure: Materials, outcomes and challenges. Acta Biomater 2011;7(1):1-15.

23. Tous E, Purcell B, Ifkovits JL, Burdick JA. Injectable acellular hydrogels for cardiac repair. J Cardiovasc Transl Res 2011;4(5):528-542.

24. Drury JL, Mooney DJ. Hydrogels for tissue engineering: scaffold design variables and applications. Biomaterials 2003;24(24):4337-4351.

25. Ruel-Gariepy E, Leroux JC. In situ-forming hydrogels: Review of temperature-sensitive systems. Eur J Pharm Biopharm 2004;58(2):409-426.

26. Lee KY, Mooney DJ. Hydrogels for tissue engineering. Chem Rev 2001;101(7):1869-1879.

27. Burdick JA, Mauck RL, Gorman JH,III, Gorman RC. Acellular biomaterials: An evolving alternative to cell-based therapies. Science Translational Medicine 2013;5(176):176ps4.

28. Kovar JL, Simpson MA, Schutz-Geschwender A, Olive DM. A systematic approach to the development agents for optical imaging of mouse of fluorescent contrast cancer models. Anal Biochem 2007;367(1):1-12.

29. Weissleder R, Ntziachristos V. Shedding light onto live molecular targets. Nat Med 2003;9(1):123-128.

30. Soranno DE, Lu HD, Weber HM, Rai R, Burdick JA. Immunotherapy with injectable hydrogels to treat obstructive nephropathy. Journal of Biomedical Materials Research Part a 2014;102(7):2173-2180.

31. Yuan Z, Zakhaleva J, Ren H, Liu J, Chen W, Pan Y. Noninvasive and high-resolution optical monitoring of healing of diabetic dermal excisional wounds implanted with biodegradable in situ gelable hydrogels. Tissue Engineering Part C-Methods 2010;16(2):237-247.

32. Mottu F, Rufenacht DA, Doelker E. Radiopaque polymeric materials for medical applications - Current aspects of biomaterial research. Invest Radiol 1999;34(5):323-335.

33. Blakely B, Lee BH, Riley C, McLemore R, Pathak CP, Vernon BL. Formulation and characterization of radio-opaque conjugated in situ gelling materials. Journal of Biomedical Materials Research Part B-Applied Biomaterials 2010;93B(1):9-17.

34. Yu SB, Watson AD. Metal-based x-ray contrast media. Chem Rev 1999;99(9):2353-2377.

35. Leon CM, Lee BH, Preul M, McLemore R, Vernon BL. Synthesis and characterization of radio-opaque thermosensitive poly[N-isopropylacrylamide-2,2 '-(ethylenedioxy)bis(ethylamine)-2,3,5-triiodobenzamide]. Polym Int 2009;58(8):847-850.

36. McRobbie DW, Moore EA, Graves MJ, Prince MR. MRI: From Picture to Proton. Cambridge: Cambridge University Press; 2003.

37. Wehrli FW. Magnetic resonance imaging. In: Byran RN, editor. Introduction to the Science of Medical Imaging. New York, NY: Cambridge University Press; 2010. p. 160.

38. Dixon JA, Spinale FG. Large animal models of heart failure: A critical link in the translation of basic science to clinical practice. Circ Heart Fail 2009;2(3):262-271.

39. McGarvey JM, Kondo N, Witschey WRT, Takebe M, Aoki C, Burdick JA, et al. Injectable microsphere gel progressively improves global ventricular function, regional contractile strain, and mitral regurgitation after myocardial infarction. in review .

40. Witschey WRT, Pilla JJ, Ferrari G, Koomalsingh K, Haris M, Hinmon R, et al. Rotating frame spin lattice relaxation in a swine model of chronic, left ventricular myocardial infarction. Magn Reson Med 2010;64(5):1454-1461.

41. Hornak JP. The Basics of MRI. Henietta, NY: Interactive Learning Software; 1996.

42. Steffans JC, Sakuma H, Bourne MW, Higgins CB. Magnetic resonance imaging in ischemic heart disease. Am Heart J 1996;132(1 Pt 1):156-173.

43. Reeder SB, Du YP, Lima JA, Bluemke DA. Advanced cardiac MR imaging of ischemic heart disease. Radiographics 2001;21(4):1047-1074.

44. Chiribiri A, Bettencourt N, Nagel E. Cardiac magnetic resonance stress testing: results and prognosis. Curr Cardiol Rep 2009;11(1):54-60.

45. Rerkpattanapipat P, Link KM, Hamilton CA, Hundley WG. Detecting left ventricular myocardial ischemia during intravenous dobutamine with cardiovascular magnetic resonance imaging (MRI). J Cardiovasc Magn Reson 2001;3(1):21-25.

46. Viswamitra S, Higgins CB, Meacham DF, Mehta JL. Magnetic resonance imaging in myocardial ischemia. Curr Opin Cardiol 2004;19(5):510-516.

47. Sakuma H. Magnetic resonance imaging for ischemic heart disease. J Magn Reson Imaging 2007;26(1):3-13.

48. Unlu M, Anik Y, Demirci A, Ural D, Kahraman G, Komsuoglu B. Cardiac MRI in ischemic heart disease with severe coronary artery stenosis. Acad Radiol 2006;13(11):1387-1393.

49. Yokoyama K, Nitatori T, Kanke N, Suzuki S. Efficacy of cardiac MRI in the evaluation of ischemic heart disease. Magn Reson Med Sci 2006;5(1):33-40.

50. Ishida M, Kato S, Sakuma H. Cardiac MRI in ischemic heart disease. Circ J 2009;73(9):1577-1588.

51. Watzinger N, Maier R, Reiter U, Reiter G, Fuernau G, Wonisch M, et al. Clinical applications of cardiovascular magnetic resonance. Curr Pharm Des 2005;11(4):457-475.

52. Ligabue G, Fiocchi F, Ferraresi S, Barbieri A, Romagnoli R, Torricelli P. How to quantify infarct size on delayed-enhancement MR images: A comparison between visual and quantitative approach. Radiol Med 2007;112(7):959-968.

53. Axel L, Dougherty L. Heart wall motion: Improved method of spatial modulation of magnetization for MR imaging. Radiology 1989;172(2):349-350.

54. Axel L, Dougherty L. MR imaging of motion with spatial modulation of magnetization. Radiology 1989;171(3):841-845.

55. Zerhouni EA, Parish DM, Rogers WJ, Yang A, Shapiro EP. Human heart: tagging with MR imaging - A method for noninvasive assessment of myocardial motion. Radiology 1988;169(1):59-63.

56. Wenk JF, Eslami P, Zhang Z, Xu C, Kuhl E, Gorman JH, et al. A novel method for quantifying the in-vivo mechanical effect of material injected into a myocardial infarction. Ann Thorac Surg accepted for publication.

57. Dang AB, Guccione JM, Mishell JM, Zhang P, Wallace AW, Gorman RC, et al. Akinetic myocardial infarcts must contain contracting myocytes: finite-element model study. Am J Physiol Heart Circ Physiol 2005;288(4):H1844-50.

58. Guccione JM, Moonly SM, Moustakidis P, Costa KD, Moulton MJ, Ratcliffe MB, et al. Mechanism underlying mechanical dysfunction in the border zone of left ventricular aneurysm: a finite element model study. Ann Thorac Surg 2001;71(2):654-662.

59. Walker JC, Ratcliffe MB, Zhang P, Wallace AW, Fata B, Hsu EW, et al. MRI-based finite-element analysis of left ventricular aneurysm. Am J Physiol Heart Circ Physiol 2005;289(2):H692-700.

60. Wall ST, Walker JC, Healy KE, Ratcliffe MB, Guccione JM. Theoretical impact of the injection of material into the myocardium: A finite element model simulation. Circulation 2006;114(24):2627-2635.

61. Wenk JF, Wall ST, Peterson RC, Helgerson SL, Sabbah HN, Burger M, et al. A method for automatically optimizing medical devices for treating heart failure: Designing polymeric injection patterns. J Biomech Eng 2009;131(12):121011.

62. Ifkovits JL, Tous E, Minakawa M, Morita M, Robb JD, Koomalsingh KJ, et al. Injectable hydrogel properties influence infarct expansion and extent of postinfarction left ventricular remodeling in an ovine model. Proc Natl Acad Sci U S A 2010;107(25):11507-11512.

63. Ikara Holdings Inc. IK-5001 for the Prevention of Remodeling of the Ventricle and Congestive Heart Failure After Acute Myocardial Infarction. In: ClinicalTrials.gov [Internet].

Bethesda (MD): National Library of Medicine (US). 2010- [cited 2014 Nov 21]. Available at: http://ClinicalTrials.gov/show/NCT01226563. NLM Identifier: NCT01226563.

64. LoneStar Heart Inc. An Open Label Rollover Trial for Patients Randomized to the Control Group of Study LSH-10-001. In: ClinicalTrials.gov [Internet]. Bethesda (MD): National Library of Medicine (US). 2014- [cited 2014 Nov 21]. Available at: http://ClinicalTrials.gov/show/NCT02226679. NLM Identifier: NCT02226679.

CHAPTER 2

Research Overview

2.1. Objectives

Cardiovascular disease is the leading cause of death in the U.S. Each year, over one million of U.S. residents have myocardial infarctions (MI) and roughly one-third of them progress to heart failure and death. MI leads to abnormal stress distributions in the myocardium, which results in maladaptive biologic processes that may lead to altered contractile properties and heart failure. Although numerous surgical and pharmacological have been shown to delay the onset of heart failure post-MI, they do little to address the myocardial tissue remodeling that occurs following infarction. Hence, there is a need for new therapeutic interventions that target the post-MI left ventricular (LV) remodeling process to further limit progression to heart failure.

Injectable biomaterials, specifically hydrogels, have become an attractive therapy to provide mechanical stabilization to attenuate adverse remodeling after MI. Despite the wide range of injectable hydrogels investigated for MI-induced remodeling, there is a lack of techniques to evaluate the properties of injected hydrogels and their impact on myocardial tissue *in vivo*. Imaging modalities, such as magnetic resonance imaging (MRI), can noninvasively characterize biomaterial and myocardial properties, which may lead to better design principles for future biomaterial optimization. Therefore, the purpose of this dissertation is to use injectable hyaluronic acid (HA) hydrogels and MRI as a platform to investigate the presence and composition of hydrogels once injected into the myocardium and the effect of injectable hydrogels on myocardial tissue properties for the attenuation of LV remodeling post-MI.

Towards this goal, an HA hydrogel system will be developed and examined for the range of properties that are attainable. After understanding how hydrogel properties can be tuned for an

intended application, non-contrast MRI techniques will be used to visualize and quantify differences in hydrogel distribution based on gelation in myocardial explants and differences with macromer concentration and chemistry using chemical exchange saturation transfer (CEST). Finally, a single degradable hydrogel formulation will be applied to an *in vivo* infarct model and MRI will be used to evaluate differences in myocardial tissue properties after hydrogel delivery throughout the remodeling process.

2.2. Specific Aims and Hypotheses

The *global hypothesis* of this dissertation is that MRI can be used to evaluate the properties of injectable materials once delivered to the myocardium and systematically investigate the therapeutic effects of injectable materials on tissue properties of the remodeling myocardium post-MI. This advance would provide technology and insight into design criteria for targeted biomaterial therapies for MI repair. This hypothesis will be systematically investigated using the following three Specific Aims.

Specific Hypothesis 1: Hydrogel degradation, mechanics, and rate of gelation can be controlled by altering macromer chemistry, macromer concentration, and initiation conditions.

Specific Aim 1: Synthesize and characterize degradable HA hydrogels with a range of properties, particularly gelation, degradation, and mechanics.

HA will be modified with a hydrolytically degradable functional group, hydroxyethyl methacrylate (HeMA), to generate the gel precursor, HeMA-HA. HeMA-HA can be crosslinked through a radical polymerization reaction to form HA hydrogels and will be further optimized to obtain formulations with a range of gelation times, degradation profiles, and mechanical properties. These properties will be assessed *in vitro* using rheological characterization, an uronic acid assay to measure HA release, and compressive mechanical testing, respectively. Characterization will be performed for both pure HeMA-HA homopolymer hydrogels and copolymer hydrogels with a hydrolytically stable macromer, methacrylated HA (MeHA). Hydrogels

will be formed with a range of initiator concentrations, macromer modifications, and macromer concentrations to explore the parameter space of tunable properties. The ability to tune hydrogel properties will then be utilized in subsequent imaging (Aim 2) and *in vivo* (Aim 3) studies.

Specific Hypothesis 2: Non-contrast MRI can be used to visualize and quantify differences in hydrogel distribution volume and macromer chemistry within myocardial tissue.

Specific Aim 2: Visualize HA hydrogels using MRI as a means to examine hydrogel dispersion and detect differences in hydrogel chemical composition *ex vivo*.

The gelation of HA hydrogels will be altered to form hydrogels with varied distribution in myocardial tissue, through changes in initiator concentration and macromer modification. Three-dimensional hydrogel dispersion volumes will be visualized and quantified using conventional (T_2-weighted) MRI. As an alternative to the radically polymerized MeHA and HeMA-HA hydrogels, guest-host chemistry will also be introduced into HA hydrogels to form materials through supramolecular self-assembly. Thus, the effect of both the timing of gelation and the mechanism of hydrogel formation on hydrogel distribution in myocardial tissue will be assessed.

To expand upon traditional MRI approaches, a new MRI acquisition technique will be explored that is based on chemical exchange saturation transfer (CEST), where the signal relies on the exchange of protons in specific molecules (either endogenous to or engineered into the material) with bulk water protons. CEST MRI will be used to identify the exchangeable proton groups in HA hydrogels and manipulate those protons to visualize HeMA-HA hydrogels either alone or after injection into tissue. Changes in the CEST contrast with changes in hydrogel bulk properties (i.e. macromer concentration) will be investigated. To detect differences in hydrogel chemistry using CEST MRI, an arginine-based peptide will be coupled to HeMA-HA hydrogels to introduce an additional exchangeable proton group known to generate a CEST effect.

Specific Hypothesis 3: The delivery of HA hydrogels to the myocardium post-MI alters LV volumes, cardiac function, and myocardial wall thicknesses, strains and stiffnesses to attenuate remodeling.

Specific Aim 3: Assess the temporal effects of degradable HA hydrogel therapy on long-term myocardial tissue remodeling post-MI using cardiac MRI and finite element (FE) modeling in an *in vivo* porcine infarct model.

A previously characterized HeMA-HA hydrogel formulation (selected based on Aim 1) will be applied to an *in vivo* porcine infarct model and cardiac MRI will be used to evaluate myocardial tissue properties over time, up to 12 weeks post-MI. More specifically, cine MRI will assess global LV structure and function, late-gadolinium enhancement (LGE) MRI will visualize changes (i.e. thinning, expansion) in the infarct region, and spatial modulation of magnetization (SPAMM) tagging will measure myocardial strains as an assessment of wall motion and contractility. Finite element (FE) modeling with MRI-derived strain inputs will be used to simulate the impact of injectable hydrogels on regional myocardial stiffness over time.

2.3. Chapter Outline

Chapter 1 presented the translational motivation for designing injectable hydrogels as bulking agents to attenuate LV remodeling and the use of imaging, specifically MRI, as a tool to noninvasively assess the effects of these therapies. An extensive review of natural and synthetic injectable hydrogels as acellular, cellular, and therapeutic delivery vehicle therapies for MI treatment will be presented in Chapter 3. Chapter 4 will then focus on the *in vitro* characterization of hydrolytically degradation HA hydrogels. The effect of altering material parameters (e.g. initiator concentration, macromer modification, and macromer concentration) on the resulting hydrogel properties (e.g. gelation, degradation, and mechanics) will be investigated in both pure HeMA-HA and HeMA-HA/MeHA copolymer hydrogels.

Based on an understanding of the tunability of injectable HA hydrogels, the next portion of the dissertation (Chapters 5 and 6) will focus on the noninvasive characterization of hydrogel properties in myocardial explants using non-contrast agent based-MRI techniques. Chapter 5 will explore the use of conventional MRI to qualitatively and quantitatively assess three-dimensional HA hydrogel dispersion. Differences in hydrogel volume distribution in tissue will be induced by alterations in gelation conditions. Chapter 6 will utilize MRI with endogenous CEST contrast to detect differences in material properties (i.e. macromer concentration) and visualize HA hydrogels in tissues by manipulating the exchangeable protons. In contrast to traditional MRI, CEST MRI will be applied to discriminate between injectable materials based on their distinctive chemistries.

After exploring the ability to examine differences in hydrogel properties after injection into the myocardium, the following portion of the dissertation (Chapter 7) will focus on understanding the impact of hydrogels on the surrounding myocardial tissue properties in an *in vivo* porcine infarct model. Cardiac MRI will be used to temporally evaluate the effect of injectable HA hydrogels on remodeling post-MI by measuring global LV volumes and functional outputs as well as regional thicknesses, wall strains, and myocardial stiffnesses with the use of FE modeling. Finally, Chapter 8 will summarize the main conclusions and discuss the limitations and future directions of each Specific Aim.

CHAPTER 3

A Review of Hydrogels in Cardiac Tissue Engineering

(Adapted from: Dorsey SM, Burdick JA. In: Khademhosseini A, Demirci U, editors. Applications of Hydrogels in Regenerative Medicine, in press.)

3.1. Introduction

Heart failure is a major public health issue that affects almost 23 million individuals worldwide and 5 million individuals in the US alone.[1] As discussed in Chapter 1, survival after the diagnosis of heart failure has improved but the death rates remain high, with half of patients dying within 5 years.[2] In fact, one in every nine U.S. death certificates in 2010 mentioned heart failure as a contributing factor.[2] Moreover, the majority of heart failure cases have been attributed to the process of left ventricular (LV) remodeling following myocardial infarction (MI).[2,3] As described in Chapter 1, injectable hydrogels are a promising therapy to attenuate this adverse remodeling by limiting infarct expansion to prevent progression to heart failure. In contrast to LV restraints and surgical reconstruction of the LV as means to alter geometry post-MI, injectable hydrogels offers the potential of minimally-invasively, percutaneous delivery to facilitate clinical translation.

Both natural and synthetic materials have been explored as acellular bulking agents to mechanically stabilize the myocardium and as delivery vehicles for cells and/or therapeutic molecules to modulate the maladaptive biological processes after infarction (**Figure 3.1**). Various materials, cells, and therapeutic molecules have shown positive outcomes in animal models and, in doing so, provide insight for future material development and optimization. However, many questions remain before injectable hydrogel systems can be safely translated to patients. Future work should focus on elucidating the mechanism behind the positive outcomes of hydrogel delivery *in vivo* and the application of these systems to clinically relevant scenarios, including

minimally-invasive, percutaneous delivery. Further development of injectable hydrogel systems for cardiac repair will have considerable clinical impact with respect to broadening our understanding of the mechanisms of remodeling post-MI and improving therapies to prevent progression to heart failure. Towards this goal, this chapter will focus the *in vivo* applications of biomaterials for 1) tissue bulking, 2) cell delivery, 3) small molecule delivery, and 4) combined cell and molecule delivery (**Figure 3.1**) approaches, with an emphasis on injectable hydrogels.

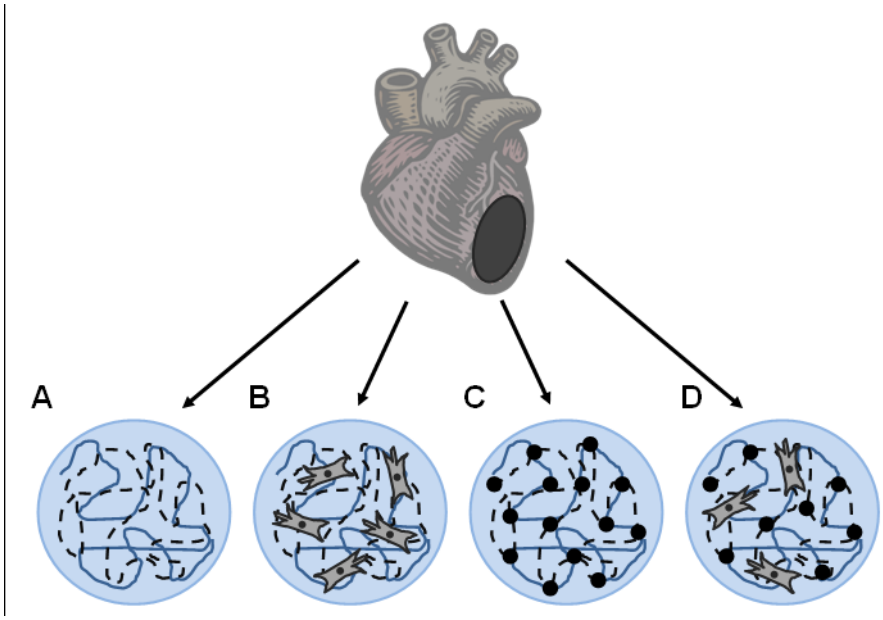

Figure 3.1. Schematic of injectable hydrogel strategies for MI repair. Hydrogels can be used as acellular bulking agents (A) or as a delivery vehicle for cells (B), therapeutic molecules (C), or a combination of cells and molecules (D).

3.2. Acellular Approaches

3.2.1. LV Restraints

Over the past decade, it has become evident that the regional mechanical changes in the myocardial tissue properties following MI must be considered when designing biomaterial-based approaches for cardiac repair.[4,5] After MI, the myocardial wall thins in the infarct region and the

LV dilates as the heart shifts to a more spherical shape; this leads to an increase in stress in the borderzone (BZ) regions surrounding the infarct. As described by the Law of Laplace (**Equation 3.1**), stress (T) is directly proportional to pressure (P) and the radius of curvature (R) and inversely proportional to the myocardial thickness (h). Therefore, an increase in the ventricular radius (R) and decrease in wall thickness (h) leads to an increase in myocardial stress.

$$T = \frac{P*R}{h} \qquad (3.1)$$

Previous strategies to attenuate LV expansion include the use of polymeric meshes wrapped around the heart or sutured to the infarct surface, referred to as LV restraints. The theory behind the use of ventricular restraints is that by forcing the heart to maintain its elliptical shape and preventing an increase in the ventricular radius (R) of the LV, this will, in turn, lead to decreased myocardial wall stress (T) to ultimately attenuate LV remodeling.[6-9]

Several studies examined the use of biomaterial supports to restrain the LV to prevent dilatation and adverse remodeling.[10] Kelley et al. demonstrated preserved LV geometry and cardiac function in a sheep MI model with suturing of a poly(propylene) (Marlex) mesh to the infarct.[7] Subsequently, Bowen et al. demonstrated that the poly(propylene) restraint has biological significance, leading to increased collagen and decreased protease (MMP-1, MMP-2) activity in the BZ myocardium.[11] Since these initial studies, the use of heart-wrapping techniques has shown that infarct expansion limitation has a pronounced effect in ameliorating post-MI remodeling[6-9,12], motivating translation to clinical trials. Acorn Cardiovascular, Inc. (St. Paul, Minnesota) developed the first commercially available restraint, consisting of a knitted polyester mesh to be fitted around both ventricles. In both canine[13,14] and ovine[12,15] infarct models, the Acorn CorCap restraint decreased LV volumes and improved function. This led to a clinical trial encompassing 300 patients where the use of CorCap decreased LV volumes, improved quality of life, and decreased the likelihood of additional cardiac procedures.[16] More recently, Paracor Medical (Sunnyvale, California) developed a HeartNet LV support system made from a nitinol

mesh that is placed around the ventricles. Similarly, both canine[17] and ovine[18] MI models showed decreased LV end diastolic volume (EDV) and end systolic volume (ESV). An initial safety and feasibility clinical study suggested a functional and clinical benefit from the Paracore HeartNet device,[19] leading to a phase II clinical trial (PEERLESS-HF).[20] However, the clinical trial was stopped prematurely due to limited effects on certain functional end points.[21] Ultimately, despite promising results in both large animal models and clinical trials, a major limitation of polymeric LV restraints is the highly invasive surgical procedure necessary for implantation. Thus, minimally invasive approaches are needed to limit infarct expansion and preserve LV geometry post-MI.

3.2.2. Injectable Hydrogels as Bulking Agents

Similar to infarct restraints, acellular injectable biomaterials can also limit infarct expansion by bulking the damaged myocardial wall to provide mechanical stabilization.[23] Infarcts naturally stiffen over time as wound healing progresses and collagen is deposited. Therefore, the goal of injectable hydrogels is to modify the material properties of the infarct region before the body compensates for the remodeling process; in doing so, infarct expansion and remodeling post-MI can be limited.[23] Referring back to the Law of Laplace (**Equation 3.1**), the theory behind the use of injectable hydrogels as bulking agents is that they increase the wall thickness (h) to decrease LV dilatation (R) and in turn, decrease wall stress (T). Theoretical finite element (FE) models have been used to evaluate the ability of injectable biomaterials to attenuate remodeling (**Figure 3.2**).[22,24,25] Simulated injections of a non-contractile material into an infarcted LV were shown to decrease LV dilatation and reduce elevated myofiber stresses.[24] In a subsequent study, injection of a tissue filler into the infarct reduced stress in the LV and improved ejection fraction (EF) in an ovine infarct model.[25] For the first time, the use of injectable biomaterials presents the real possibility of limiting adverse LV remodeling using minimally invasive delivery.

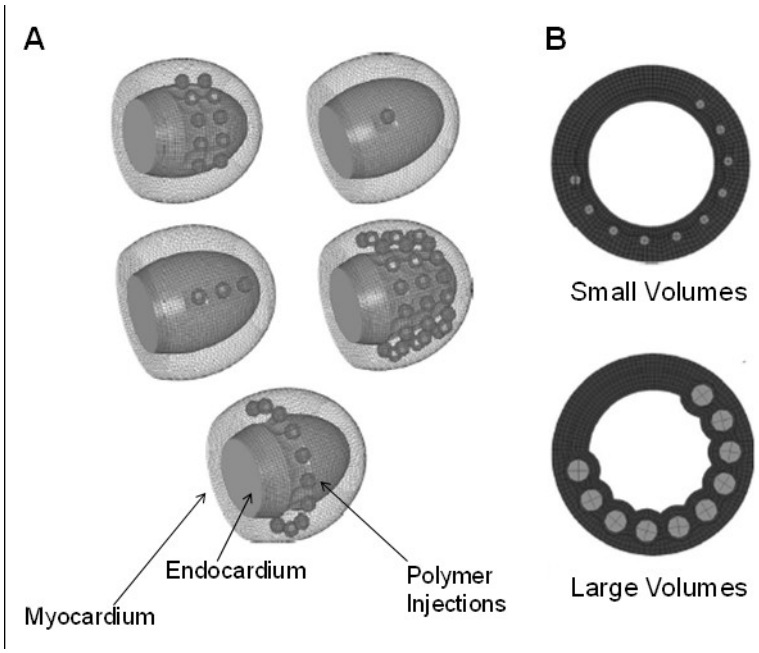

Figure 3.2. Finite element (FE) model of simulated polymer injections, demonstrating injected materials and the importance of injection pattern (A) and volume of material dispersion (B) in decreasing myocardial stress. Figure adapted from [22].

3.2.2.1. Natural Acellular Hydrogels

Hydrogels can be grouped into either natural or synthetic materials. Natural materials offer several advantages due to their inherent biological properties, including presentation of receptor-binding ligands and susceptibility to cell-triggered proteolytic degradation[26,27] For cardiac applications where the goal is to replace or repair the damaged ECM, natural biomaterials more closely mimic features of the native ECM, enabling them to increase cell adhesion, activate cell proliferation, and maintain cell differentiation.[28] Commonly used natural, injectable materials for cardiac repair include fibrin, alginate, collagen, Matrigel, chitosan, hyaluronic acid, keratin, and decellularized matrices (**Table 3.1**).

Fibrin: Fibrin, a fibrillar protein consisting of fibrinogen and thrombin, is natively a blood component critical to the clotting cascade. A two component system is required to form fibrin

hydrogels: 1) fibrinogen and aprotinin, a fibrinolysis inhibitor, and 2) thrombin, factor XIIIa, and calcium chloride ($CaCl_2$). When combined, fibrinogen converts to fibrin and self-assembles to form a mesh crosslinked by factor XIIIa. Fibrin naturally has binding domains for soluble growth factors and cellular integrin receptors, making it an ideal candidate for wound healing applications.[29] Fibrin hydrogels have been used for MI therapy[30-33] due to favorable properties such as biodegradability, mechanical strength, and angiogenic activity.[34]

Christman et al. first injected fibrin and showed positive outcomes on cardiac function.[30-32] Specifically, MI was induced in rats (temporary coronary occlusion) followed by injection of fibrin glue ten days later. Assessment five weeks after delivery revealed preserved infarct wall thickness and fractional shortening (FS) as compared to bovine serum albumin (BSA) controls.[30] In a subsequent study, Christman et al. showed that injectable fibrin alone significantly decreased infarct area and increased arteriole density in the infarct region as compared to control BSA injections.[31] The ability of injectable fibrin to induce neovascularization in the infarct region was later confirmed by Huang et al.[33]

Alginate: Alginate is a naturally occurring, linear polysaccharide derived from seaweed. Its tailorability and non-thrombogenicity make it attractive for cardiac repair.[35-37] It consists of linked ß-D-mannuronate and α-L-guluronate residues that crosslink into hydrogels in the presence of calcium.[38] Alginate's unique gelation enables delivery using minimally invasive, catheter-based intracoronary infusion, which relies on the infarct myocardium's leaky vasculature. Due to inadequate levels of calcium in the vasculature, alginate does not crosslink until it reaches the infarct, where high levels of calcium induce gelation.[36]

Landa et al. delivered alginate to rats at seven and 60 days post-MI (permanent coronary occlusion) for acute and chronic remodeling, respectively.[37] Eight weeks after injection, delivery into recent or old infarcts increased scar thickness and attenuated LV systolic and diastolic dilatation and dysfunction. However, FS was not improved in either group.[37] These results provide insight into the timing for hydrogel delivery post-MI. In contrast, Leor et al. delivered

alginate hydrogels to a clinically relevant, porcine MI model using a coronary catheter.[36] To investigate the effects of delivering different hydrogel volumes, alginate solutions at incremental volumes (1, 2, or 4 mL) were delivered four days post-MI (temporary occlusion). At 60 days after delivery, intracoronary injection of alginate (2 and 4 mL) prevented and even reversed LV systolic and diastolic dilatation. In addition, the 2 mL alginate injection led to myofibroblast infiltration and increased scar thickness as compared to saline controls.[36] Similar to the study by Landa et al., there were no significant FS improvements.

Due to the positive results of alginate in both small[37] and large[36] animal models, it has become the first injectable acellular biomaterial used in clinical trials. An injectable system of sodium alginate and calcium gluconate was first developed and tested by BioLineRx, Ltd. as BL-1040. In a phase I/II pilot clinical trial, the safety and feasibility of BL-1040 was demonstrated in 27 patients, including improved survival, preserved LV EDV and ESV, prevention of FS deterioration, improved mitral regurgitation, and limitation of systolic wall thinning (NCT00557531).[39] Since then, BioLine, Ltd. out-licensed BL-1040 to Ikaria Holdings, Inc., which is currently performing a placebo-controlled, double-blind phase II clinical trial with 300 patients (NCT01226563).[40] More recently, LoneStar Heart, Inc. developed an injectable alginate hydrogel (Algisyl-LVR) that demonstrated improved LV function and decreased myofiber stress[41] in a safety and feasibility phase II clinical trial of 11 patients with dilated cardiomyopathy undergoing open-heart surgery (NCT00847964).[42,43] Subsequently, in an ongoing randomized, controlled phase II/III clinical trial, Algisyl-LVR was delivered to 35 heart failure patients and compared to 38 patients who received standard medical care. Primary 6-month results showed significantly improved clinical outcomes in terms of peak maximum oxygen uptake VO_2 and a 6-minute walk test with hydrogel therapy (NCT01311791),[44] leading to an open-label rollover trial for those enrolled in the control portion of the study (NCT02226679).[45]

Several studies have studied the effect of modifying normally non-adhesive alginate with adhesive peptides such as Arg-Gly-Asp (RGD) or Tyr-Ile-Gly-Ser-Arg (YIGSR).[46,47] Yu et al.

delivered modified and unmodified alginate to rats five weeks post-MI (temporary occlusion).[46] Five weeks after injection, delivery of either RGD modified or unmodified alginate led to decreased EDV and ESV, improved FS, significantly increased myocardial wall thickness, and significantly increased arteriogenesis as compared to BSA controls. Although both groups led to increased arterioles in the infarct, the RGD modified alginate group had the highest number of arterioles,[46] demonstrating that surface modification can influence the infarct microenvironment. Further, Tsur-Gang et al. delivered unmodified alginate, alginate modified with adhesion peptides RGD and YIGSR, and alginate modified with a non-specific peptide, RGE, to rats seven days post-MI (permanent occlusion).[47] In this case, unmodified alginate led to the best improvements in infarct thickness, LV geometry, and FS 60 days after injection. However, no significant differences were seen in relative infarct thickness, cell infiltration, or blood vessel density between the groups.[47] Differences in material viscosity may explain some of these findings.

Due to the positive benefits of fibrin and alginate alone, Mukherjee et al. delivered a fibrin-alginate composite to pigs one week post-MI (permanent occlusion).[48] Injections were performed using a double-barrel syringe; one component was composed of fibrinogen, fibronectin, factor XIII, plasminogen, and gelatin-grafted alginate dissolved in an aprotinin solution while the other consisted of thrombin and $CaCl_2$. Assessment performed at one, two, and three weeks after delivery demonstrated significantly increased wall thickness at one week and limited LV expansion at two and three weeks post-injection. However, no functional improvements were observed. In addition, the composite led to significantly reduced soluble collagen vulnerable to protease degradation and decreased protease levels (e.g., MMP-2) in the infarct as compared to saline controls, providing a potential mechanism for attenuated infarct expansion.[48]

Collagen: Collagen is the most abundant protein in the human body and the predominant ECM protein. Due to extensive ECM damage post-MI, delivery of injectable collagen is well-suited for cardiac repair.[49] Collagen can be prepared in an injectable form which self-assembles at physiological pH and temperature into a fibrous hydrogel.[50] In addition, collagen has been shown

to promote angiogenesis and myoblast infiltration in the ischemic myocardium.[33] Dai et al. delivered commercially available Zyderm (INAMED Corp., Santa Barbara, California), a bovine dermal collagen (95% collagen type I, 5% collagen type III) to rats one week post-MI (permanent occlusion).[51] Six weeks after delivery, collagen treated animals had higher stroke volume (SV), increased EF, increased wall thickness, and absence of paradoxical LV systolic bulging as compared to controls.[51] Unlike other natural hydrogels for cardiac repair, this study did not show increased angiogenesis or cell infiltration, potentially due to differences in collagen types or concentration injected, limiting cell migration into the infarct.

Matrigel: As an alternative to pure collagen, Matrigel (BD Biosciences) is a commercially available, purified matrix isolated from a mouse sarcoma line that encompasses collagen as well as basement membrane proteins, including laminin and entactin, and growth factors.[52,53] Similar to collagen, it undergoes a phase transition at physiological temperature to generate hydrogels. Ou et al. delivered Matrigel to rats immediately post-MI (permanent occlusion) and demonstrated significantly increased vessel density, enhanced recruitment of cardiac progenitor cells (CPCs), improved LV peak rate of pressure rise, increased wall thickness, and enhanced EF four weeks post-MI.[54] In contrast, Kofidis et al. delivered growth-factor free Matrigel to mice immediately post-MI (permanent occlusion) but did not demonstrate significantly increased FS at two weeks post-MI as compared to controls but did show trends towards increased scar thickening and improved function.[55] In another study, Kofidis et al. delivered Matrigel to a rat MI model and saw trends towards increased wall thickness and decreased end diastolic diameter (EDD) compared to controls two weeks post-MI.[56]

Chitosan: Chitosan is a non-mammalian, linear polysaccharide derived by deacetylating chitin, the main component of crustacean exoskeletons. Chitosan undergoes a temperature-induced phase transition to form hydrogels at physiological temperature when mixed with glycerol phosphate and a glyoxal salt solution.[57,58] Gelation temperature can be altered by changing the glyoxal concentration and degradation kinetics can be controlled by the degree of

deacetylation.[59-61] Lu et al. delivered a previously developed chitosan hydrogel[59] to rats one week post-MI (permanent occlusion). Four weeks after injection, the myocardial wall thickness was significantly increased, LV EDD and end systolic diameter (ESD) significantly decreased, EF and FS enhanced, infarct size decreased, and microvessels within the infarct increased for animals treated with chitosan as compared to saline controls.[57] These results were further confirmed by Wang et al.[62] and Liu et al.[58] where chitosan alone resulted in significant improvements in EF, FS, infarct size, wall thickness, and vessel density.

Hyaluronic acid: Hyaluronic acid (HA) is a linear polysaccharide abundant in the body that serves a role in processes such as scar reduction, cell migration, and angiogenesis.[63] Even though HA is naturally derived, it is often chemically modified to tune its material properties and enable hydrogel formation.[64-66] Yoon et al. developed HA hydrogels consisting of acrylated HA with thiol-terminated PEG crosslinkers (PEG-SH_4). Injection into rats two weeks post-MI (permanent occlusion) led to increased vessel formation, decreased apoptosis, reduced infarct area, and significantly enhanced EF and SV as compared to infarct controls at four weeks after delivery. Interestingly, results showed increased wall thickness while histology revealed complete hydrogel degradation at four weeks.[64]

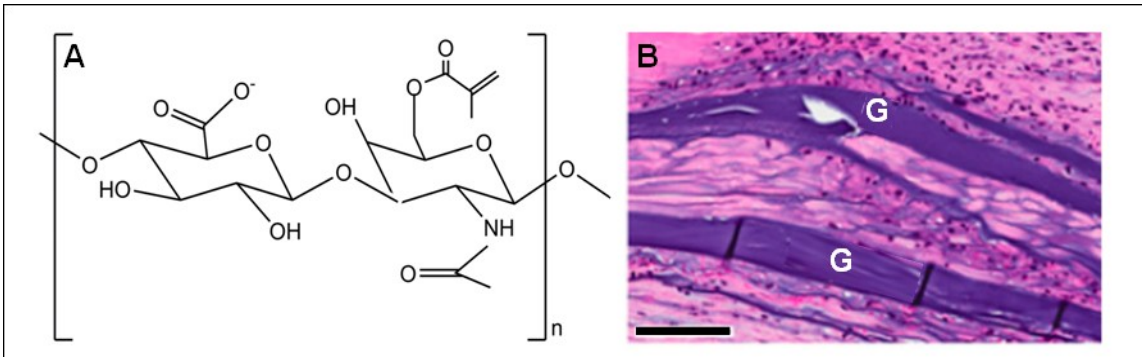

Figure 3.3. Natural, injectable hydrogel for acellular cardiac repair. Chemical structure of methacrylated HA (A) and representative H&E stain of the hydrogel at 8 weeks post-MI (B). G = Gel, Scale bar = 50 mm. Figure adapted from [65].

Ifkovits et al. developed methacrylated HA (MeHA) hydrogels crosslinked with redox radical initiators, ammonium persulfate (APS) and *N*,*N*,*N*′,*N*′-tetramethylethylenediamine (TEMED).[65] Two formulations with different initial mechanics but similar degradation were injected into sheep thirty minutes post-MI (permanent occlusion). Both hydrogels significantly increased wall thickness relative to infarct controls eight weeks post-MI (**Figure 3.3**). However, only the higher modulus gels significantly reduced infarct expansion with trends toward decreased EDV and ESV and increased EF.[65] In a subsequent study, Tous et al. compared stable MeHA hydrogels with hydrolytically degradable HA hydrogels and demonstrated that stable hydrogels improved wall thickness and LV volumes more efficiently than degradable hydrogels.[66] These studies highlight the importance of material properties (e.g., mechanics, degradation) in MI repair.

Keratin: Keratin is another injectable, natural hydrogel being explored for cardiac applications. It can be extracted from human hair or animal wool and processed into an injectable material that self-assembles into a fibrous hydrogel.[67] Shen et al. delivered keratin-based hydrogels to rats immediately post-MI (permanent occlusion) and revealed increased angiogenesis, increased wall thickness, decreased infarct size, and enhanced EF and FS as compared to saline controls at four and eight weeks post-MI.[68] Based on these results, keratin-based hydrogels are a promising acellular therapy for cardiac repair.

Decellularized ECM: Decellularization of tissues is appealing for tissue engineering because tissue-specific materials can be generated from the same tissue being treated.[69] Decellularized ECM more closely mimics the unique ECM composition of each tissue, which includes specific fibrous proteins (collagen, fibrin, elastin, etc.), proteoglycans and glycosaminoglycans. In addition, its natural thermoresponsive behavior enables it to be a liquid hydrogel precursor at 25°C and then self-assemble to form nanofibrous hydrogels at 37°C.[70-73]

Singelyn et al. utilized a decellularized porcine ECM that self-assembles to form a myocardial matrix at physiological temperature.[70-72] When injected into the LV of healthy rats, it induced significant increases in arteriole formation 11 days after injection.[70] Injection into infarcted

rats two weeks post-MI (temporary occlusion) led to preserved cardiac function and structure at one and four weeks after delivery, as evidenced by maintained EF, EDV, and ESV. Histology revealed increased proliferating cells and recruitment of endogenous CPCs to the infarct. A feasibility study was then performed to assess the efficacy of catheter delivery in a porcine model; histology confirmed hydrogel retention and distribution. This was the first study to successfully demonstrate transendocardial injections of an *in situ* gelling material in a clinically relevant, large animal model.[71] In a subsequent study, Seif-Naraghi et al. delivered this porcine ECM hydrogel to pigs two weeks post-MI (permanent occlusion) using a NOGA-guided MyoStar catheter (Biologics Delivery Systems, Irwindale, California). Three months after delivery, echocardiography revealed increased cardiac function, decreased LV volumes, and improved global wall motion scores.[72]

Okada et al. developed injectable hydrogels from decellularized small intestinal submucosa (SIS) and injected them into mice immediately post-MI (permanent occlusion).[73] Two hydrogel forms, SIS-B and SIS-C, were evaluated for their therapeutic potential post-MI. SIS-B was characterized to have increased mechanical properties and significantly more basic fibroblast growth factor (bFGF) as compared to SIS-C. Assessment at two and six weeks post-MI revealed SIS-B delivery led to reduced infarct size, increased capillary density, preserved LV end systolic geometry, and improved cardiac contractility whereas SIS-C had minimal to no benefits as compared to saline controls.[73] Since no further information was provided on the two SDS forms, it can be hypothesized that the outcomes were due to differences in bFGF concentration.

3.2.2.2. Synthetic Acellular Hydrogels

Despite several advantageous properties, natural materials are generally limited in the ability to tailor their properties. In contrast, synthetic materials have defined material properties, including molecular weight, gelation, hydrophilic/hydrophobic properties, degradation, and mechanics, without batch-to-batch variations.[27] Despite their inherent lack of bioactivity, synthetic materials can be modified with cell binding sites or adhesive ligands to encourage cell interaction.[74] For cardiac applications, synthetic materials can be designed to trigger cellular

events, minimize the immune response, and degrade at a controlled rate, thus enabling cell integration and potentially, improvements in cardiac function long-term.[26] Various synthetic materials have been explored for cardiac repair therapy, including poly(N-isopropylacrylamide) (PNIPAAm) and poly(ethylene glycol) (PEG) based hydrogels (**Table 3.1**).

Poly(N-isopropylacrylamide) (PNIPAAm): Several studies have focused on the use of PNIPAAm-based hydrogels due to their thermoresponsive properties.[75-78] Fujimoto et al. developed a hydrogel from the copolymerization of NIPAAm, acrylic acid (AAc) and hydroxylethyl methacrylate-poly(trimethylene carbonate) (HEMAPTMC) to generate poly(NIPAAm-co-AAc-co-HEMAPTMC), which gels at 37°C and degrades over five months.[75] Injection into rats two weeks post-MI (permanent occlusion) led to significantly increased wall thickness, maintained LV end diastolic area, and preserved percent LV fractional area change compared to saline controls at four and eight weeks post-MI. There was also enhanced capillary density and positive staining for α-smooth muscle actin in the infarct, providing insight to the mechanism of functional repair.[75]

Similarly, Wang et al. developed a thermosensitive hydrogel consisting of biodegradable dextran grafted to hydrophobic poly(ε-caprolactone)-2-hydroxylethyl methacrylate (PCL-HEMA) and copolymerized with thermoresponsive PNIPAAm to form Dex-PCL-HEMA/PNIPAAm.[76] Injection into rabbits four days post-MI (permanent occlusion) led to significantly increased EF, reduced EDD and ESD, increased end systolic pressure (ESP), decreased end diastolic pressure (EDP), increased cardiac contractility, and reduced infarct size as compared to saline controls at one month after delivery. Hydrogel treatment led to significantly increased infarct thickness despite no histological evidence of the material remaining at 30 days.[76]

Wall et al. developed semi-interpenetrating polymer network (sIPN) hydrogels with RGD adhesion sites and MMP degradable crosslinkers.[77] Thermoresponsive poly(*N*-isopropylacrylamide-*co*-acrylic acid) [p(NIPAAm-*co*-AAc)] was gelled using free radical polymerization induced by APS and TEMED. Injection into mice immediately post-MI (permanent ligation) led to significantly increased wall thickness and increased FS as compared to saline

controls with a trend towards improved EF at six weeks post-MI. In addition, there were no statistical differences in FS or EF between animals treated with sIPN injection as compared to sham-operated, noninfarcted mice by six weeks.[77]

Polyethylene glycol (PEG): PEG and its derivatives have been widely studied as injectable hydrogels for MI repair.[79-84] Jiang et al. developed a novel hydrogel consisting of α-cyclodextrin (α-CD) and linear triblock copolymer, poly(ethylene glycol)-*b*-polycaprolactone-(dodecanedioic acid)-polycaprolactone-poly(ethylene glycol) (MPEG-PCL-MPEG), where degradation is controlled by the triblock copolymer.[79] Injection into rabbits one week post-MI (permanent occlusion) resulted in significantly improved LV EF, decreased EDD and ESD, reduced scar thickness, and decreased infarct size at four weeks after delivery. In a subsequent study, Wang et al. applied the same α-CD/MPEG-PCL-MPEG hydrogel to rats five minutes post-MI (permanent occlusion) and demonstrated significantly improved FS, decreased LV EDD and ESD, increased ESP, and decreased infarct size as compared to saline controls one month after delivery.[82] In both studies, no significant improvements were seen in infarct neovascularization.

Wu et al. developed a thermoresponsive PEG-based hydrogel consisting of an aliphatic, triblock copolymer, poly (δ-valerolactone)-*block*-poly (ethylene glycol)-*block*-poly (δ-valerolactone) (PVL-*b*-PEG-*b*-PVL).[83] This polymer dissolves in water at room temperature, but gels at 37°C. Injection into rats one week post-MI (permanent occlusion) led to significantly increased EF, improved end systolic elastance, improved preload recruitable strong work, reduced ESV and EDV, decreased infarct area, increased wall thickness, and increased blood vessel density five weeks after injection.[83] Similarly, Kraehenbuehl et al. delivered a MMP-responsive, PEG-vinylsulfone (PEG-VS) hydrogel to rats one hour post-MI (permanent occlusion) and showed significantly increased EF and decreased ESV with trends toward decreased EDV and reduced infarct size as compared to saline controls at six weeks post-MI.[84]

Table 3.1. Summary of acellular hydrogel systems and their assessment in animal MI models.

Material	Animal/ MI Model	Injection Time (post-MI)	Injection Volume	Evaluation Time (post-delivery)	Ref.
Alginate	Rat; Proximal LCA ligation	1 week and 2 months	100-150 µL	2 months	37
	Swine; Transient LAD occlusion	4 days	1, 2, and 4 mL	2 months	36
	Rat; Proximal LCA ligation	1 week	130 µL	2 months	47
Collagen	Rat; Proximal LCA ligation	1 week	100 µL	6 weeks	51
Matrigel	Rat; LAD ligation	Immediate	50 µL x 5 sites	4 weeks	54
Hyaluronic acid	Rat; LCX ligation	2 weeks	50 µL	4 weeks	64
	Sheep; LAD and D2 ligation	30 minutes	200 µL x 20 sites	2 and 8 weeks	65
	Sheep; LAD and D2 ligation	30 minutes	200 µL x 20 sites	2 and 8 weeks	66
Keratin	Rat; LAD ligation	Immediate	100 µL	4 and 8 weeks	68
Decellularized ventricular ECM	Rat; LAD ligation/ reperfusion	2 weeks	75 µL	1 and 4 weeks	71
	Swine; LAD embolization	2 weeks	250 µL x 14-15 sites	3 months	72
Decellularized SIS ECM	Mouse; LAD ligation	Immediate	20 µL	2 and 6 weeks	73
Poly(NIPAAm-co-AAc-co-HEMAPTMC)	Rat; LAD ligation	2 weeks	100 µL x 5 sites	4 and 8 weeks	75
Dex-PCL-HEMA/ PNIPAAm	Rabbit; Proximal LCA ligation	4 days	50 µL x 4 sites	1 month	76
αCD/MPEG-PCL-MPEG	Rabbit; LAD ligation	1 week	50 µL x 4 sites	4 weeks	79
PEG-VS	Rat; LAD ligation	2 minutes	100 µL (via 2-3 sites)	4 and 13 weeks	80
	Rat; LCA ligation	9 days	100 µL	7 and 50 days	81

*SIS = small intestinal submucosa, LAD = left anterior descending coronary artery; LCX = left circumflex coronary artery, LCA = left coronary artery, OM1 = obtuse marginal I branch, OM2 = obtuse marginal II branch, D2 = second diagonal branch

In contrast to degradable PEG hydrogels, Dobner et al. delivered a non-degradable PEG-VS hydrogel polymerized with dithiothreitol (DTT) to rats two minutes post-MI (permanent occlusion).[80] At four weeks post-MI, the PEG-VS hydrogel significantly increased wall thickness and decreased LV EDD. However, at 13 weeks, the pathological progression of the treatment animals was similar to that of saline controls. FS was not improved in hydrogel animals at either time point.[80] Rane et al. applied the same bioinert, non-degradable PEG-VS hydrogel to rats nine days post-MI (permanent occlusion) and demonstrated significant increases in wall thickness as compared to saline controls at 50 days post-MI.[81] Despite this, there was a steady decline in cardiac function and expansion of LV volumes in both the hydrogel and control animals. In addition, there were no significant differences in neovascularization or cell infiltration between hydrogel and control groups.[81] Similar to Dobner et al., Rane et al. found that increased wall thickness alone was insufficient to cause positive structural and functional outcomes. These studies suggest that the bioactivity and ability for cells to infiltrate degradable biomaterials are important to preserving cardiac function post-MI. In addition, prolonged material presence alone may be insufficient to attenuate adverse LV remodeling.

3.3. Cellular Approaches

3.3.1. Cell Delivery

MI results in the loss of over one billion cardiomyocytes in the infarct region.[85] It was previously believed that after such massive cardiomyocyte loss, the adult myocardium lacked an intrinsic regenerative capacity for repair.[86] Recently, studies have confirmed the activation of resident cardiac stem/progenitor cells and/or recruitment of endogenous stem cells post-MI.[87] However, this innate regenerative capacity is not sufficient to compensate for the large-scale tissue loss post-MI.[88] Thus, the delivery of exogenous cells has emerged as a therapy for MI repair.[89] A variety of cell types have been shown to be effective for cardiac repair, including fetal or neonatal cardiomyocytes, embryonic stem cells (ESCs), skeletal myoblasts, bone marrow-derived stem cells (BSCs), adipose-derived stem cells, and cardiac stem cells (CSCs).[90,91]

ESCs offer the advantage of differentiating into both cardiomyocyte and vascular lineages but are limited due to their immunogenicity, risk of tumor development, and ethical concerns.[92] Skeletal myoblasts have fewer ethical concerns and offer the advantages of being autologous, easy to obtain and expand, and resistant to ischemia.[93] However, they cannot differentiate into cardiomyocytes[94] and, even though they are naturally contractile, they have a limited ability to contract synchronously with host cardiomyocytes.[95] BSCs are another autologous option that can be readily isolated, rapidly expanded in culture, and can maintain or modify their phenotype to complement the host tissue.[96] The bone marrow is a common source of adult stem/progenitor cells, including mesenchymal stem cells (MSCs), endothelial progenitor cells (EPCs), and hematopoietic stem cells (HSCs).[97] However, it remains unclear if BSCs can truly differentiate into cardiomyocytes *in vivo*.[94] In contrast, resident CSCs are multipotent and can differentiate into cardiomyocytes *in vivo,*[87] but there are concerns with scalability and autologous isolation from patients with recent MI.[98] Thus, each cell type offers a unique set of advantages and limitations, making it challenging to select an ideal cell source for cardiac repair.

Cell delivery, or cellular cardiomyoplasty, involves directly delivering cells to the infarcted myocardium using intramyocardial injection, intracoronary infusion, or interstitial retrograde coronary venous delivery. The feasibility of delivering cells alone to the heart has been confirmed for nearly two decades.[99] While both animal models[91] and clinical studies[90] demonstrate significant improvements in cardiac function, this improvement is often not clinically relevant and, for the most part, transient.[100] This transiency is due to unsatisfactory cell retention, survival, and engraftment.[89] Regardless of the delivery method, there is lack of cell retention at the injection site due to the low viscosity of a cell-saline suspension, causing the cells to leak out during injection.[101] Of the small percentage of cells that do engraft, they often lack appropriate functionality to have a therapeutic effect.[102] Hofmann et al. and Hou et al. showed that less than 10% of BMCs delivered are detected two hours after injection.[103,104] Of the retained cells, approximately 90% die within the first week due to the myriad of stresses encountered upon injection into the infarct, including physical stress, ischemia due to microvasculature obstruction,

myocardial hypoxia, inflammation, and release of cytokines and reactive oxygen species.[105] In addition, due to ECM breakdown post-MI, the retained cells lack an anchoring matrix which may result in anoikis, a form of programmed cell death due to loss of normal cell-matrix interactions.[106] Ultimately, in spite of enthusiasm for cell delivery, regeneration of functional, integrated myocardium in the infarct has yet to be demonstrated in large animal models or patients.

Due to these challenges, biomaterials have been explored to enhance cell retention and engraftment for cardiac repair by improving cell attachment, migration, and survival upon delivery.[33] In addition, biomaterials can enhance tissue angiogenesis,[31,33] activate cells to produce cytokines,[33] enhance cell retention,[31] and influence cell differentiation.[107] Polymers can be designed to influence integrin binding sites with a range of matrix pore sizes, substrate topography, and substrate rigidity.[108] Biomaterial approaches for cell delivery include *in vitro* engineered cardiac muscle patches and injectable biomaterials.

3.3.2. Cardiac Patches

Cardiac patches may provide structural support to limit LV dilation post-MI, similar to LV restraints, but with the added benefit of cell delivery. They are constructed by seeding cells onto a biomaterial scaffold *in vitro* for subsequent *in vivo* implantation onto the infarcted myocardium.[109,110] Theoretically, cardiac function improves through the combination of cell-mediated remodeling[111] and material-based mechanical stabilization which attenuates myocardial dilatation.[112] Because the cells are anchored to the scaffold, cardiac patches lead to better engraftment when compared to cell delivery alone.[112]

Li et al. demonstrated the use of a cardiac patch to deliver cells for cardiac repair.[113] Fetal cardiomyocytes were seeded on a gelatin mesh *in vitro* and subsequently implanted onto the infarct of a rat MI model, leading to prolonged cell survival over five weeks and a trend towards improved LV function.[113] Since this early study, a variety of natural and synthetic cardiac patches have led to positive functional outcomes *in vivo* as compared to injection of cells

alone.[109,110] Hamdi et al. compared delivery of skeletal myoblasts through intramyocardial injection, formation as a cell sheet, or using a collagen-based cardiac patch at four weeks post-MI.[114] Animals that received the cell sheet or cell seeded scaffold had significantly improved EF and increased vessel density one month after delivery as compared to culture medium controls.[114] The promising results in animal models have led to clinical trials involving cardiac patches for MI repair. In the MAGNUM phase I clinical trial, BMCs were seeded on type I collagen cardiac patches and delivered to ten patients with coronary artery bypass grafts and intrainfarct implantation of autologous bone marrow cells. The combined cell injection and cardiac patch approach led to improved LV EDV and increased scar thickness as compared to cell injection alone.[115] Additional studies using 3D fibrin cardiac patches have shown similar results.[116-118]

Despite success with cardiac patches, major drawbacks still remain. Although the purpose is to improve cell engraftment, the reality is there is low engraftment within patches when implanted *in vivo* due to inadequate angiogenesis.[112,116,117] Low vascularization limits graft thickness due to an inability to support the high oxygen and nutrient demands of cells at depths greater than ~100 μm.[119] In addition, the patches must be sutured to the infarct,[35] a technique which may be useful to prevent LV dilatation but is unlikely to directly contribute to myocardial contractility and function. The location of the patch on the epicardial surface of the heart also limits the region of therapeutic benefit. Most importantly, the invasive surgical procedure necessary for implantation limits clinical translation.

3.3.3. Injectable Hydrogels for Cell Delivery

Injectable hydrogels for cell delivery offer the advantage of enhancing cell retention, survival, and engraftment with the potential for minimally-invasive, percutaneous catheter-based delivery,[36,71,72] which may enhance clinical translation.[37,53,57,120] As compared to rigid cardiac patches with limited radial engraftment, injectable hydrogels can form *in situ*, integrate into the host tissue, and adapt to the surrounding contracting myocardium.[121] One of their major benefits is that hydrogel crosslinking typically occurs after the addition of cells, enabling complete cell

encapsulation into a viscous but flowable delivery matrix that solidifies upon injection into the myocardium. Hydrogel shape, stiffness, and thickness can be controlled to ensure formation into the geometry of the injection site.[122] Hydrogels not only provide three-dimensional support to enhance cell retention, but also permit control over the biophysical and biochemical microenvironment of the transplanted cells to prolong survival and engraftment.[123] In turn, encapsulated cells are allowed to produce their own ECM and remodel the construct into a more suitable environment.

Delivery of cells using injectable biomaterials may provide additional benefit over acellular materials. However, many studies show similar functional benefits with delivery of hydrogels alone. As previously discussed in Section 3.2.2, injection of hydrogels into the infarct region results in improved passive myocardial properties, mechanical stabilization due to LV geometry alterations, and ultimately, reduced myocardial wall stress.[24] However, to improve cardiac function long-term, the therapy should also contribute to active myocardial regeneration, including the introduction of viable, contractile tissue.[124] This can potentially be achieved by combining cell approaches with injectable hydrogels. Ultimately, hydrogels provide a platform for cell delivery, a structural matrix to direct tissue formation, and an improved microenvironment for myocardial repair.[30,74] Similar to acellular approaches both natural and synthetic hydrogels have been utilized to deliver cells for myocardial repair (**Table 3.2**).

3.3.3.1. Natural Hydrogels for Cell Delivery

Natural materials are popular choice for cell delivery due to their inherent ability to be recognized by cell-surface receptors and potential for cell-mediated remodeling, thus facilitating cell-biomaterial interactions. Similar to acellular approaches, commonly used naturally derived hydrogels for cell delivery include fibrin, alginate, collagen, Matrigel, chitosan, and self-assembling peptides.

Table 3.2. Summary of cellular hydrogel systems and their assessment in animal MI models.

Material	Animal/ MI Model	Cells Delivered	Injection Time (post-MI)	Injection Volume	Evaluation Time (post-delivery)	Ref.
Fibrin	Rat; LAD ligation/ reperfusion	Skeletal myoblasts (5×10^6)	10 days[43] or 1 week[44]	50 µL	5 weeks	30,31
	Rat; cryoinjury	BMNCs (2×10^7)	3 weeks	100 µL x 2 sites	8 weeks	127
	Sheep; LCX constriction	Endothelial cells	4 weeks	800 µL x 3 sites	2 months	129
	Rat; LAD ligation	MSCs (5×10^5)	Immediate	150 µL x 2 sites	90 minutes	128
Collagen	Rat; LAD ligation	MSCs (2×10^6)	1 week	70 µL	4 weeks	133
Matrigel	Mouse; LAD ligation	ESCs (1×10^6)	Immediate	50 µL	2 weeks	55
	Rat; LAD ligation/ heterotopic transplant	ESCs (2×10^6)	Immediate	125 µL	2 weeks	134
Chitosan	Rat; LAD ligation	ESCs (1×10^7)	1 week	100 µL	4 weeks	57
	Rat; LAD ligation	Adipose-derived MSCs (4×10^6)	1 week	100 µL (via 3 sites)	4 weeks	58
Self-assembling peptides	Minipigs; Mid-LAD ligation	BMNCs (1×10^8)	Immediate	50 µL x 40 sites	4 weeks	135
Dex-PCL-HEMA/ PNIPAAm	Rabbit; Proximal LCA ligation	BMNCs (1×10^7)	1 week	50 µL x 4 sites	1 month	78
αCD/MPEG-PCL-MPEG	Rat; LCA ligation	BMNCs (2×10^7)	1 week	50 µL x 4 sites	4 weeks	136
Oligo(PEG fumarate)	Rat; LAD ligation	ESCs (1×10^6)	1 week	100 µL (via 3 sites)	4 weeks	137
PEGylated-fibrinogen	Rat; Proximal LAD ligation	Neonatal cardio-myocytes (3×10^6)	1 week	300 µL	30 days	138

* BMNCs = bone marrow-derived mononuclear cells, MSCs = mesenchymal stem cells, ESCs = embryonic stem cells, CPCs = cardiac progenitor cells, ELC = endothelial-like cells, SMLC = smooth muscle-like cells (see **Table 3.1** for additional abbreviations)

Fibrin: Injectable fibrin has been used to deliver a variety of cell types, including skeletal myoblasts,[30,31] BSCs,[125] bone marrow mononuclear cells (BMNCs),[126,127] bone marrow-derived CSCs,[118] MSCs,[128] endothelial cells,[129] and adipose-derived stem cells.[130,131] Regardless of the cell source, delivery of cells encapsulated in fibrin leads to enhanced neovascularization, improved LV function, and attenuated LV remodeling.[132] Christman et al. demonstrated the benefits of injectable hydrogels for cell delivery over traditional cellular cardiomyoplasty.[31] Injection of skeletal myoblasts encapsulated in fibrin glue in rats one week post-MI (temporary occlusion) led to a significantly greater cell area relative to myoblasts injected in BSA five weeks after delivery, indicating that fibrin increases cell survival by potentially serving as a temporary ECM for the injected cells.[31] Similar to previous studies,[30] fibrin glue, with or without cells, induced neovascularization in the ischemic myocardium and reduced infarct expansion.

Ryu et al. delivered BMNCs with and without fibrin encapsulation to rats three weeks following MI (cryoinjury).[127] Eight weeks after delivery, histological evaluation revealed increased neovascularization when cells were delivered using fibrin hydrogels, including significantly increased microvessel density and larger internal vessel diameters, as compared to delivery of cells alone or culture medium controls.[127] However, it is unclear if the improvements were due to fibrin alone or BMMC delivery due to lack of a fibrin control. Chekanov et al. reported similar results when delivering endothelial cells with and without a fibrin matrix to an ovine chronic ischemia cardiomyopathy model.[129] Finally, Martens et al. delivered labeled MSCs encapsulated in fibrin to rats immediately post-MI (permanent occlusion) using a minimally invasive, percutaneous catheter.[128] Ninety minutes after delivery, cells delivered using fibrin had significantly increased retention in the heart and reduction of redistribution to the liver and kidney as compared to cells delivered alone.[128]

Alginate: Alginate hydrogels have also been utilized for cell delivery for cardiac repair. Yu et al. used injectable, RGD modified, alginate hydrogel microspheres to deliver encapsulated MSCs (temporary occlusion).[139] Alginate encapsulation improved cell attachment and growth and

increased angiogenic growth factor expression *in vitro*. Injection of alginate, with or without cells, into rats one week post-MI (temporary occlusion) led to preserved wall thickness and significantly improved FS at ten weeks after delivery as compared to baseline. Histology demonstrated that each treatment group (alginate alone, cells alone, and alginate with cells) reduced infarct area and increased arteriole density indicative of angiogenesis, with no significant differences between the groups. Despite comparable functional outcomes between the groups, the use of alginate significantly increased cell survival over cells alone or saline controls.[139]

Collagen: Collagen has also been used to deliver cells for MI repair. Dai et al. delivered nanoparticle labeled MSCs encapsulated in a commercially available collagen matrix to rats one week post-MI (permanent occlusion).[133] Four weeks following injection, collagen encapsulation significantly reduced MSC relocation to regions of non-infarcted myocardium and remote organs relative to delivery of cells alone. However, cell delivery using collagen hydrogels did not significantly improve LV EF as compared to saline controls. EF was significantly increased in animals that received collagen alone, consistent with a previous study,[51] as well as cells alone as compared to saline.[133] To assess the translational potential of collagen-cell systems, Thompson et al. injected autologous BMCs encapsulated in a collagen hydrogel into the myocardium of pigs using a composite catheter system (TransAccess).[140] Histology revealed hydrogel retention in the myocardium immediately after injection and at 14 and 28 days following injection, indicating the efficacy of intramyocardial catheter delivery. However, since this procedure was only performed on non-infarcted hearts, it is difficult to assess the effects of this therapy on LV remodeling.[140]

Matrigel: Several cell types have been delivered using Matrigel hydrogels, including ESCs[55,134] and ESC-derived cardiomyocytes.[53] Laflamme et al. delivered human ESC-derived cardiomyocytes encapsulated in Matrigel to rats four days post-MI (temporary occlusion) and saw preserved cell retention in the infarct as compared to cell delivery in serum free medium at one week after injection.[53] Kofidis et al. delivered labeled mouse ESCs encapsulated in Matrigel to a rat heterotopic heart transplant model immediately post-MI (permanent occlusion).[134] Two weeks

later, delivery of Matrigel encapsulated ESCs led to significantly increased FS, increased thickness in the posterior and septal walls, and reduced EDD as compared with controls (infarcted, Matrigel alone, ESCs alone).[134] These functional and structural results were confirmed in a subsequent study using a mouse MI model. In this study, the Matrigel encapsulated ESCs showed expression of gap junction protein connexin 43 at intercellular sites, indicating possible connections with the host myocardium.[55]

Composites of collagen and Matrigel have also been used for MI repair. The Zimmerman group developed a novel cardiac muscle construct known as engineered heart tissue (EHT), which consists of neonatal cardiomyocytes with an artificial ECM made from collagen type I, Matrigel and cell growth medium.[141] Due to the properties of collagen and Matrigel, EHT remains a liquid at room temperature but solidifies at 37°C. Zhang et al. delivered liquid EHT as an injectable hydrogel to rats three weeks post-MI (permanent occlusion). One month after delivery, collagen-Matrigel encapsulated cardiomyocytes led to increased wall thickness, decreased LV ESD, and enhanced FS as compared to matrix alone, cells alone, or medium controls.[142]

Chitosan: Chitosan hydrogels have also been used for cell delivery post-MI. Lu et al. delivered chitosan encapsulated ESCs to rats one week post-MI (permanent occlusion) and saw significantly improved 24-hour cell retention and four-week graft size as compared to delivery of ESCs alone.[57] In addition, delivery of ESCs encapsulated in chitosan led to significantly increased microvasculature density in the infarct, increased wall thickness, reduced infarct area, decreased EDD and ESD, and improved FS and EF at four weeks after injection as compared to chitosan alone, ESCs alone, or saline controls.[57] These results were later confirmed by delivering a chitosan hydrogel with encapsulated adipose-derived MSCs to a rat MI model. Even though injection of chitosan or cells alone improved cardiac structure and function as compared to saline controls, the combination of cells with chitosan further improved outcomes.[58]

Self-assembling peptides: Self-assembling peptides consist of alternating hydrophilic and hydrophobic amino acids that can form stable β-sheets. At physiological osmolarity and pH, these

peptides self-assemble to form nanofibrous hydrogels. Due to the ability of their structure to promote cell organization, these biologically inspired materials have been used for cell delivery in both small[143,144] and large[135] animal models. Various cells have been delivered, including cardiomyocytes,[143,145] CPCs,[146] skeletal myoblasts,[144] and BMNCs.[135] Dubois et al. injected skeletal myoblasts with self-assembling peptides into rats two weeks post-MI (permanent ligation).[144] One month after injection, peptide nanofibers alone significantly increased angiogenesis, but did not improve encapsulated skeletal myoblast survival. Consistent with the decreased cell survival, no functional improvements were seen in any of the therapy groups relative to culture medium controls.[144] In contrast, Lin et al. used self-assembling peptides to deliver cells to a large animal MI model.[135] Injection of BMNCs and self-assembling peptides to minipigs immediately post-MI (permanent occlusion) significantly increased EF as compared to all other groups (cells alone, peptides alone, saline controls) and increased interventricular septum (IVS) systolic and diastolic thickness relative to saline controls at four weeks after delivery. In addition, peptide nanofibers alone significantly enhanced diastolic function as evidenced by increased IVS diastolic thickness relative to BMNCs or saline controls, whereas BMNCs alone significantly improved EF and increased IVS systolic thickness relative to saline controls. Overall, the delivery of cells and nanofibers led to the greatest improvements in cardiac function.[135]

3.3.3.2. Synthetic Hydrogels for Cell Delivery

Synthetic hydrogels can also be used as cell carriers post-MI. Due to their tunability, small peptides can be added to promote cell interactions or degradation. Similar to acellular gels, the primary synthetic materials used for cell delivery are PNIPAAm- and PEG-based hydrogels.

Poly(N-isopropylacrylamide) (PIPAAm): Thermoresponsive PIPAAm hydrogels have successfully encapsulated and delivered cells post-MI in several studies.[77,78] Li et al. delivered BMNCs encapsulated in a thermoresponsive Dex-PCL-HEMA/PNIPAAm hydrogel to rabbits one week post-MI (permanent occlusion), as previously discussed in Section 3.2.2.2.[78] Histology performed 48 hours after injection showed significantly increased cell retention in the infarct with

the presence of the hydrogel as compared to BMNCs alone. Thirty days post injection, delivery of BMNCs in hydrogels significantly decreased infarct size, increased neovascularization, reduced LV EDD and ESD, and increased EF as compared to cells alone, hydrogel alone, or culture medium controls. Even though material alone led to improved structural and functional cardiac outcomes relative to the medium control, there were no improvements in neovascularization, providing motivation for cell encapsulation strategies to repair the damaged myocardium.[78] Similarly, Wall et al. injected bone marrow-derived MSCs encapsulated in p(NIPAAm-*co*-AAc) hydrogels into mice immediately post-MI (permanent occlusion) and saw trends towards increased FS and EF and decreased EDV at 2 weeks as compared to saline controls.[77]

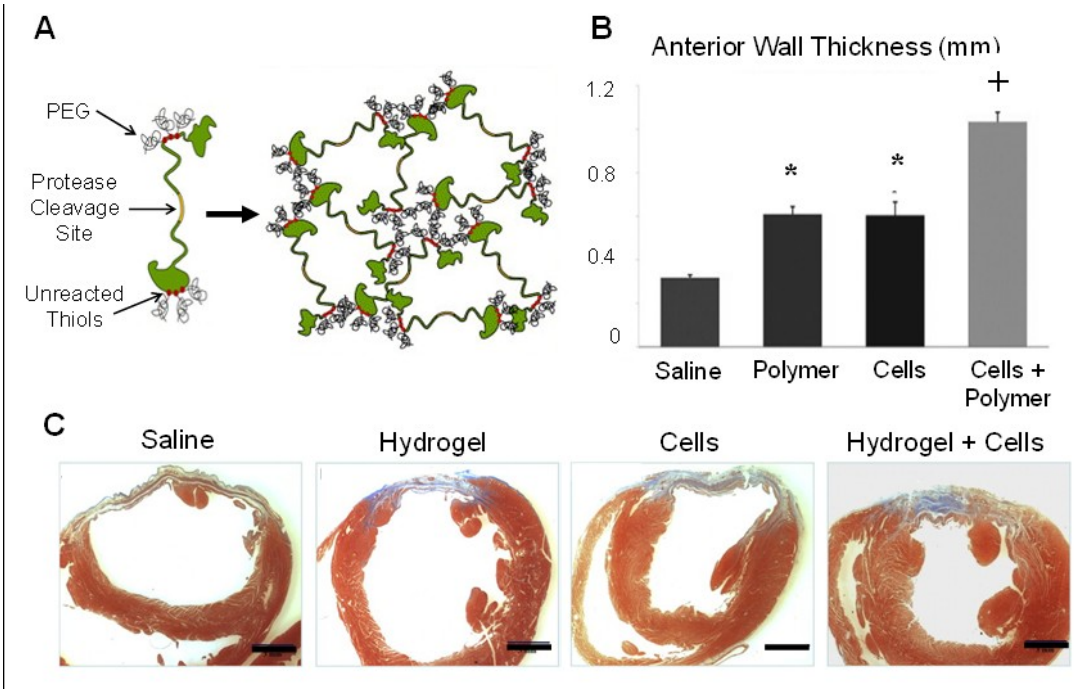

Figure 3.4. Synthetic hydrogel for cell delivery post-MI. Schematic of PEG-fibrinogen hydrogel assembly (A). Infarct thickness (B) and Masson's Trichrome staining (C) of infarcted hearts injected with saline, PEG hydrogel alone, rat cardiomyocytes alone, or combined cell-hydrogel therapy at 30 days post-MI. Scale bar = 3 mm. *p<0.05 vs. saline controls, †<0.005 vs. all other groups. Figure adapted from [138].

Poly(ethylene glycol) (PEG): PEG hydrogels have delivered several cell types, including ESC-derived vascular cells,[84] BMNCs,[117,136] and ESCs.[137] Wang et al. delivered BMNCs encapsulated in an α-CD/MPEG-PCL-MPEG hydrogel to rabbits seven days post-MI (permanent occlusion), as previously discussed in Section 3.2.2.2.[136] Four weeks after delivery, hydrogel encapsulated BMNCs led to significantly increased cell retention and neovascularization in the infarct, decreased LV EDD, reduced infarct size, and increased EF as compared to cells alone or saline controls.[136] Similarly, Wang et al. delivered ESCs encapsulated in a biodegradable oligo(poly[ethylene glycol] fumarate) (OPF) hydrogel to rats one week post-MI (permanent occlusion) and showed significantly improved 24-hour cell retention and four-week graft size relative to ESCs delivery alone.[137] Four weeks after injection, delivery of OPF encapsulated ESCs significantly decreased infarct area, reduced collagen deposition in the infarct (fibrosis), increased infarct neovascularization, decreased LV EDV and ESV, and increased FS as compared to ESCs alone, OPF alone, or saline controls. Even though outcomes were most pronounced with the cell-hydrogel system, delivery of OPF alone or ESCs alone led to significantly reduced infarct area, decreased fibrosis, reduced LV volumes and enhanced FS as compared to saline controls. In addition, each treatment group showed significantly decreased protease expression (i.e., MMP-2, MMP-9) relative to saline controls, with the cell-hydrogel system leading to the greatest decrease, which could favor infarct stiffening at later time points.[137]

Building on the benefits of synthetic and natural systems, Habib et al. used a photopolymerizable, biodegradable PEGylated-fibrinogen hydrogel to deliver neonatal rat cardiomyocytes to rats one week post-MI (permanent occlusion).[138] Thirty days following injection, delivery of hydrogel encapsulated neonatal cardiomyocytes encapsulated led to significantly increased FS as compared to all other groups (cells alone, hydrogel alone, saline controls), decreased wall motion score index (measure of regional systolic function) relative to saline controls, and preserved LV EDD as compared to hydrogel alone or saline. Histology revealed that co-injection of the cells and hydrogel significantly increased the cell-graft area and wall thickness as compared to all other groups (**Figure 3.4**).[138]

Table 3.3. Summary of hydrogels for molecule delivery and their evaluation in animal MI models.

Material	Animal/ MI Model	Molecules Delivered	Injection Time (post-MI)	Injection Volume	Evaluation Time (post-delivery)	Ref.
Alginate	Rat; LAD ligation	IGF-1 (250 ng), HGF (250 ng)	6 days	120 µL	4 weeks	147
	Rat; LAD ligation	VEGF (3 µg), PDGF (3 µg)	1 week	100 µL	4 weeks	148
Chitosan	Rat; LAD ligation	FGF (2 µg)	1 week	100 µL (via 3 sites)	4 weeks	62
Hyaluronic acid	Mouse; cryoinjury	SDF-1α (0.25 µg)	Immediate	25 µL	1 week	149
Gelatin	Rat; LAD ligation	FGF (120 µg)	Immediate	57 µL x 6 sites	2 and 4 weeks	150
	Dog; LAD ligation	FGF (100 µg)	Immediate	1 mL x 5 sites	10 and 17 days	151
Self-assembling peptides	Rat; LCA ligation	FGF (40 ng), PDGF (160 ng)	Immediate	50 µL (via 3 sites)	4 and 8 weeks	152
	Rat; LCA ligation	SDF-1α (30 nmol/L)	Immediate	80 µL (via 3 sites)	4 weeks	153
αCD/MPEG-PCL-MPEG	Rat; LCA ligation	EPO (600 U)	5 minutes	100 µL x 3 sites	1 month	82
PVL-*b*-PEG-*b*-PVL	Rat; LAD ligation	VEGF (40 ng)	1 week	25 µL x 4 sites	1, 2, 3, and 5 weeks	83

* IGF-1 = insulin-like growth factor 1, HGF = hepatocyte growth factor, VEGF = vascular endothelial growth factor, PDGF = platelet derived growth factor, FGF = fibroblast growth factor, SDF-1α = stromal cell derived factor-1 alpha, EPO = erythropoietin (see Tables 1 and 2 for additional abbreviations)

3.4. Injectable Hydrogels for Molecule Delivery

In addition to providing mechanical stabilization to the injured myocardium and serving as an exogenous cell delivery vehicle, injectable hydrogels can encapsulate and deliver therapeutic molecules to the myocardium post-MI. Tissue repair is a complex process controlled in part by growth factors and cytokines that regulate the pathways of wound healing and tissue generation. Therefore, delivery of exogenous molecules, such as growth factors, cytokines, and stem-cell

mobilizing factors, can modulate endogenous biological responses post-MI.[154] Delivery of therapeutic molecules alone, either by direct myocardial injection or systemic intravenous circulation, has helped restore cardiac function in some animal models.[155] However, clinical trials have been less conclusive and there are limitations with molecule delivery alone, such as the need for high concentrations or repeated doses due to high diffusion rates and short half-lives.[156] In addition, systemic delivery introduces numerous safety concerns and off-target effects, such as increased incidence of restenosis, elevated blood pressure and viscosity, and thrombolytic events in congestive heart failure patients.[157] Due to limitations in molecule delivery alone, injectable hydrogels have been used as vehicles to localize molecules and tailor release kinetics through changes in polymer-molecule interactions, polymer hydrophobicity, and hydrogel degradation (**Figure 3.5**).[158,159] Hydrogels can both sustain local molecule release and prolong molecule bioactivity.[160] For cardiac applications, injectable hydrogels deliver anti-apoptotic molecules, angiogenic factors, or chemoattractants to attenuate remodeling post-MI (**Table 3.3**).

3.4.1. Anti-Apoptotic Factors

Hydrogels have been used to deliver anti-apoptotic factors post-MI to attenuate further cardiomyocyte loss. Ruvinov et al. delivered insulin-like growth factor 1 (IGF-1) and hepatocyte growth factor (HGF) via alginate microparticles to rats six days post-MI (permanent occlusion).[147] This growth factor combination was selected due to the cytoprotective properties of IGF-1 and pro-angiogenic and anti-fibrotic effects of HGF. To increase growth factor affinity to the hydrogel, alginate was chemically modified with sulfate groups; due to differences in sulfate affinity between IGF-1 and HGF, there was sequential release of IGF-1 then HGF. Four weeks post injection, the dual IGF-1/HGF affinity-bound alginate hydrogel significantly decreased fibrosis, reduced apoptosis, increased vessel density and area, and increased cardiomyocyte proliferation relative to IGF/HGF alone and hydrogel alone. Compared to saline controls, the hydrogel system significantly increased scar thickness, limited infarct expansion and reduced fibrosis. There was also evidence of cardiogenesis (GATA-4-positive cells) indicative of endogenous regeneration.[147]

Davis et al. used self-assembling peptide nanofibers to deliver IGF-1 to rats immediately post-MI (permanent occlusion).[143] To sustain IGF-1 release, biotinylated IGF-1 was tethered to biotinylated self-assembling peptides using a streptavidin linker complexed to the IGF-1. This strategy enables IGF-1 binding but does not prevent peptide self-assembly into hydrogels. A preliminary study in healthy rats demonstrated that tethering of IGF-1 to peptide nanofibers led to significant retention in the myocardium for 28 days and preserved bioactivity for 14 days as compared to untethered IGF-1 or IGF alone. However, when delivered to the rat MI model, no differences in cardiac function were observed between treatment groups at 1 or 21 days post-MI.[143] In contrast, Kraehenbuehl et al. demonstrated improvements in cardiac function with hydrogel-based growth factor delivery. Thymosin ß-4 (Tβ4), a pro-angiogenic and pro-survival factor, was encapsulated in an MMP degradable PEG-VS hydrogel and injected into rats one hour post-MI (permanent occlusion).[84] Six weeks later, PEG hydrogels with or without Tβ4 led to significantly decreased LV ESV and increased EF as compared to saline controls, with a trend towards decreased infarct size and reduced LV EDV. However, outcomes were more pronounced with Tβ4. Interestingly, delivery of Tβ4 using PEG hydrogels led to a significantly smaller LV ESV as compared to hydrogels alone, demonstrating the beneficial effects of growth factor delivery.[84]

3.4.2. Angiogenic Factors

Hydrogels can also deliver pro-angiogenic factors to increase vascularization to the ischemic myocardium and generate an environment more conducive to cell infiltration for repair. Basic fibroblast growth factor (bFGF) is a powerful angiogenic molecule that has been delivered using hydrogels to sustain its release and prolong its activity.[60,62,150-152,161-164] For instance, bFGF encapsulation in gelatin hydrogel microspheres increases its *in vivo* half-life from days to weeks.[161-163] Hence, gelatin has been used to deliver FGF in both small[150] and large[151] animal models. Shao et al. delivered gelatin encapsulated bFGF to rats immediately post-MI (permanent occlusion) and saw significantly increased capillary and arteriolar density in the BZ, reduced cardiomyocyte apoptosis, increased infarct thickness, and reduced infarct expansion as

compared to saline controls at four weeks after delivery.[150] Similarly, Liu et al. delivered gelatin encapsulated bFGF microspheres to dogs immediately post-MI (permanent occlusion) and found significantly increased microvessel density and improved EF as compared to controls of gelatin microspheres in saline at 10 and 17 days post-MI.[151] Similar improvements in vascularization and cardiac function have been shown for bFGF delivery from chitosan hydrogels post-MI.[62,164]

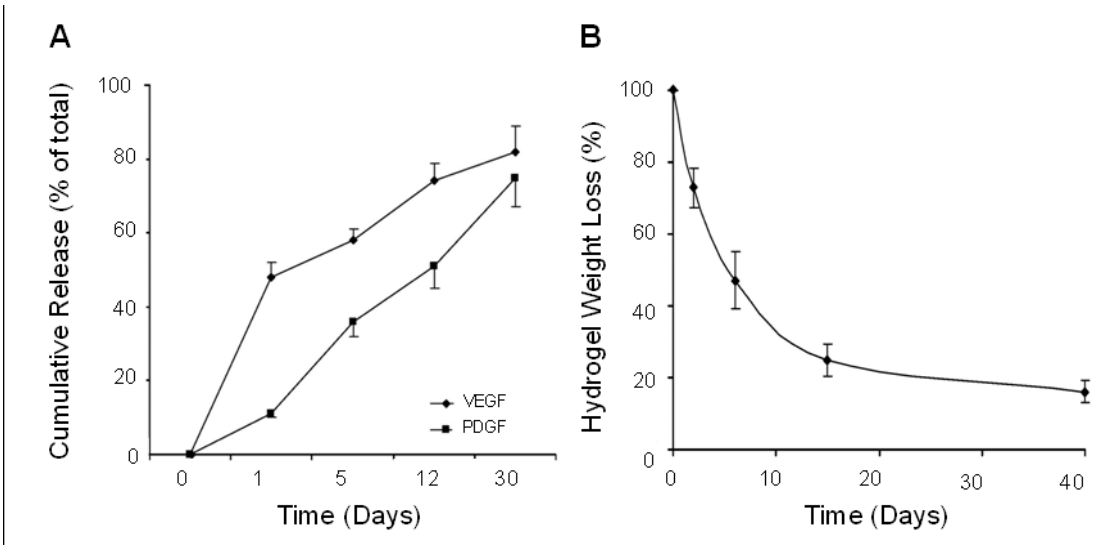

Figure 3.5. Molecule release from injectable, natural hydrogels. Growth factor release of VEGF and PDGF (A) tracks with alginate hydrogel degradation (B) *in vitro*. Figure adapted from [148].

Despite increased neovascularization with pro-angiogenic factor delivery, there is concern that the newly formed vessels lack stability and connectivity.[165] To enhance vessel stability, multiple pro-angiogenic factors can be simultaneously or sequentially released from hydrogels.[148,152,166] Kim et al. delivered both bFGF and platelet derived growth factor (PDGF) using self-assembling peptides to rats immediately post-MI (permanent occlusion).[152] The goal is to first stimulate vessel formation using bFGF, then recruit smooth muscle cells to form stable vasculature using PDGF. In addition, self-assembling peptide nanofibers alone recruit endothelial cells and vascular smooth muscle cells,[145] where both cell types are needed for stable vessel formation. Dual bFGF/PDGF delivery from peptide nanofibers significantly reduced infarct size,

increased wall thickness, decreased cardiomyocyte apoptosis, and increased capillary and arteriole density at four and eight weeks after delivery and significantly improved cardiac function and contractility (LV EDP, +dP/dt, -dP/dt) after four weeks relative to sucrose controls. Similarly, Hao et al. sequentially delivered vascular endothelial growth factor (VEGF) then PDGF from alginate hydrogels (**Figure 3.5**) to rats one week post-MI (permanent occlusion).[148] Four weeks later, sequential release of VEGF then PDGF significantly increased α-actin positive vessels density, indicating smooth muscle cell vessel stabilization, and increased the systolic velocity-time integral, a marker of myocardial function, as compared to VEGF or PDGF alone.[148]

To further control angiogenic factor delivery, Wu et al. conjugated VEGF to a PVL-*b*-PEG-*b*-PVL hydrogel (as discussed Section 3.2.2.2) and injected the system into rats one week post-MI (permanent occlusion).[83] Five weeks after delivery, animals that received VEGF tethered to the hydrogel had improved EF and FE, increased contractility (+dP/dt, -dP/dt), preserved EDV and ESV, increased wall thickness, and increased vessel density as compared to VEGF mixed with the hydrogel, hydrogel alone, or saline controls.[83] Similar to previous studies,[143,147] conjugating biomolecules to injectable hydrogels prolongs their release and biological effects.

3.4.3. Chemoattractants

In addition to promoting cell survival and angiogenesis, therapeutic molecule delivery from injectable hydrogels can also focus on recruiting endogenous cells to repair the damaged myocardium. Stromal cell derived factor-1 alpha (SDF-1α) is a chemokine shown to selectively recruit stem and progenitor cells.[149,153] Segers et al. locally delivered SDF-1α to rats immediately post-MI (permanent occlusion) using self-assembling peptide nanofibers.[153] SDF-1α release was tailored by tethering it to the hydrogel using a peptide sequence susceptible to endogenous protease cleavage. Four weeks following injection, delivery of SDF-1α tethered to peptide nanofibers significantly increased recruitment of cells expressing the SDF-1α receptor (CXCR4+/c-Kit+ cells), increased capillary and arteriole density in the infarct, and improved EF relative to infarct controls.[153] Similar to self-assembling peptides being well-suited for molecule

delivery due to their ability to tether proteins,[154] HA has been shown to cooperate with SDF-1α mediated BMC homing[167] and thus, may be well-suited for SDF-1α delivery. In addition to their native binding affinity, both SDF-1α and HA stimulate BMC chemotaxis *in vitro* through their CXCR4 and CD44 receptors, respectively.[149] Purcell et al. delivered SDF-1α encapsulated in a degradable HA hydrogel to mice immediately post-MI (cryoinjury) to assess their synergistic effects on cell homing.[149] Seven days after delivery, HA hydrogel encapsulation of SDF-1α led to significantly increased endogenous BMC homing and engraftment in the infarct as compared to SDF-1α alone or hydrogel alone.[149] In a subsequent study, MacArthur et al. demonstrated that sustained release of an engineered SDF-1α analog (ESA) from degradable HA hydrogels causes both endogenous EPC recruitment to the myocardium and preserved LV function.[168]

3.5. Combined Hydrogel Delivery of Cells and Molecules

Building from the benefits of delivery of hydrogels alone and hydrogels with encapsulated cells or molecules, optimal therapies may rely on a combination of all three. Growth and differentiating factors can further improve encapsulated cell survival and differentiation and impact the nearby environment to facilitate graft integration. Relative to other material delivery systems, hydrogels are advantageous due to their ability to simultaneously mechanically support the myocardium and serve as a controlled delivery platform. By improving long-term cell survival and engraftment, myocardial reconstruction and/or stem-cell mediated regeneration can occur.

Both natural and synthetic hydrogels have been used to simultaneously deliver cells and anti-apoptotic or angiogenic therapeutic molecules to the infarct post-MI (**Table 3.4**). Laflamme et al. delivered Matrigel encapsulated human ESC-derived cardiomyocytes with pro-survival growth factors, including IGF-1, cyclosporine A, anti-apoptotic peptide Bcl-XL BH4, caspase inhibitor ZVAD-fmk and vasodilator pinacidil, to rats four days post-MI (temporary occlusion).[53] Delivery of Matrigel with both cells and growth factors led to significantly increased cell engraftment in the infarct as compared to delivery of cells with Matrigel alone one week following injection. Four weeks after delivery, the hydrogel-cell-growth factor system significantly increased FS and

preserved LV EDD as compared to non-cardiac cells with growth factors, growth factors alone, or culture media controls.[53] In a subsequent study, Fernandes et al. delivered the same system to rats one month post-MI (temporary occlusion) and saw successful cell engraftment into the infarct three months after injection. Despite improved cell engraftment, there were no significant differences in LV EDD, EDV and ESV, SV, or FS between any of the groups at any time point.[120]

Davis et al. delivered neonatal cardiomyocytes and IGF-1 tethered to self-assembling peptide nanofibers to rats immediately post-MI (permanent occlusion).[143] A preliminary study in healthy rats demonstrated that peptide tethered IGF-1 delivery significantly decreased activation of caspase-3, an apoptosis marker, in the encapsulated cardiomyocytes and increased transplanted cell area, as compared to untethered IGF-1 or no IGF-1 controls two weeks after delivery. Three weeks after delivery to the rat MI model, the tethered IGF-1 cell therapy significantly decreased apoptosis of the encapsulated cardiomyocytes compared with peptides alone or untethered IGF-1 and overall, significantly decreased LV dilatation and increased FS as compared with all other groups.[143] In another study by the same group, Padin-Iruegas et al. delivered rat CPCs with IGF-1-modified self-assembling peptide nanofibers to rats immediately post-MI (permanent occlusion).[146] One month following delivery, CPCs encapsulated in IGF-1 tethered peptides significantly enhanced myocardial regeneration (as indicated by increased cardiomyocyte mass, volume, and number), decreased infarct size, decreased wall stress, enhanced contractility (+dP/dt, -dP/dt), and increased EF as compared to CPCs or IGF-1 tethered peptides alone.[146] In contrast to previous studies,[169] Dubois et al. delivered skeletal myoblasts encapsulated in PDGF loaded self-assembling peptide nanofibers to rats two weeks post-MI (permanent occlusion) and saw no improvements in LV EF or encapsulated cell survival despite increases in angiogenesis as compared to medium controls at one month after injection.[144]

Table 3.4. Summary of hydrogels for cell and molecule delivery and their *in vivo* assessment.

Material	Animal/ MI Model	Cells and Molecules Delivered	Injection Time (post-MI)	Injection Volume	Evaluation Time (post-delivery)	Ref.
Fibrin with PLGA nano-spheres	Rat; LCA ligation	BMNCs (2×10^7), TGF-β1 (2 ng)	1 week	100 µL	4 weeks	126
Matrigel	Rat: LAD ligation/ reperfusion	ESC-derived cardio-myocytes (1×10^7), IGF-1 (7 ng), pinacidil (50 µM), cyclosporine A (0.2 µM), Bcl-X_L BH4 (50 nM), ZVAD (100 µM)	4 days[61] or 1 month[128]	70 µL	1and 4 weeks[61] or 1, 2, and 3 months[128]	7, 11, 50
Self-assembling peptides	Rat; LCA ligation	Skeletal myoblasts (5×10^6), PDGF (100 ng)	2 weeks	200 µL (via 3-4 sites)	1 month	144
	Rat; LCA ligation	Neonatal cardiomyocyte (5×10^5), IGF-1 (25 ng)	Immediate	80 µL	1, 14, 21, and 28 days	143
	Rat; LCA ligation	CPCs (1×10^5), IGF-1 (1 ng)	Immediate	5 µL/ injection (multiple sites)	1 month	146
PEG-VS	Rat; LAD ligation	ESC-derived ELCs (6.6×10^5) and SMLCs (3.3×10^5) , Tβ4 (2.5 µg)	1 hour	60 µL	3 days and 6 weeks	84
PEGylated-fibrinogen	Mouse; LAD ligation	BMNCs (5×10^5), HGF (100 ng)	Immediate	50 µL	2 and 4 weeks	117

* PLGA = poly(lactic-*co*-glycolic acid), CPCs = cardiac progenitor cells, ELC = endothelial-like cells, SMLC = smooth muscle-like cells, TGF-β1 = transforming growth factor-beta 1, Bcl-XL BH4 = cell-permeable TAT peptide, ZVAD = benzyloxycarbonyl-Val-Ala-Asp(O-methyl)-fluoromethyl ketone, FGF = fibroblast growth factor, Tβ4 = thymosin beta-4 (see **Tables 1, 2, and 3** for additional abbreviations).

Synthetic hydrogels have also been used to simultaneously deliver cells and biomolecules for MI repair. Kraehenbuehl et al. delivered human ESC-derived endothelial- and smooth muscle like cells (ELCs, SMLCs) encapsulated in an MMP degradable, PEG-VS hydrogel loaded with Tβ4 to rats one hour post-MI (permanent ligation).[84] Six weeks post-MI, delivery of ELCs/SMLCs encapsulated in a Tβ4-loaded hydrogel significantly increased neovascularization in the infarct, decreased infarct size, reduced LV EDV ESV, and increased EF relative to saline controls. Also, the combined cell-Tβ4 delivery from PEG hydrogels significantly increased EF compared to PEG hydrogels with Tβ4 or PEG hydrogels alone.[84] Zhang et al. delivered murine BMNCs and HGF covalently bound to PEGylated-fibrinogen hydrogels to mice immediately post-MI (permanent occlusion) and saw significantly decreased apoptosis in the BZ and infarct, increased angiogenesis, decreased fibrosis, decreased LV EDV and ESV, and increased EF as compared to saline controls at four weeks post-MI.[117] Delivery of BMNCs alone led to significantly decreased apoptosis in BZ regions, increased angiogenesis, and decreased fibrosis whereas delivery of HGF-bound hydrogel led to significantly decreased apoptosis and increased angiogenesis in the infarct relative to saline controls. In addition, BMNCs delivery using a HGF-loaded hydrogel significantly increased cell engraftment in the infarct 15-fold relative to delivery of BMNCs alone. All treatment groups (BMSCs, hydrogel+HGF, hydrogel+HGF+BMNCs) improved LV volumes and FS relative to controls, with no statistical difference in FS between groups.[117]

3.6. Future Directions and Conclusions

As discussed throughout this chapter, a range of injectable hydrogels, cell types, and molecules have been delivered with the intent of attenuating remodeling post-MI. Although many hydrogels have shown positive outcomes in animal models, only one material has progressed to advanced clinical trials (NCT01226563, NCT01311791).[39,40,42,44,45] Therefore, several areas must be explored prior to clinical translation. For example, the exact mechanism by which injectable biomaterials lead to positive functional outcomes is not fully understand and is likely quite complex, involving both mechanical (e.g., stress reduction) and biological (e.g., exogenous cell

delivery, endogenous cell recruitment, angiogenesis, inflammatory response) interactions. It is evident that increased myocardial wall thickness,[32,37,48,80,81] decreased infarct size,[32] and/or increased angiogenesis[51,79,136] do not directly correlate with improved cardiac function; thus, finding specific correlations may improve future therapy design. Theoretical FE models provide some insight into the mechanisms by which injectable materials impact LV remodeling[22,24,25] and further development of such models may improve our understanding of material injection post-MI.

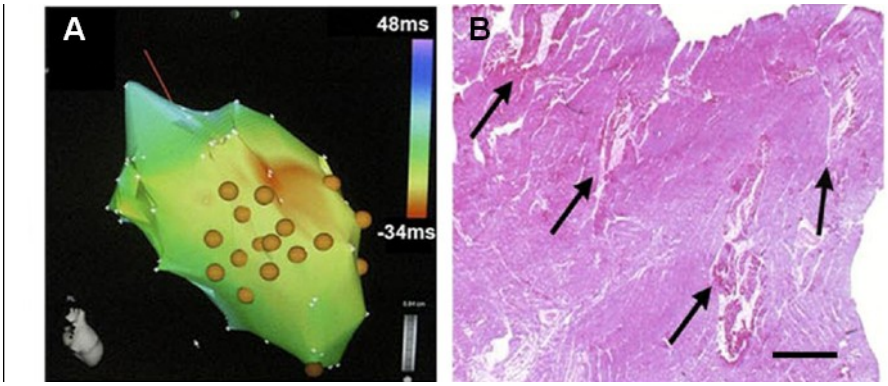

Figure 3.6. Percutaneous catheter delivery of decellularized ventricular ECM to healthy rats. NOGA maps representing injection sites (A) and representative H&E stain indicating presence of hydrogel within the myocardium (B). Scale bar = 1 mm. Figure adapted from [71].

From a translational perspective, it is important to elucidate the effects of hydrogel properties (e.g., mechanics, degradation), injection parameters (e.g., volume, number of injection), mode of delivery (e.g., direction injection vs. catheter delivery) (**Figure 3.6**), and timing of delivery (e.g., acute vs. chronic MI) on LV remodeling. Much of this can be explored through both experimental and modeling approaches and by selecting the most appropriate mimic of clinical scenarios to enhance our understanding of outcomes. Future studies should further investigate the mechanisms by which hydrogels act on the heart, including both biological and mechanical effects, and focus on clinically relevant parameters, such as the mode of delivery. This information has considerable clinical impact with respect to improved therapies to attenuate LV remodeling and ultimately, to aid patients by preventing progression to heart failure.

3.7. References

1. Bui AL, Horwich TB, Fonarow GC. Epidemiology and risk profile of heart failure. Nat Rev Cardiol 2011;8(1):30-41.

2. Go AS, Mozaffarian D, Roger VL, Benjamin EJ, Berry JD, Blaha MJ, et al. Heart disease and stroke statistics-2014 update: A report from the American Heart Association. Circulation 2014;129(3):e28-e292.

3. Gheorghiade M, Bonow RO. Chronic heart failure in the United States: A manifestation of coronary artery disease. Circulation 1998;97(3):282-289.

4. Nelson DM, Ma Z, Fujimoto KL, Hashizume R, Wagner WR. Intra-myocardial biomaterial injection therapy in the treatment of heart failure: Materials, outcomes and challenges. Acta Biomater 2011;7(1):1-15.

5. Holmes JW, Borg TK, Covell JW. Structure and mechanics of healing myocardial infarcts. Annu Rev Biomed Eng 2005;7:223-253.

6. Enomoto Y, Gorman JH,3rd, Moainie SL, Jackson BM, Parish LM, Plappert T, et al. Early ventricular restraint after myocardial infarction: extent of the wrap determines the outcome of remodeling. Ann Thorac Surg 2005;79(3):881-7; discussion 881-7.

7. Kelley ST, Malekan R, Gorman JH,3rd, Jackson BM, Gorman RC, Suzuki Y, et al. Restraining infarct expansion preserves left ventricular geometry and function after acute anteroapical infarction. Circulation 1999;99(1):135-142.

8. Pilla JJ, Blom AS, Gorman JH,3rd, Brockman DJ, Affuso J, Parish LM, et al. Early postinfarction ventricular restraint improves borderzone wall thickening dynamics during remodeling. Ann Thorac Surg 2005;80(6):2257-2262.

9. Moainie SL, Guy TS, Gorman JH,3rd, Plappert T, Jackson BM, St John-Sutton MG, et al. Infarct restraint attenuates remodeling and reduces chronic ischemic mitral regurgitation after postero-lateral infarction. Ann Thorac Surg 2002;74(2):444-9; discussion 449.

10. Mann D. Mechanisms and models in heart failure - A combinatorial approach. Circulation 1999;100(9):999-1008.

11. Bowen FW, Jones SC, Narula N, St John Sutton MG, Plappert T, Edmunds LH,Jr, et al. Restraining acute infarct expansion decreases collagenase activity in borderzone myocardium. Ann Thorac Surg 2001;72(6):1950-1956.

12. Blom A, Mukherjee R, Pilla J, Lowry A, Yarbrough W, Mingoia J, et al. Cardiac support device modifies left ventricular geometry and myocardial structure after myocardial infarction. Circulation 2005;112(9):1274-1283.

13. Chaudhry PA, Mishima T, Sharov VG, Hawkins J, Alferness C, Paone G, et al. Passive epicardial containment prevents ventricular remodeling in heart failure. Ann Thorac Surg 2000;70(4):1275-1280.

14. Sabbah HN. The cardiac support device and the myosplint: treating heart failure by targeting left ventricular size and shape. Ann Thorac Surg 2003;75(6 Suppl):S13-9.

15. Pilla JJ, Blom AS, Brockman DJ, Bowen F, Yuan Q, Giammarco J, et al. Ventricular constraint using the acorn cardiac support device reduces myocardial akinetic area in an ovine model of acute infarction. Circulation 2002;106(12 Suppl 1):I207-11.

16. Starling RC, Jessup M, Oh JK, Sabbah HN, Acker MA, Mann DL, et al. Sustained benefits of the CorCap Cardiac Support Device on left ventricular remodeling: Three year follow-up results from the Acorn clinical trial. Ann Thorac Surg 2007;84(4):1236-1242.

17. George I, Cheng Y, Yi G, He K, Li X, Oz MC, et al. Effect of passive cardiac containment on ventricular synchrony and cardiac function in awake dogs. Eur J Cardiothorac Surg 2007;31(1):55-64.

18. Magovern J, Teekell-Taylor L, Mankad S, Dasika U, McGregor W, Biederman R, et al. Effect of a flexible ventricular restraint device on cardiac remodeling after acute myocardial infarction. Asaio Journal 2006;52(2):196-200.

19. Klodell CT,Jr, Aranda JM,Jr, McGiffin DC, Rayburn BK, Sun B, Abraham WT, et al. Worldwide surgical experience with the Paracor HeartNet cardiac restraint device. J Thorac Cardiovasc Surg 2008;135(1):188-195.

20. Abraham WT, Anand I, Aranda JM, Jr., Boehmer J, Costanzo MR, DeMarco T, et al. Randomized controlled trial of ventricular elastic support therapy in the treatment of symptomatic heart failure: Rationale and design. Am Heart J 2012;164(5):638-645.

21. Costanzo MR, Ivanhoe RJ, Kao A, Anand IS, Bank A, Boehmer J, et al. Prospective Evaluation of Elastic Restraint to Lessen the Effects of Heart Failure (PEERLESS-HF) trial. J Card Fail 2012;18(6):446-458.

22. Wenk JF, Wall ST, Peterson RC, Helgerson SL, Sabbah HN, Burger M, et al. A method for automatically optimizing medical devices for treating heart failure: Designing polymeric injection patterns. J Biomech Eng 2009;131(12):121011.

23. Tous E, Purcell B, Ifkovits JL, Burdick JA. Injectable acellular hydrogels for cardiac repair. J Cardiovasc Transl Res 2011;4(5):528-542.

24. Wall ST, Walker JC, Healy KE, Ratcliffe MB, Guccione JM. Theoretical impact of the injection of material into the myocardium: A finite element model simulation. Circulation 2006;114(24):2627-2635.

25. Wenk JF, Eslami P, Zhang Z, Xu C, Kuhl E, Gorman,Joseph H.,,III, et al. A novel method for quantifying the in-vivo mechanical effect of material injected into a myocardial infarction. Ann Thorac Surg 2011;92(3):935-941.

26. Karam JP, Muscari C, Montero-Menei CN. Combining adult stem cells and polymeric devices for tissue engineering in infarcted myocardium. Biomaterials 2012;33(23):5683-5695.

27. Lutolf M, Hubbell J. Synthetic biomaterials as instructive extracellular microenvironments for morphogenesis in tissue engineering. Nat Biotechnol 2005;23(1):47-55.

28. Sui R, Liao X, Zhou X, Tan Q. The current status of engineering myocardial tissue. Stem Cell Rev 2011;7(1):172-180.

29. Barsotti MC, Felice F, Balbarini A, Di Stefano R. Fibrin as a scaffold for cardiac tissue engineering. Biotechnol Appl Biochem 2011;58(5):301-310.

30. Christman KL, Fok HH, Sievers RE, Fang Q, Lee RJ. Fibrin glue alone and skeletal myoblasts in a fibrin scaffold preserve cardiac function after myocardial infarction. Tissue Eng 2004;10(3-4):403-409.

31. Christman KL, Vardanian AJ, Fang Q, Sievers RE, Fok HH, Lee RJ. Injectable fibrin scaffold improves cell transplant survival, reduces infarct expansion, and induces neovasculature formation in ischemic myocardium. J Am Coll Cardiol 2004;44(3):654-660.

32. Yu J, Christman KL, Chin E, Sievers RE, Saeed M, Lee RJ. Restoration of left ventricular geometry and improvement of left ventricular function in a rodent model of chronic ischemic cardiomyopathy. J Thorac Cardiovasc Surg 2009;137(1):180-187.

33. Huang NF, Yu J, Sievers R, Li S, Lee RJ. Injectable biopolymers enhance angiogenesis after myocardial infarction. Tissue Eng 2005;11(11-12):1860-1866.

34. Thompson WD, Smith EB, Stirk CM, Marshall FI, Stout AJ, Kocchar A. Angiogenic activity of fibrin degradation products is located in fibrin fragment E. J Pathol 1992;168(1):47-53.

35. Leor J, Aboulafia-Etzion S, Dar A, Shapiro L, Barbash IM, Battler A, et al. Bioengineered cardiac grafts: A new approach to repair the infarcted myocardium? Circulation 2000;102(19 Suppl 3):III56-61.

36. Leor J, Tuvia S, Guetta V, Manczur F, Castel D, Willenz U, et al. Intracoronary injection of in situ forming alginate hydrogel reverses left ventricular remodeling after myocardial infarction in Swine. J Am Coll Cardiol 2009;54(11):1014-1023.

37. Landa N, Miller L, Feinberg MS, Holbova R, Shachar M, Freeman I, et al. Effect of injectable alginate implant on cardiac remodeling and function after recent and old infarcts in rat. Circulation 2008;117(11):1388-1396.

38. Rowley J, Madlambayan G, Mooney D. Alginate hydrogels as synthetic extracellular matrix materials. Biomaterials 1999;20(1):45-53.

39. BioLineRX Ltd. Safety and Feasibility of the Injectable BL-1040 Implant. In: ClinicalTrials.gov [Internet]. Bethesda (MD): National Library of Medicine (US). 2007- [cited 2014 Nov 21]. Available at: http://ClinicalTrials.gov/show/NCT00557531. NLM Identifier: NCT00557531.

40. Ikara Holdings Inc. IK-5001 for the Prevention of Remodeling of the Ventricle and Congestive Heart Failure After Acute Myocardial Infarction. In: ClinicalTrials.gov [Internet]. Bethesda (MD): National Library of Medicine (US). 2010- [cited 2014 Nov 21]. Available at: http://ClinicalTrials.gov/show/NCT01226563. NLM Identifier: NCT01226563.

41. Lee LC, Wall ST, Klepach D, Ge L, Zhang Z, Lee RJ, et al. Algisyl-LVR (TM) with coronary artery bypass grafting reduces left ventricular wall stress and improves function in the failing human heart. Int J Cardiol 2013;168(3):2022-2028.

42. LoneStar Heart Inc. Safety and Feasibility of Algisyl-LVR as a Method of Left Ventricular Restoration in Patients with DCM Undergoing Open-heart Surgery. In: ClinicalTrials.gov [Internet]. Bethesda (MD): National Library of Medicine (US). 2009- [cited 2014 Nov 21]. Available at: http://ClinicalTrials.gov/show/NCT00847964. NLM Identifier: NCT00847964.

43. Lee RJ, Hinson A, Helgerson S, Bauernschmitt R, Sabbah HN. Polymer-based restoration of left ventricular mechanics. Cell Transplant 2013;22(3):529-533.

44. LoneStar Heart Inc. A Randomized, Controlled Study to Evaluate Algisyl-LVR as a Method of Left Ventricular Augmentation for Heart Failure. In: ClinicalTrials.gov [Internet]. Bethesda (MD): National Library of Medicine (US). 2011- [cited 2014 Nov 21]. Available at: http://ClinicalTrials.gov/show/NCT01311791. NLM Identifier: NCT01311791.

45. LoneStar Heart Inc. An Open Label Rollover Trial for Patients Randomized to the Control Group of Study LSH-10-001. In: ClinicalTrials.gov [Internet]. Bethesda (MD): National Library of Medicine (US). 2014- [cited 2014 Nov 21]. Available at: http://ClinicalTrials.gov/show/NCT02226679. NLM Identifier: NCT02226679.

46. Yu J, Gu Y, Du KT, Mihardja S, Sievers RE, Lee RJ. The effect of injected RGD modified alginate on angiogenesis and left ventricular function in a chronic rat infarct model. Biomaterials 2009;30(5):751-756.

47. Tsur-Gang O, Ruvinov E, Landa N, Holbova R, Feinberg MS, Leor J, et al. The effects of peptide-based modification of alginate on left ventricular remodeling and function after myocardial infarction. Biomaterials 2009;30(2):189-195.

48. Mukherjee R, Zavadzkas JA, Saunders SM, McLean JE, Jeffords LB, Beck C, et al. Targeted myocardial microinjections of a biocomposite material reduces infarct expansion in pigs. Ann Thorac Surg 2008;86(4):1268-1276.

49. Parenteau-Bareil R, Gauvin R, Berthod F. Collagen-based biomaterials for tissue engineering applications. Materials 2010;3(3):1863-1887.

50. Rosenblatt J, Devereux B, Wallace D. Injectable collagen as a pH-sensitive hydrogel. Biomaterials 1994;15(12):985-995.

51. Dai W, Wold LE, Dow JS, Kloner RA. Thickening of the infarcted wall by collagen injection improves left ventricular function in rats: a novel approach to preserve cardiac function after myocardial infarction. J Am Coll Cardiol 2005;46(4):714-719.

52. Hughes CS, Postovit LM, Lajoie GA. Matrigel: A complex protein mixture required for optimal growth of cell culture. Proteomics 2010;10(9):1886-1890.

53. Laflamme MA, Chen KY, Naumova AV, Muskheli V, Fugate JA, Dupras SK, et al. Cardiomyocytes derived from human embryonic stem cells in pro-survival factors enhance function of infarcted rat hearts. Nat Biotechnol 2007;25(9):1015-1024.

54. Ou L, Li W, Zhang Y, Wang W, Liu J, Sorg H, et al. Intracardiac injection of matrigel induces stem cell recruitment and improves cardiac functions in a rat myocardial infarction model. J Cell Mol Med 2011;15(6):1310-1318.

55. Kofidis T, Lebl DR, Martinez EC, Hoyt G, Tanaka M, Robbins RC. Novel injectable bioartificial tissue facilitates targeted, less invasive, large-scale tissue restoration on the beating heart after myocardial injury. Circulation 2005;112(9 Suppl):I173-7.

56. Kofidis T, de Bruin JL, Hoyt G, Ho Y, Tanaka M, Yamane T, et al. Myocardial restoration with embryonic stem cell bioartificial tissue transplantation. J Heart Lung Transplant 2005;24(6):737-744.

57. Lu WN, Lu SH, Wang HB, Li DX, Duan CM, Liu ZQ, et al. Functional improvement of infarcted heart by co-injection of embryonic stem cells with temperature-responsive chitosan hydrogel. Tissue Eng Part A 2009;15(6):1437-1447.

58. Liu Z, Wang H, Wang Y, Lin Q, Yao A, Cao F, et al. The influence of chitosan hydrogel on stem cell engraftment, survival and homing in the ischemic myocardial microenvironment. Biomaterials 2012;33(11):3093-3106.

59. Hoemann CD, Chenite A, Sun J, Hurtig M, Serreqi A, Lu Z, et al. Cytocompatible gel formation of chitosan-glycerol phosphate solutions supplemented with hydroxyl ethyl cellulose is due to the presence of glyoxal. J Biomed Mater Res A 2007;83A(2):521-529.

60. Chenite A, Chaput C, Wang D, Combes C, Buschmann M, Hoemann C, et al. Novel injectable neutral solutions of chitosan form biodegradable gels in situ. Biomaterials 2000;21(21):2155-2161.

61. Ruel-Gariepy E, Shive M, Bichara A, Berrada M, Le Garrec D, Chenite A, et al. A thermosensitive chitosan-based hydrogel for the local delivery of paclitaxel. Eur J Pharm Biopharm 2004;57(1):53-63.

62. Wang H, Zhang X, Li Y, Ma Y, Zhang Y, Liu Z, et al. Improved myocardial performance in infarcted rat heart by co-injection of basic fibroblast growth factor with temperature-responsive Chitosan hydrogel. Journal of Heart and Lung Transplantation 2010;29(8):881-887.

63. Toole BP. Hyaluronan: From extracellular glue to pericellular cue. Nat Rev Cancer 2004;4(7):528-539.

64. Yoon SJ, Fang YH, Lim CH, Kim BS, Son HS, Park Y, et al. Regeneration of ischemic heart using hyaluronic acid-based injectable hydrogel. J Biomed Mater Res B Appl Biomater 2009;91(1):163-171.

65. Ifkovits JL, Tous E, Minakawa M, Morita M, Robb JD, Koomalsingh KJ, et al. Injectable hydrogel properties influence infarct expansion and extent of postinfarction left ventricular remodeling in an ovine model. Proc Natl Acad Sci U S A 2010;107(25):11507-11512.

66. Tous E, Ifkovits JL, Koomalsingh KJ, Shuto T, Soeda T, Kondo N, et al. Influence of injectable hyaluronic acid hydrogel degradation behavior on infarction-induced ventricular remodeling. Biomacromolecules 2011;12(11):4127-4135.

67. Rouse JG, Van Dyke ME. A Review of Keratin-Based Biomaterials for Biomedical Applications. Materials 2010;3(2):999-1014.

68. Shen D, Wang X, Zhang L, Zhao X, Li J, Cheng K, et al. The amelioration of cardiac dysfunction after myocardial infarction by the injection of keratin biomaterials derived from human hair. Biomaterials 2011;32(35):9290-9299.

69. Crapo PM, Gilbert TW, Badylak SF. An overview of tissue and whole organ decellularization processes. Biomaterials 2011;32(12):3233-3243.

70. Singelyn JM, DeQuach JA, Seif-Naraghi SB, Littlefield RB, Schup-Magoffin PJ, Christman KL. Naturally derived myocardial matrix as an injectable scaffold for cardiac tissue engineering. Biomaterials 2009;30(29):5409-5416.

71. Singelyn JM, Sundaramurthy P, Johnson TD, Schup-Magoffin PJ, Hu DP, Faulk DM, et al. Catheter-deliverable hydrogel derived from decellularized ventricular extracellular matrix increases endogenous cardiomyocytes and preserves cardiac function post-myocardial infarction. J Am Coll Cardiol 2012;59(8):751-763.

72. Seif-Naraghi SB, Singelyn JM, Salvatore MA, Osborn KG, Wang JJ, Sampat U, et al. Safety and efficacy of an injectable extracellular matrix hydrogel for treating myocardial infarction. Sci Transl Med 2013;5(173):173ra25.

73. Okada M, Payne TR, Oshima H, Momoi N, Tobita K, Huard J. Differential efficacy of gels derived from small intestinal submucosa as an injectable biomaterial for myocardial infarct repair. Biomaterials 2010;31(30):7678-7683.

74. Davis ME, Hsieh PC, Grodzinsky AJ, Lee RT. Custom design of the cardiac microenvironment with biomaterials. Circ Res 2005;97(1):8-15.

75. Fujimoto KL, Ma Z, Nelson DM, Hashizume R, Guan J, Tobita K, et al. Synthesis, characterization and therapeutic efficacy of a biodegradable, thermoresponsive hydrogel designed for application in chronic infarcted myocardium. Biomaterials 2009;30(26):4357-4368.

76. Wang T, Wu DQ, Jiang XJ, Zhang XZ, Li XY, Zhang JF, et al. Novel thermosensitive hydrogel injection inhibits post-infarct ventricle remodelling. Eur J Heart Fail 2009;11(1):14-19.

77. Wall ST, Yeh C, Tu RYK, Mann MJ, Healy KE. Biomimetic matrices for myocardial stabilization and stem cell transplantation. J Biomed Mater Res A 2010;95A(4):1055-1066.

78. Li X, Wang T, Jiang X, Lin T, Wu D, Zhang X, et al. Injectable hydrogel helps bone marrow-derived mononuclear cells restore infarcted myocardium. Cardiology 2010;115(3):194-199.

79. Jiang X, Wang T, Li X, Wu D, Zheng Z, Zhang J, et al. Injection of a novel synthetic hydrogel preserves left ventricle function after myocardial infarction. J Biomed Mater Res A 2009;90A(2):472-477.

80. Dobner S, Bezuidenhout D, Govender P, Zilla P, Davies N. A synthetic non-degradable polyethylene glycol hydrogel retards adverse post-infarct left ventricular remodeling. J Card Fail 2009;15(7):629-636.

81. Rane AA, Christman KL. Biomaterials for the treatment of myocardial infarction: A 5-year update. J Am Coll Cardiol 2011;58(25):2615-2629.

82. Wang T, Jiang XJ, Lin T, Ren S, Li X, Zhang X, et al. The inhibition of postinfarct ventricle remodeling without polycythaemia following local sustained intramyocardial delivery of erythropoietin within a supramolecular hydrogel. Biomaterials 2009;30(25):4161-4167.

83. Wu J, Zeng F, Huang X, Chung JC, Konecny F, Weisel RD, et al. Infarct stabilization and cardiac repair with a VEGF-conjugated, injectable hydrogel. Biomaterials 2011;32(2):579-586.

84. Kraehenbuehl TP, Ferreira LS, Hayward AM, Nahrendorf M, van der Vlies AJ, Vasile E, et al. Human embryonic stem cell-derived microvascular grafts for cardiac tissue preservation after myocardial infarction. Biomaterials 2011;32(4):1102-1109.

85. Beltrami CA, Finato N, Rocco M, Feruglio GA, Puricelli C, Cigola E, et al. Structural basis of end-stage failure in ischemic cardiomyopathy in humans. Circulation 1994;89(1):151-163.

86. Soonpaa MH, Field LJ. Survey of studies examining mammalian cardiomyocyte DNA synthesis. Circ Res 1998;83(1):15-26.

87. Beltrami AP, Barlucchi L, Torella D, Baker M, Limana F, Chimenti S, et al. Adult cardiac stem cells are multipotent and support myocardial regeneration. Cell 2003;114(6):763-776.

88. Zenovich AG, Taylor DA. Atherosclerosis as a disease of failed endogenous repair. Front Biosci 2008;13:3621-3636.

89. Reinecke H, Murry CE. Taking the death toll after cardiomyocyte grafting: a reminder of the importance of quantitative biology. J Mol Cell Cardiol 2002;34(3):251-253.

90. Menasche P. Stem cells for clinical use in cardiovascular medicine: Current limitations and future perspectives. Thromb Haemost 2005;94(4):697-701.

91. Segers VF, Lee RT. Stem-cell therapy for cardiac disease. Nature 2008;451(7181):937-942.

92. Zimmermann WH. Embryonic and embryonic-like stem cells in heart muscle engineering. J Mol Cell Cardiol 2011;50(2):320-326.

93. Menasche P. Skeletal myoblasts and cardiac repair. J Mol Cell Cardiol 2008;45(4):545-553.

94. Murry CE, Soonpaa MH, Reinecke H, Nakajima H, Nakajima HO, Rubart M, et al. Haematopoietic stem cells do not transdifferentiate into cardiac myocytes in myocardial infarcts. Nature 2004;428(6983):664-668.

95. Murry CE, Whitney ML, Reinecke H. Muscle cell grafting for the treatment and prevention of heart failure. J Card Fail 2002;8(6 Suppl):S532-41.

96. Le Blanc K, Pittenger M. Mesenchymal stem cells: Progress toward promise. Cytotherapy 2005;7(1):36-45.

97. Orlic D. BM stem cells and cardiac repair: where do we stand in 2004? Cytotherapy 2005;7(1):3-15.

98. Smits AM, van Laake LW, den Ouden K, Schreurs C, Szuhai K, van Echteld CJ, et al. Human cardiomyocyte progenitor cell transplantation preserves long-term function of the infarcted mouse myocardium. Cardiovasc Res 2009;83(3):527-535.

99. Koh GY, Klug MG, Soonpaa MH, Field LJ. Differentiation and long-term survival of C2C12 myoblast grafts in heart. J Clin Invest 1993;92(3):1548-1554.

100. D'Alessandro DA, Michler RE. Current and future status of stem cell therapy in heart failure. Curr Treat Options Cardiovasc Med 2010;12(6):614-627.

101. Terrovitis JV, Smith RR, Marban E. Assessment and optimization of cell engraftment after transplantation into the heart. Circ Res 2010;106(3):479-494.

102. Choi YS, Dusting GJ, Stubbs S, Arunothayaraj S, Han XL, Collas P, et al. Differentiation of human adipose-derived stem cells into beating cardiomyocytes. J Cell Mol Med 2010;14(4):878-889.

103. Hofmann M, Wollert KC, Meyer GP, Menke A, Arseniev L, Hertenstein B, et al. Monitoring of bone marrow cell homing into the infarcted human myocardium. Circulation 2005;111(17):2198-2202.

104. Hou D, Youssef EA, Brinton TJ, Zhang P, Rogers P, Price ET, et al. Radiolabeled cell distribution after intramyocardial, intracoronary, and interstitial retrograde coronary venous delivery: Implications for current clinical trials. Circulation 2005;112(9 Suppl):I150-I156.

105. Robey TE, Saiget MK, Reinecke H, Murry CE. Systems approaches to preventing transplanted cell death in cardiac repair. J Mol Cell Cardiol 2008;45(4):567-581.

106. Zvibel I, Smets F, Soriano H. Anoikis: Roadblock to cell transplantation? Cell Transplant 2002;11(7):621-630.

107. Matsumoto T, Mooney DJ. Cell instructive polymers. Adv Biochem Eng Biotechnol 2006;102:113-137.

108. Li S, Huang NF, Hsu S. Mechanotransduction in endothelial cell migration. J Cell Biochem 2005;96(6):1110-1126.

109. Cohen S, Leor J. Rebuilding broken hearts. Biologists and engineers working together in the fledgling field of tissue engineering are within reach of one of their greatest goals: constructing a living human heart patch. Sci Am 2004;291(5):44-51.

110. Tran N, Li Y, Bertrand S, Bangratz S, Carteaux JP, Stoltz JF, et al. Autologous cell transplantation and cardiac tissue engineering: potential applications in heart failure. Biorheology 2003;40(1-3):411-415.

111. Schachinger V, Assmus B, Erbs S, Elsasser A, Haberbosch W, Hambrecht R, et al. Intracoronary infusion of bone marrow-derived mononuclear cells abrogates adverse left ventricular remodelling post-acute myocardial infarction: insights from the reinfusion of enriched progenitor cells and infarct remodelling in acute myocardial infarction (REPAIR-AMI) trial. Eur J Heart Fail 2009;11(10):973-979.

112. Simpson D, Liu H, Fan TH, Nerem R, Dudley SC,Jr. A tissue engineering approach to progenitor cell delivery results in significant cell engraftment and improved myocardial remodeling. Stem Cells 2007;25(9):2350-2357.

113. Li RK, Jia ZQ, Weisel RD, Mickle DA, Choi A, Yau TM. Survival and function of bioengineered cardiac grafts. Circulation 1999;100(19 Suppl):II63-9.

114. Hamdi H, Furuta A, Bellamy V, Bel A, Puymirat E, Peyrard S, et al. Cell delivery: Intramyocardial injections or epicardial deposition? A head-to-head comparison. Ann Thorac Surg 2009;87(4):1196-1204.

115. Chachques JC, Trainini JC, Lago N, Cortes-Morichetti M, Schussler O, Carpentier A. Myocardial Assistance by Grafting a New Bioartificial Upgraded Myocardium (MAGNUM trial): Clinical feasibility study. Ann Thorac Surg 2008;85(3):901-908.

116. Zhang G, Wang X, Wang Z, Zhang J, Suggs L. A PEGylated fibrin patch for mesenchymal stem cell delivery. Tissue Eng 2006;12(1):9-19.

117. Zhang G, Hu Q, Braunlin EA, Suggs LJ, Zhang J. Enhancing efficacy of stem cell transplantation to the heart with a PEGylated fibrin biomatrix. Tissue Eng Part A 2008;14(6):1025-1036.

118. Guo HD, Wang HJ, Tan YZ, Wu JH. Transplantation of marrow-derived cardiac stem cells carried in fibrin improves cardiac function after myocardial infarction. Tissue Eng Part A 2011;17(1-2):45-58.

119. Ott HC, Matthiesen TS, Goh SK, Black LD, Kren SM, Netoff TI, et al. Perfusion-decellularized matrix: using nature's platform to engineer a bioartificial heart. Nat Med 2008;14(2):213-221.

120. Fernandes S, Naumova AV, Zhu WZ, Laflamme MA, Gold J, Murry CE. Human embryonic stem cell-derived cardiomyocytes engraft but do not alter cardiac remodeling after chronic infarction in rats. J Mol Cell Cardiol 2010;49(6):941-949.

121. Traverse JH. Using biomaterials to improve the efficacy of cell therapy following acute myocardial infarction. J Cardiovasc Transl Res 2012;5(1):67-72.

122. Nicodemus GD, Bryant SJ. Cell encapsulation in biodegradable hydrogels for tissue engineering applications. Tissue Eng Part B Rev 2008;14(2):149-165.

123. Bian W, Liau B, Badie N, Bursac N. Mesoscopic hydrogel molding to control the 3D geometry of bioartificial muscle tissues. Nat Protoc 2009;4(10):1522-1534.

124. Gaudette GR, Cohen IS. Cardiac regeneration: Materials can improve the passive properties of myocardium, but cell therapy must do more. Circulation 2006;114(24):2575-2577.

125. Nakamuta JS, Danoviz ME, Marques FLN, dos Santos L, Becker C, Goncalves GA, et al. Cell therapy attenuates cardiac dysfunction post myocardial infarction: Effect of timing, routes of injection and a fibrin scaffold. Plos One 2009;4(6):e6005.

126. Yang HS, Bhang SH, Kim I, Lee T, Kang J, Lee D, et al. In Situ cardiomyogenic differentiation of implanted bone marrow mononuclear cells by local delivery of transforming growth factor-beta 1. Cell Transplant 2012;21(1):299-312.

127. Ryu JH, Kim IK, Cho SW, Cho MC, Hwang KK, Piao H, et al. Implantation of bone marrow mononuclear cells using injectable fibrin matrix enhances neovascularization in infarcted myocardium. Biomaterials 2005;26(3):319-326.

128. Martens TP, Godier AFG, Parks JJ, Wan LQ, Koeckert MS, Eng GM, et al. Percutaneous cell delivery into the heart using hydrogels polymerizing in situ. Cell Transplant 2009;18(3):297-304.

129. Chekanov V, Akhtar M, Tchekanov G, Dangas G, Shehzad MZ, Tio F, et al. Transplantation of autologous endothelial cells induces angiogenesis. Pacing Clin Electrophysiol 2003;26(1 Pt 2):496-499.

130. Danoviz ME, Nakamuta JS, Marques FLN, dos Santos L, Alvarenga EC, dos Santos AA, et al. Rat adipose tissue-derived stem cells transplantation attenuates cardiac dysfunction post infarction and biopolymers enhance cell retention. Plos One 2010;5(8):e12077.

131. Zhang X, Wang H, Ma X, Adila A, Wang B, Liu F, et al. Preservation of the cardiac function in infarcted rat hearts by the transplantation of adipose-derived stem cells with injectable fibrin scaffolds. Exp Biol Med (Maywood) 2010;235(12):1505-1515.

132. Jawad H, Ali NN, Lyon AR, Chen QZ, Harding SE, Boccaccini AR. Myocardial tissue engineering: a review. J Tissue Eng Regen Med 2007;1(5):327-342.

133. Dai W, Hale SL, Kay GL, Jyrala AJ, Kloner RA. Delivering stem cells to the heart in a collagen matrix reduces relocation of cells to other organs as assessed by nanoparticle technology. Regen Med 2009;4(3):387-395.

134. Kofidis T, de Bruin JL, Hoyt G, Lebl DR, Tanaka M, Yamane T, et al. Injectable bioartificial myocardial tissue for large-scale intramural cell transfer and functional recovery of injured heart muscle. J Thorac Cardiovasc Surg 2004;128(4):571-578.

135. Lin Y, Yeh M, Yang Y, Tsai D, Chu T, Shih Y, et al. Intramyocardial peptide nanofiber injection improves postinfarction ventricular remodeling and efficacy of bone marrow cell therapy in pigs. Circulation 2010;122(11):S132-S141.

136. Wang T, Jiang X, Tang Q, Li X, Lin T, Wu D, et al. Bone marrow stem cells implantation with alpha-cyclodextrin/MPEG-PCL-MPEG hydrogel improves cardiac function after myocardial infarction. Acta Biomaterialia 2009;5(8):2939-2944.

137. Wang H, Liu Z, Li D, Guo X, Kasper FK, Duan C, et al. Injectable biodegradable hydrogels for embryonic stem cell transplantation: improved cardiac remodelling and function of myocardial infarction. J Cell Mol Med 2012;16(6):1310-1320.

138. Habib M, Shapira-Schweitzer K, Caspi O, Gepstein A, Arbel G, Aronson D, et al. A combined cell therapy and in-situ tissue-engineering approach for myocardial repair. Biomaterials 2011;32(30):7514-7523.

139. Yu J, Du KT, Fang Q, Gu Y, Mihardja SS, Sievers RE, et al. The use of human mesenchymal stem cells encapsulated in RGD modified alginate microspheres in the repair of myocardial infarction in the rat. Biomaterials 2010;31(27):7012-7020.

140. Thompson CA, Nasseri BA, Makower J, Houser S, McGarry M, Lamson T, et al. Percutaneous transvenous cellular cardiomyoplasty. A novel nonsurgical approach for myocardial cell transplantation. J Am Coll Cardiol 2003;41(11):1964-1971.

141. Zimmermann WH, Fink C, Kralisch D, Remmers U, Weil J, Eschenhagen T. Three-dimensional engineered heart tissue from neonatal rat cardiac myocytes. Biotechnol Bioeng 2000;68(1):106-114.

142. Zhang P, Zhang H, Wang H, Wei Y, Hu S. Artificial matrix helps neonatal cardiomyocytes restore injured myocardium in rats. Artif Organs 2006;30(2):86-93.

143. Davis ME, Hsieh PC, Takahashi T, Song Q, Zhang S, Kamm RD, et al. Local myocardial insulin-like growth factor 1 (IGF-1) delivery with biotinylated peptide nanofibers improves cell therapy for myocardial infarction. Proc Natl Acad Sci U S A 2006;103(21):8155-8160.

144. Dubois G, Segers VFM, Bellamy V, Sabbah L, Peyrard S, Bruneval P, et al. Self-assembling peptide nanofibers and skeletal myoblast transplantation in infarcted myocardium. J Biomed Mater Res Part B Appl Biomater 2008;87B(1):222-228.

145. Davis ME, Motion JP, Narmoneva DA, Takahashi T, Hakuno D, Kamm RD, et al. Injectable self-assembling peptide nanofibers create intramyocardial microenvironments for endothelial cells. Circulation 2005;111(4):442-450.

146. Padin-Iruegas ME, Misao Y, Davis ME, Segers VF, Esposito G, Tokunou T, et al. Cardiac progenitor cells and biotinylated insulin-like growth factor-1 nanofibers improve endogenous and exogenous myocardial regeneration after infarction. Circulation 2009;120(10):876-887.

147. Ruvinov E, Leor J, Cohen S. The promotion of myocardial repair by the sequential delivery of IGF-1 and HGF from an injectable alginate biomaterial in a model of acute myocardial infarction. Biomaterials 2011;32(2):565-578.

148. Hao X, Silva EA, Mansson-Broberg A, Grinnemo KH, Siddiqui AJ, Dellgren G, et al. Angiogenic effects of sequential release of VEGF-A165 and PDGF-BB with alginate hydrogels after myocardial infarction. Cardiovasc Res 2007;75(1):178-185.

149. Purcell BP, Elser JA, Mu A, Margulies KB, Burdick JA. Synergistic effects of SDF-1 alpha chemokine and hyaluronic acid release from degradable hydrogels on directing bone marrow derived cell homing to the myocardium. Biomaterials 2012;33(31):7849-7857.

150. Shao ZQ, Takaji K, Katayama Y, Kunitomo R, Sakaguchi H, Lai ZF, et al. Effects of intramyocardial administration of slow-release basic fibroblast growth factor on angiogenesis and ventricular remodeling in a rat infarct model. Circ J 2006;70(4):471-477.

151. Liu Y, Sun L, Huan Y, Zhao H, Deng J. Effects of basic fibroblast growth factor microspheres on angiogenesis in ischemic myocardium and cardiac function: analysis with dobutamine cardiovascular magnetic resonance tagging. Eur J Cardiothorac Surg 2006;30(1):103-107.

152. Kim JH, Jung Y, Kim S, Sun K, Choi J, Kim HC, et al. The enhancement of mature vessel formation and cardiac function in infarcted hearts using dual growth factor delivery with self-assembling peptides. Biomaterials 2011;32(26):6080-6088.

153. Segers VF, Tokunou T, Higgins LJ, MacGillivray C, Gannon J, Lee RT. Local delivery of protease-resistant stromal cell derived factor-1 for stem cell recruitment after myocardial infarction. Circulation 2007;116(15):1683-1692.

154. Segers VF, Lee RT. Protein therapeutics for cardiac regeneration after myocardial infarction. J Cardiovasc Transl Res 2010;3(5):469-477.

155. Urbanek K, Rota M, Cascapera S, Bearzi C, Nascimbene A, De Angelis A, et al. Cardiac stem cells possess growth factor-receptor systems that after activation regenerate the

infarcted myocardium, improving ventricular function and long-term survival. Circ Res 2005;97(7):663-673.

156. Epstein S, Fuchs S, Zhou Y, Baffour R, Kornowski R. Therapeutic interventions for enhancing collateral development by administration of growth factors: basic principles, early results and potential hazards. Cardiovasc Res 2001;49(3):532-542.

157. Vandervelde S, van Luyn MJ, Tio RA, Harmsen MC. Signaling factors in stem cell-mediated repair of infarcted myocardium. J Mol Cell Cardiol 2005;39(2):363-376.

158. Kretlow JD, Klouda L, Mikos AG. Injectable matrices and scaffolds for drug delivery in tissue engineering. Adv Drug Deliv Rev 2007;59(4-5):263-273.

159. Chen RR, Mooney DJ. Polymeric growth factor delivery strategies for tissue engineering. Pharm Res 2003;20(8):1103-1112.

160. Langer R, Folkman J. Polymers for the sustained release of proteins and other macromolecules. Nature 1976;263(5580):797-800.

161. Tabata Y, Hijikata S, Ikada Y. Enhanced vascularization and tissue granulation by basic fibroblast growth-factor impregnated in gelatin hydrogels. J Controlled Release 1994;31(2):189-199.

162. Iwakura A, Fujita M, Kataoka K, Tambara K, Sakakibara Y, Komeda M, et al. Intramyocardial sustained delivery of basic fibroblast growth factor improves angiogenesis and ventricular function in a rat infarct model. Heart Vessels 2003;18(2):93-99.

163. Sakakibara Y, Yamamoto M, Nishimura K, Nishina T, Miwa S, Handa N, et al. Prevasculrization using gelatin microsphere containing basic-fibroblast growth factor enhances the benefits of cardiomyocytes transplantation in rats with ischemic cardiomyopathy. Circulation 2000;102(18):650-650.

164. Fujita M, Ishihara M, Morimoto Y, Simizu M, Saito Y, Yura H, et al. Efficacy of photocrosslinkable chitosan hydrogel containing fibroblast growth factor-2 in a rabbit model of chronic myocardial infarction. J Surg Res 2005;126(1):27-33.

165. Yancopoulos G, Davis S, Gale N, Rudge J, Wiegand S, Holash J. Vascular-specific growth factors and blood vessel formation. Nature 2000;407(6801):242-248.

166. Banquet S, Gomez E, Nicol L, Edwards-Levy F, Henry JP, Cao R, et al. Arteriogenic therapy by intramyocardial sustained delivery of a novel growth factor combination prevents chronic heart failure. Circulation 2011;124(9):1059-1069.

167. Avigdor A, Goichberg P, Shivtiel S, Dar A, Peled A, Samira S, et al. CD44 and hyaluronic acid cooperate with SDF-1 in the trafficking of human CD34(+) stem/progenitor cells to bone marrow. Blood 2004;103(8):2981-2989.

168. MacArthur JW,Jr., Purcell BP, Shudo Y, Cohen JE, Fairman A, Trubelja A, et al. Sustained release of engineered stromal cell-derived factor 1-alpha from injectable hydrogels effectively recruits endothelial progenitor cells and preserves ventricular function after myocardial infarction. Circulation 2013;128(11):S79-S86.

169. Hsieh PC, Davis ME, Gannon J, MacGillivray C, Lee RT. Controlled delivery of PDGF-BB for myocardial protection using injectable self-assembling peptide nanofibers. J Clin Invest 2006;116(1):237-248.

CHAPTER 4

In Vitro Characterization of Hydrolytically Degradable Hyaluronic Acid Hydrogels

4.1. Introduction

Injectable biomaterials have become an attractive therapy to attenuate LV remodeling. Particularly, acellular hydrogels have been explored to limit infarct expansion by bulking the myocardial wall to modulate myocardial remodeling.[1] Hydrogels are water-swollen networks of polymer chains with a high degree of flexibility, similar to natural tissue[2] and, as a result, have been explored for a variety of tissue engineering and drug delivery applications.[3-6] For cardiac repair post-MI, hydrogels can be used to mechanically stabilize the myocardial wall as well as modulate maladaptive biological processes through delivery of therapies, such as cells and growth factors,[7-11] as thoroughly discussed in Chapter 3. Moreover, recent work from our group was the first to demonstrate the importance of injectable biomaterial properties, specifically mechanical stiffness and degradation, on attenuating LV remodeling in an ovine infarct model.[12,13] However, despite the wide range of materials investigated for MI repair, there is still a need for tunable hydrogel systems to further investigate the correlation between specific hydrogel properties and the resulting *in vivo* outcomes.

One such tunable biomaterial is hyaluronic acid (HA). HA is a linear, negatively charged, non-sulfated glycosaminoglycans (GAG) ubiquitously found in the extracellular matrix (ECM) of tissues.[14] More specifically, HA is an ideal candidate for cardiac repair because it is found in the native cardiac ECM and plays a role in cardiac embryogenesis, angiogenesis, cell migration and scar reduction. It helps maintain myocardial homeostasis both structurally through its mechanical properties and functionally through cell and growth factor interactions.[15-17] Furthermore, HA can be readily modified with numerous reactive groups (e.g., aldehydes,[18,19] malemides,[20] hydrazides

and dihydrazides,[19,21,22] thiols,[23,24] norbornenes,[24] adamantanes,[25] cyclodextrins,[25] and methacrylates and acrylates[12-14,26-28]) at the carboxyl and hydroxyl groups on each repeat unit to enable tunability of material properties towards specific applications,[14,29,30] including MI repair.[12,13] In addition to the type and degree of HA modification, the macromer molecular weight and concentration can also be varied to tailor material properties.[13,14,27,28]

The addition of reactive groups not only enables tunability of material properties but also crosslinking into hydrogels, where the mechanism of gelation depends on the specific functional group.[31] Hydrogels form by various gelation mechanisms, including self-assembly, ionic crosslinking, covalent crosslinking through chemical reactions, and inherent phase transition behavior.[32] Due to their unique gelation properties, hydrogels offer the advantage of initially being in a viscous form during delivery and then solidifying into a stable gel once delivered to the intended target tissue. One crosslinking approach is to radically polymerize the methacrylate groups on HA using an initiator or stimulus, such as light, temperature, or oxidation-reduction (redox) species; the radicals propagate through the methacrylate vinyl groups to form kinetic chains to crosslink the macromer.[12-14,26-28,31] The properties of the resulting hydrogel thus depend on the concentration of the initiator as well as the macromer modification and concentration. Previous studies have demonstrated that the mechanical properties of methacrylated HA (MeHA, **Figure 4.1B**) hydrogels can be tuned through both the macromer modification and initiator concentration: as the amount of reactive methacrylates or free radicals increases, the crosslinking density and thus, mechanics increase.[12,13] In addition, crosslinking via redox chemical initiators[12,13,33] circumvents the depth penetration limitations of photopolymerization[14,28,31] and increases the potential for clinical translation because the pre-polymer solution can be administered (ideally via catheter) directly to the target organ.

To further tune hydrogel properties (i.e., degradation), HA can also be modified to include a hydrolytically degradable functional group, hydroxyethyl methacrylate (HeMA), to produce the gel precursor HeMA-HA (**Figure 4.1A**). Similar to MeHA, HeMA-HA contains a reactive

methacrylate for free-radical initiated crosslinking: when the macromer is mixed with chemical initiators, stable hydrogels form within minutes.[12] In contrast to MeHA, HeMA-HA contains ester bonds that are hydrolytically unstable. While HA is enzymatically degraded in the body by hyaluronidases,[16,34] this process occurs over the time frame of months to years and is dependent on the physiological concentration of hyaluronidase *in vivo*. The addition of HeMA enables finely-tuned, multimodal hydrogel degradation: enzymatic degradation through the HA backbone and hydrolysis through the ester groups of HeMA. In this tunable system, the rate of crosslinking, and therefore gelation onset, can be controlled through the initiator concentration whereas the rate of degradation and maintenance of mechanical properties can be controlled through the HeMA modification on HA and the HA concentration.

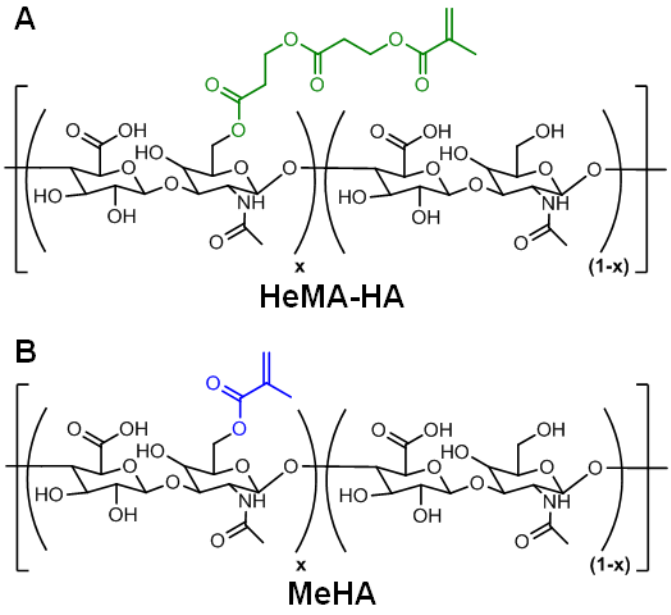

Figure 4.1. Chemical structures of HeMA-HA (A) and MeHA (B) macromers.

In this chapter, the tunability of HA hydrogels was examined in two systems: 1) pure HeMA-HA hydrogels and 2) copolymer hydrogels consisting of HeMA-HA and MeHA. A two component redox initiator system of ammonium persulfate (APS) and N,N,N,N',N'-tetramethylenediamine (TEMED) was used to induce polymerization of both macromers into

hydrogels. In addition to offering the potential for noninvasive, catheter-based delivery, the use of redox initiators for crosslinking provides enhanced control over gelation timing.[12,13] Kinetic chains were formed through crosslinking the reactive methacrylate groups on all macromers to generate hydrogel networks where the bulk properties depended on three parameters: initiator concentration, macromer modification, and macromer concentration. The effect of altering each of these material parameters on the resulting hydrogel properties (i.e., gelation, degradation, and mechanics) was investigated to provide insight into the design and material properties of HA hydrogels towards the identification of optimal material properties for targeted MI therapies.

4.2. Materials and Methods

4.2.1. Synthesis of Hydroxyethyl Methacrylated HA (HeMA-HA) Macromer

HA was modified with hydroxyethyl methacrylate (HeMA) by coupling HA-tetrabutylammonium salt (HA-TBA) to 2-hydroxyethyl-methacryl-succinate (HeMA-COOH), as previously described.[12] HA-TBA was synthesized by converting HA-sodium salt (HA-Na, 75 kDa, Lifecore) to a TBA salt using an acidic ion exchange (25°C, 8hrs) with Dowex resin (50W×8-200, Sigma), followed by neutralization with TBA hydroxide (TBA-OH, Sigma) to pH 7.02-7.05 and subsequent lyophilization.[30] The conversion of Na to TBA enabled HA-TBA to be soluble in dimethyl sulfoxide (DMSO). ^{1}H-NMR (Bruker, 360 MHz) was used to determine the amount of TBA coupled to HA. HeMA-COOH was synthesized by reacting 2-hydroxyethyl-methacrylate (Acros) with succinic anhydride (Sigma) in dichloroethane (DCE) via a ring opening polymerization (65°C, 16hrs) catalyzed by N-methylimidazole (Sigma). HeMA-COOH was purified by washing with hydrochloric acid then deionized (DI) water. Excess DCE was removed by rotary evaporator. ^{1}H-NMR (Bruker, 360 MHz) was performed to confirm HeMA-COOH formation and purity. Finally, HA-TBA was coupled to HeMA-COOH in anhydrous DMSO (Acros) through an esterification reaction (45°C, 20hrs) using 4-dimethylaminopyridine (DMAP, Sigma) and the coupling agent di-tert-butyl dicarbonate (BOC_2O, Sigma) (**Figure 4.2A**). The macromer was purified by dialyzing against DI water, acetone precipitating, and dialyzing again. The macromer

was then lyophilized and the HeMA modification on HA was assessed with ^{1}H-NMR (Bruker, 360 MHz) (**Figure 4.2B**). Modification was altered by varying the ratio of BOC_2O to HeMA-COOH.

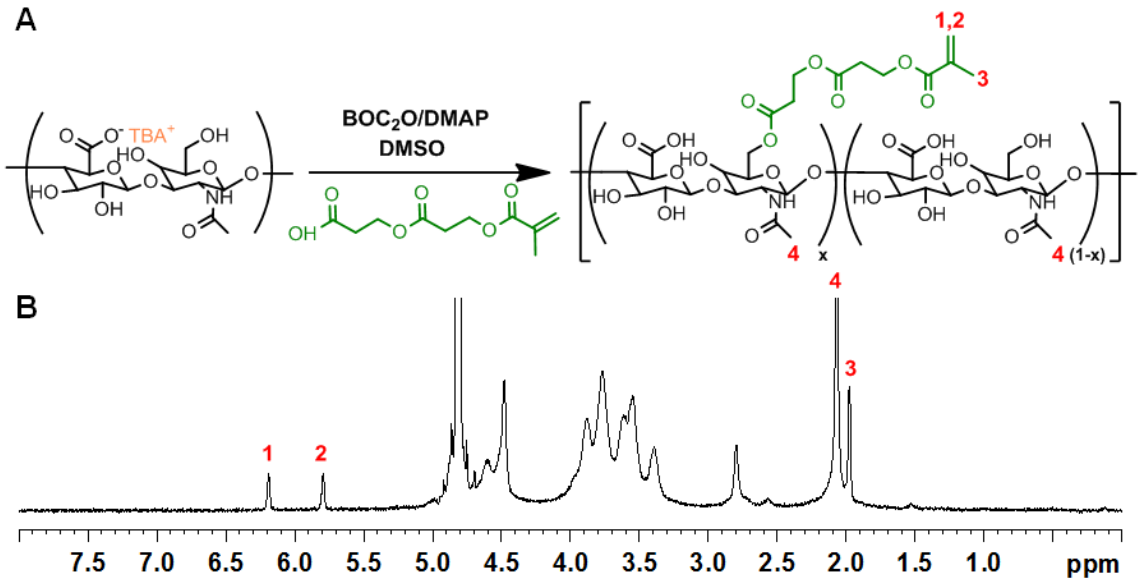

Figure 4.2. HeMA-HA macromer synthesis. HeMA-HA was synthesized by coupling HeMA-COOH to HA-TBA using DMAP and the coupling agent BOC_2O in DMSO (A). Methacrylation were assessed with ^{1}H-NMR by normalizing to the integral of peak 4 (B).

4.2.2. Synthesis of Methacrylated HA (MeHA) Macromer

As previously described, methacrylated HA (MeHA) was synthesized by reacting a 1 wt% solution of Na-HA (75 kDa, Lifecore) with a 20-fold excess of methacrylic anhydride (MA; Sigma) in DI H_2O on ice.[14] The solution was titrated with concentrated sodium hydroxide (Sigma) to maintain a constant pH of 8.0 (4°C, 24hrs) (**Figure 4.3A**). The macromer was purified by dialyzing against DI H_2O and subsequently lyophilized. ^{1}H-NMR (Bruker, 360 MHz) was used to assess purity and the extent of methacrylation on the HA backbone (**Figure 4.3B**). Modification was altered by varying the amount of MA relative to HA.

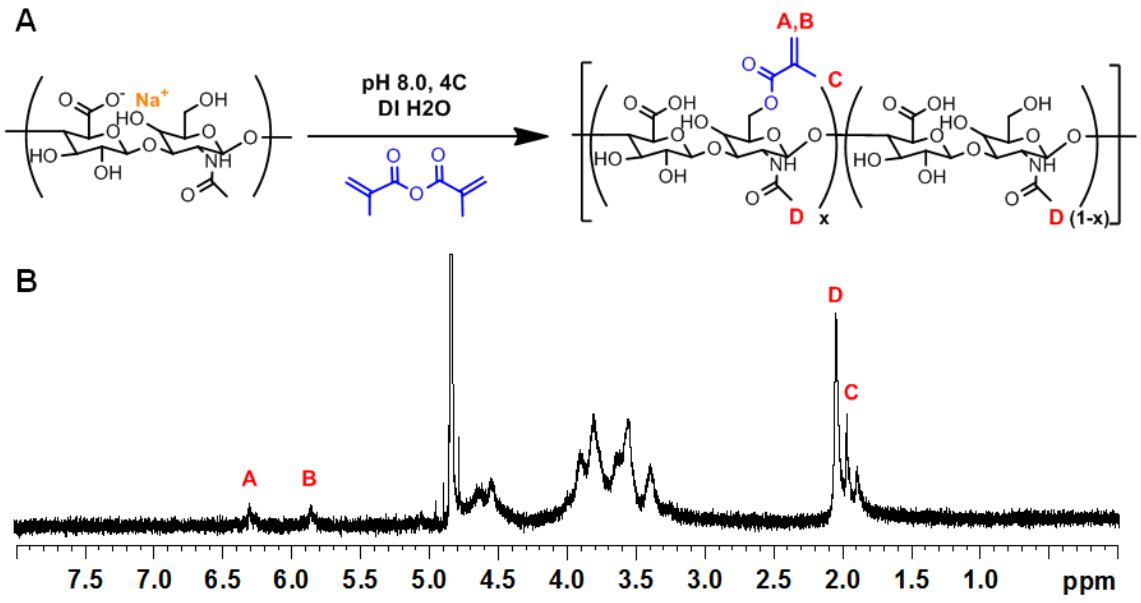

Figure 4.3. MeHA macromer synthesis. MeHA was synthesized by reacting Na-HA with a excess of methacrylic anhydride (MA) at 4°C in DI water. The pH was maintained at 8.0 using NaOH (A). Methacrylation was assessed with ^{1}H-NMR by normalizing to the integral of peak D (B).

4.2.3. HA Hydrogel Formation

HA macromers were crosslinked into hydrogels and characterized *in vitro* for gelation, degradation, and initial and temporal mechanics. Hydrogel formation was induced by crosslinking the methacrylate groups on HA using a redox radial initiator system of APS (Sigma) and TEMED (Sigma) (**Figure 4.4A**).[33] APS and TEMED were mixed with HA macromers dissolved in PBS to initiate gelation. For initial characterization studies of 10% and 35% modified HeMA-HA, 10 mM APS and 10 mM TEMED was used to induce crosslinking. For all subsequent studies, an initiator concentration of 5 mM APS and 5 mM TEMED was used (**Tables 4.1, 4.2**). Gel onset and completion were quantified using an AR2000ex Rheometer (TA Instruments) by monitoring the storage (G') and loss (G") moduli over time at 37°C under 1% strain and a frequency of 1 Hz in a cone-plate geometry (1°, 20 mm diameter) (**Figure 4.4B**).[12] Gel onset was defined as the time where G' and G" intersect and the viscosity (|n*|) was greater than one. Gel completion was

defined as the time where the percent change in both G' and |n*| were less than 1% for ten consecutive time steps.

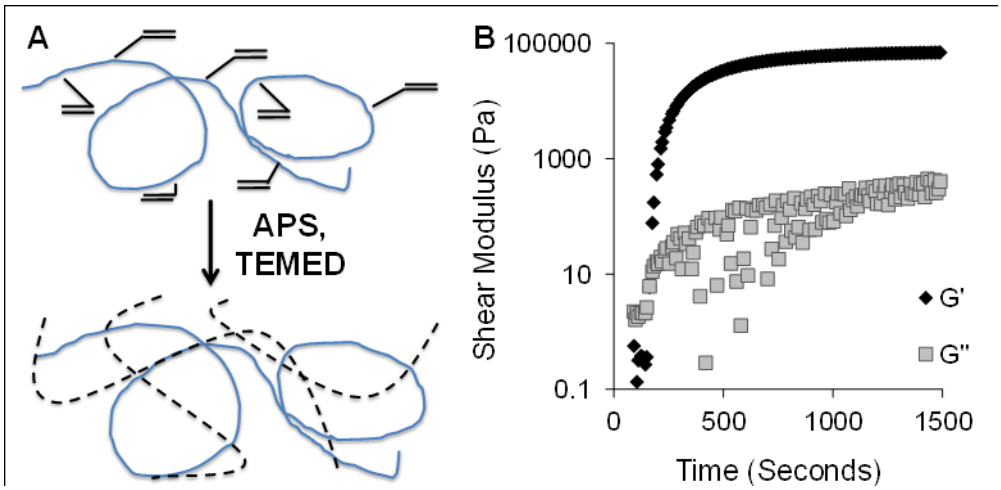

Figure 4.4. Mechanism of hydrogel formation. Hydrogel formation was induced using a two component radical initiator system of APS and TEMED (A). Representative rheological time sweep after mixing HeMA-HA macromer initiators, where the intersection of the storage (G') and loss (G") moduli is defined as gel onset (B).

4.2.4. *In Vitro* Hydrogel Characterization

For *in vitro* characterization of degradation and compressive mechanics, hydrogels (~50 µL) were formed in between two glass slides within a Teflon mold sealed with vacuum grease by mixing macromer solutions with APS and TEMED and incubating at 37°C for 30 minutes. Unless otherwise specified, degradation was monitored in PBS at 37°C. In all cases, HA mass loss was quantified using an uronic acid assay.[35,36] Hyaluronidase (Sigma) was added to PBS solutions surrounding the hydrogels at 0.3 mg/mL to completely enzymatically degrade the hydrogels after 20 weeks, if necessary. Compressive mechanical testing was performed using a Dynamic Mechanical Analyzer (DMA, Q800 TA Instruments) at a strain rate of 10%/min and compressive moduli were calculated from 10 to 20% strain.[37] Degradation and mechanics were assessed

immediately after gelation (day 0) and at desired time points throughout the degradation process (i.e., 1, 7, 14, 28, 56, 84 days, etc. after gelation).

Table 4.1. *In vitro* characterization studies of pure HeMA-HA hydrogels.

	Macromer		Chemical Initiators	
Study	**Mod. (%)**	**Conc. (wt%)**	**APS Conc. (mM)**	**TEMED Conc. (mM)**
1	10	4, 7, 10	5, 7.5, 10	5, 7.5, 10
	35	4, 7, 10	5, 7.5, 10	5, 7.5, 10
2	10	4, 7, 10	10	10
	35	4, 7, 10	10	10
3	25	7	5, 7.5, 10	5, 7.5, 10
4	10	2, 4, 6, 8, 10, 12	5	5
	25	2, 4, 6, 8, 10, 12	5	5
	40	2, 4, 6, 8, 10, 12	5	5
5	10	8, 10, 12	5	5
	40	4, 5, 6	5	5

Characterization studies were performed on two hydrogel systems 1) pure HeMA-HA hydrogels (**Table 4.1**) and 2) HeMA-HA/MeHA copolymer hydrogels (**Table 4.2**). Initial HeMA-HA hydrogel characterization studies examined the effect of altering macromer concentration and modification on hydrogel properties using 10% and 35% modified HeMA-HA at 4, 7, and 10 wt% gelled using 10 mM APS/TEMED. To select a single initiator concentration for gelation, the compressive modulus at one day after hydrogel formation was measured for hydrogels formed at three initiator concentrations (5 mM, 7.5 mM, 10 mM APS/TEMED) for the two modifications at the three macromer concentrations. A subsequent study examined differences in crosslinking density due to initiator concentration using three initiator concentrations (5 mM, 7.5 mM, 10 mM APS/TEMED) at a single macromer modification (25% modified) and macromer concentration (7 wt%). After varying the initiators, a concentration of 5 mM APS and 5 mM TEMED was selected for use in all subsequent studies (**Table 4.1**). To further examine the tunability of HeMA-HA

hydrogels, a more extensive study was performed with varying both the macromer modification (10%, 25%, 40% modified HeMA-HA) and concentration (2, 4, 6, 8, 10, 12 wt%). Based on this study, six hydrogel formulations at various macromer modifications and concentrations (10% modified at 8, 10, 12 wt%; 40% modified at 4, 5, 6 wt%) were selected for temporal assessment.

Table 4.2. *In vitro* characterization studies of HeMA-HA and MeHA copolymer hydrogels.

	Macromer		**Copolymer Ratio (v/v)**		**Chemical Initiators**	
Study	**Mod. (%)**	**Conc. (wt%)**	**HeMA-HA**	**MeHA**	**APS Conc. (mM)**	**TEMED Conc. (mM)**
1	25% HeMA-HA, 30% MeHA	4, 6, 8, 10	100	0	5	5
			75	25	5	5
			50	50	5	5
			25	75	5	5
			0	100	5	5
2	25% HeMA-HA, 30% MeHA	5, 6, 7	75	25	5	5
			25	75	5	5

To further evaluate the tunability of hydrogel degradation in this HA system, copolymers of HeMA-HA and MeHA were formulated into hydrogels by mixing different volumetric ratios of the macromers dissolved at the same concentrations in PBS. The amount of MeHA introduced into HeMA-HA hydrogels (100:0, 75:25, 50:50, 25:75, 0:100 HeMA-HA:MeHA) was varied at various macromer concentrations (4, 6, 8, 10 wt%). Based on this initial study, six copolymer hydrogel formulations at three macromer concentrations (5, 6, 7 wt%) and two copolymer ratios (75: 25, 25:75 HeMA-HA:MeHA) were selected for assessment of temporal mechanics. Macromer modification (25% modified HeMA-HA; 30% modified MeHA) and initiator concentration (5 mM APS/TEMED) were maintained throughout these copolymer hydrogel characterization studies (**Table 4.2**).

4.2.5. Statistical Analysis

Data is presented as mean ± standard deviation (SD) or mean ± standard error of the mean (SEM), as indicated in each figure legend. Statistical differences between groups were assessed using a one-way ANOVA with Tukey's post hoc evaluation (JMP Statistical Software; SAS Institute; Cary, NC). A $p<0.05$ was considered statistically significant.

4.3. Results

4.3.1. HA Macromer Synthesis and Characterization

Two HA macromers were synthesized for evaluation in *in vitro* characterization studies (**Figure 4.1**). First, HA was chemically modified to include a hydrolytically degradable group, HeMA, to enable both free-radical initiated crosslinking through the methacrylate and tunable degradation through the ester bond hydrolysis (**Figure 4.2**). Secondly, a non-hydrolytically degradable methacrylate group was added to the HA backbone to facilitate free radial initiated crosslinking in a stable hydrogel system as a comparison to the hydrolytically degradable macromer described above, HeMA-HA (**Figure 4.3**). As described above, ^{1}H NMR was used to evaluate the degree of modification on all macromers (**Figures 4.2B, 4.3B**). Each macromer was synthesized at a range of modifications for subsequent *in vitro* characterization (**Tables 4.1, 4.2**).

4.3.2. *In Vitro* Characterization of HeMA-HA Hydrogels

For the initial HeMA-HA *in vitro* characterization study, initiator concentration, macromer modification, and macromer concentration were simultaneously varied to assess their impact on initial compressive mechanics. Two macromer modifications (10%, 35%) were investigated at three macromer concentrations (4, 7, 10 wt%) and three initiator concentrations (5 mM, 7.5 mM, 10 mM APS/TEMED) (**Table 4.1**). An increase in any of the three parameters led to an increase in compressive moduli (**Figure 4.5**). At each initiator concentration, increased modification resulted in significantly increased ($p<0.05$) mechanics for all groups. Similarly, increased moduli

due to increased macromer concentration were statistically significant except when comparing 4 wt% and 7 wt% gels formed using 5 mM and 10 mM APS/TEMED with 10% modified HeMA-HA. At each modification, differences in moduli based on initiator concentration were not statistically significant (*p>0.05*) whereas differences due to macromer concentration were statistically significant except for comparison between 4 wt% and 7 wt% gels formed from 10% modified HeMA-HA. Finally, at each macromer concentration, changes in initiator concentration did not result in statistically significant changes in mechanics whereas changes in macromer modification did. The largest differences in mechanics with changes in initiator concentration were seen with 35% modified gels at 10 wt% (**Figure 4.5**). However, due to minimal changes in mechanics with changes in initiator concentration, subsequent experiments investigated simultaneously altering the macromer modification and concentration at a constant initiator concentration.

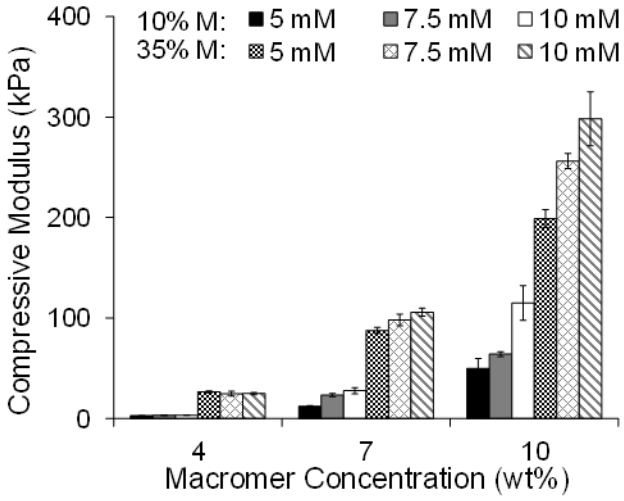

Figure 4.5. Tunability of mechanical properties of HeMA-HA hydrogels. Compressive moduli at day 1 after hydrogel formation, *n=3-4/group*, as a function of initiator concentration, macromer modification, and macromer concentration. Data presented as mean ± SD. See Appendix 4.1 for statistics information.

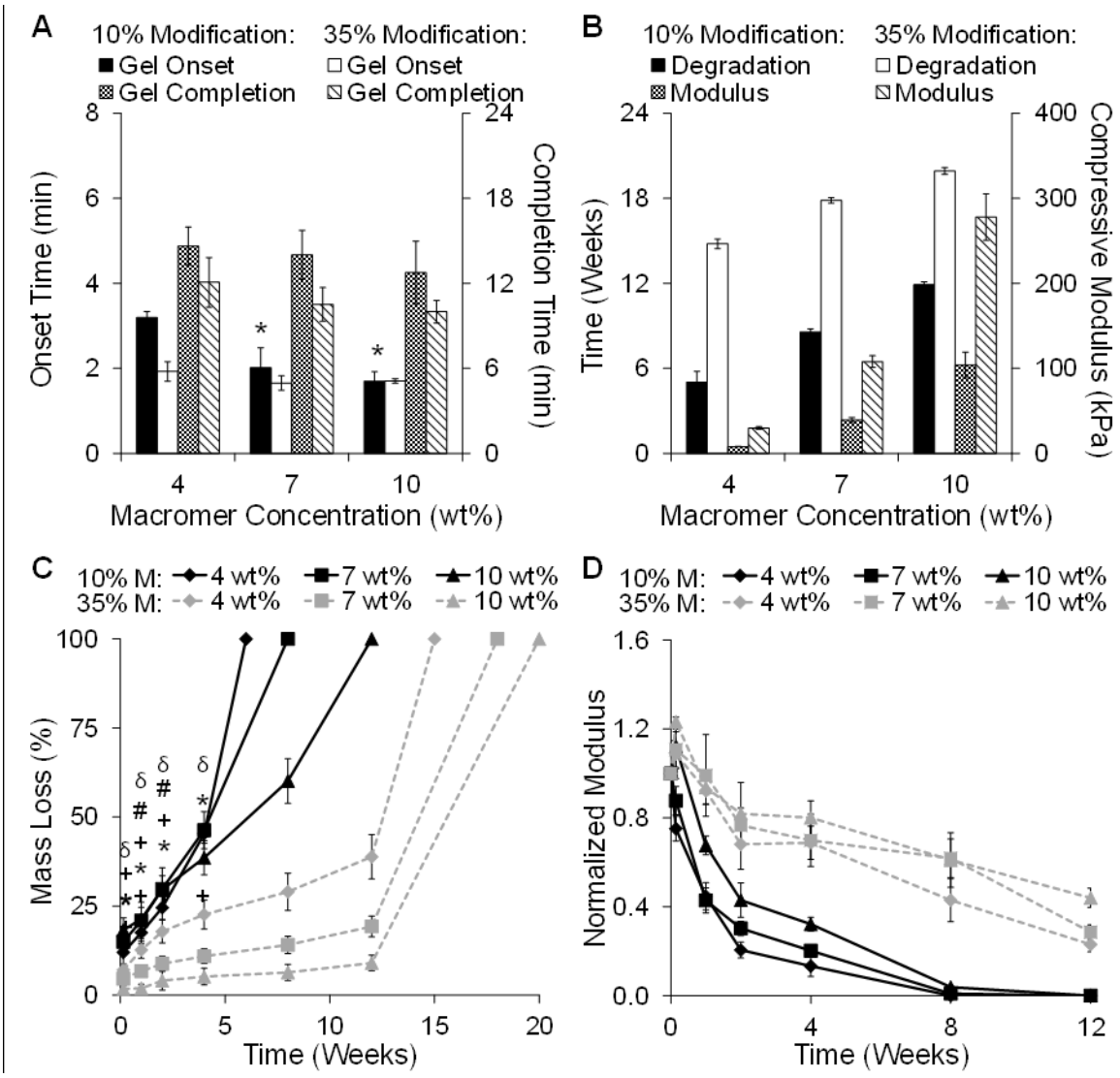

Figure 4.6. Initial *in vitro* characterization studies of pure HeMA-HA hydrogels at various macromer modifications and concentrations. Gel onset and completion, *n=3-4/group*, as a function of macromer modification and concentration gelled using 10 mM APS/TEMED (A). Degradation time and initial (day 0) compressive moduli, *n=3-4/group* (B). Temporal degradation (C) and mechanics (D), *n=3-4/group*. Data presented as mean ± SD. *$^{*}p<0.05$* vs. 10% modified HeMA-HA at 4 wt% in panel A. All groups were significant (*$p<0.05$)* in panel B. In panel C, *$^{*}p<0.05$* for 4 vs. 7 wt%, *$^{+}p<0.05$* for 7 vs. 10 wt%, and *$^{\#}p<0.05$* for 4 vs. 7 wt% for 10% modified gels and *$^{\delta}p<0.05$* for 7 vs. 10 wt% for 25% modified gels. See Appendix 4.1 for more statistics.

Hydrogel properties (i.e., gelation, degradation, and mechanics) were then examined for the two macromer modifications and three macromer concentrations but a single initiator concentration of 10 mM APS/TEMED (**Table 4.1**). Assessment of gelation demonstrated that as macromer modification or macromer concentration increased, the time to gel onset or completion decreased (**Figure 4.6A**). Within a single modification (i.e., 10% modified HeMA-HA), increased macromer concentration led to a statistically significant decrease in gel onset. Similar to gelation, as the macromer modification or concentration increased, the time to degradation and the initial compressive modulus increased (**Figure 4.6B**). All final degradation times and initial moduli were statistically significant for each time point, both between modifications at a single macromer concentration and between macromer concentrations within a single modification.

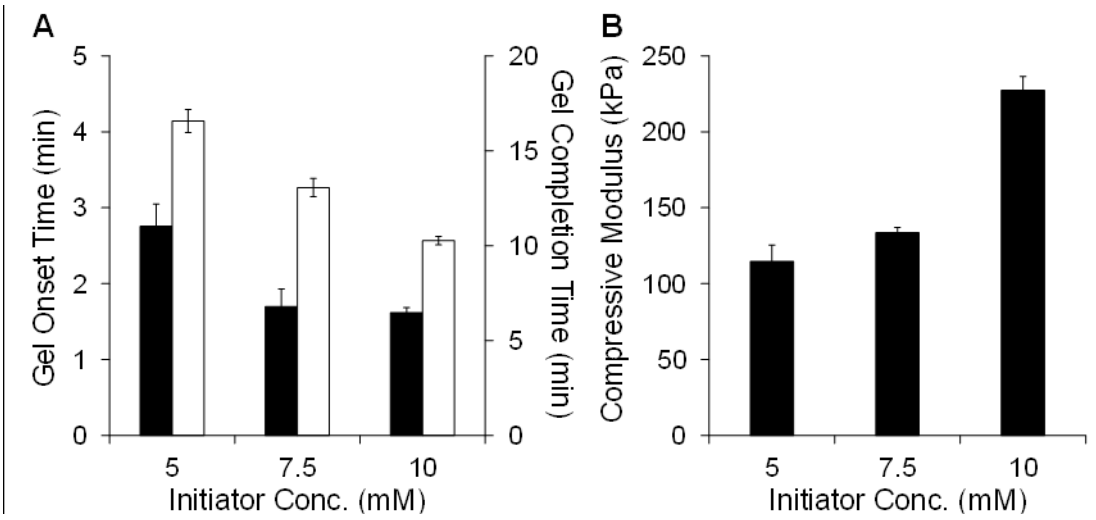

Figure 4.7. Effect of initiator concentration on HeMA-HA hydrogel gelation and mechanics. Gel onset and completion, *n=3-4/group*, as a function of initiator concentration at a single modification (25%) and macromer concentration (7 wt%) (A). Initial (day 0) compressive moduli, *n=3-4/group* (B). Data presented as mean ± SD. All values were statistically significant (*p<0.05)* aside from comparison of gel onset between 7.5 mM and 10 mM APS/TEMED in panel A.

Degradation assessment revealed that increased modification led to a statistically significant decrease in hydrogel mass loss at each time point except for 4 wt% gels one week

after gelation (**Figure 4.6C**). Temporal degradation (**Figure 4.6C**) and mechanics (**Figure 4.6D**) further showed that increased macromer modification or concentration led to gels that degraded more slowly and maintained their mechanics longer. Formulations with a higher modification but lower macromer concentration degraded slower than formulations with a lower modification but higher macromer concentration (**Figure 4.6C,D**). Thus, altering the macromer modification along with the concentration can tailor hydrogel degradation while maintaining similar initial mechanics.

Simultaneously, the effect of altering the initiator concentration was examined in hydrogels at a single macromer modification (25%) and concentration (7 wt%) (**Table 4.1**). As predicted from the initial study using 10% and 35% modified HeMA-HA, as initiator concentration increased, the time to gel onset and completion decreased whereas the mechanics increased (**Figure 4.7A**). All gel onset times, gel completion times, and initial compressive moduli were statistically significant ($p<0.05$) between initiator concentrations aside from comparison of gel onset between hydrogels gelled using 7.5 mM and 10 mM APS/TEMED ($p>0.05$). Based on this study, a single initiator concentration of 5 mM APS/TEMED was selected for subsequent studies.

To further explore the effect of altering the macromer modification and concentration on hydrogel gelation, degradation, and mechanics, a more thorough study was performed with gels formed from three macromer modifications (10%, 25%, 40%) each at six concentrations (2, 4, 6, 8, 10, 12 wt%) (**Table 4.1**). As anticipated from **Figure 4.7**, increased macromer modification or concentration resulted in decreased time to gel onset or completion (**Figure 4.7A**). Statistically significant differences in gelation were observed for comparisons between modifications relative to 10% modified gels at each macromer concentration. Similarly, as predicted from **Figure 4.6**, increased macromer modification or concentration led to increased degradation time and initial compressive mechanics (**Figure 4.7B**). The majority of degradation and mechanics comparisons between modifications at a given macromer concentration and between macromer concentrations at a single modification were statistically significant (**Appendix 4.1**).

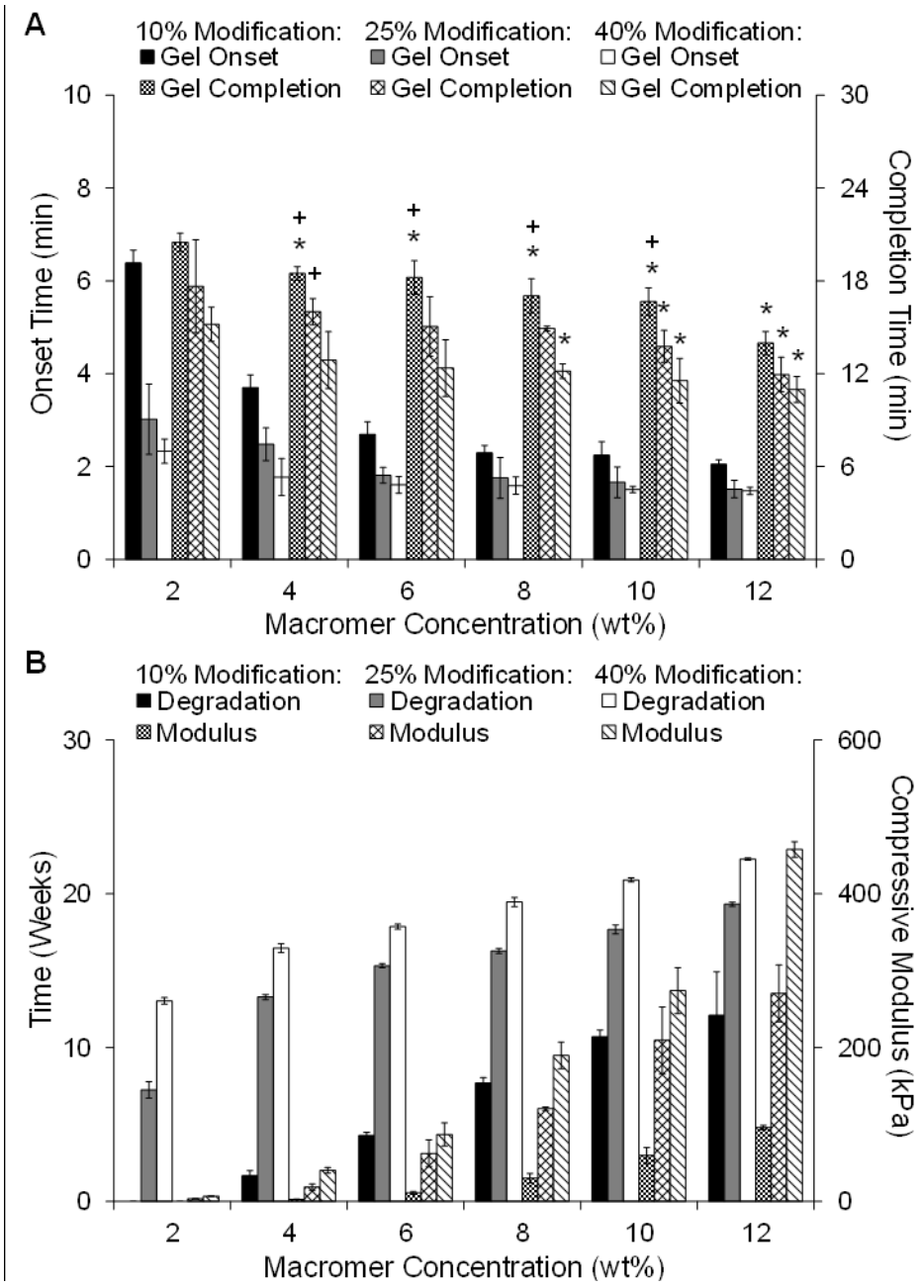

Figure 4.8. Extensive analysis of the effect of macromer modification and concentration on HeMA-HA hydrogel properties. Gelation onset and completion, *n=3-4/group*, for gels formed with 5 mM APS/TEMED (A). Degradation time and initial compressive moduli, *n=3-4/group*, (B). Data presented as mean ± SD. In panel A, $^{*}p<0.05$ vs. 2 wt% and $^{+}p<0.05$ vs. 12 wt% for gel completion comparisons at the same modification. See Appendix 4.1 for additional statistics.

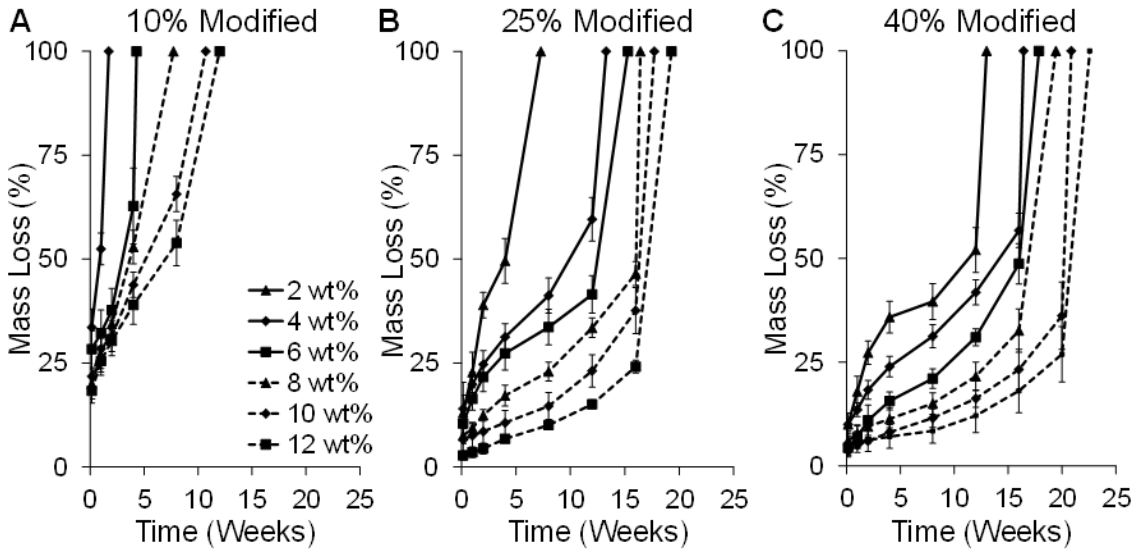

Figure 4.9. Tuning HeMA-HA hydrogel degradation by altering the macromer modification and concentration. Temporal degradation profiles of hydrogels, *n=3-4/group*, formed from 10% modified (A), 25% modified (B), and 40% modified (C) HeMA-HA at various macromer concentrations. Data presented as mean ± SD. See Appendix 4.1 for statistical information.

Hydrogel mass loss over time showed that increased macromer modification or concentration prolonged hydrogel degradation (**Figure 4.8**). Comparisons between modifications at each macromer concentration showed that all 10% modified gels had a statistically significant increase in mass loss at each time point as compared to both 25% and 40% modified gels. Comparisons between 25% and 40% modified hydrogels became progressively more significantly different over time: at day one, mass loss of 25% and 40% modified gels was not statistically significant ($p>0.05$) but past day one, mass loss between 25% and 40% modified gels diverged and remained significantly different ($p<0.05$) for the remainder of the study. These differences arose at 1 week for 6 wt% gels, 2 weeks for 2 wt% gels, 8 weeks for 4 wt% and 8 wt% gels, 12 weeks for 10 wt% gels, and 16 weeks for 12 wt% gels. Within each modification, comparisons between macromer concentrations were statistically varied but gradually became more statistically significant with time in all three groups (**Appendix 4.1**).

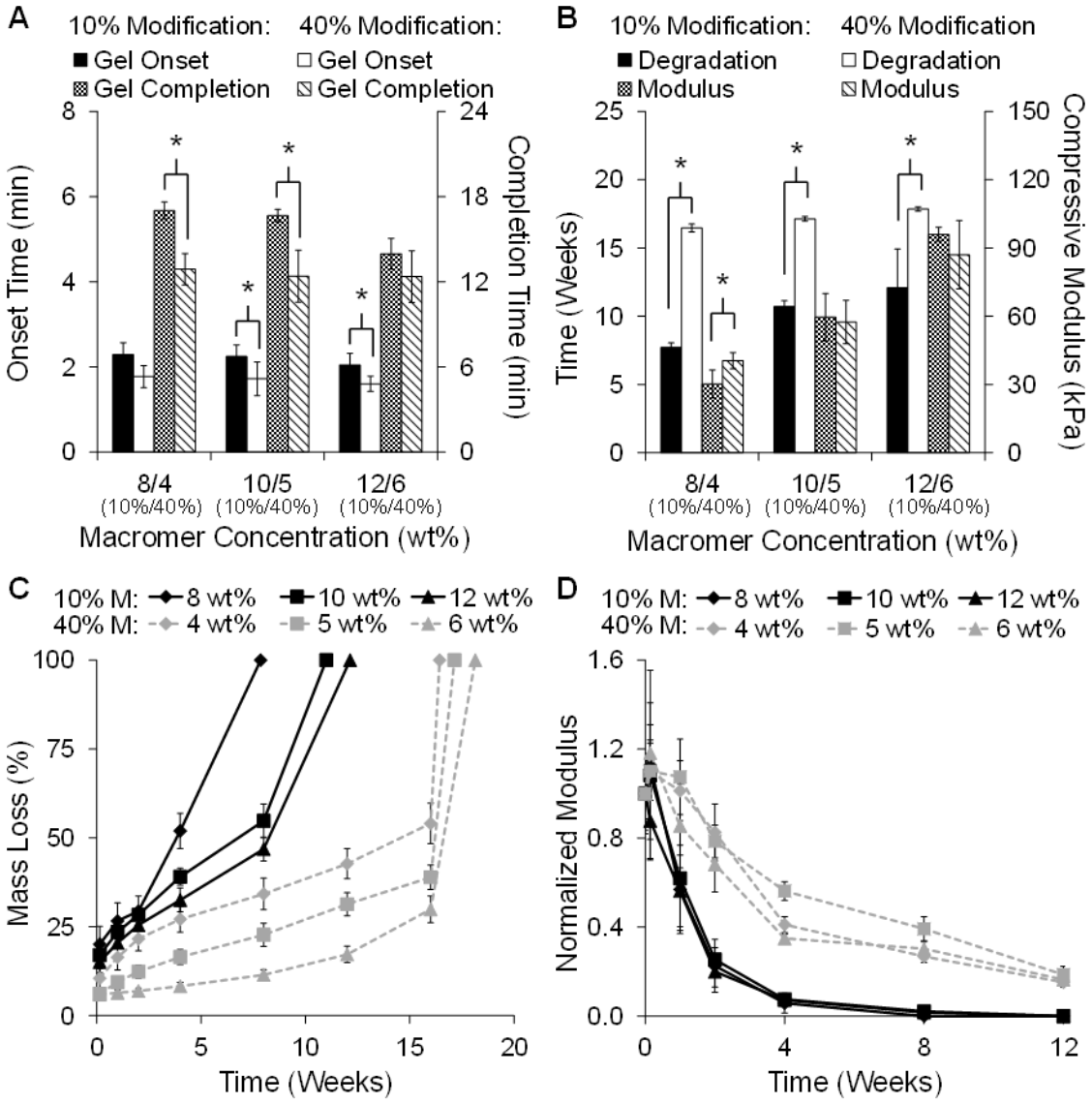

Figure 4.10. *In vitro* characterization of selected HeMA-HA hydrogel formulations with similar gelation and initial mechanics but different rates of degradation. Gelation onset and completion, *n=3-4/group*, as a function of HeMA-HA modification and macromer concentration gelled using 5 mM APS/TEMED (A). Degradation time and initial compressive moduli, *n=3-4/group* (B). Temporal degradation (C) and mechanics (D) profiles, *n=3-4/group*. Data presented as mean ± SD. In panels A and B, *$p<0.05$. Additional statistical information is present in Appendix 4.1.

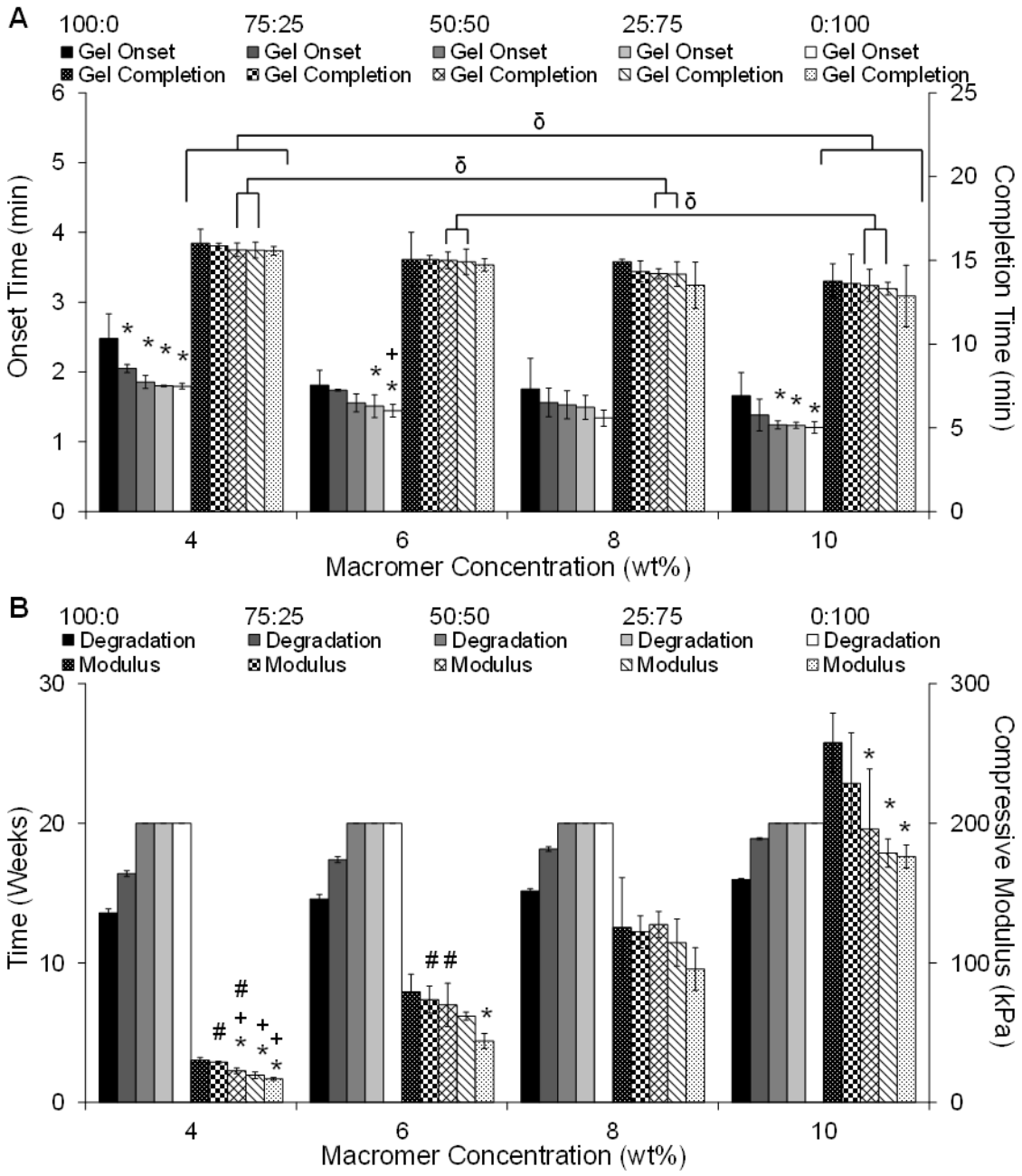

Figure 4.11. Effect of combining non-degradable MeHA and degradable HeMA-HA into a single copolymer hydrogel system at various macromer concentrations. Gel onset and completion, *n=3-4/group*, as a function of HeMA-HA:MeHA ratio (v/v) at various macromer concentrations (A). Degradation time and initial compressive moduli, *n=3-4/group* (B). All remaining hydrogels were

degraded at 20 weeks after formation. Data presented as mean ± SD. In panel A, *$p<0.05$ *vs*. 100:0 and $^{+}p<0.05$ *vs*. 75:25 for gel onset comparisons at each macromer concentration. For gel completions comparisons between concentrations, $^{\delta}p<0.05$ for all 4 vs. 10 wt% ratios, 4 vs. 8 wt% at 25:75 and 50:50, and 6 vs. 10 wt% at 25:75 and 50:50. In panel B, all degradation values were statistically significant ($p<0.05$). For initial moduli comparisons, *$p<0.05$ *vs*. 100:0, $^{+}p<0.05$ *vs*. 75:25, and $^{\#}p<0.05$ *vs*. 0:100 copolymers. See Appendix 4.1 for more statistical information.

The thorough HeMA-HA characterization study (**Figures 4.8, 4.9**) was used to select a limited number of formulations to investigate temporally for changes in mechanics. By altering a combination of the macromer modification and concentration, the goal was to examine mechanical changes in hydrogels with similar gelation and initial mechanics but different rates of degradation. Therefore, the properties of following pairs of formulations were compared: 1) 10% modified HeMA-HA at 8 wt% vs. 40% modified at 4 wt%, 2) 10% modified at 10 wt% vs. 40% modified at 5 wt%, and 2) 10% modified at 12 wt% vs. 40% modified at 6 wt% (**Table 4.1**). Comparing between the hydrogels in each pair, *in vitro* assessment demonstrated similar gelation properties that were not statistically significant ($p>0.05$) for the first hydrogel pair for time to gelation onset (**Figure 4.10A**). In addition, initial compressive mechanics were similar within the pairs and not statistically significant for both the second and third pairs (**Figure 4.10B**). As anticipated, despite similarities in gelation and mechanics, the degradation was significantly different ($p<0.05$) between the formulations in all three hydrogel pairs (**Figure 4.10B**).

The degradation (**Figure 4.10C**) and temporal mechanics (**Figure 4.10D**) were then examined for three pairs of hydrogel formulations out to 12 weeks. Degradation for 40% modified hydrogels was statistically less than 10% modified gels at each time point (**Figure 4.10C**). As the study progressed, differences in degradation between the gels within each pair became evident. In contrast, compressive moduli were not statistically significant within the pairs at the earlier time points, but became statistically different ($p<0.05$) at 2 weeks and beyond (**Figure 4.10D**). Thus, there was a narrow window during which the degradation was varied but mechanics maintained.

The mechanics for all 10% modified gels were not statistically significant throughout the study regardless of macromer concentration. As predicted from **Figure 4.9**, all 10% modified gels had statistically greater mass loss and significantly lower ($p<0.05$) mechanics than all 40% modified gels at each time point. Despite similarities in initial mechanics within each pair (**Figure 4.10B**), as the hydrogels degraded, the moduli became gradually different over time (**Figure 4.10D**), demonstrating the interdependence between degradation and mechanics in HeMA-HA hydrogels.

4.3.3. Characterization of HeMA-HA/MeHA Copolymer Hydrogel Properties

To further explore the tunability of HA hydrogels, the properties of a HeMA-HA and MeHA copolymer system of were assessed. Copolymer blends were generated using macromers of approximately the same modification (i.e., 25% modified HeMA-HA, 30% modified MeHA) but different ratios of HeMA-HA to MeHA (i.e., 75:25, 50:50, 25:75 for HeMA-HA:MeHA). The three copolymers were also compared to pure HeMA-HA (i.e., 100:0) and pure MeHA (i.e., 0:100) gels (**Table 4.2**). For the initial study, the properties were examined at four macromer concentrations (4, 6, 8, 10 wt%), which were selected based on the previous HeMA-HA studies (Section 4.3.2). At each macromer concentration, the gel onset and completion time decreased as the amount of MeHA increased (**Figure 4.11A**). The accelerated gelation with increased MeHA was statistically significant relative to pure HeMA-HA hydrogels, particularly for the 4 wt% and 10 wt% gels. Gel completion was relatively unaffected by MeHA content, with statistically significant differences only seen between macromer concentrations (**Appendix 4.1**). As anticipated, pure HeMA-HA hydrogels degraded at the quickest rate and pure MeHA gels at the slowest, with copolymers falling in between; as the ratio of MeHA increased, degradation significantly increased ($p<0.05$) (**Figure 4.11B**). In contrast, the initial moduli decreased as the amount of MeHA increased, with hydrogels made from HeMA-HA alone having the highest mechanics and those made from MeHA alone displaying the lowest mechanics (**Figure 4.11B**). Pure HeMA-HA hydrogels had statistically higher mechanics relative to MeHA homopolymer hydrogels at all macromer concentrations aside from 6 wt% and relative to certain copolymer hydrogels at 4 wt% and 10 wt%.

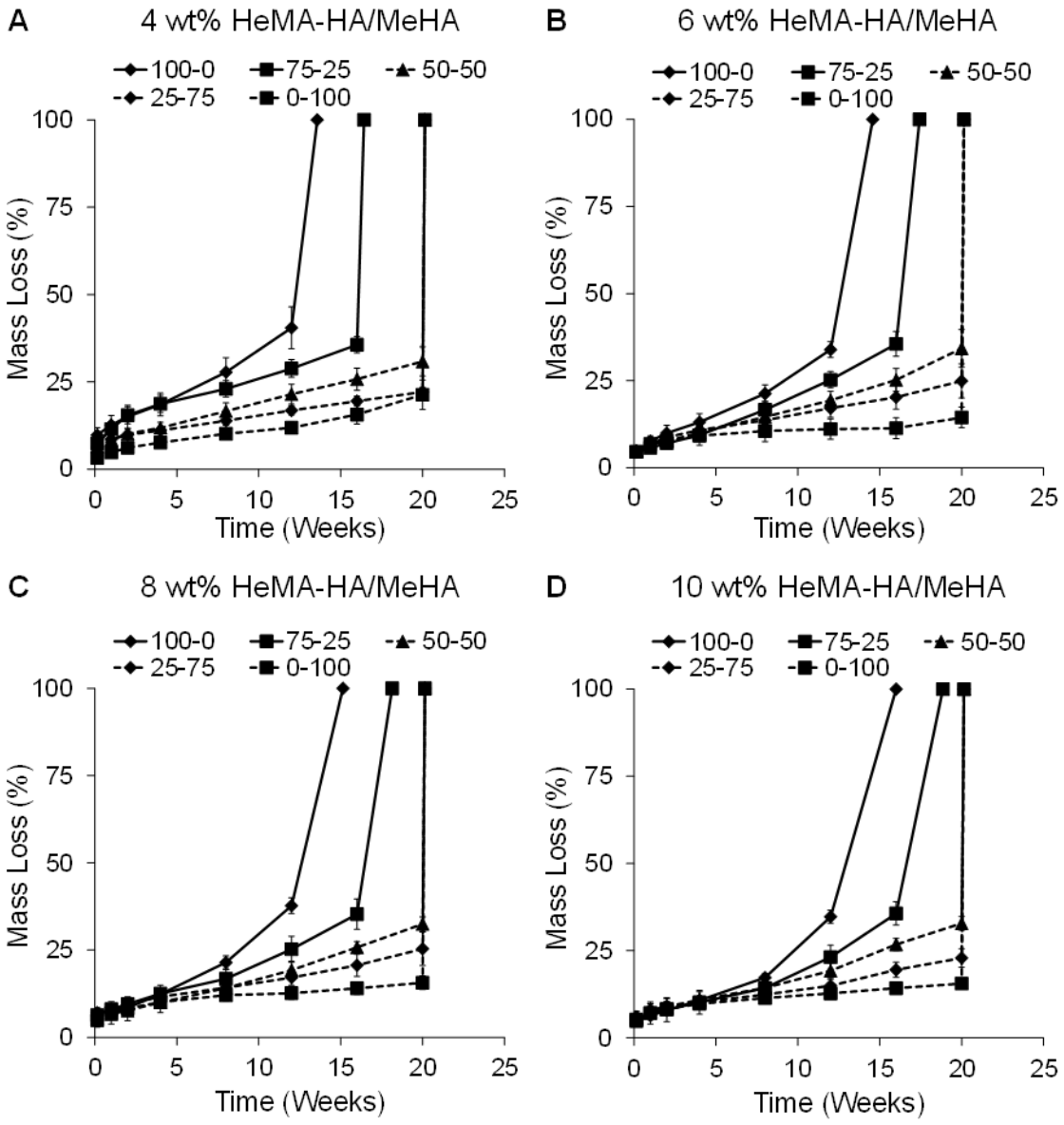

Figure 4.12. Tuning hydrogel degradation by altering the ratio of HeMA-HA to MeHA at various macromer concentrations. Temporal degradation of HeMA-HA:MeHA copolymer hydrogels, *n=3-4/group*, formed using different copolymer ratios at macromer concentrations of 4 wt% (A), 6 wt% (B), 8 wt% (C), and 10 wt% (D). All remaining hydrogels were degraded at 20 weeks after formation. Data presented as mean ± SD. Refer to Appendix 4.1 for statistical assessment.

Quantification of hydrogel mass loss as a measure of degradation over time demonstrated that HA release from hydrogels containing MeHA was minimal throughout the 20 week study whereas pure HeMA-HA hydrogels degraded prior to the final time point (**Figure 4.12**). The degradation rate of HeMA-HA homopoloymers was statistically higher than MeHA homopolymer hydrogels at all time points for 4 wt% gels, past week 2 for 6 wt% gels, past week 4 for 8 wt% gels, and past week 8 for 12 wt% gels. As the amount of MeHA incorporated into the copolymer hydrogels increased, the amount of HA released at each time point decreased, particularly at later time points (prior to gel degradation at week 20). For the earlier time points, hydrogel mass loss was similar between both the homopolymer and copolymer hydrogels. At 8 weeks, a burst of HA release was observed in the HeMA-HA hydrogels that was statistically significant relative to all copolymer ratios and for all macromer concentrations aside from 10 wt% (which reached statistical significance for all copolymer ratios by 12 weeks).

Similar to the previous HeMA-HA characterization studies (Section 4.3.2), specific formulations were selected for temporal mechanical assessment. Two copolymer ratios (75:25, 25:75, HeMA-HA:MeHA) were examined at three macromer concentrations (5, 6, 7 wt%) (**Table 4.2**). These particular ratios and macromer concentrations were selected for temporal assessment with the goal of having similar initial mechanics but different rates of degradation: the ratios were used to tune the degradation where as the macromer concentrations were used to target different mechanical profiles. At each macromer concentration, the gelation onset times were significantly greater ($p<0.05$) for the 75:25 copolymer hydrogels as compared to the 25:75 hydrogels whereas the gel completion times were not statistically significant (**Figure 4.13A**). As intended, statistically significant ($p<0.05$) degradation times were generated by altering the copolymer ratio (**Figure 4.13B**). The initial mechanics were similar between the copolymer ratios for all macromer concentrations and statistically significantly so for 6 wt% and 7 wt% hydrogels (**Figure 4.13B**). In addition, statistically significant differences in initial moduli were generated by altering the macromer concentration at each copolymer ratio.

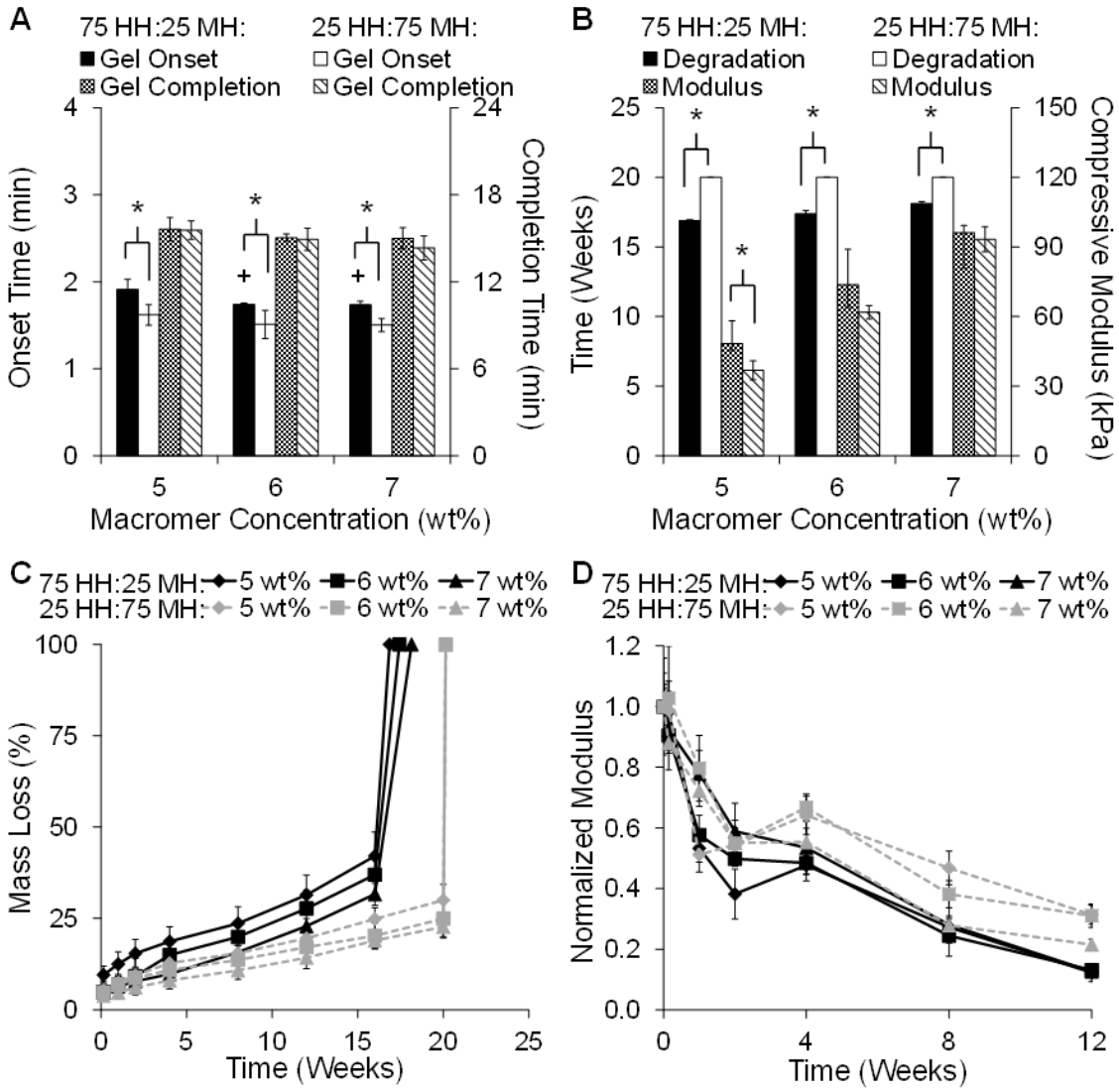

Figure 4.13. *In vitro* characterization of selected HeMA-HA/MeHA copolymer hydrogels. Gel onset and completion, *n=3-4/group*, as a function of copolymer ratio and macromer concentration gelled using 5 mM APS/TEMED (A). Degradation time and initial compressive moduli, *n=3-4/group* (B). Temporal degradation (C) and mechanics (D) profiles, *n=3-4/group*. All remaining 25:75 hydrogels were degraded at 20 weeks. Data presented as mean ± SD. For panel A, $^{+}p<0.05$ vs. 5 wt% gels at the same ratio. For panels A and B, $^{*}p<0.05$ for 75:25 vs. 25:75 copolymers. See Appendix 4.1 for additional statistical comparisons.

As predicted from the previous copolymer study (**Figure 4.12**), temporal assessment of degradation (**Figure 4.13C**) and mechanics (**Figure 4.13D**) demonstrated that copolymer ratio had a larger impact on the rate of hydrogel degradation and decline in mechanics over time than macromer concentration. When comparing between the two copolymer ratios, the 5 wt% copolymer hydrogels had statistically significant ($p<0.05$) amounts of hydrogel mass loss at each time point whereas the 6 wt% and 7 wt% copolymer hydrogels developed statistically significant differences after 8 and 12 weeks, respectively (**Figure 4.13C**). These differences in degradation were maintained for the rest of the study. In addition, the initial (day 0) compressive moduli were not statistically significant ($p>0.05$) for comparison between the two copolymer ratios at each macromer concentration and this was maintained until 12 weeks, at which time the moduli for the ratios diverged and became statistically significant (**Figure 4.13D**). More importantly, statistically significant differences in compressive moduli based on changes in macromer concentration persisted until week 8 for both copolymer ratios, where higher macromer concentration led to prolonged retention of mechanics. Thus, degradation was successfully tuned based on the copolymer ratio whereas mechanics were tuned using differences in macromer concentration.

4.4. Discussion

In this chapter, characterization studies were performed to better understand techniques to tune hydrogel properties and to select formulations for subsequent imaging (Chapters 5, 6) and *in vivo* (Chapter 7) studies. The initial characterization experiment simultaneously investigated the effect of altering the initiator concentration, macromer modification, and macromer concentration to tune HeMA-HA hydrogel mechanics. As the concentration of APS and TEMED increased, more free radicals were generated in the pre-polymer solution, leading to accelerated kinetic chain formation between methacrylate groups on the HA backbone (**Figure 4.5**). Initiator concentration had a larger impact on hydrogels formed at higher macromer modifications and concentrations (i.e., 35% modified HeMA-HA at 10 wt%). As more potential crosslinking options became available (due to an increase in modification or concentration), the initiator concentration

became the rate limiting step in hydrogel formation. This suggests that a portion of the methacrylates remained unreacted in the lower initiator concentration groups for the 10 wt%, 35% modified hydrogels, leading to lower mechanics. Particularly at lower modifications or macromer concentrations, initiator concentration within the range investigated played a minor role in altering hydrogel mechanics, implying that all possible methacrylates were crosslinked using the lowest initiator concentration of 5 mM APS/TEMED. Therefore, subsequent characterization studies focused on altering the macromer modification and concentration at a single initiator concentration. Based on previous *in vivo* work from our group,[12,13] an initiator concentration of 5 mM APS/TEMED was selected so the resulting hydrogels would form instantaneously upon delivery to the target site (i.e., myocardium) but allow sufficient time for injection prior to gelation.

In pure HeMA-HA hydrogels, as either the modification or macromer concentration increased, the number of reactive methacrylates available for crosslinking increased. For a single initiator concentration, this led a decrease in the gelation time since crosslinks formed more rapidly (**Figures 4.6A, 4.8A**). Similarly, an increase in the modification or macromer concentration increased the total number of efficient crosslinks per unit volume (i.e., crosslinking density), which resulted in stiffer gels that required a greater force to deform during bulk compression (**Figures 4.6B, 4.8B**).[38] Past work by our group confirmed that changes in HA modification correlate with changes in bulk hydrogel mechanics.[12,13] Furthermore, in HeMA-HA hydrogels, crosslinks are formed through the HeMA groups, which are also the sites susceptible to hydrolysis at the ester bonds. Thus, degradation and mechanics are intertwined. As anticipated, the increase in crosslinking density with increased modification or macromer concentration led to more bonds needing to hydrolyze and less free volume to accommodate water and hence, slower degradation (**Figures 4.6C, 4.9)**. For hydrogels with approximately the same initial mechanics, formulations with a higher modification but lower macromer concentration maintained their mechanics for longer and degraded slower than formulations with a lower modification but higher macromer concentration (**Figure 4.10**). Thus, by altering the modification along with the macromer concentration, the degradation and mechanics of HeMA-HA hydrogels were tailored.

As another approach to tuning HA hydrogel properties, MeHA was introduced at different ratios to examine the effect of introducing a non-hydrolytically degradable macromer into a hydrolytically degradable HeMA-HA hydrogel system. Previous work by our group with MeHA and α-hydroxy ester block copolymers demonstrated that hydrogel properties (i.e., mechanics, degradation) can be tailored by adjusting the ratio of the MeHA block to the hydrolytically degradable block.[12,39] Assessment of gelation demonstrated that increased MeHA incorporation relative to HeMA-HA resulted in accelerated gelation times, potentially due to the smaller size of the methacrylate (Me) functional group leading lower viscosity of the macromer solution and more rapid crosslink formation (**Figure 4.11A**). However, the initial compressive moduli prior to swelling decreased as the amount of MeHA present increased, indicating less overall crosslink formation with MeHA hydrogels for the same modification of HeMA and Me on HA (**Figure 4.11B**). Due to the difference in length between the two functional groups, this suggests that crosslinking was preferenced to the HeMA groups since they extend further outward from the HA chains.

Degradation was tuned based the degree of MeHA incorporation, where more MeHA, and thus, less hydrolytically susceptible ester bonds, led to prolonged degradation (**Figure 4.12**). In all macromer concentrations, hydrogel mass loss was similar between the copolymer and homopolymer hydrogels until about 8 weeks (**Figure 4.12**). After this point, a burst release of HA was observed from the HeMA-HA hydrogels due to the bulk degradation exhibited by hydrolytically degradable gels: as the hydrogels swell and crosslinks are moved farther apart, a threshold in the number of crosslinks broken is reached, resulting in an exponential increase in mass loss. Due to the extensive amount of time required for MeHA degradation, degradation was evaluated out to 20 weeks, at which point the hydrogels were degraded via exogenous hyaluronidase. Temporal changes in mechanics with degradation were then evaluated for two copolymer formulations (**Figure 4.13**). The ratios of 75:25 and 25:75 for HeMA-HA:MeHA were selected to generate differences in degradation (with similar initial mechanics within a given macromer concentration, **Figure 4.13B**) whereas the different macromer concentrations were selected to target different mechanical profiles that would be relevant to post-MI remodeling.[40] As

anticipated, as more ester (HeMA) groups were present, the hydrogels became more susceptible to hydrolysis and therefore, degraded and lost their mechanics at a faster rate (**Figure 4.13C,D**).

4.5. Conclusions

In summary, this chapter highlights the versatility of HeMA-HA-based systems to generate hydrogels with a range of gelation, degradation and mechanical profiles to fit a specific, desired application. Pure HeMA-HA hydrogels served as a platform to investigate changes in macromer modification and concentration within a homopolymer system, where increases in either macromer modification or concentration led to accelerated gelation, prolonged degradation, and high mechanics. The incorporation of MeHA to form a copolymer hydrogel system provided the opportunity to tune degradation based on the functional group manipulated for hydrogel crosslinking. While both HeMA-HA and MeHA are enzymatically degradable through the HA backbone, HeMA-HA hydrogels are also susceptible to hydrolysis of the HeMA side groups, leading to more rapid degradation. Whereas the use of copolymers was effective in tuning hydrogel properties, the remainder of this dissertation will focus primarily on the use of MeHA and HeMA-HA homopolymers for simplicity in experimental design. The next two chapters will focus on the ability to image injectable HA hydrogels in myocardial explants using MRI.

4.6. References

1. Christman KL, Lee RJ. Biomaterials for the treatment of myocardial infarction. J Am Coll Cardiol 2006;48(5):907-913.

2. Drury JL, Mooney DJ. Hydrogels for tissue engineering: scaffold design variables and applications. Biomaterials 2003;24(24):4337-4351.

3. Lee KY, Mooney DJ. Hydrogels for tissue engineering. Chem Rev 2001;101(7):1869-1879.

4. Nguyen MK, Lee DS. Injectable biodegradable hydrogels. Macromol Biosci 2010;10(6):563-579.

5. Burdick JA. Injectable gels for tissue/organ repair. Biomed Mater 2012;7(2):020201.

6. Yu L, Ding J. Injectable hydrogels as unique biomedical materials. Chem Soc Rev 2008;37(8):1473-1481.

7. Nelson DM, Ma Z, Fujimoto KL, Hashizume R, Wagner WR. Intra-myocardial biomaterial injection therapy in the treatment of heart failure: Materials, outcomes and challenges. Acta Biomater 2011;7(1):1-15.

8. Shapira K, Dikovsky D, Habib M, Gepstein L, Seliktar D. Hydrogels for cardiac tissue regeneration. Biomed Mater Eng 2008;18(4-5):309-314.

9. Tous E, Purcell B, Ifkovits JL, Burdick JA. Injectable acellular hydrogels for cardiac repair. J Cardiovasc Transl Res 2011;4(5):528-542.

10. Johnson TD, Christman KL. Injectable hydrogel therapies and their delivery strategies for treating myocardial infarction. Expert Opin Drug Deliv 2013;10(1):59-72.

11. Dorsey SM, Burdick JA. Hydrogels for cardiac repair. In: Khademhosseini A, Demirci U, editors. Applications of Hydrogels in Regenerative Medicine; in press.

12. Tous E, Ifkovits JL, Koomalsingh KJ, Shuto T, Soeda T, Kondo N, et al. Influence of injectable hyaluronic acid hydrogel degradation behavior on infarction-induced ventricular remodeling. Biomacromolecules 2011;12(11):4127-4135.

13. Ifkovits JL, Tous E, Minakawa M, Morita M, Robb JD, Koomalsingh KJ, et al. Injectable hydrogel properties influence infarct expansion and extent of postinfarction left ventricular remodeling in an ovine model. Proc Natl Acad Sci U S A 2010;107(25):11507-11512.

14. Burdick JA, Chung C, Jia X, Randolph MA, Langer R. Controlled degradation and mechanical behavior of photopolymerized hyaluronic acid networks. Biomacromolecules 2005;6(1):386-391.

15. Toole BP. Hyaluronan in morphogenesis. J Intern Med 1997;242(1):35-40.

16. Toole BP. Hyaluronan: From extracellular glue to pericellular cue. Nat Rev Cancer 2004;4(7):528-539.

17. Li Y, Toole BP, Dealy CN, Kosher RA. Hyaluronan in limb morphogenesis. Dev Biol 2007;305(2):411-420.

18. Jha AK, Hule RA, Jiao T, Teller SS, Clifton RJ, Duncan RL, et al. Structural analysis and mechanical characterization of hyaluronic acid-based doubly cross-linked networks. Macromolecules 2009;42(2):537-546.

19. Purcell BP, Lobb D, Charati MB, Dorsey SM, Wade RJ, Zellars KN, et al. Injectable and bioresponsive hydrogels for on-demand matrix metalloproteinase inhibition. Nat Mater 2014;13(6):653-661.

20. Holloway JL, Ma H, Rai R, Burdick JA. Modulating hydrogel crosslink density and degradation to control bone morphogenetic protein delivery and in vivo bone formation. J Controlled Release 2014;191:63-70.

21. Pouyani T, Prestwich G. Functionalized derivatives of hyaluronic-acid oligosaccharides - Drug carriers and novel biomaterials. Bioconjug Chem 1994;5(4):339-347.

22. Vercruysse K, Marecak D, Marecek J, Prestwich G. Synthesis and in vitro degradation of new polyvalent hydrazide cross-linked hydrogels of hyaluronic acid. Bioconjug Chem 1997;8(5):686-694.

23. Shu X, Liu Y, Luo Y, Roberts M, Prestwich G. Disulfide cross-linked hyaluronan hydrogels. Biomacromolecules 2002;3(6):1304-1311.

24. Gramlich WM, Kim IL, Burdick JA. Synthesis and orthogonal photopatterning of hyaluronic acid hydrogels with thiol-norbornene chemistry. Biomaterials 2013;34(38):9803-9811.

25. Rodell CB, Kaminski AL, Burdick JA. Rational design of network properties in guest-host assembled and shear-thinning hyaluronic acid hydrogels. Biomacromolecules 2013;14(11):4125-4134.

26. Gramlich WM, Holloway JL, Rai R, Burdick JA. Transdermal gelation of methacrylated macromers with near-infrared light and gold nanorods. Nanotechnology 2014;25(1):014004.

27. Khetan S, Burdick JA. Patterning network structure to spatially control cellular remodeling and stem cell fate within 3-dimensional hydrogels. Biomaterials 2010;31(32):8228-8234.

28. Chung C, Mesa J, Randolph M, Yaremchuk M, Burdick J. Influence of gel properties on neocartilage formation by auricular chondrocytes photoencapsulated in hyaluronic acid networks. Journal of Biomedical Materials Research Part a 2006;77A(3):518-525.

29. Khetan S, Burdick J. Cellular encapsulation in 3D hydrogels for tissue engineering. J Vis Exp 2009;(32). pii: 1590. doi(32):10.3791/1590.

30. Sahoo S, Chung C, Khetan S, Burdick JA. Hydrolytically degradable hyaluronic acid hydrogels with controlled temporal structures. Biomacromolecules 2008;9(4):1088-1092.

31. Burdick JA, Prestwich GD. Hyaluronic acid hydrogels for biomedical applications. Adv Mater 2011;23(12):H41-H56.

32. Ruel-Gariepy E, Shive M, Bichara A, Berrada M, Le Garrec D, Chenite A, et al. A thermosensitive chitosan-based hydrogel for the local delivery of paclitaxel. Eur J Pharm Biopharm 2004;57(1):53-63.

33. Temenoff JS, Kasper FK, Mikos AG. Fumarate-based macromers as scaffolds for tissue engineering applications. In: Ashammakhi N, Reis R, Chiellini E, editors. Topics in Tissue Engineering. 3rd ed. Oulu, Finland: University of Oulu; 2007. p. 6.1-6.16.

34. Fraser J, Laurent T, Laurent U. Hyaluronan: Its nature, distribution, functions and turnover. J Intern Med 1997;242(1):27-33.

35. Bitter T, Muir HM. A modified uronic acid carbazole reaction. Anal Biochem 1962;4:330-334.

36. Platzer M, Ozegowski JH, Neubert RH. Quantification of hyaluronan in pharmaceutical formulations using high performance capillary electrophoresis and the modified uronic acid carbazole reaction. J Pharm Biomed Anal 1999;21(3):491-496.

37. Anseth KS, Bowman CN, Brannon-Peppas L. Mechanical properties of hydrogels and their experimental determination. Biomaterials 1996;17(17):1647-1657.

38. Kablik J, Monheit GD, Yu L, Chang G, Gershkovich J. Comparative physical properties of hyaluronic acid dermal fillers. Dermatol Surg 2009;35(1):302-312.

39. Chung C, Beecham M, Mauck RL, Burdick JA. The influence of degradation characteristics of hyaluronic acid hydrogels on in vitro neocartilage formation by mesenchymal stem cells. Biomaterials 2009;30(26):4287-4296.

40. Sutton M, Sharpe N. Left ventricular remodeling after myocardial infarction - Pathophysiology and therapy. Circulation 2000;101(25):2981-2988.

4.7. Appendix 4.1. Statistical comparisons for selected *in vitro* characterization figures.

Figure 4.5. Tunability of mechanical properties of HeMA-HA hydrogels.

Within each initiator concentration, all comparisons between modifications were statistically significant ($p<0.05$) except for 4 wt% hydrogels at 10 mM APS/TEMED. All comparisons between macromer concentrations for a given initiator concentration were statistically significant ($p<0.05$) aside from 4 vs. 7 wt% for 10% modified hydrogels formed using 5 mM and 10 mM APS/TEMED. Statistical comparison between initiator concentrations were statistically significant ($p<0.05$) for all comparisons to 5 mM except for 35% modified HeMA-HA at 4 wt%. Between initiator concentrations, all comparisons to 5 mM were statistically significant ($p<0.05$) except for 35% modified hydrogels at 4 wt% and 10% modified hydrogels at 10 wt%. Comparisons in moduli for 7.5 vs. 10 mM were statistically significant ($p<0.05$) for 10 wt% gels at both modifications and for 10% modified gels at 10 wt%.

Figure 4.6. Initial *in vitro* characterization studies of pure HeMA-HA hydrogels at various modifications and macromer concentrations.

$^{*}p<0.05$ vs. 10% modified HeMA-HA at 4 wt% in panel A. Between modifications, gel onset at 4 wt% and gel completion at 7 wt% were statically significant ($p<0.05$). All groups were statistically significant ($p<0.05$) in panel B. In panel C, comparisons between modifications are all statistically significant ($p<0.05$) except for 4 wt% hydrogels at 1 week. For comparisons between macromer concentrations, $^{*}p<0.05$ for 4 vs. 7 wt%, $^{+}p<0.05$ for 7 vs. 10 wt%, and $^{\#}p<0.05$ for 4 vs. 7 wt% for 10% modified hydrogels and $^{\delta}p<0.05$ for 7 vs. 10 wt% for 25% modified hydrogels. In panel D, all compressive moduli prior to normalization were statistically significant ($p<0.05$) except for 10% vs. 35% mod for 4 wt% hydrogels at days 0, 14 and 28, 4 vs. 7 wt% for 10% modified gels at days 7, 14, and 28, and 7 vs. 10 wt% for 10% modified gels at days 14 and 56.

Figure 4.8. Extensive analysis on the effect of macromer modification and concentration on HeMA-HA hydrogel properties.

In panel A, gelation comparisons between modifications were statistically significant ($p<0.05$) for all macromer concentrations relative to 10% modification except for 10% vs. 25% modified gels at 4 wt% for gel onset and 2 wt% for gel completion. For 25% vs. 40% modified gels, values were significant ($p<0.05$) at 4 wt% for gel onset and at 8 wt% and 10 wt% for gel completion. Gel onset comparisons between macromer concentrations were statistically significant ($p<0.05$) for all 10% modified hydrogels except 6 vs. 8 wt%, 6 vs. 10 wt%, 8 vs. 10 wt%, 8 vs. 12 wt%, and 10 vs. 12 wt%. For the other two modifications, gel onset was statistically significant ($p<0.05$) for all other macromer concentrations relative to 2 wt% except for 2 vs. 4 wt% for 25% modified hydrogels. For gel completion comparisons, $^{*}p<0.05$ vs. 2 wt% and $^{+}p<0.05$ vs. 12 wt% at the same modification. In panel B, all degradation comparisons were statistically significant ($p<0.05$) except for 10% modified hydrogels at 2 vs. 4 wt% and 10 vs. 12 wt%. Comparison of initial mechanics was statistically significant ($p<0.05$) between modifications aside from 25% vs. 40% modified gels at 4 wt%. Between macromer concentrations, all moduli were statistically significant ($p<0.05$) aside from 2 vs. 4 wt% gels at all modifications, 4 vs. 6 wt% gels at 10% and 25% modifications, and 2 vs. 6 wt% hydrogels at 40% modification.

Figure 4.9. Tuning HeMA-HA hydrogel degradation by altering the macromer modification and concentration.

Between modifications, all mass loss values were statically significant ($p<0.05$) aside certain 25% vs. 40% comparisons: at day 1 - 2, 4, 6, 8, 10, and 12 wt%; at week 1 - 2, 4, 8, 10, and 12 wt%; at week 2 - 4, 8, 10, and 12 wt%; at week 4 - 4, 8, 10, and 12 wt%; at week 8 - 8 and 12 wt%; at week 12 - 12 wt%; and at week 16 - 12 wt%. Comparisons between macromer concentrations at each modification were statistically significant ($p<0.05$) except for the following cases. For 10% modified hydrogels: day – 4 vs. 6 wt%, 6 vs. 10 wt%, 8 vs. 10 wt%, 8 vs. 12 wt%, 10 vs. 12 wt%; week 1 – 6 vs. 8 wt%, 6 vs. 10 wt%, 6 vs. 12 wt%, 8 vs. 10 wt%, 8 vs. 12 wt%, 10 vs. 12 wt%; week 2 – 6 vs. 8 wt%, 6 vs. 10 wt%, 8 vs. 10 wt%, 10 vs. 12 wt%; and week 4 – 8 vs. 10 wt%, 10 vs. 12 wt%. For 25% modified hydrogels: day 1 – 2 vs. 4 wt%, 2 vs. 6 wt%, 2 vs. 8

wt%, 4 vs. 6 wt%, 6 vs. 8 wt%, 6 vs. 10 wt%, 8 vs. 12 wt%, 10 vs. 12 wt%; week 1 – 2 vs. 4 wt%, 4 vs. 6 wt%, 8 vs. 10 wt%, 10 vs. 12 wt%; week 2 – 4 vs. 6 wt%, 8 vs. 10 wt%, 10 vs. 12 wt%; week 4 – 4 vs. 6 wt%, 10 vs. 12 wt%; and week 8 – 10 vs. 12 wt%. For 40% modified hydrogels: day 1 and week 1 – 2 vs. 4 wt%, 6 vs. 8 wt%, 6 vs. 10 wt%, 6 vs. 12 wt%, 8 vs. 10 wt%, 8 vs. 12 wt%, 10 vs. 12 wt%; week 1 – 6 vs. 8 wt%, 6 vs. 10 wt%, 6 vs. 12 wt%, 8 vs. 10 wt%, 8 vs. 12 wt%, 10 vs. 12 wt%; weeks 2 and 4 - 6 vs. 8 wt%, 8 vs. 10 wt%, 8 vs. 12 wt%, 10 vs. 12 wt%; weeks 8, 12, and 16 – 8 vs. 10 wt%, 10 vs. 12 wt%; and week 20 – 10 vs. 12 wt%.

Figure 4.10. *In vitro* characterization of selected HeMA-HA hydrogel formulations with similar gelation and initial mechanics but different rates of degradation.

In panels A and B, $*p<0.05$. In panel C, comparisons between similar formulations (i.e., 10% mod at 8 wt% vs. 40% mod at 4 wt%) at each time point were statistically significant ($p<0.05$). At each time point, differences in degradation between 10% and 40% modified hydrogels were statistically significant ($p<0.05$). In panel D, comparisons between similar formulations were statistically significant ($p<0.05$) at 2, 4, 8, and 12 weeks. Differences in moduli between the two modifications were significant ($p<0.05$) at 1, 2, 4, 8, and 12 weeks.

Figure 4.11. Effect of combining non-degradable MeHA and degradable HeMA-HA into a single copolymer hydrogel system at various macromer concentrations.

In panel A, gel onset comparisons between macromer concentrations at each ratio were statistically significant ($p<0.05$) except for 6 vs. 8 wt% at all ratios, 8 vs. 10 wt% in 0:100 and 75:25 copolymers, and all pure HeMA-HA (100:0) hydrogels. For gel onset comparisons between ratios at each macromer concentration, $*p<0.05$ vs. 100:0 and $^{+}p<0.05$ vs. 75:25. For gel completions comparisons between modifications, $^{\delta}p<0.05$ for all 4 vs. 10 wt% ratios, 4 vs. 8 wt% at 25:75 and 50:50, and 6 vs. 10 wt% at 25:75 and 50:50. No gel completion comparisons between ratios were statistical significant ($p<0.05$). In panel B, all degradation comparisons between ratios at a single macromer concentration (aside from at 20 weeks) and all comparisons

between macromer concentrations at a given copolymer ratio were statistically significant ($p<0.05$). For initial moduli comparisons, $^{*}p<0.05$ vs. 100:0, $^{+}p<0.05$ vs. 75:25, and $^{\#}p<0.05$ vs. 0:100 copolymers.

Figure 4.12. Tuning hydrogel degradation by altering the ratio of HeMA-HA to MeHA at various macromer concentrations.

Comparisons between the copolymer ratios at each macromer concentration gradually became more statistically significant ($p<0.05$) with additional time points of assessment. In panel A, mass loss differences between ratios for 4 wt% hydrogels were significant ($p<0.05$) except for the following: 75:25 vs. 50:50 and 75:25 vs. 25:75 at day 1; 50:50 vs. 25:75 at day 1 and weeks 1, 2, 4, 8, and 12; 100:0 vs. 75:25 at weeks 1, 2, and 4; and 25:75 vs. 0:100 at weeks 4, 8, 12, 16 and 20. In panel B, no comparisons for 6 wt% hydrogels were statistically significant at day 1 or week 1. At weeks 2 and 4, the only significant ($p<0.05$) comparisons were between 100:0 vs. 75:25 at both weeks and 100:0 vs. 0:100 at week 4. At weeks 8 and 12, all comparisons were statistically significant ($p<0.05$) except for the following: 75:25 vs. 50:50, 75:25 vs. 25:75, 50:50 vs. 25:75, and 25:75 vs. 0:100 at week 8; 75:25 vs. 50:50 and 50:50 vs. 25:75 at week 12. At weeks 16 and 20, all comparisons were statistically significant ($p<0.05$). For panels C and D, no comparisons for were statistically significant at day 1 or weeks 1, 2, or 4. For 8 wt% hydrogels, all comparisons at 8 and 12 weeks were statistically significant ($p<0.05$) except for the following: 75:25 vs. 50:50, 75:25 vs. 25:75, 50:50 vs. 0:100, 25:75 vs. 50:50, and 25:75 vs. 0:100 at week 8; 50:50 vs. 25:75 at week 12. For 10 wt% hydrogels, all comparisons at 8 and 12 weeks were statistically significant ($p<0.05$) except for the following: 100:0 vs. 0:100 and 100:0 vs. 25:75 at week 8; 25:75 vs. 0:100 at week 12. For both panels C and D, all comparisons between ratios were statistically significant ($p<0.05$) at weeks 16 and 20. General comparisons between the macromer concentrations were statistically significant ($p<0.05$) for the following: day 1 - 4 vs. 6 wt%, 4 vs. 10 wt%, 6 vs. 8 wt%; weeks 1, 2, and 4 - 4 vs. 6 wt%, 4 vs. 8 wt%, 4 vs. 10 wt%; week 8 – 4 vs. 10 wt%; and week 16 – 4 vs. 10 wt%, 6 vs. 10 wt%, 8 vs. 10 wt%.

Figure 4.13. *In vitro* characterization of selected HeMA-HA/MeHA copolymer hydrogels.

For panel A, $^{+}p<0.05$ vs. 5 wt% gels at the same ratio. All comparisons between ratios were statistically significant (*$p<0.05$) for gel onset. There were no statistical differences in gel completion. For panel B, degradation was statistically different ($p<0.05$) between macromer concentrations for 75:25 hydrogels and between ratios at the same concentration (*$p<0.05$). Initial moduli were statistically significant ($p<0.05$) for all comparisons between macromer concentrations at each ratio and between ratios for 5 wt% hydrogels (*$p<0.05$). In panel C, comparisons in hydrogel mass loss between ratios statistically significant ($p<0.05$) for 5 wt% copolymers at all time points, 6 wt% gels at weeks 8, 12, and 16, and 7 wt% gels at weeks 12 and 16. Differences between macromer concentrations statistically significant ($p<0.05$) for 75:25 copolymers at 5 vs. 7 wt% at all time points, 5 vs. 6 wt% at day 1, week 1, and week 2, and 6 vs. 7 wt% at week 4. In panel D, comparisons between ratios were statistically significant ($p<0.05$) at week 12 for all macromer concentrations. At each ratio, all differences between macromer concentrations were statistically significant ($p<0.05$) except for 5 vs. 6 wt% gels at both ratios at week 8, 6 vs. 7 wt% gels at 25:75 at week 8, and 6 vs. 7 wt% gels at both ratios at week 12.

CHAPTER 5

Using MRI to Visualize and Quantify Hyaluronic Acid Hydrogel Distribution in Cardiac Tissue

5.1. Introduction

Injectable hydrogels have become an attractive therapy for many biomedical applications, including the attenuation of left ventricular (LV) remodeling after myocardial infarction (MI) by mechanically stabilizing the myocardial wall to reduce stress.[1] Theoretical finite element (FE) models have shown that the ability of injectable hydrogels to decrease myocardial stress post-MI depends on their material properties, such as mechanics and volume.[2-5] A FE model of injections into the borderzone region that were 20% greater than the stiffness of the native myocardium and 4.5% of the LV wall volume led to a 20% reduction in myocardial stress in the fiber direction as compared to control simulations with no injections.[2] Another FE model of simulated polymeric inclusions illustrated the importance of both the injection pattern and the volume of material dispersion, with larger numbers of injections and larger injections volumes having the greatest potential to decrease myocardial fiber stress following infarction.[3] These theoretical models illustrate the correlation between positive mechanical outcomes and material properties, particularly the material distribution volume. However, the optimal material volume necessary to maximize the mechanical benefit remains unclear. One challenge in identifying optimal material distribution is the ability to noninvasively assess material properties in tissues.

Traditional assessment of hydrogel dispersion centers on the use of histological and immunohistochemical techniques that, while effective, are ultimately invasive, destructive, and limited to two-dimensional slices which prevent accurate three-dimensional volume assessment.

In contrast, imaging offers a noninvasive approach to temporally obtain information regarding the presence and distribution of hydrogels throughout tissue. Various imaging techniques have been show to be useful for material assessment. Optical imaging can be used for both two- and three-dimensional *in vivo* material visualization, either through multiphoton microscopy with the use of coupled fluorescent dyes or optical coherence tomography, respectively. However, optical imaging of materials is limited to small animals[6-8] or superficial locations within centimeters of the tissue surface[9] since light intensity decays exponentially with increasing tissue depth, thus decreasing image sensitivity and resolution.[10,11]

Similarly, x-ray imaging can also be used to assess materials in both two- and three-dimensions using standard radiographic or computed tomography (CT) techniques, respectively, where image contrast is generated based on difference in the amount of x-rays exiting adjacent objects of interest. Therefore, the ability to detect materials using x-rays is dependent on their atomic make-up, or density, which is often similar to that of native soft tissues.[12] Micro-CT (μCT) has thus been used extensively to monitor materials for bone applications[13-15] but requires incorporation of contrast agents with high atomic numbers, such as iodine or gold,[12,16,17] for soft tissue applications. Unlike fluorophores for optical imaging, x-ray contrast agents require relatively high concentrations for visualization leading to concerns with toxicity and potential alteration of materials properties.[16,18] Moreover, for *in vivo* applications, frequent temporal material assessment using x-ray imaging is challenging due to the increased risk of biological (more specifically, carcinogenic) damage with repeated exposure to ionizing radiation.[19]

To circumvent the depth limitations of optical imaging and ionizing radiation concerns of x-ray imaging, magnetic resonance imaging (MRI) can be used to image injectable materials. MRI is particularly well-suited for material assessment due to its ability to provide accurate and reproducible images with high spatial and temporal resolution in three dimensions.[20] As discussed in Chapter 1, image contrast in MRI is based on differences in the response of water protons in materials or tissues to the presence of magnetic fields. Due to their intrinsic spin

property, when protons are placed in a static magnetic field of strength B (referred to as B_0), they act like a bar magnet and align themselves with the main B_0 magnetic field oriented along the z-axis.[21,22] To generate a signal from the protons, the protons must be rotated to the x-y plane using a secondary magnetic field (B_1) that is applied with a radiofrequency (RF) coil within the main magnet.[23] As the protons relax back to their equilibrium state, they give off the energy they obtained from the applied RF pulse in the form of a free-induction decay (FID) echo, which is detected by the RF coil as the MR signal.[23] Differences in signal between adjacent materials or tissues are due to differences in the rate at which their protons relax to equilibrium (i.e., relaxation properties). Transverse (T_2) and longitudinal (T_1) relaxation are processes that describe the rate of proton dephasing in the transverse (i.e., x-y) plane and return to alignment with the B_0 field along the longitudinal (i.e., z-) axis.[21,22] Differences in T_1/T_2 relaxation can be exposed based on the degree of rotation of the protons caused by the B_1 field, which is specified in the pulse sequence, or series of RF pulses. Therefore, tuning the RF pulse sequence can be used to enhance differences in relaxation properties, and thus, endogenous MR image contrast.

Pulse sequences commonly used for conventional MRI include spin echo, gradient echo, and inversion recovery sequences. In a spin echo sequence, a 90^o RF pulse is applied to rotate the protons into the x-y plane, at which point they begin dephasing from one another by T_2 relaxation. An 180^o pulse is then applied to rapidly rephase the protons and result in signal (i.e., FID echo) generation.[21] The time between when the 90^o pulse is applied and the echo acquired is referred to as the echo time (TE). Multiple 90^o-180^o RF pulse trains are needed to generate an image and to improve the image signal-to-noise ratio (SNR); the time between pulse train repetitions is called the repetition time (TR).[22] In contrast to a spin-echo sequence, an inversion recovery sequence involves first rotating the protons 180^o. As the protons relax along the z-axis by T_1 processes, a 90^o RF pulse is applied to rotate the protons into the x-y plane where the signal can be detected.[21] Finally, in a gradient echo sequence, the RF pulse produces an angle of proton rotation between 0^o and 90^o; since the protons are only partially flipped into the x-y plane, some of the longitudinal magnetization is maintained, leading to rapid signal generation.[21] Each

pulse sequence has its benefits. Whereas gradient echo imaging enables rapid acquisition, spin echo imaging introduces a T_2 dependence and gradient echo imaging highlights differences based on T_1. Thus, tailoring the pulse sequence, both through the type and selection of the TE and TR times, can result in differences in image contrast based on intrinsic MR properties.

Conventional MRI has been used to image injectable biomaterials based on their intrinsic MR properties (e.g., T_1/T_2 relaxation times, proton density) in both animals and humans.[24] However, much of the work has been limited to synthetic injectable materials, such as poly(lactic acid),[25] poly(L-lactide),[26] or poly(ethylene glycol),[24] since their intrinsic MR properties often differ from those of the surrounding tissue. An alternative approach is to incorporate an exogenous contrast agents into the biomaterial, such as iron oxide (FeO)[27] or gadolinium (Gd^{+3}),[28] to generate or enhance the differences in relaxation properties and thus, increase image contrast-to-noise (CNR). However, similar to the x-ray contrast agent concerns discussed above, high concentrations of MR contrast agents are required to generate an effect due to inherent sensitivity limitations with MRI. These high concentrations not only have the potential to alter the injected biomaterials' properties and disturb the physiologic environment surrounding the injection site but also will produce local toxicity if not properly coated or chelated for the duration of their time *in vivo*.[29] Thus, there remains a need to develop MRI techniques to image natural, injectable materials without the use of contrast agents.

Towards this goal, this chapter used non-contrast based MRI to image injectable hyaluronic acid (HA) hydrogels and assess their material properties following injection into myocardial tissue. As discussed in Section 4.1, HA is a linear polysaccharide found in native cardiac extracellular matrix and can be modified with numerous reactive groups. The addition and amount of these reactive groups enables both hydrogel formation and tuning of hydrogel properties (e.g., distribution volume). This chapter builds off the previous characterization chapter to investigate the ability to tailor hydrogel three-dimensional volume distribution in tissue by altering material properties. Ultimately, the use of MR imaging as a tool to noninvasively

investigate material properties could provide insight on material design criteria for injectable biomaterials to attenuate LV modeling.

5.2. Materials and Methods

5.2.1. Synthesis and Gelation of MeHA Macromers

Methacrylated HA (MeHA) was synthesized as previously discussed in Section 4.2.2 through the reaction of HA (75 kDa, Lifecore) and methacrylic anhydride (MA, Sigma) in deionized (DI) water at pH 8.0 (4°C, 24hrs), followed by dialysis against DI water for purification. The macromer was then frozen and lyophilized.[30] HA methacrylation was altered by varying the amount of MA to HA and assessed with ^{1}H-NMR (Bruker, 360 MHz), as shown in Section 4.2.2. Two MeHA functionalizations were examined in subsequent *ex vivo* MR imaging applications: ~30% (i.e., low MeHA) and ~60% (i.e., high MeHA) modification of the HA repeat units.

For gelation, the methacrylate groups on MeHA were crosslinked using a two-component redox radial initiator system of ammonium persulfate (APS, Sigma) and N,N,N,N',N'-tetramethylenediamine (TEMED, Sigma).[31] APS and TEMED were mixed with MeHA dissolved in PBS (4 wt%) to induce hydrogel formation. Macromers were crosslinked using two concentrations of the initiators (low A/T: 5 mM APS and 5 mM TEMED or high A/T: 12.5 mM APS, 6.25 mM TEMED) to form the following four hydrogel formulations: 1) low MeHA, low A/T, 2) high MeHA, low A/T, 3) low MeHA, high A/T, and 4) high MeHA, high A/T. Gelation was evaluated by monitoring the storage (G') and loss (G") moduli over time at 37°C using an AR2000ex Rheometer (TA Instruments) under 1% strain and a frequency of 1 Hz in a cone-plate geometry (1°, 20 mm diameter),[32] as in Section 4.2.3. Gelation onset was defined as the time point when the G' and G" intersected and the viscosity (|n*|) was greater than one. Gel onset times were subsequently used to dictate the timing for hydrogel injection into myocardial explants.

5.2.2. Synthesis and Gelation of Guest-Host HA Macromers

In collaboration with another graduate student in our group (Christopher Rodell), guest-host macromers were synthesized by functionalizing HA (90 kDa, Lifecore) with either adamantine (guest) or β-cyclodextrin (host), as previously described.[33] Briefly, adamantine modified HA (Ad-HA) was formed by coupling 1-adamantane acetic acid to HA-tetrabutyl-ammonium salt (HA-TBA) through an esterifiction reaction in dimethyl sulfoxide (DMSO) mediated by 4-dimethylaminopyridine (DMAP, Sigma) and the coupling agent di-tert-butyl dicarbonate (BOC_2O, Sigma) (45°C, 24hrs).[33] Purification was carried out by dialyzing against DI water, acetone precipitating, and dialyzing again. Cyclodextrin modified HA (CD-HA) was synthesized by coupling 6-(6-aminohexyl)amino-6-deoxy- β-cyclodextrin (β-CD-HAD) to HA-TBA through an amidation reaction with (benzotriazol-1-yloxy)tris(dimethylamino)phosphonium hexafluorophosphate (BOP, Sigma) as the coupling agent in DMSO (25°C, 2hrs).[33] The macromer was then purified by extensive dialysis against DI water and filtration to remove insoluble byproducts from the reaction. Both guest-host macromers were frozen, lyophilized, and assessed using ^{1}H-NMR (Bruker, 360 MHz) to determine the functionalization. For subsequent imaging work in this chapter, adamantine and cyclodextrin modifications of ~50% and ~20% of the HA repeat units were selected, respectively.

Hydrogel formation occurred by supramolecular self-assembly of the guest-host components on HA upon mixing solutions of the two macromers dissolved in PBS. Manual stirring was used to ensure homogenous interaction and assembly (**Figure 5.1**). Entrapped air bubbles were removed by brief centrifugation. Hydrogels were formed such that the net polymer concentration was 5 wt% and the adamantine and cyclodextrin components were stoichiometrically balanced. Rheology properties were assessed at 37ºC using the cone and plate geometry (1°, 20 mm diameter) discussed in Section 5.2.1 above to obtain oscillatory time sweeps under 1% strain and a frequency of 1 Hz.[33]

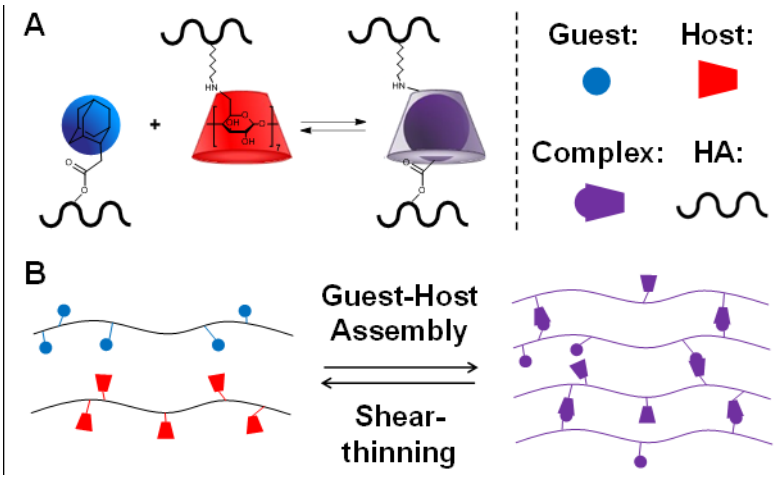

Figure 5.1. Formation of self-assembling, guest-host HA hydrogels with shear-thinning properties. Reversible interaction of adamantane (Ad, guest) and β-cyclodextrin (CD, host) functionalized HA to form a guest-host complex (A). Schematic of guest-host hydrogel formation by supramolecular self-assembly and disassembly in the presence of shear forces (B). Figure adapted from [33].

5.2.3. Synthesis and Gelation of HeMA-HA Macromers

As described previously in Section 4.2.1, HA was modified with hydrolytically degradable hydroxyethyl methacrylate (HeMA) to form the gel precursor HeMA-HA by coupling HA-TBA (75 kDa HA) to 2-hydroxyethyl-methacryl-succinate (HeMA-COOH).[32] Similar to the synthesis of Ad-HA above, the reaction was performed in DMSO using DMAP (Sigma) and BOC_2O (Sigma) (45°C, 20hrs). The macromer was purified by dialyzing against DI water at 4°C, acetone precipitating, and dialyzing again. The solution was then frozen and lyophilized to obtain the final product. The HeMA modification on HA was evaluated using ^{1}H-NMR (Bruker, 360 MHz) and found to be ~25% of the HA repeat units, as shown in Section 4.2.1.

Similar to MeHA gelation, HeMA-HA hydrogel formation was induced by crosslinking the macromer dissolved in PBS (8 wt%) with the chemical initiators APS (5 mM, Sigma) and TEMED (5 mM, Sigma).[31] As in Section 4.2.3, rheology was used to assess gelation, where the gel onset

and completion times were defined on the time sweeps as when G' and G" intersected and when there was less than a 1% change in both G' and viscosity (|n*|) for ten time steps, respectively.

5.2.4. MRI of MeHA in Myocardial Explants

MeHA hydrogel distribution volume within the myocardium was assessed in healthy lamb LV tissue obtained from a local butcher shop. *Ex vivo* samples were prepared by simulating the *in vivo* injection protocol that will be described in Section 5.2.6. In general, the MeHA macromer (low: 30%, high: 60% modified) was dissolved in PBS (4 wt%) and mixed with the specified chemical initiators (low: 5/5 mM APS/TEMED, high: 12.5/6.25 mM APS/TEMED). Three minutes after adding the initiators (based on rheology, as discussed in Section 5.2.1), 0.3 mL of the prepolymer solution was injected into the myocardial LV explant at a depth of approximately 1 cm from the epicardial surface. After waiting thirty minutes to ensure sufficient time for gelation, the composite hydrogel/tissue samples (about 2 x 2 cm) were collected from the LV to include the transmural injection site from the epicardium to endocardium. Prior to initial imaging session (which occurred less than 2 hrs following injection), tissue samples were stored in PBS (Life Technologies) supplemented with Penicillin-Streptomycin (1%, P/S; Life Technologies).

Explants containing MeHA hydrogel injections were imaged using a 9.4 T horizontal bore small animal MR scanner (Varian, Palo Alto, CA) using a 35-mm diameter commercial quadrature ^{1}H coil (m2m Imaging Corp., Cleveland, OH). Imaging parameters were adjusted to exploit the differences in intrinsic MR properties between the material and myocardium. A T_2-weighted spin-echo pulse sequence was used and the echo time (TE) was varied (30, 40, 50, 60 ms) at a constant repetition time (TR, 5.8 sec) to generate optimal image contrast by visual inspection. Similarly, the voxel size was adjusted (0.23 x 0.23 x 1.00 mm^3 vs. 0.23 x 0.23 x 0.23 mm^3) to optimize image resolution. As described in Kichula et al.,[5] the final imaging parameters selected following optimization were as follows: echo time = 40 ms, repetition time = 5.8 sec, averages = 2, field of view = 30 x 30 mm^2, matrix size =128 x 128, slices = 128, slice thickness = 0.23 mm, voxel size = 0.23 x 0.23 x 0.23 mm^3.

Prior to assessing differences in hydrogel distribution between the four MeHA hydrogel formulations (introduced in Section 5.2.1), uncrosslinked MeHA was injected into myocardial explants (*n=3 samples*) and imaged at various time points following injection (i.e., at days 0, 1, 2, 3, 4, and 5) to assess changes in the MR signal of the macromer alone relative to the background myocardial signal using the selected imaging parameters. Between scans, the uncrosslinked macromer-explant samples were immersed in 50 mL of sterile PBS (Life Technologies) supplemented with Penicillin-Streptomycin (1%, P/S; Life Technologies). While at room temperature, the solution of sterile PBS with P/S was changed six times each day to remove the uncrosslinked macromer by diffusion. Overnight, tissue samples were stored at 4°C in 200 mL of sterile PBS. To assess differences in signal intensity, images were first converted into NIFTI files using ImageJ software (NIH; Bethesda, MD) and then converted to their correct dimensions with the medical imaging processing tool convert3D (c3D[34]). Subsequently, a MRI bias correction was performed with an N4 intensity normalization algorithm (Insight Segmentation and Registration Toolkit, ITK; NIH; Bethesda, MD), as previously described,[35,36] and the difference in signal intensity between the injected uncrosslinked macromer and surrounding background myocardial tissue was quantified over the 6 day time course (i.e., days 0-5). For each sample, the percent change in intensity was calculated for five slices in three regions throughout the transmural cross-section of the LV wall (i.e., near the epicardium, myocardium, and endocardium).

Based on the uncrosslinked macromer study, differences in hydrogel distribution between the four MeHA hydrogel formulations (*n = 4/formulation*) were assessed three days following injection into myocardial explants. As described previously, samples were maintained at room temperature in 50 mL of sterile PBS with P/S that was changed 6 times per day and stored overnight at 4°C in 200 mL of sterile PBS. Similarly, images were converted to a NIFTI file format, the dimensions were corrected with c3D, and the MRI bias correction was performed to normalize intensity. The volumes of the injected hydrogels were quantified using a combination of automated and manual segmentation schemes. An automated segmentation was first performed using Atropos software (an ITK-based multivariate *n*-class open source segmentation algorithm

distributed with ANTs)[37,38] where the input domain was chosen to be only the tissue portion of the images. The segmentation was initialized by specifying that three different tissue spaces (i.e. segmentation regions) were present: 1) myocardial tissue, 2) hydrogel, and 3) tissue/hydrogel composite. After applying a smoothing factor of 0.1 (Markov random field value 1.0, 1x1x1), each voxel was then assigned to one of the three tissue labels depending on its intensity. Based on a comparison to the uncrosslinked MeHA studies at day 3, the crosslinked hydrogel was defined to be regions where the percent change in intensity between the hydrogel and myocardium was above 7%. A manual segmentation was then performed to further distinguish the crosslinked hydrogel from the myocardium, particularly in the edges of the questionable composite label regions from the automated segmentation. From the segmentations, hydrogel distribution volumes were quantified and 3D reconstructions generated using ITK-SNAP software.[34]

5.2.5. MRI of Guest-Host Hydrogels in Myocardium

Similar to the *ex vivo* MeHA studies, explanted healthy porcine hearts were acquired from a local distributor for MRI assessment of guest-host hydrogel distribution in myocardial tissue. Guest-host HA hydrogels were pre-formed in ½ cc syringes by manually mixing the two components (Ad-HA and Cd-HA) and centrifuging to remove air. Hydrogels were formed at a final HA concentration of 5 wt% using 50% modified Ad-HA and 20% modified CD-HA. Guest-host hydrogels were injected into LV wall of explanted hearts at a depth of about 1 cm from the epicardial surface using a 28G ½" needle to generate high shear forces for injectability. For imaging at 9.4 T, the sites of hydrogel injection were then isolated from the myocardial explant and included the transmural thickness of the LV wall. For 3 T MR scans, the entire heart remained intact. Tissue samples were stored in PBS with P/S (1%, Life Technologies) before initial imaging (<2 hrs post-injection) and between subsequent time points, if applicable, with the same rinsing protocol as above (Section 5.2.4).

Explants with guest-host hydrogel injections were first imaged using the 9.4 T horizontal bore MR scanner (Varian) and 35-mm ^{1}H coil utilized for *ex vivo* MeHA hydrogel imaging (Section

5.2.4). A T_2-weighted spin echo pulse sequence was used with the following imaging parameters: echo time = 40 ms, repetition time = 4 sec, averages = 4, field of view = 36 x 36 mm^2, matrix size = 256 x 256, slices = 32, slice thickness = 0.25 mm, voxel size = 0.14 x 0.14 x 0.25 mm^3. The TE was selected from the previously optimized 9.4 T imaging parameters (Section 5.2.4) due to its impact on the contrast generated in a T_2-weighted sequence. The remaining parameters were altered from the previous 9.4 T scans based on sample size and scan time considerations. To examine differences in hydrogel dispersion with injection volume, guest-host hydrogels were injected at three volumes (50 µL, 150 µL, and 300 µL) and imaged at three time points over the course of a week (days 0, 3, and 7 following injection).

To move towards more clinically relevant scan parameters, an array of nine, 300 µL guest-host hydrogels were injected into full porcine explants and imaged using a clinical 3 T Tim Magnetom Trio Scanner (Siemens Medical Solutions; Malvern, PA) with an 8-channel ^1H head coil (Nova Medical; Wilmington, MA). Unlike at 9.4 T where the tissue samples were maintained under ambient conditions, samples imaged at 3T were submerged in PBS for the duration of the scan time to minimize dielectric artifacts near the tissue surface. However, similar to imaging at 9.4 T, a T_2-weighted turbo spin echo pulse sequence was used and the scan parameters were first optimized by varying the TE (51, 61, 71, 81, 91 ms) at a constant TR (7 sec) as well as varying the TR (6, 7, 8 sec) at a constant TE (71 ms). Based on this optimization study and in consideration with sample size and scan time limitations, the following scan parameters were used to obtain T_2-weighted short-axis images: echo time = 71 ms, repetition time = 6 sec, averages = 2, field of view = 100 x 100 mm^2, matrix size = 320 x 320, slices = 50, slice thickness = 1 mm, voxel size = 0.31 x 0. 31 x 1.00 mm^3.

The MR images from both the 9.4 T and 3 T scans were analyzed by segmenting the guest-host hydrogels from the myocardial tissue in the T_2-weighted short-axis images acquired from apex to base and reconstructing the 3D volumes of the injected hydrogels. To do so, images were first converted into NIFTI files using ImageJ for use in ITK-SNAP segmentation software.[34]

Each short-axis image was first pre-processed by altering signal intensity thresholds to define the boundary between the hydrogel from the surrounding myocardium. An automated snake (i.e. active contour) segmentation algorithm[34] was initialized from within each hydrogel injection site and allowed to deform until the boundary between the hydrogel and myocardium was met. Manual edge corrections were then performed, where necessary, to adjust the hydrogel segmentation based on visual inspection. Subsequently, ITK-SNAP was used to reconstruct the segmented two-dimensional slices containing hydrogel injection sites into 3D hydrogel distribution volumes. The volume of each injected guest-host hydrogel was then quantified from its 3D reconstruction. Unlike the MeHA hydrogel/myocardial composites which required an initial automated segmentation using Atropos to fully detect the injected hydrogel (Section 5.2.4), all segmentations, reconstructions, and quantifications were performed in ITK-SNAP.

5.2.6. *Ex Vivo* MRI of HeMA-HA Hydrogels from *In Vivo* Injections

To investigate the translational potential of this imaging technique for hydrogel assessment, HeMA-HA hydrogels were injected *in vivo* into a healthy ovine heart and imaged *ex vivo* following sacrifice. A single HeMA-HA hydrogel formulation was used: 25% modified HeMA-HA at 8 wt% gelled using 5 mM APS and 5 mM TEMED. The animal received care in compliance with the University of Pennsylvania's Institutional Animal Care and Use Committee's protocols in accordance with guidelines for human case (National Institutes of Health, Publication 85-23, revised 1996). For material injections, one male Dorset sheep (35-40 kg) was sedated (intramuscular ketamine, 25-30 mg/kg), intubated, and mechanically ventilated. General anesthesia was maintained using a mixture of inhaled isoflurane (1.5-3.0%) and oxygen.[39] The animal underwent a left thoracotomy to expose the LV free wall and received three 500 μL injections of the HeMA-HA prepolymer solution that was mixed for 2 minutes (based on rheology) prior to injection and gelation in the posterolateral wall. Following material injection, wire markers were sutured to the epicardium near the injection sites for aid in material localization and the chest wall was closed. A few hours following injection (~4 hrs), the sheep was euthanized by an

over dose of potassium chloride and sodium thiopental while under general anesthesia. The animal was pronounced dead after ECG silence was seen for 3-5 minutes and cardiac arrest confirmed. The heart containing the *in vivo* injections was removed and prepared for *ex vivo* MRI.

The full heart explant was placed in a MR compatible container and immersed in Fomblin Y (Sigma) to fill the void spaces and reduce susceptibility artifacts. The container holding the explant was then submerged in a second, larger phantom filled with PBS to aid in shimming to correct for magnetic field (B_0) inhomogeneity. Similar to the guest-host *ex vivo* hydrogel imaging, HeMA-HA hydrogels were imaged in the explanted myocardial heart using the 3 T MR Scanner (Siemens) with an 8-channel ^1H head coil (Section 5.2.5). T_2-weighted short-axis images were acquired from the apex to base for hydrogel volume reconstructions during post-processing. As determined from the previous 3 T scan (Section 5.2.5), the whole explanted heart was imaged using the following parameters: echo time = 71 ms, repetition time = 6 sec, averages = 4, field of view = 100 x 100 mm^2, matrix size = 320 x 320, slices = 40, slice thickness = 1 mm, voxel size = 0.31 x 0. 31 x 1.00 mm^3. The volumes of the injected HeMA-HA hydrogels were subsequently segmented, reconstructed, and quantified using ITK-SNAP software,[34] as described above in Section 5.2.5. Briefly, an automated segmentation was initially performed to isolate the hydrogel injection sites from the surrounding myocardium for each short-axis slice, followed by edge manual corrections. 3D reconstructions of the segmented hydrogels were generated and the corresponding volumes calculated for each injection using ITK-SNAP.

Relaxation time mapping was performed using a spin-echo-prepared FLASH sequence with scan parameters identical to the corresponding T_2-weighted image acquisition above to generate T_1, $T_{1\rho}$ and T_2 maps of a single short-axis slice for each hydrogel injection. For the T_1 maps, the inversion time (TI) was varied as follows: 50, 100, 300, 500, 700, 1000, 1300, 1600, and 2000 ms. Using a custom MATLAB (Natick, MA) code, the signal intensity in each TI image was fit to the longitudinal magnetization (M_z) equation to calculate the T_1 for each pixel, where *t* is the inversion time (**Equation 5.1**[21]):

$$M_z(t) = M_0 * \left(1 - 2e^{-t/T_1}\right) \quad (5.1)$$

Similarly, the $T_{1\rho}$ and T_2 maps were generated from scans with the following spin-lock (TSL) and echo (TE) times, respectively: 0, 20, 40, 60, 80, and 100 ms. In this case, the signal in each TSL or TE image was fit to the transverse magnetization (M_{xy}) equation to calculate the T1r or T2 for each pixel, where *t* is the spin-lock or echo time, respectively (**Equation 5.2**[21]):

$$M_{xy}(t) = M_{xy}(0) * e^{-t/T_2} \quad (5.2)$$

5.2.7. Statistical Analysis

Data is presented as mean ± standard deviation (SD) or mean ± standard error of the mean (SEM), as indicated in each figure caption. Differences were assessed using a one-way ANOVA with Tukey's post hoc evaluation. A $p<0.05$ was considered to be statistically significant.

5.3. Results

5.3.1. MRI Visualization and Quantification of *Ex Vivo* MeHA Hydrogel Distribution

Four MeHA hydrogel formulations were selected based on varying a combination of the macromer modification and redox initiator concentrations (**Figure 5.2A)**. As anticipated from previous studies by our group,[40] the material properties (i.e., gelation) were tuned such that higher methacrylation and higher initiator concentrations led to accelerated hydrogel formation (**Figure 5.2B**). Hydrogels formed from a highly modified MeHA using a high concentration of initiators gelled most rapidly (1.75 ± 0.03 min) whereas hydrogels formed using a less modified MeHA with a low initiator concentration gelled the slowest (5.2 ± 0.2 min). Moreover, initiator concentration had a greater impact on gelation than macromer modification. These formulations (which have been used previously[5,32,40]) were applied for subsequent *ex vivo* imaging studies due to statistically significant ($p<0.05$) differences in their gelation onset times for all comparisons.

A

	Formulation	HA Mod	APS (A) and TEMED (T) Conc.
1	Low MeHA, Low A/T	~30%	A: 5 mM T: 5 mM
2	High MeHA, Low A/T	~60%	A: 5 mM T: 5 mM
3	Low MeHA, High A/T	~30%	A: 12.5 mM T: 6.25 mM
4	High MeHA, High A/T	~60%	A: 12.5 mM T: 6.25 mM

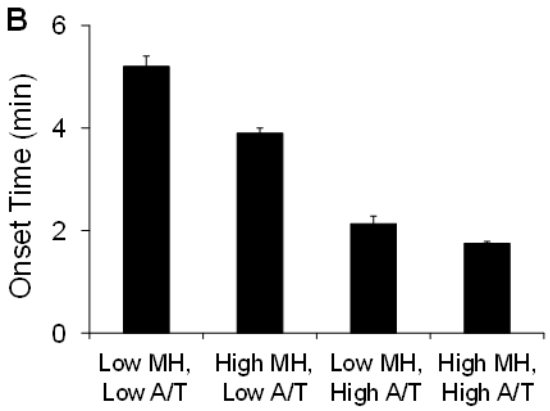

Figure 5.2. Selection and gelation of MeHA hydrogel formulations applied for *ex vivo* MRI assessment. MeHA hydrogels with varying properties formed by altering a combination of the macromer modification and initiator concentration (A). Gelation onset as a function hydrogel formulation, *n=3-4/group* (B). Data presented as mean ± SD. *p<0.05* for all comparisons.

Prior to examining differences in hydrogel distribution in myocardial explants between the four formulations, the imaging parameters were optimized at 9.4 T. Using a T_2-weighted spin echo pulse sequence, the TE was varied at a constant TR (5.8 sec). Higher TE values (i.e., 60 ms) led to images with overall lower signal intensity whereas lower TE values (i.e., 30 ms) resulted in images with higher overall signal intensity (**Figure 5.3A**). Based on visual inspection of the differences in image contrast between the injected hydrogel and surrounding myocardium, an intermediate TE of 40 ms was selected for subsequent hydrogel distribution assessment. In addition, the image resolution was optimized by altering the voxel size, where the slice thickness was decreased to obtain images with smaller voxels. Reconstruction and quantification of hydrogel distribution volume demonstrated that the hydrogel volume calculated from MRI decreased as the voxel size decreased, suggesting that use of larger voxels for imaging overestimated the hydrogel volume (**Figure 5.3B**). Thus, the smaller, isotropic voxel size (i.e., 0.23 x 0.23 x 0.23 mm^3) was selected for further imaging.

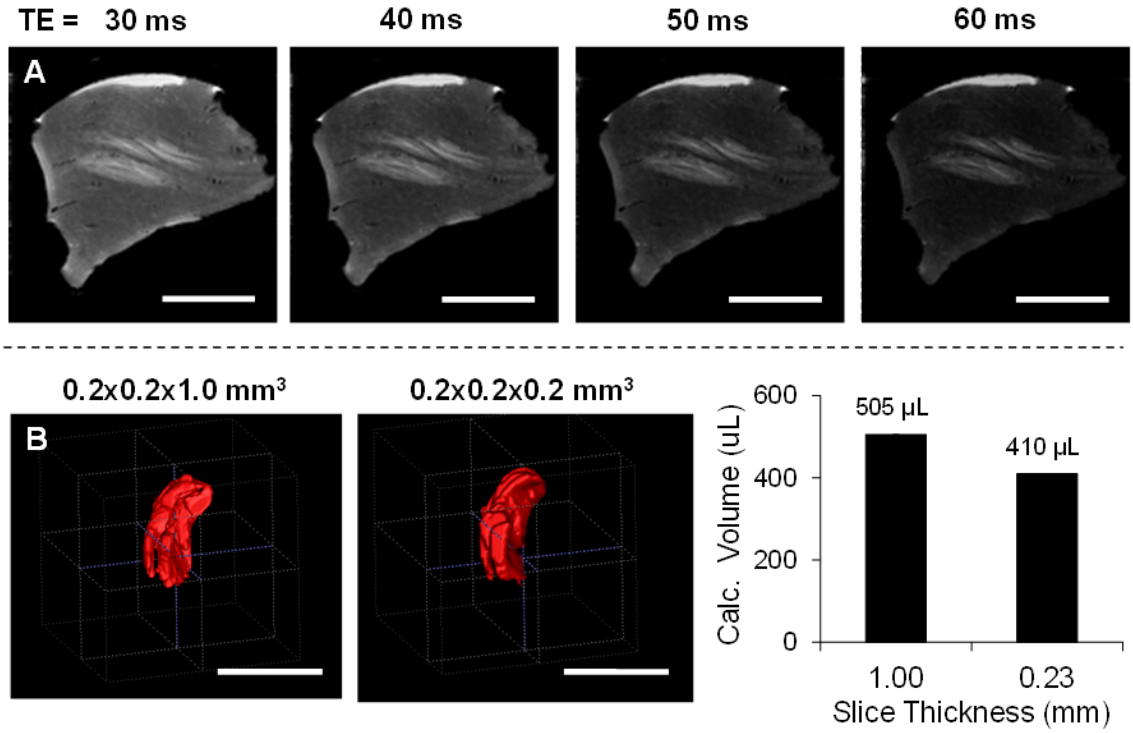

Figure 5.3. Optimization of MR imaging parameters for MeHA hydrogels in explants at 9.4 T. Representative cross-sections of T_2-weighted MRI of a single MeHA hydrogel formulation (high MeHA, low A/T) injected into myocardial explants and imaged using different echo time (TE) values, as indicated (A). Representative 3D reconstructions (left) and quantified volumes (right) as a function of slice thickness for a 300 µL MeHA hydrogel (high MeHA, low A/T) injection imaged using different voxel sixes (low resolution: 0.23 x 0.23 x 1.00 mm^3, high resolution: 0.23 x 0.23 x 0.23 mm^3), *n=1* (B). Scale bars = 1 cm.

To determine the optimal day for imaging myocardial explants after MeHA hydrogel injections, a study was performed where uncrosslinked MeHA was injected into explants and imaged over five days following injection. At each time point, the image contrast between the hydrogel and surrounding myocardium was assessed both qualitatively (**Figure 5.4A**) and quantitatively (**Figure 5.4B**) by calculating the percent change in signal intensity between the injection area (dictated from day 0) and the background myocardial tissue. Assessment at day 0

(i.e., <2 hours after injection) demonstrated the uncrosslinked MeHA macromer could be clearly discerned initially, with a greater than 30% higher signal intensity than the myocardium. As the study progressed, the difference in signal intensity between the uncrosslinked macromer and the surrounding myocardium decreased with time. A plateau was reached by day 3 following injection, where the difference in intensity remained less than 5% for all additional time points (**Figure 5.4B**). Thus, this time point was chosen to evaluate differences in hydrogel distribution.

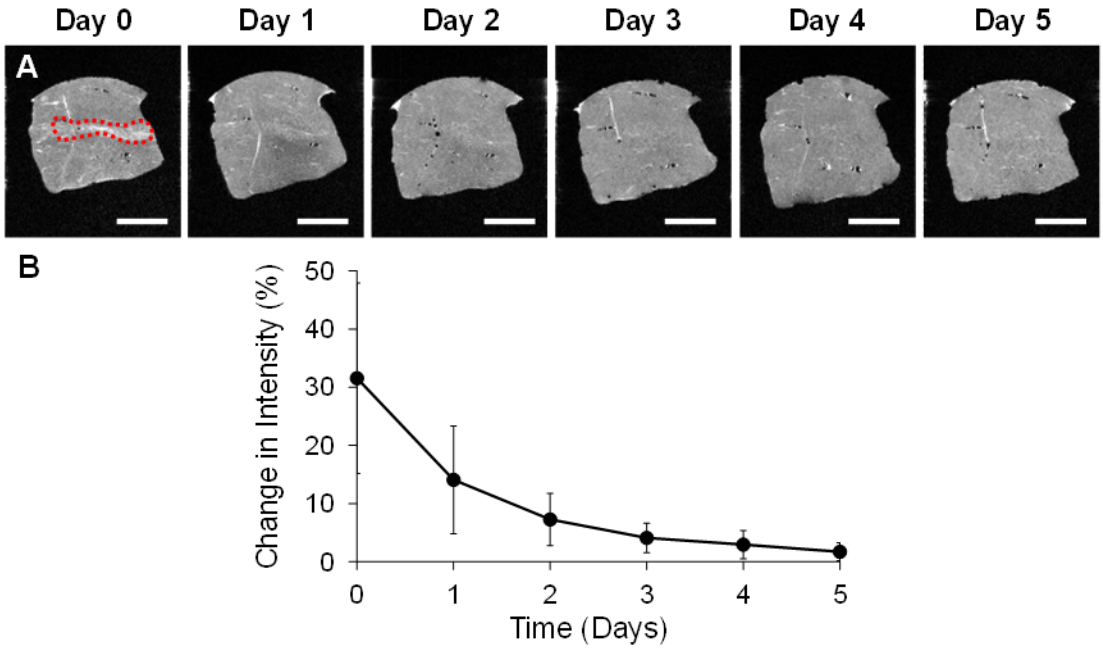

Figure 5.4. Determination of optimal day for imaging MeHA hydrogels in myocardial explants. Representative cross-sections of T_2-weighted MRI of uncrosslinked MeHA macromer injected into a myocardial explant and imaged over 5 days following injection (day 0) (A). Scale bars= 1 cm. Quantification of the percent change in signal intensity between the uncrosslinked injection site (outlined at day 0, dashed shape) and the surrounding myocardial tissue as background, *n=3* (B). Data presented as mean ± SD.

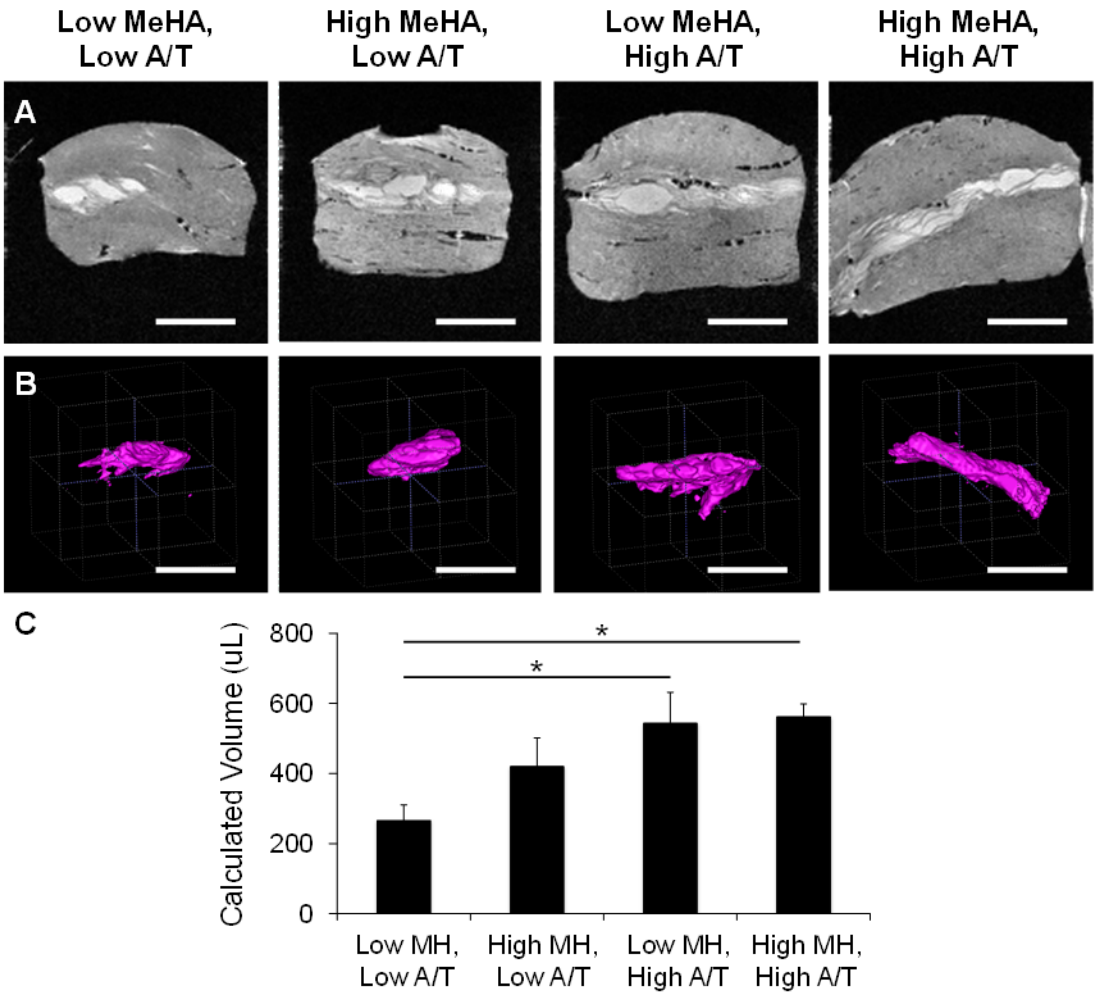

Figure 5.5. Visualization and quantification of MeHA hydrogel distribution volumes in myocardial explants at 9.4 T. Representative cross-sections of each MeHA hydrogel formulation at day 3 following injection into myocardial LV tissue (A). Representative 3D reconstructions of hydrogel distribution volume for 300 µL injections of each formulation (B). Scale bars = 1 cm in panels A and B. Volume quantification of the injection region as a function hydrogel formulation, *n=4/group* (C). Data presented as mean ± SEM. *$p<0.05$ vs. low MeHA, low A/T hydrogel formulation.

Differences in hydrogel distribution in myocardial tissue between the four crosslinked MeHA formulations were then investigated using MRI. Visual (**Figure 5.5A,B**) and quantitative (**Figure 5.5C**) assessment of the dispersion volumes of the crosslinked portion of the hydrogels

demonstrated that increased macromer modification or initiator concentration led to higher volumes. Macromer modification had a pronounced impact on the distribution volumes, particularly at the lower initiator concentration where a lower modification led to smaller crosslinked volumes. Moreover, comparing between initiator concentrations within each modification, lower amounts of initiators led to smaller crosslinked volumes as compared to higher initiator concentration. This trend was most pronounced in the lower modification case where the difference was statistically significant ($p<0.05$). Furthermore, the quantified volumes of the crosslinked portions of the hydrogels were higher than the injected volume (300 μL) for all formulations aside from the low MeHA, low A/T hydrogels (**Figure 5.5C**). In addition, while the hydrogel dispersion geometries varied both within and between formulations, generally most injections took on an ellipsoidal shape, as demonstrated by the cross-sectional slices (**Figure 5.5A**) and corresponding 3D volume reconstructions (**Figure 5.5B**).

5.3.2. Guest-Host HA Hydrogel Distribution in Explants from MRI Assessment

After examining differences in hydrogel dispersion based differences in the rate of hydrogel formation, an alternative HA hydrogel system was introduced to examine differences in hydrogel distribution based on the gelation mechanism. Through collaboration with another student in our group, guest-host hydrogels were formed through the supramolecular self-assembly of adamantine (Ad, guest) and β-cyclodextrin (CD, host) modified HA (**Figure 5.1**).[33] Previous rheological studies demonstrated that both dissolved macromers were viscous solutions individually, but upon mixing of Ad-HA and CD-HA, near-instantaneous hydrogel assembly occurred with an increase in moduli (i.e., G', G") of several orders of magnitude.[33]

Similar to the MeHA hydrogel studies, guest-host hydrogels were injected into myocardial explants and imaged using a 9.4 T MR scanner to obtain T_2-weighted images. Visualization of the hydrogels in both 2D cross-sectional slices (**Figure 5.6A**) and 3D volume reconstructions (**Figure 5.6B**) revealed distinct, solid plugs in the myocardium that were relatively spherical in geometry. Quantification of hydrogel dispersion volumes from the 3D reconstructions demonstrated that

differences in injection volume (e.g., 50 µL, 150 µL, 300 µL) could be accurately detected with little variation between the calculated and injected volumes, particularly at day 0 (i.e., <2 hours after injection) (**Figure 5.6C**). To assess changes in hydrogel distribution over time, the samples were imaged at various times over a week (i.e., days 0, 3, and 7) with continual washing and buffer exchange throughout to remove uncrosslinked material, if it were present. Regardless of the injected volume, 3D reconstructions revealed minimal changes in hydrogel surface features over time (**Figure 5.6B**) and corresponding quantifications demonstrated little changes in guest-host hydrogel distribution volumes (**Figure 5.6C**). The slight increase in the calculated hydrogel volume over time was most observable in the hydrogel with the smallest injection volume (50 µL), where an approximately 20% increase was seen by day 7 relative to day 0. The larger injection volumes (150 µL or 300 µL) had about a 13% increase in calculated volume by day 7.

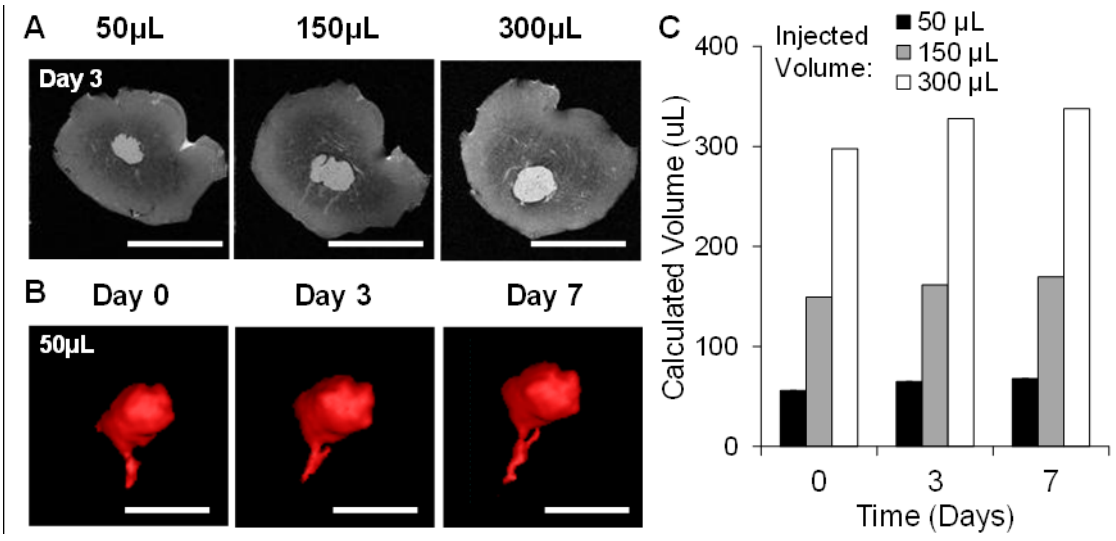

Figure 5.6. Visualization and quantification of guest-host HA hydrogel distribution in myocardial explants at 9.4 T. Representative cross-sections of T_2-weighted MRI of guest-host hydrogels at day 3 after injection into myocardial explants at different volumes, as indicated (A). Scale bars = 2 cm. Representative 3D reconstructions of the 50 µL guest-host hydrogel distribution volume at different time points following injection, as indicated (B). Scale bars = 1 cm. Quantification of volumes from reconstructions of each hydrogel imaged at different times after injection, *n=1* (C).

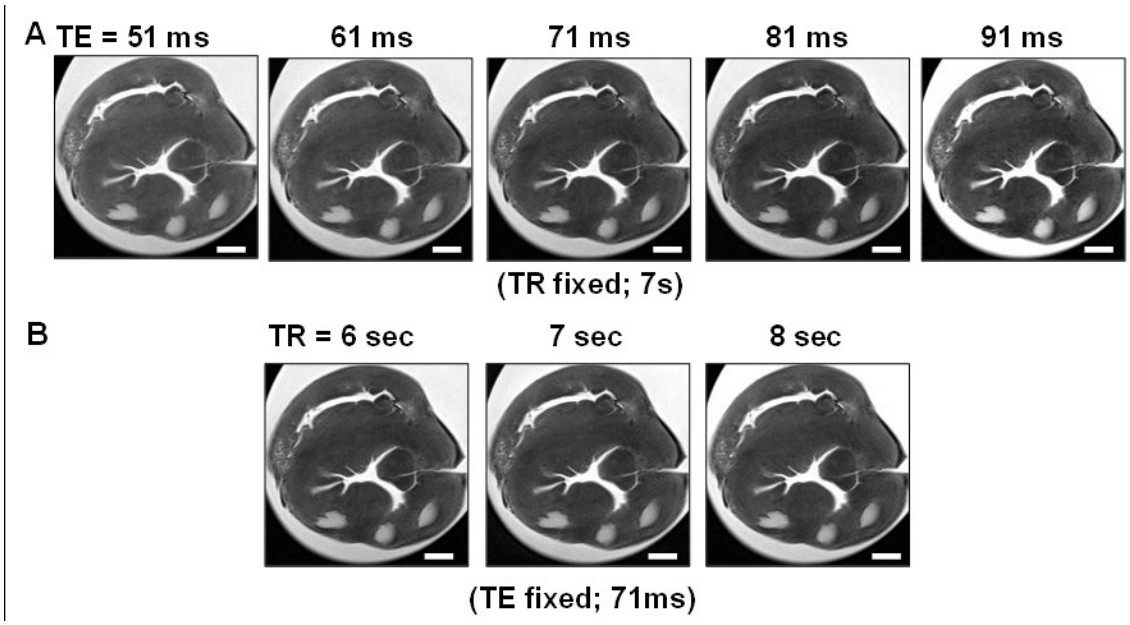

Figure 5.7. Optimization of MR parameters for imaging HA hydrogels in explants at 3 T. Representative short axis, T_2-weighted MRI slices of 300 µL guest-host hydrogel injections in an explanted porcine heart. To optimize the echo time (TE), images were acquired at various TE values but a constant repetition time (TR), as indicated (A). MR images were also acquired at various TR values but a constant TE, as indicated, to opmize the TR (B). Scale bars = 2 cm.

The imaging principles utilized at 9.4 T where then applied to clinical field strength of 3 T to assess guest-host hydrogel distribution. Prior to visualizing and quantifying hydrogel dispersion volumes in the myocardium, the imaging parameters were first optimized by making systematic changes in the TE and TR for a T_2-weighted spin echo pulse sequence. Similar to the parameter optimization scans at 9.4 T (**Figure 5.3A**), overall image signal intensity was altered with changes in TE at a constant TR (7 sec), where the intensity of the PBS surrounding the explants increased with increased TE (**Figure 5.7A**). Visual assessment of the differences in image contrast between the hydrogel and myocardium led to the selection of an intermediate TE of 71 ms for subsequent scans. In addition, minimal differences in signal intensity were observed when altering the TR at a constant TE (71 ms) (**Figure 5.7B**). Thus, to minimize scan times, a TR of 6 sec was selected for assessment of hydrogel distribution. Based on the voxel size optimization scans at 9.4 T above

(**Figure 5.3B**), the slice thickness was minimized as much as possible within the scanner limitations and considering the necessary field of view for the larger tissue size.

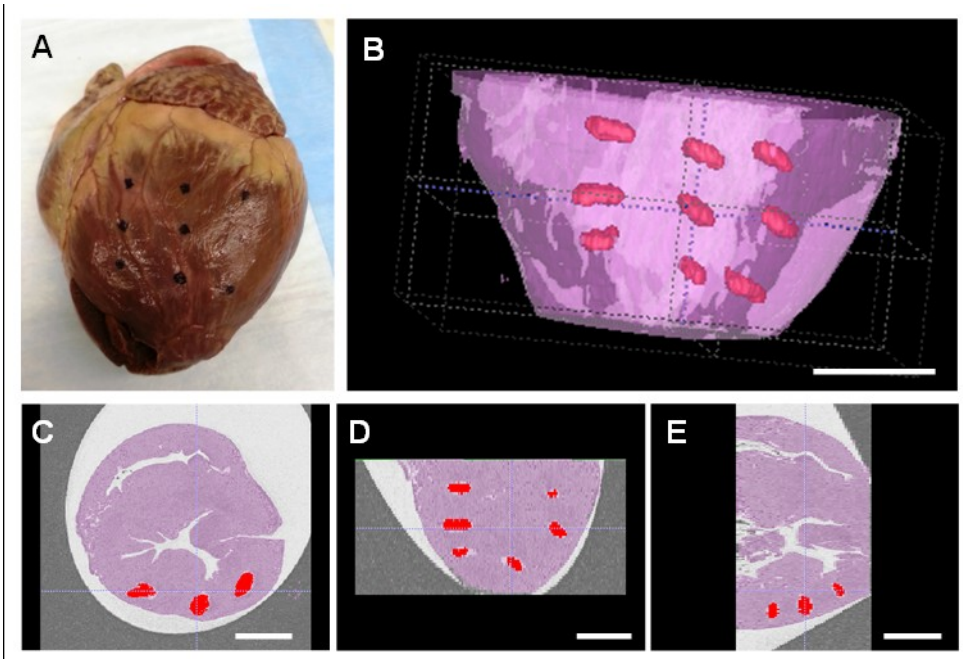

Figure 5.8. Examination of guest-host HA hydrogel distribution in whole heart explant at 3 T. Whole explanted porcine heart indicating array of 9 sites for 300 µL guest-host hydrogel injections (A). 3D reconstruction of distribution volume of 9 hydrogel injections in explant (B). Representative short axis cross-section of 3D reconstructed hydrogel volumes in the axial plane (C). Representative long axis slices in the coronal and sagittal planes of the reconstructed hydrogel injections (D, E). Average reconstructed volume = 316.4 (± 58.9) µL. Scale bars = 2 cm.

Using the optimized scan parameters, an array of nine guest-host hydrogel injections in a full heart explant (**Figure 5.8A**) was visualized using a 3T MR scanner. The pattern of nine injections was clearly observed in the 3D volume reconstruction (**Figure 5.8B**) and corresponding short- and long-axis cross-sections of the reconstruction (**Figure 5.8C,D,E**). Similar to the 9.4 T assessment of guest-host hydrogels in myocardial explants (**Figure 5.6**), each of the nine hydrogel injections formed a solid, spherical plug in the myocardial tissue that was distinct from

the other injections. The average reconstructed hydrogel distribution volume over the nine injection sites was calculated to be 316.4 (± 58.9) µL, which differed from the injected volume of 300 µL by approximately 5.5%. Thus, at both 9.4 T and 3T, the reconstructed distribution volumes of guest-host hydrogels in the myocardium were similar to those of the injected volume.

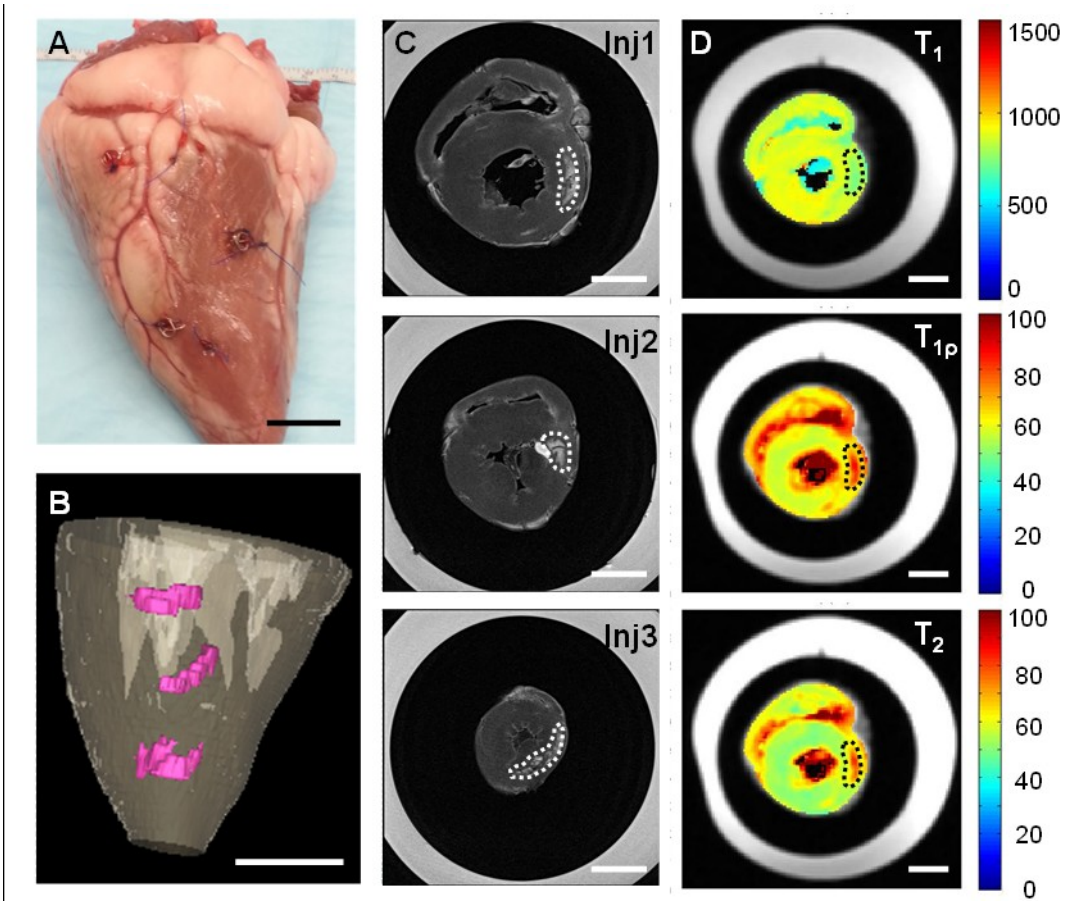

Figure 5.9. Assessment of HeMA-HA hydrogel distribution in myocardial explant from *in vivo* injections at 3 T. Explanted ovine heart indicating three sites used for *in vivo* HeMA-HA hydrogel injections (A). 3D reconstruction of distribution volume of three, 500 µL HeMA-HA injections performed *in vivo* but imaged *ex vivo* (B). Average reconstructed volume = 463.5 (± 66.2) µL. Representative short axis, cross-sectional T_2 weighted MRI slices of each HeMA-HA hydrogel injection (dashed lines) corresponding to 3D reconstruction (C). Representative slices of T_1, $T_{1\rho}$, and T_2 maps of the first HeMA-HA hydrogel injection (dashed lines) (D). Scale bars = 2 cm.

5.3.3. MRI Evaluation of HeMA-HA Hydrogel Distribution *Ex Vivo* from *In Vivo* Delivery

To further the translatability of using T_2-weighted MRI to visualize and quantify HA hydrogel distribution in the myocardium, HeMA-HA hydrogels were injected *in vivo* and evaluated *ex vivo* using a clinical 3 T MR scanner. Prior to *in vivo* delivery, the gelation properties of HeMA-HA hydrogel formulation selected for T_2-weighed MRI were characterized. Rheological assessment demonstrated that gelation onset occurred at 2.1 ± 0.5 min and gel completion occurred at 15.9 ± 2.9 min after mixing the dissolved macromer and chemical initiators. The gel onset time dictated the timing for *in vivo* injection. The three HeMA-HA injections performed *in vivo* were clearly visible in both the 3D volume reconstruction (**Figure 5.9B**) and corresponding T_2-weighted short-axis slices for each injection site (**Figure 5.9C**). The sites of the markers sutured to the epicardial surface immediately following injection (**Figure 5.9A**) correlated with the 3D locations of the hydrogels in the volume reconstruction (**Figure 5.9B**). Similar to the MeHA hydrogels, HeMA-HA hydrogel injections took on an ellipsoidal geometry, as seen in both the cross-sectional slices (**Figure 5.9C**) and 3D reconstruction (**Figure 5.9B**). The average reconstructed hydrogel distribution volume of the three injections was determined to be 463.5 (± 66.2) μL, which suggested greater than 90% retention from the injected volume of 500 μL. Relaxation time (i.e., T_1, $T_{1\rho}$, T_2) maps were then generated to visualize differences in relaxation between the hydrogel and myocardium, where each voxel is assigned to a relaxation time value (**Figure 5.9D**). The greatest differences in voxel intensity between the hydrogel and myocardium were seen in the $T_{1\rho}$ and T_2 maps.

5.4. Discussion

In this chapter, non-contrast based MRI was used to visualize and quantify HA hydrogel distribution in the myocardium based on intrinsic differences in the MR properties (i.e., T_2 relaxation) between the injected hydrogel and surrounding tissue. As discussed in Section 5.1, these differences can be manipulated to increase image contrast by altering both the RF pulse sequence as well as the imaging parameters (i.e., TE, TR, etc.). In this work, a spin-echo pulse

sequence was used for all scans to introduce a T_2 dependence to the acquired images and the scan parameters were optimized to generate T_2-weighted images through use of a long TR and relatively long TE. A long TR (i.e., on the order of several seconds) reduces T_1 contamination by allowing the excited protons to return to equilibrium (or near equilibrium) before subsequent RF pulse application.[21] A long TE (i.e., on the order of the tissue's TE) provides more time for the magnetization to decay before measuring the signal (i.e., FID echo)[21] so materials or tissues that have a longer T_2 will have less magnetization decay and thus, a higher signal. Based on these principles, T_2-maps of HA hydrogels injected *in vivo* but imaged *ex vivo* confirmed the differences in T_2 values between the hydrogel and myocardium, in that the hydrogel has a longer T_2 than the myocardium and thus, higher signal in T_2-weighted images (**Figure 5.9D**). Thus, T_2-weighted MRI was used to investigate differences in HA hydrogel dispersion in myocardial tissue based on changes in material properties (i.e., gelation).

To introduce differences in injectable HA hydrogel distribution volume in myocardial tissue, the materials properties were altered by either varying the time to gelation or the mechanism of gel formation. As such, MeHA hydrogel formulations were selected with different rates of gelation. To make the system injectable, macromers at different methacrylations were crosslinked into hydrogels using a redox initiation system of APS and TEMED. As anticipated from the previous characterization studies in Chapter 4, as the macromer modification or initiator concentration increased, crosslinks were formed at a quicker rate and gelation onset decreased (**Figure 5.2B**). These differences in gelation onset were used to introduce differences in the volume of hydrogel distribution in myocardial explants as assessed by MRI, as supported by previous work involving the visual inspection of HA hydrogels in myocardial tissue.[40]

Prior to assessing differences in hydrogel distribution between the four MeHA hydrogel formulations, a preliminary study was performed to better understand the portion of the injected precursor solution (i.e., crosslinked vs. uncrosslinked) would be visualized using the optimized imaging parameters (**Figure 5.4**). This study demonstrated that uncrosslinked macromer would

no longer be detectable after rinsing the tissue samples for three days following injection. Thus, since the imaging of the crosslinked formulations was performed at day 3 following injection, any uncrosslinked macromer diffused out of the tissue and only the crosslinked portion of each hydrogel was present for detection by 9.4 T MRI. As with the time to gelation, both the macromer modification and initiator concentration played a role in the hydrogel volume distribution in myocardial explants (**Figure 5.5**). Higher initiator concentration led to more rapid crosslinking, which resulted in larger volumes of crosslinked hydrogel, as assessed by MRI. In addition, higher macromer modification led to a larger distribution volume of crosslinked hydrogel. In both cases, the increased volumes could be attributed to an increased density of macromer reactive groups and radical initiators leading to more complete gelation and thus, measurability by MRI. Similarly, the smaller volumes observed with low macromer modification and initiator concentration formulations could be contributed to an increased susceptibility of the precursor solutions to be diluted by the fluids within the tissue, thus leading to inefficient gel formation and lower crosslinked hydrogel volumes. The injection of all formulations at 3 minutes after mixing the dissolved macromers and initiators may have resulted in too much time lapse until gelation for the low initiator formulations, leading to extensive dispersion of the precursor solution and limited proximity of the reactive groups to one another to form crosslinks. Tailoring the injection timing to the rheological properties may prevent this extensive dispersion, as seen in recent work.[32]

Differences in hydrogel formulation also led to differences in the distribution of the hydrogels within the myocardial fibers. More specifically, hydrogels crosslinked using the high initiator concentration exhibited more frequent “plugs” (i.e., areas of mostly hydrogel) than hydrogels formed with the low initiator concentration. Hydrogels with the low initiator concentration also dispersed more evenly within the fibers since the slower gelation times and lower precursor solution viscosity enabled uniform penetration of the tissue prior to crosslinking. Nevertheless, regardless of formulation, all MeHA hydrogels took on a similar ellipsoidal geometry that was oriented such that the major axis of the ellipsoid was in the same direction as the myocardial fibers. The ellipsoidal distribution of the MeHA injections combined with higher

volume quantifications than the injection volume (300 μL) demonstrated that these materials dispersed amongst the myocardial fibers during gelation and formed a composite with the surrounding myocardial tissue rather than only forming a plug that displaced the tissue.

To examine differences in injected hydrogel dispersion based on the mechanism of gel formation, an alternative hydrogel system was introduced based on guest-host chemistry. Unlike MeHA hydrogels which formed by covalent crosslinking over the span of a few minutes (i.e., 2-5 min, based on rheology; **Figure 5.2B**), guest-host HA hydrogels self-assembled near-instantaneously by reversible, physical interactions (**Figure 5.1**), as demonstrated by rheology in previous work.[33] This difference in hydrogel formation, in turn, led to differences in distribution in myocardial tissue. In contrast to the previous *in situ* gelling MeHA hydrogels which dispersed along the myocardial fibers forming a composite (**Figure 5.5**), guest-host hydrogels formed distinct, solid plugs within the myocardial tissue due to their instantaneous formation and stable interaction between the guest and host components (**Figure 5.6**). The volumes calculated from the 3D reconstructions of the guest-host hydrogel injections were similar to the injected volume, demonstrating retention of the hydrogels at the injection site independent of injection volume (50-300 μL examined; **Figure 5.6C**). Furthermore, guest-host hydrogels also remained stable over time with 3D reconstructions and corresponding volume quantifications demonstrating little change in volumes over one week (**Figure 5.6B,C**). The slight increases in the calculated volumes over time can be attributed to moderate hydrogel swelling since minimal changes in surfaces features were observed. Some spreading between the muscle fibers was observed in discrete small channels but not to the extent seen with MeHA hydrogels. To move towards clinically relevant imaging settings, guest-host hydrogels were then injected into a whole heart explant and imaged at 3 T. Despite the decrease in field strength from 9.4 T, guest-host HA hydrogels formed discrete plugs within the myocardium with calculated volumes comparable to the injected volume (**Figure 5.8**).

To demonstrate the translational applications of T_2-weighted MRI of injectable hydrogels, HA hydrogels were injected *in vivo* and imaged *ex vivo* at 3 T following animal sacrifice. A single HeMA-HA hydrogel formulation was selected from previous characterization studies (Section 4.3.2) for *in vivo* delivery. The macromer concentration was selected to be relatively high (8 wt%) to improve the T_2-based MRI contrast between the hydrogel and myocardium but without the precursor solution being too viscous to be injectable. The initiator concentrations (5 mM APS, 5 mM TEMED) were selected to balance the need for relatively rapid hydrogel formation (i.e., over the time span of a few minutes) with providing sufficient time for *in vivo* delivery. Despite delivery in an *in vivo* setting, each of the three injections was retained within the myocardium at the injection site (**Figure 5.9**). In both the short-axis cross-sections and corresponding 3D reconstruction, HeMA-HA hydrogels were elliptical in shape and oriented themselves to the curvature of the contractile LV tissue that is known to move in both a radial (i.e., inward or contractile) and circumferential (i.e., twisting) direction (**Figure 5.9B,C**).[41,42] The quantified dispersion volumes were similar but slightly less than the injection volume (500 μL), suggesting a lack of complete material retention following delivery into the contracting myocardium. However, based on surgeon's visual observation of ~75-80% material retention upon injection, the calculated volumes were higher than the retained volumes, indicating that the HeMA-HA hydrogels distributed along the myocardial fibers and formed a composite, similar to the MeHA hydrogels previously examined. Finally, relaxation maps (combined with the T_2-weighted pulse sequence utilized) confirmed that the differences in image contrast between the injected HA hydrogels and surrounding myocardium were due to differences in T_2 relaxation (**Figure 5.9D**).

5.5. Conclusions

In this chapter, T_2-weighted MRI was used to qualitatively and quantitatively assess differences in injectable HA hydrogel distribution in the myocardium. Differences in hydrogel dispersion in myocardial explants were introduced by changing the time to gelation and the gelation mechanism. Gelation onset was altered in stable MeHA hydrogels by varying both the

macromer modification and initiator concentration, which led to differences in the crosslinked portion of the hydrogel volume that was reconstructed from MRI. The ability of covalently crosslinked MeHA hydrogels to disperse through the myocardial fibers was then compared to the tissue distribution of physically crosslinked guest-host hydrogels, which formed discrete plugs in myocardial explants. Therefore, tuning of HA hydrogel material properties (i.e., gelation) can be used to tailor hydrogel distribution in tissue for an intended application. In the case of LV remodeling post-MI, previous modeling studies have shown that hydrogel dispersion correlates with resulting cardiac outcomes[3] and thus, the ability to noninvasively assess injectable material properties following delivery into tissue could ultimately provide insight into their *in vivo* function. The next chapter will address an alternative non-contrast MRI technique to visualizing injectable HA hydrogels based on differences in exchangeable protons rather than relaxation times.

5.6. References

1. Christman KL, Lee RJ. Biomaterials for the treatment of myocardial infarction. J Am Coll Cardiol 2006;48(5):907-913.

2. Wall ST, Walker JC, Healy KE, Ratcliffe MB, Guccione JM. Theoretical impact of the injection of material into the myocardium: A finite element model simulation. Circulation 2006;114(24):2627-2635.

3. Wenk JF, Wall ST, Peterson RC, Helgerson SL, Sabbah HN, Burger M, et al. A method for automatically optimizing medical devices for treating heart failure: Designing polymeric injection patterns. J Biomech Eng 2009;131(12):121011.

4. Wenk JF, Eslami P, Zhang Z, Xu C, Kuhl E, Gorman,Joseph H.,,III, et al. A novel method for quantifying the in-vivo mechanical effect of material injected into a myocardial infarction. Ann Thorac Surg 2011;92(3):935-941.

5. Kichula ET, Wang H, Dorsey SM, Szczesny SE, Elliott DM, Burdick JA, et al. Experimental and computational investigation of altered mechanical properties in myocardium after hydrogel injection. Ann Biomed Eng 2014;42(7):1546-1556.

6. Artzi N, Oliva N, Puron C, Shitreet S, Artzi S, Ramos AB, et al. In vivo and in vitro tracking of erosion in biodegradable materials using non-invasive fluorescence imaging. Nature Materials 2011;10(9):704-709.

7. MacArthur JW,Jr., Purcell BP, Shudo Y, Cohen JE, Fairman A, Trubelja A, et al. Sustained release of engineered stromal cell-derived factor 1-alpha from injectable hydrogels effectively recruits endothelial progenitor cells and preserves ventricular function after myocardial infarction. Circulation 2013;128(11):S79-S86.

8. Soranno DE, Lu HD, Weber HM, Rai R, Burdick JA. Immunotherapy with injectable hydrogels to treat obstructive nephropathy. Journal of Biomedical Materials Research Part a 2014;102(7):2173-2180.

9. Yuan Z, Zakhaleva J, Ren H, Liu J, Chen W, Pan Y. Noninvasive and high-resolution optical monitoring of healing of diabetic dermal excisional wounds implanted with biodegradable in situ gelable hydrogels. Tissue Engineering Part C-Methods 2010;16(2):237-247.

10. Kovar JL, Simpson MA, Schutz-Geschwender A, Olive DM. A systematic approach to the development agents for optical imaging of mouse of fluorescent contrast cancer models. Anal Biochem 2007;367(1):1-12.

11. Weissleder R, Ntziachristos V. Shedding light onto live molecular targets. Nat Med 2003;9(1):123-128.

12. Mottu F, Rufenacht DA, Doelker E. Radiopaque polymeric materials for medical applications - Current aspects of biomaterial research. Invest Radiol 1999;34(5):323-335.

13. Holloway JL, Ma H, Rai R, Burdick JA. Modulating hydrogel crosslink density and degradation to control bone morphogenetic protein delivery and in vivo bone formation. J Controlled Release 2014;191:63-70.

14. Vandeweghe S, Coelho PG, Vanhove C, Wennerberg A, Jimbo R. Utilizing micro-computed tomography to evaluate bone structure surrounding dental implants: A comparison with histomorphometry. J Biomed Mater Res Part B 2013;101(7):1259-1266.

15. Yang Y, Dorsey SM, Becker ML, Lin-Gibson S, Schumacher GE, Flaim GA, et al. X-ray imaging optimization of 3D tissue engineering scaffolds via combinatorial fabrication methods. Biomaterials 2008;29(12):1901-1911.

16. Blakely B, Lee BH, Riley C, McLemore R, Pathak CP, Vernon BL. Formulation and characterization of radio-opaque conjugated in situ gelling materials. Journal of Biomedical Materials Research Part B-Applied Biomaterials 2010;93B(1):9-17.

17. Yu SB, Watson AD. Metal-based x-ray contrast media. Chem Rev 1999;99(9):2353-2377.

18. Leon CM, Lee BH, Preul M, McLemore R, Vernon BL. Synthesis and characterization of radio-opaque thermosensitive poly[N-isopropylacrylamide-2,2 '-(ethylenedioxy)bis(ethylamine)-2,3,5-triiodobenzamide]. Polym Int 2009;58(8):847-850.

19. Brenner DJ, Hall EJ. Current concepts - Computed tomography - An increasing source of radiation exposure. N Engl J Med 2007;357(22):2277-2284.

20. Dixon JA, Spinale FG. Large animal models of heart failure: A critical link in the translation of basic science to clinical practice. Circ Heart Fail 2009;2(3):262-271.

21. Hornak JP. The Basics of MRI. Henietta, NY: Interactive Learning Software; 1996.

22. Wehrli FW. Magnetic resonance imaging. In: Byran RN, editor. Introduction to the Science of Medical Imaging. New York, NY: Cambridge University Press; 2010. p. 160.

23. McRobbie DW, Moore EA, Graves MJ, Prince MR. MRI: From Picture to Proton. Cambridge: Cambridge University Press; 2003.

24. Hillel AT, Unterman S, Nahas Z, Reid B, Coburn JM, Axelman J, et al. Photoactivated composite biomaterial for soft tissue restoration in rodents and in humans. Science Translational Medicine 2011;3(93):93ra67.

25. Stroman P, Dorvil J, Marois Y, Poddevin N, Guidoin R. In vivo time course studies of the tissue responses to resorbable polylactic acid implants by means of MRI. Magn Reson Med 1999;42(1):210-214.

26. Pihlajamaki H, Kinnunen J, Bostman O. In vivo monitoring of the degradation process of bioresorbable polymeric implants using magnetic resonance imaging. Biomaterials 1997;18(19):1311-1315.

27. Zhang Y, Sun Y, Yang X, Hilborn J, Heerschap A, Ossipov DA. Injectable in situ forming hybrid iron oxide-hyaluronic acid hydrogel for magnetic resonance imaging and drug delivery. Macromol Biosci 2014;14(9):1249-1259.

28. Karfeld-Sulzer LS, Waters EA, Kohlmeir EK, Kissler H, Zhang X, Kaufman DB, et al. Protein polymer MRI contrast agents: Longitudinal analysis of biomaterials in vivo. Magn Reson Med 2011;65(1):220-228.

29. van Zijl PCM, Yadav NN. Chemical Exchange Saturation Transfer (CEST): What is in a name and what isn't? Magn Reson Med 2011;65(4):927-948.

30. Burdick JA, Chung C, Jia X, Randolph MA, Langer R. Controlled degradation and mechanical behavior of photopolymerized hyaluronic acid networks. Biomacromolecules 2005;6(1):386-391.

31. Temenoff JS, Kasper FK, Mikos AG. Fumarate-based macromers as scaffolds for tissue engineering applications. In: Ashammakhi N, Reis R, Chiellini E, editors. Topics in Tissue Engineering. 3rd ed. Oulu, Finland: University of Oulu; 2007. p. 6.1-6.16.

32. Tous E, Ifkovits JL, Koomalsingh KJ, Shuto T, Soeda T, Kondo N, et al. Influence of injectable hyaluronic acid hydrogel degradation behavior on infarction-induced ventricular remodeling. Biomacromolecules 2011;12(11):4127-4135.

33. Rodell CB, Kaminski AL, Burdick JA. Rational design of network properties in guest-host assembled and shear-thinning hyaluronic acid hydrogels. Biomacromolecules 2013;14(11):4125-4134.

34. Yushkevich PA, Piven J, Hazlett HC, Smith RG, Ho S, Gee JC, et al. User-guided 3D active contour segmentation of anatomical structures: Significantly improved efficiency and reliability. Neuroimage 2006;31(3):1116-1128.

35. Sled J, Zijdenbos A, Evans A. A nonparametric method for automatic correction of intensity nonuniformity in MRI data. IEEE Trans Med Imaging 1998;17(1):87-97.

36. Tustison NJ, Avants BB, Cook PA, Zheng Y, Egan A, Yushkevich PA, et al. N4ITK: Improved N3 bias correction. IEEE Trans Med Imaging 2010;29(6):1310-1320.

37. Avants BB, Tustison NJ, Wu JC,P.A., Gee JC. An open source multivariate framework for n-tissue segmentation with evaluation on public data. Neuroinformatics 2011;9(4):381-400.

38. Vannier MW, Butterfield RL, Jordan D, Murphy WA, Levitt RG, Gado M. Multispectral analysis of magnetic-resonance images. Radiology 1985;154(1):221-224.

39. McGarvey JM, Kondo N, Witschey WRT, Takebe M, Aoki C, Burdick JA, et al. Injectable microsphere gel progressively improves global ventricular function, regional contractile strain, and mitral regurgitation after myocardial infarction. in review .

40. Ifkovits JL, Tous E, Minakawa M, Morita M, Robb JD, Koomalsingh KJ, et al. Injectable hydrogel properties influence infarct expansion and extent of postinfarction left ventricular remodeling in an ovine model. Proc Natl Acad Sci U S A 2010;107(25):11507-11512.

41. Pilla JJ, Koomalsingh KJ, McGarvey JM, Witschey WRT, Dougherty L, Gorman JH,3rd, et al. Regional myocardial three-dimensional principal strains during post-infarction left ventricular remodeling. in review .

42. Holmes JW, Borg TK, Covell JW. Structure and mechanics of healing myocardial infarcts. Annu Rev Biomed Eng 2005;7:223-253.

CHAPTER 6

Visualization of Injectable Hyaluronic Acid Hydrogels using Chemical Exchange Saturation Transfer MRI

(Adapted from: Dorsey SM, Haris M, Singh A, Witschey WRT, Rodell CB, Kogan F, Reddy R, Burdick JA. ACS Biomaterials, in review.)

6.1. Introduction

Injectable hydrogels are useful for many biomedical and pharmaceutical applications,[1-4] offering the potential for minimally invasive, site-specific delivery of materials, cells, and therapeutics directly into voids or tissues. Although numerous hydrogel systems have been developed, tools are still needed to assess and monitor the performance of hydrogels after injection. Conventional histological and immunohistochemical evaluation of injected hydrogels is time-consuming, destructive, and limited to cross-sectional slices that prevent accurate assessment of hydrogel features (e.g., distribution volume). Furthermore, to determine the optimal material design components (e.g., degradation, molecule release), noninvasive techniques to characterize hydrogels once implanted within tissues are needed.

To address this challenge, various imaging techniques can be used to noninvasively characterize hydrogels. Optical and x-ray imaging have been used for *in vivo* material visualization but optical imaging is restricted to superficial tissue locations[5-8] due to light intensity decay with increasing tissue depth[9,10] and x-ray imaging is limited by the need for high concentrations of contrast agents[11-13] which may produce toxicity or alter material properties.[12,14] As an alternative, magnetic resonance imaging (MRI) is well suited for *in vivo* material assessment at any depth due to its ability to provide accurate and reproducible images with high

spatial resolution in three dimensions.[15] MR image contrast is generated by differences in the response of bulk water protons in materials or tissues to oscillating magnetic fields; these MR properties (i.e., T_1/T_2 relaxation times, proton density) are intrinsic to the material or tissue of interest. In the case of biomaterials where the goal is to mimic native structures, their intrinsic MR properties are often similar to those of the surrounding tissue, limiting accurate imaging at clinically relevant magnetic field strengths. One approach is to incorporate exogenous contrast agents[16,17] into the biomaterial to generate or enhance the differences in relaxation properties and increase image contrast-to-noise ratio (CNR). However, due to inherent sensitivity limitations with MRI, high concentrations of contrast agent are needed, which may alter the injected biomaterials' properties, perturb the physiologic environment surrounding the injection site, or lead to toxicity.[18]

Chemical exchange saturation transfer (CEST) is a new MRI technique that generates contrast from protons in specific molecules or metabolites based on their exchange with bulk water protons (**Figure 6.1**).[18,19] Since MR signal is generated from magnetic field manipulations of bulk water protons, CEST is an indirect approach to image smaller pools of non-water protons based on their impact on the water proton signal. More specifically, CEST imaging involves saturating exchangeable protons, such as those in the material, using a frequency selective radiofrequency (RF) pulse. This pulse equalizes the number of protons aligned with and against the magnetic field, leading to zero net magnetization, which is termed "saturation" and the result of which is zero MR signal. The saturated protons then exchange with the bulk water protons and their zero (saturated) magnetization is thereby transferred to the bulk water protons, resulting in a proportionate decrease in the bulk water signal.[20] It is this decrease in the bulk water signal intensity that is detected in CEST imaging (**Figure 6.1**).

Manipulation of the CEST effect to enhance biomaterial image contrast is particularly appealing because it relies completely on the presence of exchangeable protons within the hydrogel. Unlike MRI with the use of exogenous contrast agents, CEST imaging does not perturb the intrinsic MR properties of native tissues and the image contrast generated by CEST can be

selectively turned on or off through gating the RF pulse.[21-23] In contrast to conventional T_1- and T_2-weighted MRI, since the frequency of the saturation pulse is selected to be the resonance frequency of the specific exchangeable proton group within the hydrogel, it enables the imaging technique to be highly specific for the biomaterial and thus easily distinguished from native tissues. Moreover, CEST imaging provides the opportunity for detection of different injectable biomaterials based on their specific functional groups by selectively saturating at the resonance frequency of the protons in the dominate functional group (**Figure 6.1**).

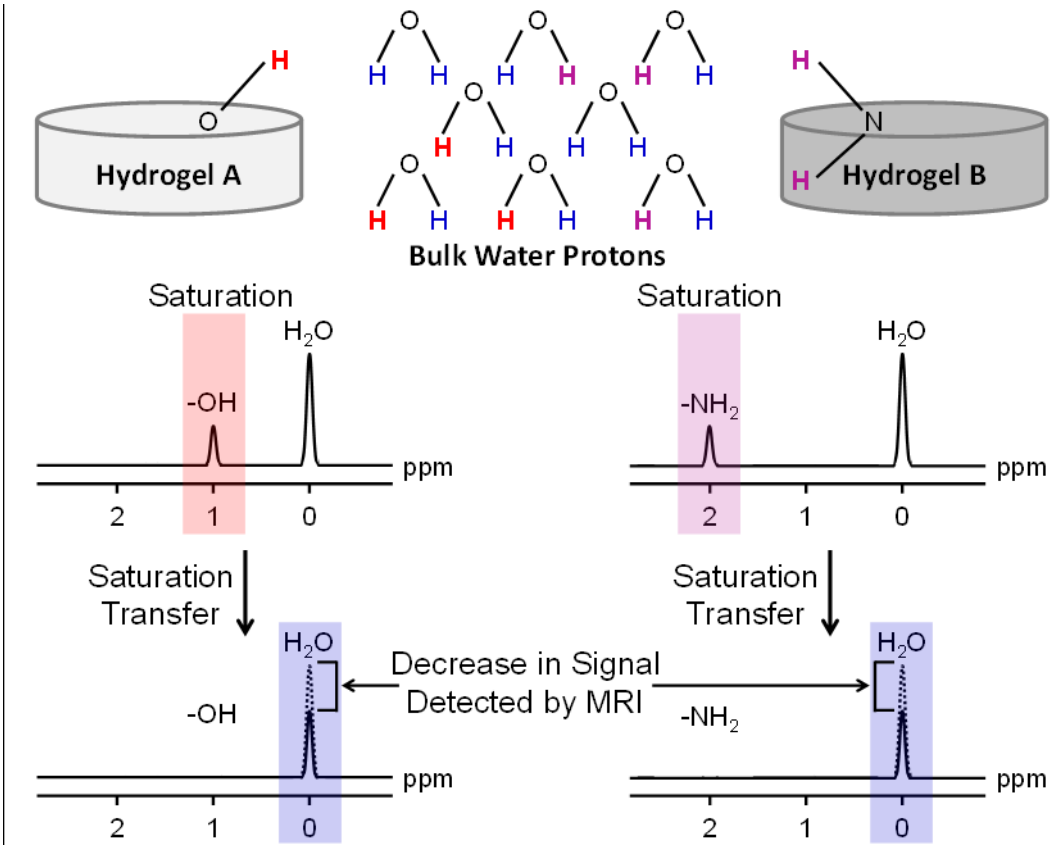

Figure 6.1. Principles of CEST for imaging hydrogels. CEST imaging can distinguish hydrogels based on their dominant exchangeable proton groups (e.g., -OH for Hydrogel A or $–NH_2$ for Hydrogel B). The exchangeable protons are saturated at their specific resonance frequency. The saturated magnetization is then transferred to the larger pool of bulk water protons, which causes a decrease in the bulk water signal that is detected as a decrease in the MRI signal.

One biomaterial of particular interest to CEST imaging is hyaluronic acid (HA). HA is a linear polysaccharide used for a variety of injectable hydrogel systems due to its native role as an extracellular matrix molecule and its ability to be modified with numerous functional groups.[24,25] The addition and amount of these groups enables hydrogel formation and tuning of both hydrogel (e.g., mechanics, degradation) and CEST properties. In addition, CEST MRI has been used *in vivo* to image endogenous glycosaminoglycans (GAGs), such as HA, through manipulation of both the amide (-NH-R) and hydroxyl (-OH) protons (**Figure 6.2**).[26] However, CEST has yet to be applied to imaging GAG-based biomaterials. In contrast to conventional GAG MRI, such as sodium (^{23}Na), $T_{1\rho}$-weighted, and delayed gadolinium-enhanced MRI, CEST MRI enables direct GAG mapping specifically and without contrast agent administration.[27] Therefore, towards the goal of developing a non-contrast MRI approach for visualizing injectable HA hydrogels *in vivo*, CEST MRI experiments were performed to characterize the CEST effect of hydroxyethyl methacrylate-modified HA (HeMA) hydrogels *in vitro* and *ex vivo* and demonstrate the clinical potential of this imaging technique for biomaterial assessment.

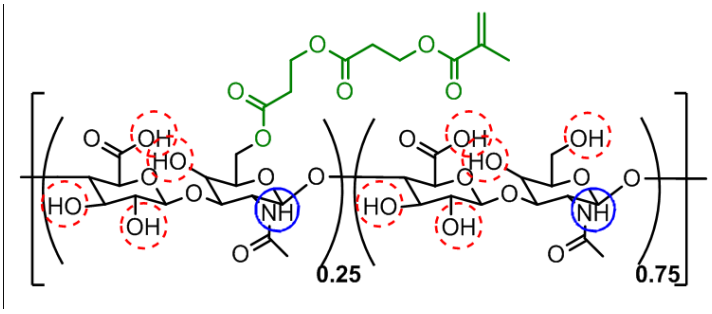

Figure 6.2. Chemical structure of HeMA-HA, indicating the exchangeable hydroxyl (dashes, red circles) and amide (solid, blue circles) protons targeted for CEST imaging.

6.2. Materials and Methods

6.2.1. HeMA-HA Macromer Synthesis

As previously described in Section 4.2.1, hydroxyethyl methacrylate-modified HA (HeMA-HA) was synthesized by coupling HA-tetrabutylammonium salt (HA-TBA) to HeMA succinate (HeMA-COOH) in dimethyl sulfoxide (DMSO) using 4-dimethylaminopyridine (DMAP, Sigma) and the coupling agent di-tert-butyl dicarbonate (BOC_2O, Sigma) (45°C, 20hrs).[28] The macromer was purified by dialyzing against deionized (DI) water at 4°C, precipitating in acetone, and dialyzing again. The macromer was then frozen and lyophilized. The extent of HA methacrylation was assessed with ^{1}H-NMR (Bruker, 360 MHz) and determined to be ~25% of the HA repeat units (**Figure 6.2**), as discussed in Section 4.2.1.

6.2.2. Peptide Coupling to HeMA-HA and Characterization

HeMA-HA was converted back to a TBA salt using an acidic ion exchange (25°C, 1hr) with Dowex resin (50W×8-200, Sigma), followed by neutralization with TBA hydroxide (TBA-OH, Sigma) to pH 7.02-7.05[29] to solubilize in DMSO. HeMA-HA-TBA was then dissolved in DMSO, reacted with N-(2-aminoethyl)maleimide trifluoroacetate salt (AEMa, Sigma) in the presence of benzotriazol-1-yloxytris(dimethylamino)-phosphonium hexafluorophosphate (BOP, Sigma) (25°C, 2hrs), dialyzed against DI water (4°C), filtered to remove insoluble byproducts, frozen, and lyophilized. Malemide functionalization of HeMA-HA was ~10% by ^{1}H-NMR (Bruker, 360 MHz). An arginine dominated (for enhanced CEST contrast[30,31]) peptide GCRRR (MW 646.35 Da) with >95% purity (per manufacturer HPLC analysis) was purchased from GenScript (Piscataway, NJ, USA) and coupled to Ma-HeMA-HA through a thiol–maleimide click reaction (1.2:1 molar ratio of cysteine:maleimide) in DI water (4°C, 4hrs).[32] The macromer was purified by dialysis against DI water (4°C), frozen, and lyophilized. ^{1}H-NMR (Bruker, 360 MHz) confirmed the complete consumption of malemide with peptide, resulting in a ~10% peptide modification of HeMA-HA.

High-resolution spectroscopy was performed on solutions of HeMA-HA (8 wt%), HeMA-HA-Peptide (8 wt%; 17.5-18.5 mM Peptide), and Peptide alone (18 mM). Solutions were prepared in double distilled water (Millipore) or 99.8% D_2O (Acros) and the pH was adjusted to 7.0±0.1 using 1 N HCl/NaOH. Solutions were transferred to 5-mm NMR tubes. A capillary containing a mixture of D_2O and tetramethylsilane (TMS) was inserted for signal locking of H_2O samples during scans and standardization of chemical shifts during post-processing, respectively. Non–water-suppressed high-resolution ^{1}H-NMR spectroscopy (Bruker, 400 MHz) was performed using a single pulse-acquire sequence (TR, 8.84 sec; number of averages, 32) with a 5-mm radiofrequency probe at room temperature (295±0.1 K). Water suppression was not used because it would mask the bulk water signal and prevent observation of exchange with the exchangeable protons via changes in spectra peaks. The temperature was varied (280±0.1 K and 295±0.1 K) for the HeMA-HA-Peptide sample to examine temperature-induced changes in the exchangeable proton peak. ^{1}H-NMR spectra were obtained from the raw free induction decay data by Fourier transformation, phase correction, and baseline removal.

6.2.3. Hydrogel Formation and Characterization

As previous described (Section 4.2.3), HA hydrogels were formed using a radical initiator system of ammonium persulfate (APS, 5mM, Sigma) and N,N,N,N',N'-tetramethylenediamine (TEMED, 5 mM, Sigma). Hydrogel formation was assessed by monitoring the storage (G') and loss (G") moduli at 37°C using an AR2000ex Rheometer (TA Instruments) at 1% strain and 1 Hz frequency in a cone-plate geometry (1°, 20 mm diameter).

6.2.4. CEST Imaging Principles

CEST images were acquired with a specially optimized saturation pulse sequence, as previously described.[33-35] CEST effects were assessed using a z-spectrum, which is generated by sweeping the frequency of saturation pulse across the proton spectrum[18,20,36] and plotting the resulting water signal amplitude as a function of the saturation pulse frequency. Z-spectral data

was collected by acquiring images from –5.0 ppm to +5.0 ppm around the bulk water resonance (0 ppm) with a 0.1 ppm or 0.2 ppm shift in offset frequency per step. The degree of asymmetry in the z-spectra was assessed using asymmetry ($CEST_{asym}$) plots, which represent the normalized difference in magnetization between the exchangeable proton resonance frequency $S(+\Delta\omega)$ and the corresponding reference frequency on the opposite and symmetrical side of the water resonance $S(-\Delta\omega)$. One approach is to normalize to the bulk water signal (S_0) after saturation at a large frequency offset (i.e., +20 ppm or +100 ppm), where $\Delta\omega$ is the frequency difference relative to water (**Equation 6.1**[26,37]):

$$CEST_{asym}\ (\Delta\omega) = \frac{S(-\Delta\omega) - S(+\Delta\omega)}{S_0} \qquad (6.1)$$

However, saturation pulses are not perfectly frequency selective and may lead to saturation of protons at nearby frequencies.[19] The smaller the $\Delta\omega$, the greater chance for direct saturation of water protons, causing a decrease in the water signal due to pulse application and not exchange. To account for the effect of partial direct water saturation, the CEST effect can be normalized to $S(-\Delta\omega)$ (**Equation 6.2**[26,37]):

$$CEST_{asym}\ (\Delta\omega) = \frac{S(-\Delta\omega) - S(+\Delta\omega)}{S(-\Delta\omega)} \qquad (6.2)$$

As with all CEST methods, B_0 and B_1 field inhomogeneities may be of concern.[19,26] Localized B_0 shimming was manually performed using the Siemens MR scanners' product interactive shim program to ensure that B_0 inhomogeneity was less than ±0.3 ppm. To further correct for field inhomogeneities, water saturation shift reference (WASSR) images and B_1 maps were collected, as previously described,[35,38,39] for use in image post-processing. WASSR images were acquired from –0.6 ppm to +0.6 ppm with a step size of 0.05 ppm using a B_1 saturation pulse amplitude of 20 or 30 Hz and duration of 200 ms and with the same sequence and readout parameters as the corresponding CEST scans.

Table 6.1. MRI scan parameters optimized for each study.

Figure	Imaging Parameters	B_1 Amplitude and Duration
6.4	Slice thickness = 10 mm, GRE flip angle = 10°, readout TR = 6.2 ms, TE = 3.0 ms, 1 average, field of view = 100 × 100 mm^2, matrix size = 128 × 128, 1 saturation pulse train every 10 sec	200 Hz, 4 sec
6.5	Slice thickness = 5 mm, GRE flip angle = 10°, readout TR = 7.3 ms, TE = 3.6 ms, 1 average, field of view = 100 × 100 mm^2, matrix size = 128 × 128, 1 saturation pulse train every 10 sec	400 Hz, 300 ms
6.6	Slice thickness = 5 mm, GRE flip angle = 10°, readout TR = 7.3 ms, TE = 3.6 ms, 1 average, field of view = 100 × 100 mm^2, matrix size = 128 × 128, 1 saturation pulse train every 10 sec	Varied
6.7	Slice thickness = 5 mm, GRE flip angle = 10°, readout TR = 6.9 ms, TE = 3.4 ms, 1 average, field of view = 110 × 110 mm^2, matrix size = 192 × 192, 1 saturation pulse train every 10 sec	400 Hz, 300 ms
6.8A	Slice thickness = 5 mm, GRE flip angle = 10°, readout TR = 6.9 ms, TE = 3.4 ms, 1 average, field of view = 110 × 110 mm^2, matrix size = 192 × 192, 1 saturation pulse train every 10 sec	300 Hz, 300 ms
6.8B	Slice thickness = 5 mm, GRE flip angle = 10°, readout TR = 6.2 ms, TE = 3.0 ms, 1 average, field of view = 100 × 100 mm^2, matrix size = 128 × 128, 1 saturation pulse train every 10 sec	300 Hz, 300 ms
6.9, 6.10	Slice thickness = 5 mm, GRE flip angle = 10°, readout TR = 6.2 ms, TE = 3.0 ms, 1 average, field of view = 100 × 100 mm^2, matrix size = 128 × 128, 1 saturation pulse train every 10 sec	Varied
6.11	Slice thickness = 5 mm, GRE flip angle = 10°, readout TR = 6.2 ms, TE = 3.0 ms, 1 average, field of view = 100 × 100 mm^2, matrix size = 128 × 128, 1 saturation pulse train every 10 sec	300 Hz, 300 ms
6.12A	Slice thickness = 5 mm, GRE flip angle = 10°, readout TR = 6.6 ms, TE = 3.2 ms, 1 average, field of view = 122 × 122 mm^2, matrix size = 192 × 192, 1 saturation pulse train every 10 sec	300 Hz, 300 ms
6.12B	Slice thickness = 5 mm, GRE flip angle = 10°, readout TR = 5.6 ms, TE = 2.7 ms, 1 average, field of view = 140 × 140 mm^2, matrix size = 128 × 128, 1 saturation pulse train every 10 sec	300 Hz, 300 ms
6.13	Slice thickness = 3 mm, GRE flip angle = 10°, readout TR = 6.2 ms, TE = 3.0 ms, 8 averages, field of view = 96 × 96 mm^2, matrix size = 128 × 128, 1 saturation pulse train every 4 sec	200 Hz, 250 ms
6.14	Slice thickness = 3 mm, GRE flip angle = 10°, readout TR = 6.2 ms, TE = 3.0 ms, 8 averages, field of view = 96 × 96 mm^2, matrix size = 128 × 128, 1 saturation pulse train every 4 sec	200 Hz, 250 ms
6.17	Slice thickness = 5 mm, GRE flip angle = 10°, readout TR = 6.9 ms, TE = 3.4 ms, 1 average, field of view = 110 × 110 mm^2, matrix size = 192 × 192, 1 saturation pulse train every 10 sec	400 Hz, 300 ms
6.18	Slice thickness = 5 mm, GRE flip angle = 10°, readout TR = 6.9 ms, TE = 3.4 ms, 1 average, field of view = 110 × 110 mm^2, matrix size = 192 × 192, 1 saturation pulse train every 10 sec	400 Hz, 300 ms

6.2.5. MR Imaging of Phantoms at 3 T and 7 T

Macromer was dissolved at different concentrations in sterile PBS (Life Technologies) and the pH of the prepolymer solution was adjusted using 1 N HCl/NaOH (Fisher) to ensure a final pH of 7.0 upon hydrogel formation. The dissolved macromer was mixed with chemical initiators (5 mM APS, 5 mM TEMED) to induce hydrogel formation. Samples of prepolymer solution were added to 10-mm NMR tubes and immersed in a PBS phantom surrounded by a custom designed Styrofoam chamber to maintain the temperature at 37±1°C. To measure the pH dependence of CEST, hydrogels were formed at a single concentration of 8 wt% while varying final pH values within a physiologic range (6.0, 7.0, 7.5). To assess the effect of temperature on the CEST contrast, hydrogels of varying concentration (2, 4, 6, 8 wt%) were also scanned at 25°C as a comparison to 37°C. Phantoms of PBS at pH 7.0 were used for background normalization.

Phantom CEST imaging was performed on 7 T and 3 T whole body scanners (Siemens Medical Solutions, Erlangen Germany) with 32-channel and 8-channel ^{1}H head coils (Nova Medical, Wilmington, MA), respectively. The imaging parameters were optimized based on the magnetic field strength, coil, sample size, and required field of view (**Table 6.1**). The readout repetition time (TR) and echo time (TE) were minimized for each scan, but varied with changes in the field of view or image matrix size. For all phantom studies, the total repetition time was set to 10 sec, meaning one saturation pulse train was initiated every 10 seconds. CEST images were acquired at varying saturation pulse (B_1) amplitudes and durations to empirically optimize the CEST saturation parameters: i) 200 Hz, 250 Hz, 300 Hz, 350 Hz, 400 Hz at 300 ms saturation duration for 7 T, ii) 100 Hz, 200 Hz, 300 Hz, 400 Hz, 500 Hz at 300 ms saturation duration for 3 T, and iii) 300 Hz for 75 ms, 150 ms, 225 ms, 300 ms, 375 ms saturation duration at 3 T.

6.2.6. MR Imaging of *Ex Vivo* Tissue at 3 T

Normal lamb and swine left ventricular (LV) myocardial samples were obtained from a local distributor (<24 hrs post mortem) and maintained in PBS until imaging. *Ex vivo* samples

were prepared by mixing the macromer and initiators (5 mM APS, 5 mM TEMED) and injecting 0.3 mL of the prepolymer solution after 2 minutes (based on rheology, as discussed in Section 4.2.3) into the LV of the explants. After waiting 30 minutes to provide sufficient time for gelation, transmural sections of the injection site were isolated. Samples were placed into test tubes (30 mm diameter) and immersed in Fomblin Y (Sigma) to fill the void spaces and reduce susceptibility artifacts. The test tube was submerged in a larger phantom filled with PBS to aid in shimming for B_0 homogeneity. CEST images were acquired using a 3 T Tim Magnetom Trio Scanner (Siemens Medical Solutions; Malvern, PA) with an 8-channel knee coil or 8-channel ^{1}H head coil (Nova Medical; Wilmington, MA). *Ex vivo* scans were performed at 25°C to avoid potential tissue degradation at 37°C and due to minimal temperature differences observed in phantoms. Scan parameters were optimized based on the coil, sample size, and required field of view (**Table 6.1**). For all explant studies, the total repetition time was set to 4 seconds to minimize overall scan time towards the goal of using the same imaging parameters for *ex vivo* and future *in vivo* scans.

Localization of CEST contrast to the site of hydrogel injection in cardiac explants was confirmed by traditional T_1-, $T_{1\rho}$- and T_2-weighted MR imaging. A spin-echo-prepared FLASH sequence with scan parameters identical to the corresponding CEST images was utilized to generate T_1, $T_{1\rho}$ and T_2 maps. For T_1 maps, the inversion time (TI) was varied as follows: 50, 100, 300, 500, 700, 1000, 1300, 1600, and 2000 ms. $T_{1\rho}$ and T_2 maps were generated from scans with the following spin-lock (TSL) and echo (TE) times, respectively: 0, 20, 40, 60, 80, and 100 ms. A spin-lock pulse amplitude of 500 Hz was used for $T_{1\rho}$ image acquisition.

6.2.7. Processing CEST MRI Data

All image processing and data analysis was performed using a custom MATLAB (Natick, MA) code. B_0 and B_1 maps were generated to correct for magnetic field inhomogeneity by estimating the local field variations to center and scale all CEST data on a voxel-by-voxel basis, as previously described.[27,35,38,39] Z-spectra were generated by plotting the signal intensity from bulk water as a function of the saturation frequency with respect to water resonance. Asymmetry

curves were generated from the z-spectral data according to **Equation 6.2** above by plotting the relative water signal difference normalized to $S(-\Delta\omega)$ at frequency offsets of 0 to 4.8 ppm.

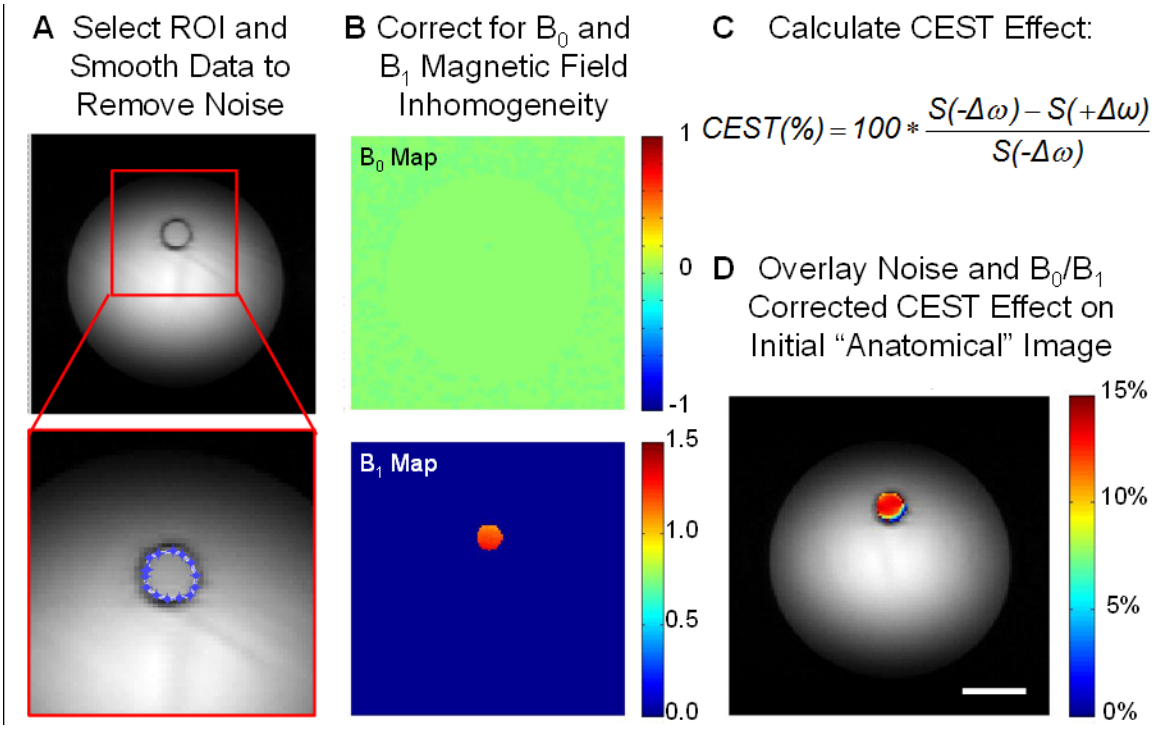

Figure 6.3. Processing of CEST data. A region of interest (ROI) was first isolated to adjust for noise (A). B_0 and B_1 maps were then used to correct for magnetic field inhomogeneity (B). CEST contrast was then calculated using the equation shown (C). Finally, the corrected CEST contrast was overlaid on the initial anatomical image (D). Scale bar = 2 cm.

To generate CEST maps, background noise was first removed by applying a signal intensity threshold, generating a mask to isolate the initial region of interest (i.e., phantom or tissue), and applying an averaging kernel to minimize spatial noise artifacts in the masked region (**Figure 6.3A**). B_0 inhomogeneity was accounted for using a combination of B_0 map and multiple CEST data acquired in the neighborhood of ±0.4 ppm off the target chemical shift.[33-35] For this B_0 correction, CEST images were analyzed from +0.6 to +1.4 ppm and +1.4 to +2.2 ppm for hydroxyl and amine proton exchange, respectively, with a step size of 0.1 ppm for phantoms and 0.2 ppm

for explants. Each voxel in the ±1.0 ppm image or ±1.8 ppm image was then replaced by the neighborhood of CEST data fit to a linear curve (**Figure 6.3B**).[35] CEST contrast was then calculated by further segmenting the region of interest (i.e., hydrogel), measuring the mean signal intensity, and inputting the intensities into **Equation 6.1** or **6.2** above, where $S(-\Delta\omega)$ and $S(+\Delta\omega)$ are the B_0 corrected signals from saturating at –1.0 ppm and +1.0 ppm or –1.8 ppm and +1.8 ppm for hydroxyl and amine proton exchange, respectively. CEST maps were then normalized to $S(-\Delta\omega)$ for phantoms or S_0 for explants (**Figure 6.3C**). Finally, maps were further corrected for B_1 inhomogeneity, as discussed above, and the effect overlaid on the initial image (**Figure 6.3D**).

6.2.8. Statistical Analysis

All data is presented as mean ± standard deviation (SD). Standard deviations were generated from variations in pixel intensity within the region of interest (i.e., hydrogel).

6.3. Results

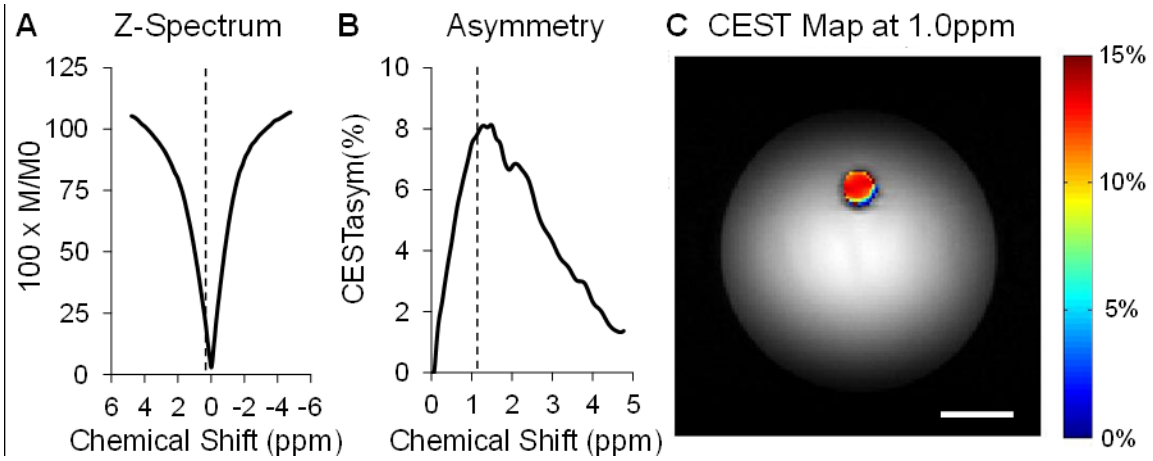

Figure 6.4. HeMA-HA as a CEST imaging agent. Z-spectrum (A) and asymmetry plot (B) of HeMA-HA hydrogel (1 wt%) at 7 T. Vertical dashed line on (B) indicates the chemical shift of the dominate exchangeable proton group (-OH). CEST map of phantom from saturation at 1.0 ppm (C). B_1 pulse parameters were an amplitude of 200 Hz and duration of 4 sec. Scale bar = 2 cm.

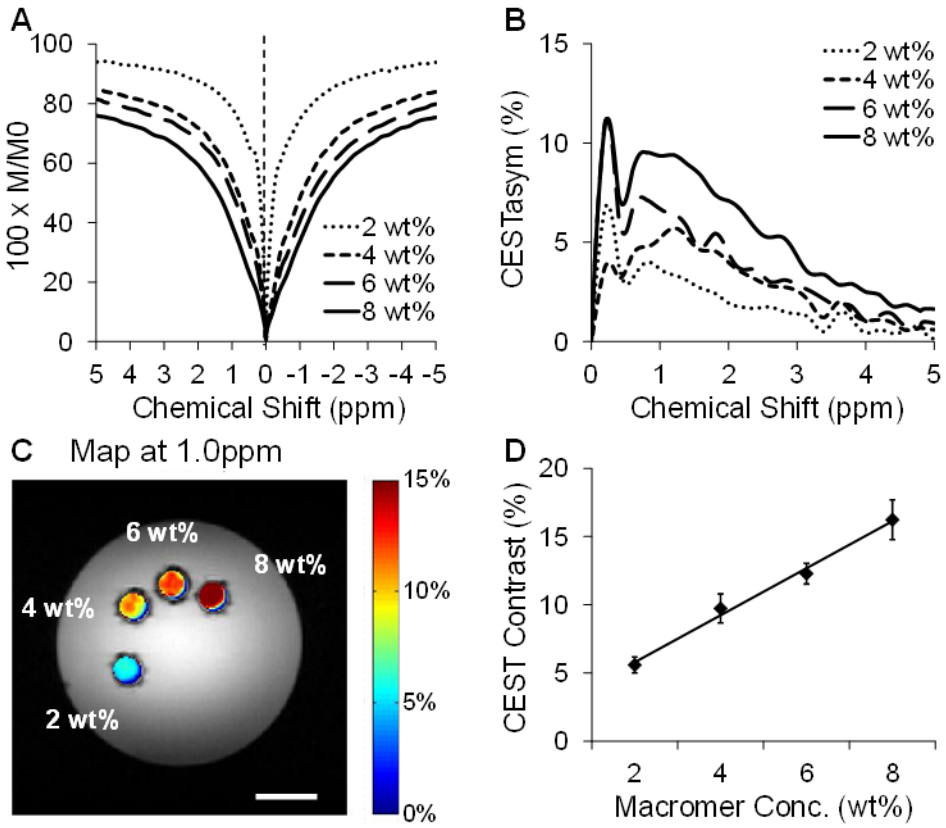

Figure 6.5. Characterization of the CEST effect of HeMA-HA hydrogels. Z-spectrum (A) and asymmetry plot (B) of HeMA-HA hydrogels at varying macromer concentrations at 7 T and 37°C. CEST map (C) and CEST effect quantification (D) of phantom from saturation at 1.0 ppm. A B_1 pulse of 400 Hz for 300 ms was used. Data presented as mean ± SD. Scale bar = 2 cm.

6.3.1. Characterization of CEST Effect of Hydrogel Phantoms

Initial CEST studies were performed using a 7 T MR scanner with a single HeMA-HA hydrogel formulation: 25% methacrylation at 1 wt% in PBS, gelled using 5 mM APS and 5 mM TEMED. The hydrogel phantom was scanned at 37°C using a long B_1 pulse duration of 4 sec (to generate the maximum CEST contrast) and a pulse amplitude of 200 Hz. The z-spectrum was symmetric around the bulk water resonance at 0 ppm (**Figure 6.4A**) while asymmetry analysis revealed a peak around 1 ppm (**Figure 6.4B**). The peak in the asymmetry plot indicated that the

chemical shift of the dominant exchangeable proton group was 1 ppm downfield from the bulk water signal. Unless specified, all frequency offsets in this work are reported with respect to the water proton resonance frequency at 0 ppm. Saturation of the protons at 1.0 ppm generated a CEST effect of 11.57±2.71%, as demonstrated in the CEST map (**Figure 6.4C**).

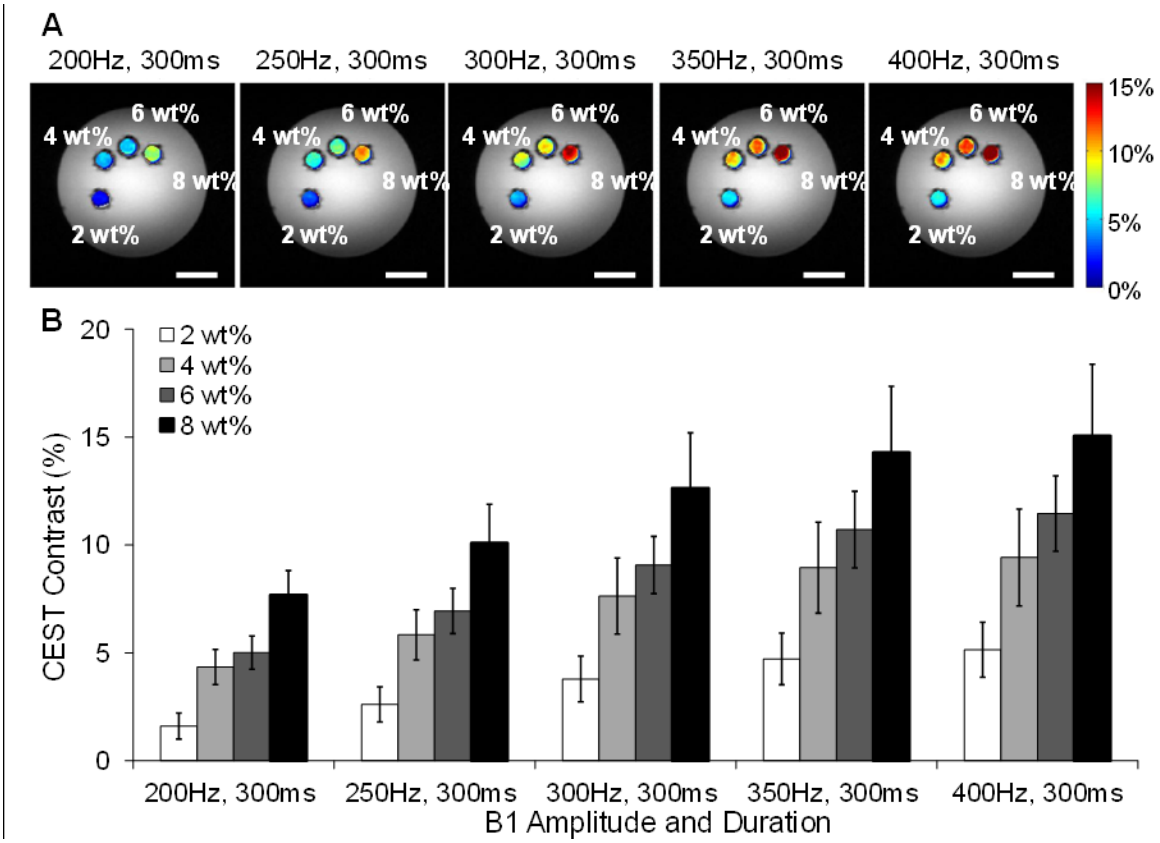

Figure 6.6. Saturation pulse dependence of CEST effect at 7T. CEST maps (A) and corresponding quantification (B) of HeMA-HA hydrogel phantoms at varying macromer concentrations from saturation at 1.0 ppm with varied B1 pulse amplitudes but a constant duration of 300 ms. Scans performed at 37°C. Data presented as mean ± SD. Scale bars = 2 cm.

Characterization studies were performed to assess the effect of altering hydrogel macromer concentration on the CEST contrast. As the macromer concentration increased, the z-spectra became increasingly broader (**Figure 6.5A**), which may have resulted from increased

steric locking of protons with increased hydrogel stiffness. This trend was also reflected in the asymmetry plots where increased z-spectral broadening led to higher peak heights (**Figure 6.5B**). Regardless of the macromer concentration, the asymmetry plots had a peak at ~1 ppm to indicate the chemical shift for saturation. CEST maps (**Figure 6.5C**) and contrast quantification (**Figure 6.5D**) from saturation at 1.0 ppm demonstrated an increase CEST contrast with increasing macromer concentration. A B_1 of 400 Hz for 300 ms was selected for this study and all subsequent phantom studies at 7 T based on optimization studies where the pulse amplitude was varied at a constant duration (**Figure 6.6**). The saturation duration was decreased from 4 sec to 300 ms to decrease specific absorption rate (SAR) concerns at 7 T and to enable comparison to scans performed using lower field strengths (i.e., 3 T), where hardware limitations arise for longer pulse durations. Of the amplitudes examined, 400 Hz generated the highest CEST effect.

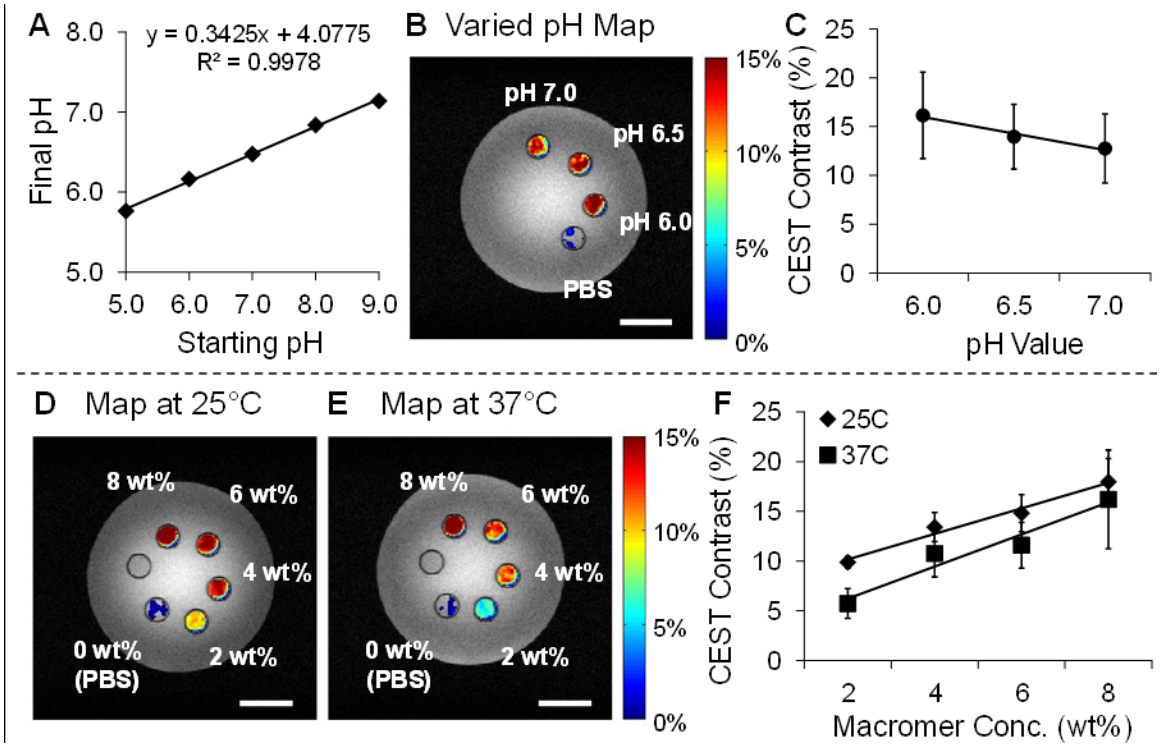

Figure 6.7. Effect of hydrogel pH and temperature on the CEST effect at 7T. *In vitro* study assessing the effect of gelation on final hydrogel pH (A). CEST map at 1.0 ppm of HeMA-HA hydrogels at a single macromer concentration (8 wt%) and uniform temperature (37°C) but

varying pH (B). Quantification of the effect of hydrogel pH on the CEST effect at 7T (C). CEST maps at 1.0 ppm of HeMA-HA hydrogels at varying concentration but uniform pH (7.0) at 25°C (D) and 37°C (E). Quantification of the effect of temperature on the CEST contrast (F). Protons saturated using a B_1 of 400 Hz for 300 ms. Data presented as mean ± SD. Scale bars = 2 cm.

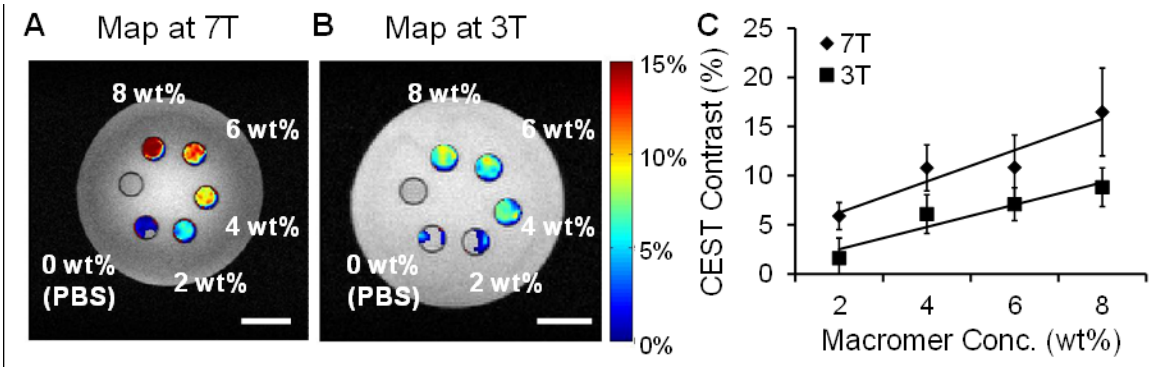

Figure 6.8. CEST effect of HeMA-HA hydrogel phantoms at varying field strengths. CEST maps at 1.0 ppm of hydrogels at varying concentration at 37°C using a magnetic field strength of 7T (A) or 3T (B). Quantification of the CEST effect at different field strengths (C). Protons saturated using a B_1 pulse of 300 Hz for 300 ms. Data presented as mean ± SD. Scale bars = 2 cm.

The impact of pH and temperature on CEST contrast was then assessed at 7 T. Prior to the CEST imaging study, the impact of hydrogel formation on pH was investigated due to the acidic and basic pH of the APS and TEMED used for crosslinking, respectively. To do so, the pH of the macromer dissolved in PBS was varied and the final pH of the resulting hydrogel was measured (**Figure 6.7A**). The line of best fit was used to determine the starting pH of the precursor solution needed to generate a hydrogel at a desired final pH. Hydrogels could be formed within the final pH range of ~5.75 to 7.25. CEST maps at 1.0 ppm of HeMA-HA hydrogels formed at varying final pH within that range (**Figure 6.7B**) and the corresponding quantification (**Figure 6.7C**) demonstrated that as hydrogel pH increased, the CEST effect decreased linearly. Similarly, CEST maps at 1.0 ppm of hydrogels at different temperatures (**Figure 6.7D,E**) and the quantification (**Figure 6.7F**) showed that as temperature increased, the CEST effect decreased.

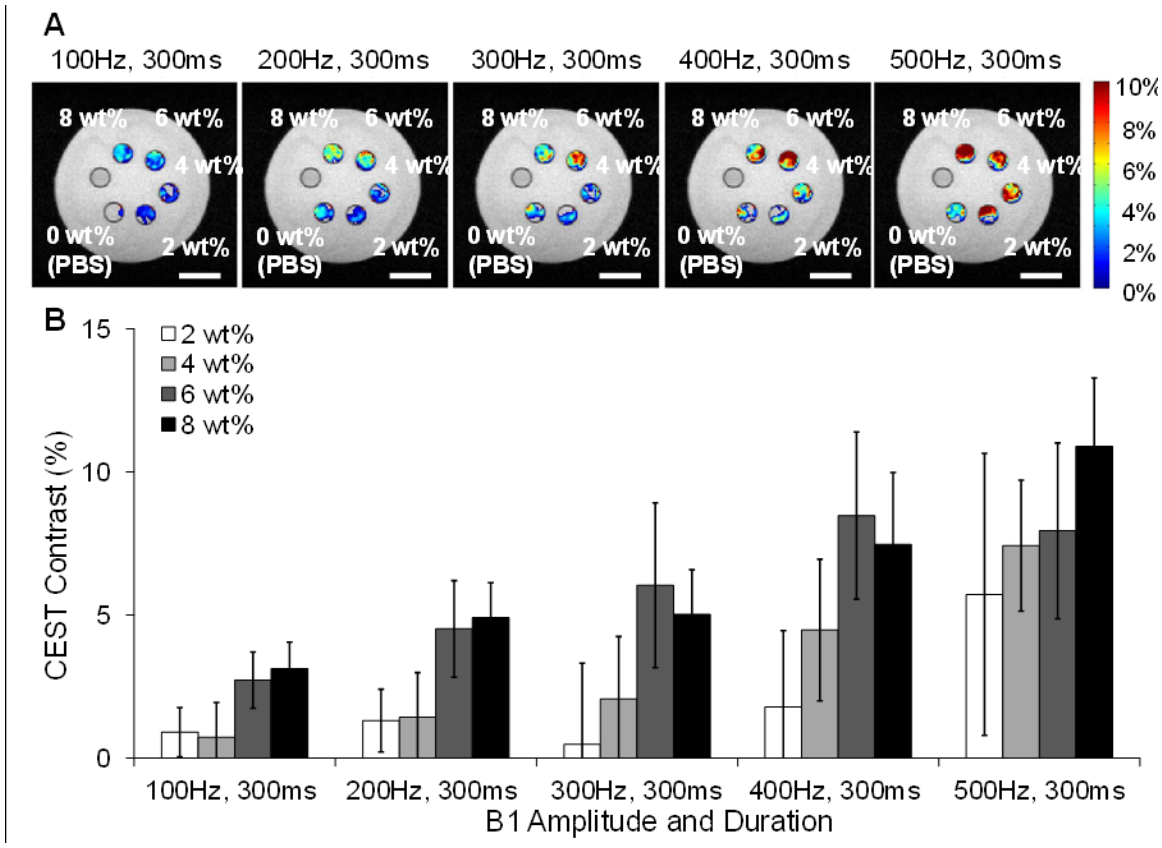

Figure 6.9. Saturation pulse amplitude dependence of CEST effect at 3T. CEST maps (A) and corresponding quantification (B) of HeMA-HA hydrogels at varying macromer concentrations from saturation at 1.0 ppm with varied B1 pulse amplitudes but a constant duration of 300 ms. Scans performed at 37°C. Data presented as mean ± SD. Scale bars = 2 cm.

To move towards clinically relevant scan parameters, the CEST effect of HeMA-HA hydrogels was assessed using at 3 T. CEST maps at 1.0 ppm (**Figure 6.8A,B**) and contrast quantification (**Figure 6.8C**) showed that as the field strength decreased, the CEST effect at each macromer concentration decreased. However, the trend of increased CEST contrast with increased macromer concentration was maintained regardless of field strength. To directly compare the results between the two fields, a B_1 pulse of 300 Hz and 300 ms was used for both the 7 T and 3 T scans. The pulse parameters were selected based on optimization studies at 3 T (**Figures 6.9 and 6.10**). A B_1 of 300 Hz for 300 ms was used for all subsequent 3 T phantom

studies. In addition, pH and temperature characterization studies were performed to confirm that as pH or temperature increased, the CEST effect also decreased at 3 T (**Figure 6.11**).

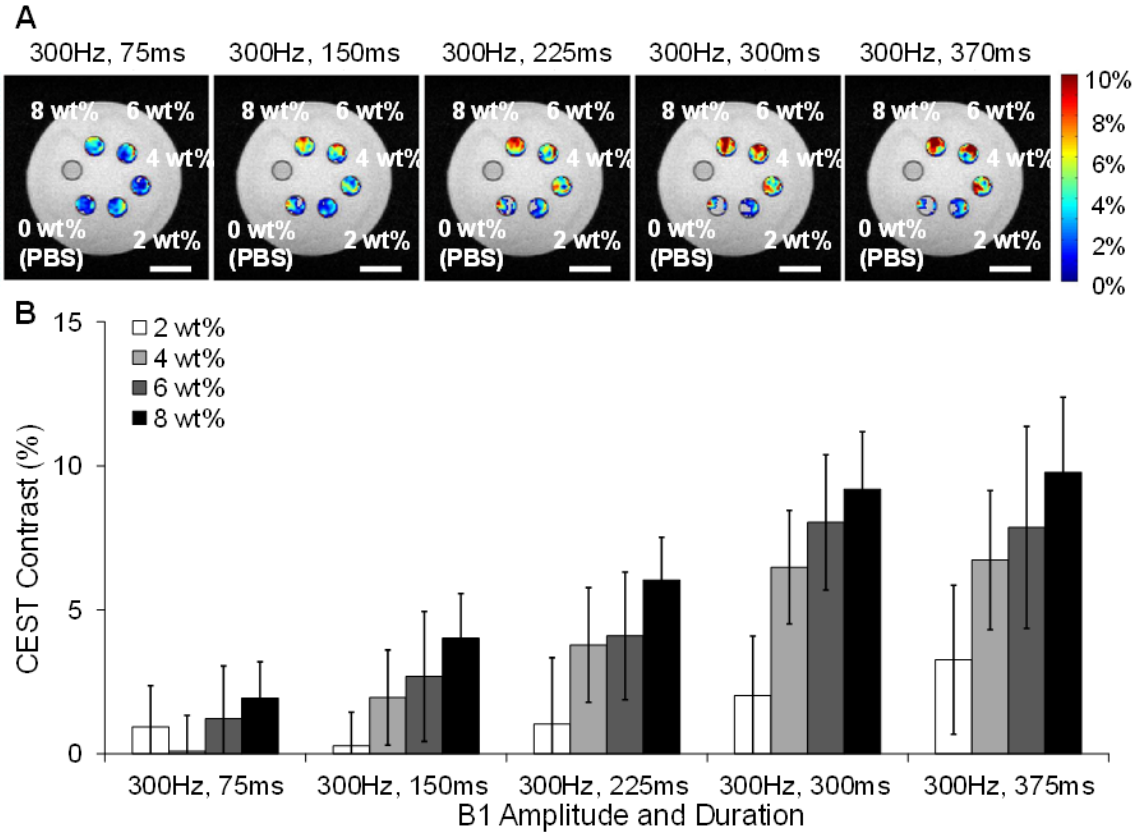

Figure 6.10. Saturation pulse duration dependence of CEST effect at 3T. CEST maps (A) and corresponding quantification (B) of HeMA-HA hydrogels at varying macromer concentrations from saturation at 1.0 ppm with varied B1 pulse durations but a constant amplitude of 300 Hz. Scans performed at 37°C. Data presented as mean ± SD. Scale bars = 2 cm.

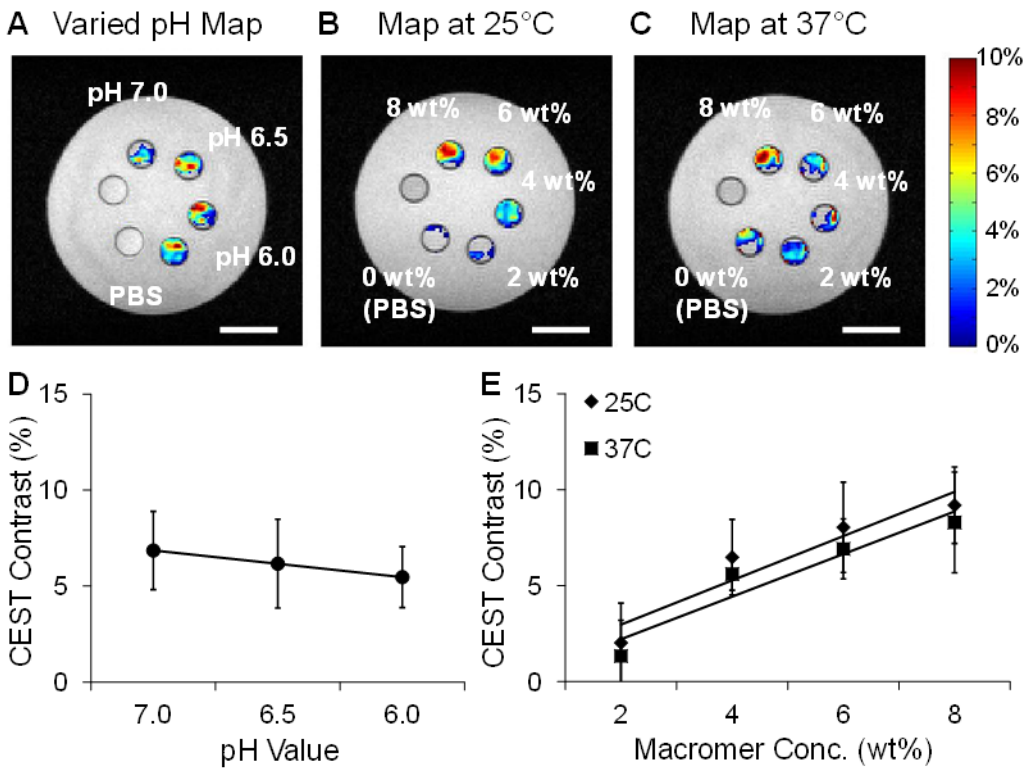

Figure 6.11. Effect of hydrogel pH and temperature on the CEST effect at 3T. CEST map at 1.0 ppm of HeMA-HA hydrogels at a single macromer concentration (8 wt%) and uniform temperature (37°C) but varying pH (A). CEST maps at 1.0 ppm of HeMA-HA hydrogels at varying concentration and uniform pH (7.0) but varying temperatures of 25°C (B) and 37°C (C). Quantification of the effect of pH (D) and temperature (E) on the CEST contrast at 3T. Protons saturated using a B_1 of 300 Hz for 300 ms. Data presented as mean ± SD. Scale bars = 2 cm.

6.3.2. *Ex Vivo* Imaging of Injectable Hydrogels

To further facilitate translation of this biomaterial imaging technique, the CEST effect of HeMA-HA hydrogels was assessed after injection into cardiac explants. CEST maps at 1.0 ppm demonstrated the ability to detect the injected hydrogel over the myocardial signal at both field strengths. At 7T (**Figure 6.12A**), a higher CEST contrast was generated from the injected hydrogel compared to that obtained at 3T (**Figure 6.12B**) due to a lower direct water saturation

effect at 7T. When the CEST effect of the hydrogel was background corrected using the surrounding myocardial signal at the corresponding field strength, the CEST contrast was similar between the two field strengths (**Figure 6.12C**). Similar to the phantom studies, a B_1 saturation pulse of 300 Hz and 300 ms was used at both field strengths. In contrast to the phantom studies performed at 37°C, explant studies were performed at 25°C due to minimal differences in the CEST effect with temperature at both 7 T (**Figure 6.7F**) and 3 T (**Figure 6.11E**).

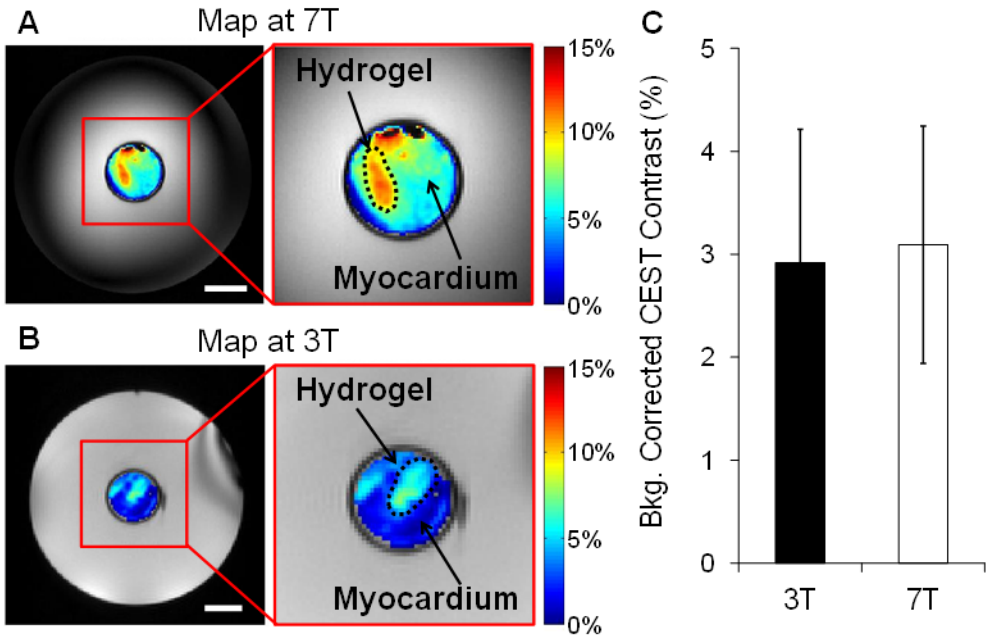

Figure 6.12. *Ex vivo* CEST effect of HeMA-HA hydrogels at varying field strengths. CEST maps at 1.0 ppm of 8 wt% HeMA-HA hydrogels injected into cardiac explants at 7 T (A) and 3 T (B). Dashed circles indicate hydrogel injection. Quantification of the CEST effect with the surrounding myocardium used for background correction (C). *Ex vivo* scans performed at 25°C. Protons saturated using a B_1 of 300 Hz for 300 ms. Data presented as mean ± SD. Scale bars = 2 cm.

The chemical shift dependence of the CEST effect was then compared in myocardial samples with and without HeMA-HA hydrogel injections at 3 T. CEST maps were generated for explants at 1.0 ppm, 1.5 ppm, and 2.0 ppm using a saturation pulse of 200 Hz for 250 ms. At 1.0

ppm, the hydrogel CEST contrast was greater than that of the surrounding myocardium (**Figure 6.13A**), as expected due to saturation of the HA hydroxyl protons. As the chemical shift difference from water ($\Delta\omega$) increased, the background myocardial CEST effect increased, decreasing the difference in contrast between the hydrogel and myocardium (**Figure 6.13**). The increased background myocardial signal with increasing chemical shift was comparable between the explant sample with (**Figure 6.13C,E**) and without (**Figure 6.13D,F**) hydrogel injections. Conventional MRI (i.e., T_1, $T_{1\rho}$, T_2) was used to confirm the location of increased CEST contrast at 1.0 ppm corresponded to the site of hydrogel injection (**Figure 6.14**).

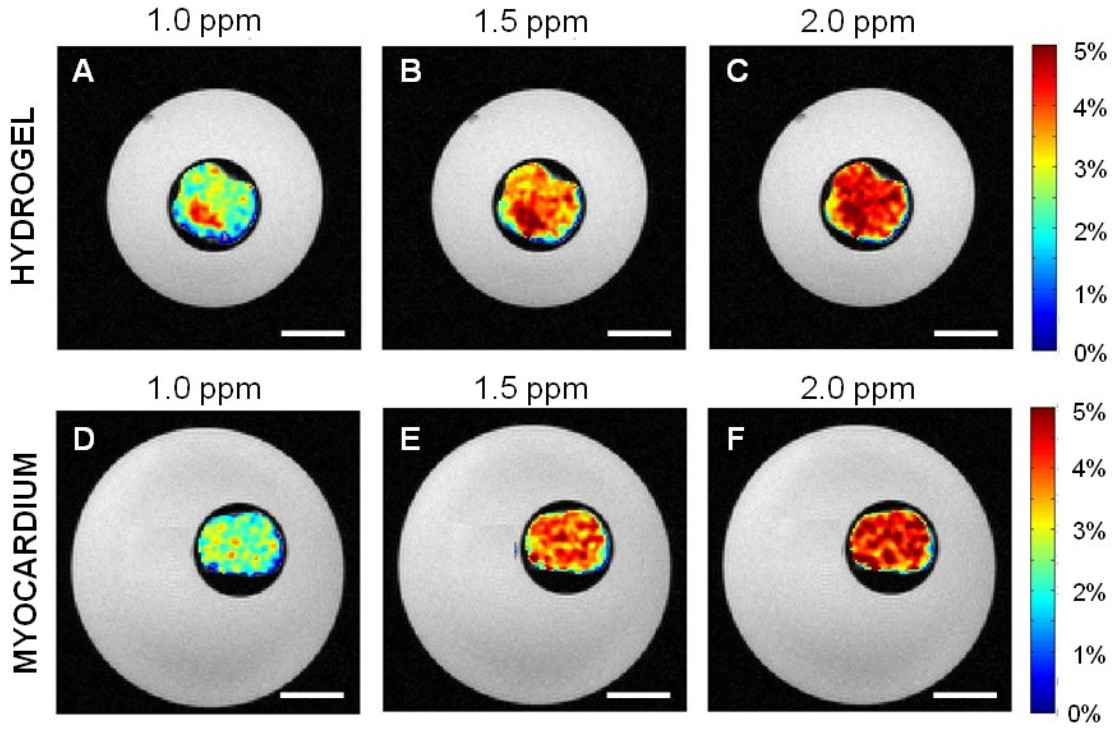

Figure 6.13. Chemical shift dependence of the CEST effect. CEST maps of a HeMA-HA hydrogel (8 wt%) injected into cardiac explants (left) as compared to myocardial samples alone (right) at 1.0 ppm (A, B), 1.5 ppm (C, D), and 2.0 ppm (E, F). Dashed circles indicate hydrogel injection (A, C, E). Scans performed at 25°C. A B_1 pulse of 200 Hz for 250 ms was used. Scale bars = 2 cm.

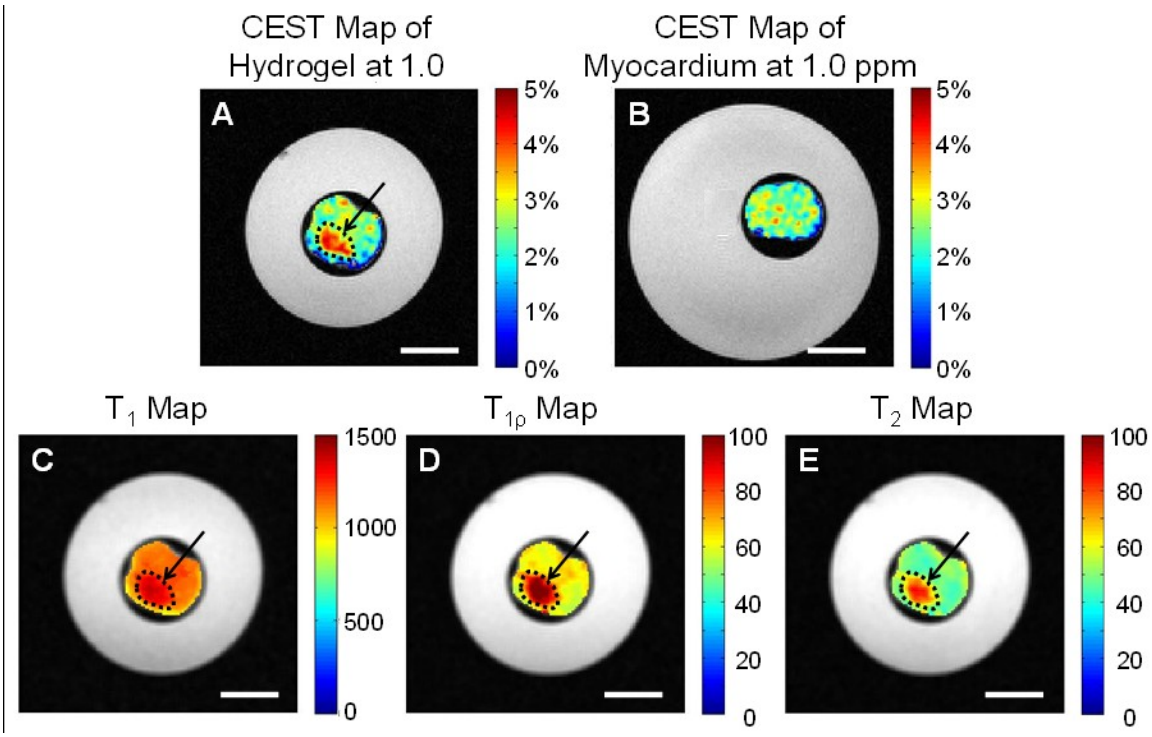

Figure 6.14. Comparison of CEST effect with traditional MRI based on relaxation properties. CEST maps at 1.0 ppm of a HeMA-HA hydrogel (8 wt%) injected into an explant (A) relative to a myocardial sample without injection (B). Protons were saturated using a B_1 of 200 Hz for 250 ms. T_1 (C), $T_{1\rho}$ (D), and T_2 (E) maps of the hydrogel-injected explant to demonstrate co-localization of the CEST effect with MRI contrast generated based on relaxation times. Scale bars = 2 cm.

6.3.3. Alteration of CEST Effect with Peptide Coupling

A peptide (GCRRR) was coupled to HeMA-HA using the reaction of maleimide-modified HA to the thiol on the cysteine of the peptide (**Figure 6.15**). This peptide sequence was selected to alter the CEST contrast based on the presence of additional exchangeable proton groups with altered chemical shift (**Figure 6.15C**).[30,31] Non–water-suppressed ^{1}H-NMR spectra at room temperature demonstrated that the additional peaks in the HeMA-HA-Peptide macromer originated from the peptide (**Figure 6.16A**). ^{1}H-NMR spectra of the HeMA-HA-Peptide dissolved in H_2O as compared to D_2O indicated the presence of the exchangeable proton peaks in the

~6.5-8.6 ppm range (with respect to TMS) when the macromer was dissolved in H_2O (**Figure 6.16B**). Exchangeable protons peaks disappeared when the macromer was dissolved in D_2O because the exchangeable protons interchanged with deuterium, which is not observable in ^{1}H-NMR spectra. Comparison of the non–water-suppressed spectra of the HeMA-HA-Peptide solution at different temperatures highlighted that the exchangeable proton peak of interest for CEST manipulation occurred at ~6.5 ppm with respect to TMS, which is ~1.8 ppm downfield from water at 4.7 ppm (**Figure 6.16B**).[40] Thus, subsequent CEST imaging experiments of HeMA-HA-Peptide hydrogels focused on saturating at 1.8 ppm downfield from water.

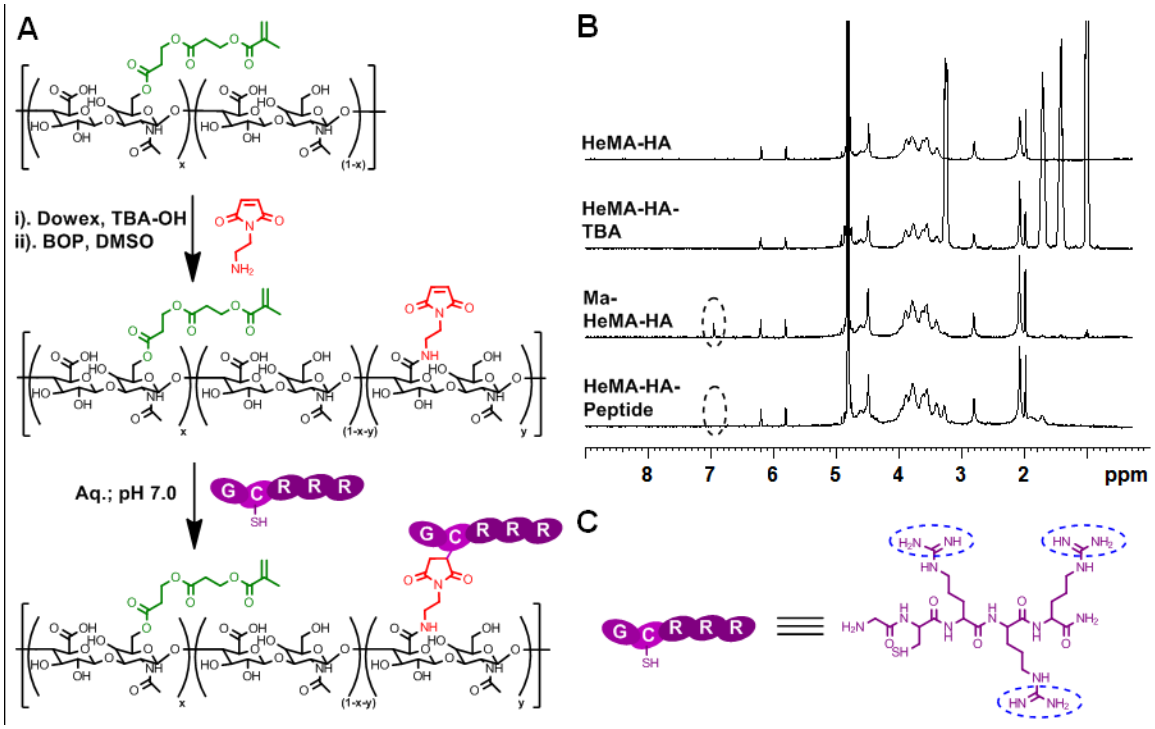

Figure 6.15. Synthesis of HeMA-HA-Peptide. HeMA-HA was converted to a TBA salt, then reacted with N-(2-aminoethyl)maleimide trifluoroacetate salt and the coupling agent BOP to introduce a malemide for subsequent coupling to the cysteine of a RRRCG peptide (A). ^{1}H-NMR was used to confirm the addition of TBA, the coupling of the malemide, and the consumption of the malemide peak (solid, red circles) with the peptide (B). The arginines in the peptide introduce additional amine functional groups (dashed, blue circles) to alter the CEST effect (C).

Phantom studies were then performed at 7 T to confirm that altering HeMA-HA-Peptide hydrogel macromer concentration alters the CEST contrast. Similar to the previous HeMA-HA phantom studies, the z-spectra became more broad (**Figure 6.17A**) and the asymmetry plot peak heights increased (**Figure 6.17B**) with increasing macromer concentration. Relative to the asymmetry plots of HeMA-HA hydrogels (**Figure 6.5B**), the addition of the peptide led to a shift in the asymmetry plots, resulting in a broad peak around ~1.8-2 ppm. CEST maps at 1.8 ppm (**Figure 6.17C**) and contrast quantification (**Figure 6.17D**) confirmed an increase in the CEST effect with increasing macromer concentration in HeMA-HA-Peptide hydrogels.

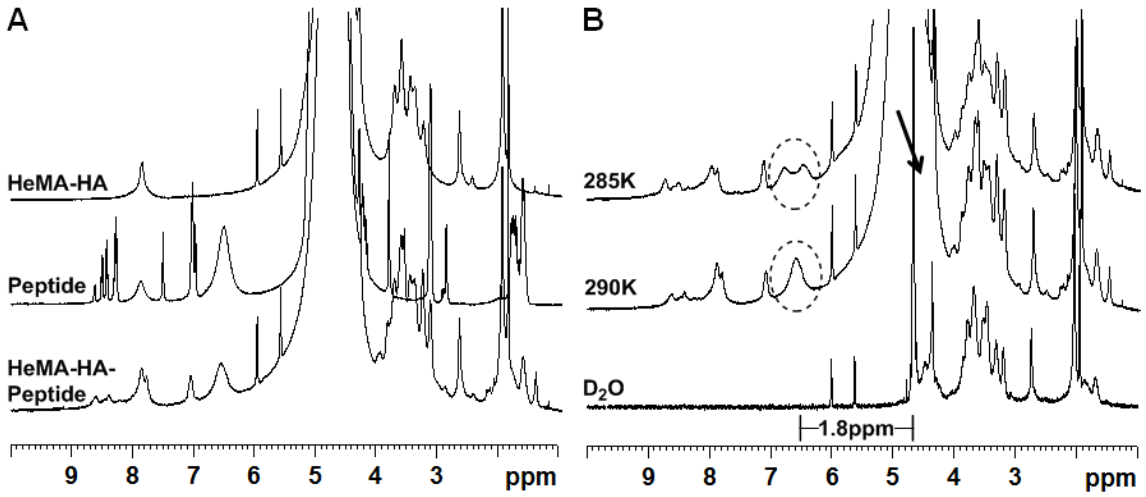

Figure 6.16. Spectroscopy characterization of HeMA-HA-Peptide. Non-water suppressed ^{1}H-NMR spectra of HeMA-HA, peptide, and HeMA-HA-Peptide solutions in H_2O at room temperature, 295 K (A). Spectra of HeMA-HA-Peptide solution in H_2O at different temperatures as compared to the macromer in D_2O to identify the exchangeable protons peaks (B). Temperature-induced changes in the exchange rate of the amine protons (dashed circles) highlight their ability to generate a CEST effect. The amine protons resonate at 1.8 ppm downfield from the bulk water protons at 4.7 ppm (relative to TMS).

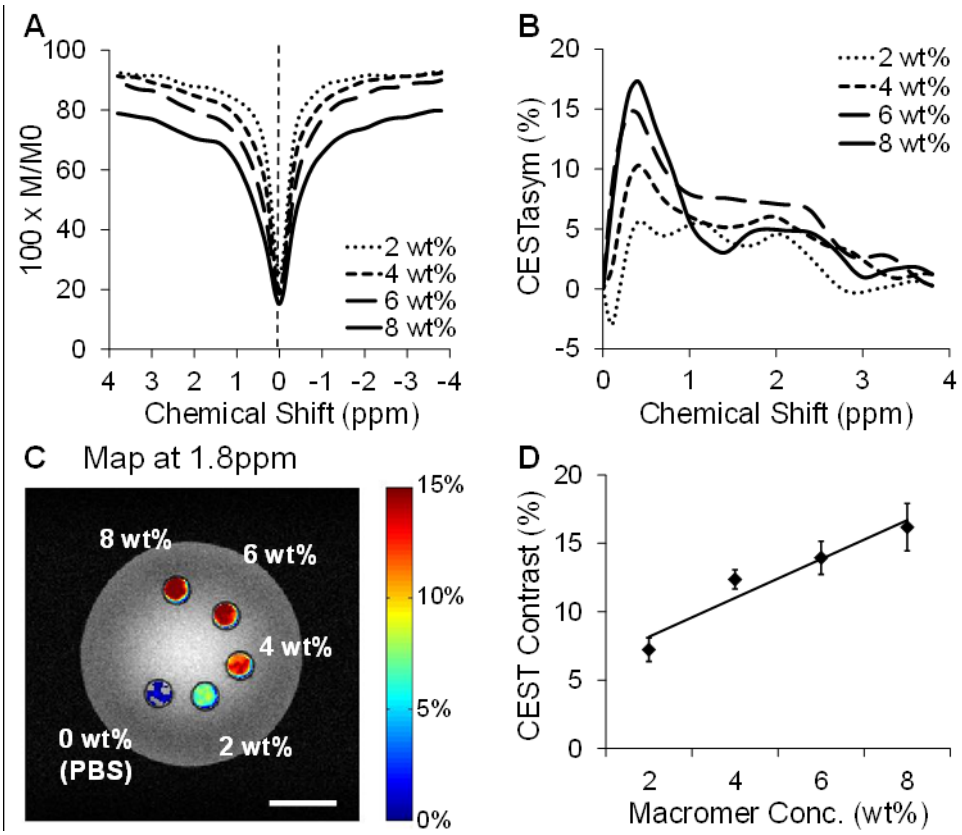

Figure 6.17. Characterization of the CEST effect of HeMA-HA-Peptide hydrogels. Z-spectrum (A) and asymmetry plot (B) of HeMA-HA-Peptide hydrogels at varying macromer concentrations at 7T using a B_1 of 400 Hz at 300 ms. CEST map from saturation at 1.8 ppm (C) and corresponding quantification of the CEST effect (D). Data presented as mean ± SD. Scale bar = 2 cm.

To further compare the CEST effect of HeMA-HA and HeMA-HA-Peptide hydrogels, phantom imaging studies were performed at 7 T, where the chemical shift of the saturation pulse was varied to highlight the differences in exchangeable proton chemistry between the two materials. CEST maps and quantification from saturation at 1.0 ppm showed a similar CEST effect for both hydrogel formulations (**Figure 6.18A-C**). In contrast, CEST maps and quantification from saturation at 1.8 ppm demonstrated that the CEST effect of HeMA-HA-Peptide hydrogels was maintained (relative to their CEST effect at 1.0 ppm), whereas the CEST contrast of HeMA-HA hydrogels decreased by a factor of two (**Figure 6.18D-F**).

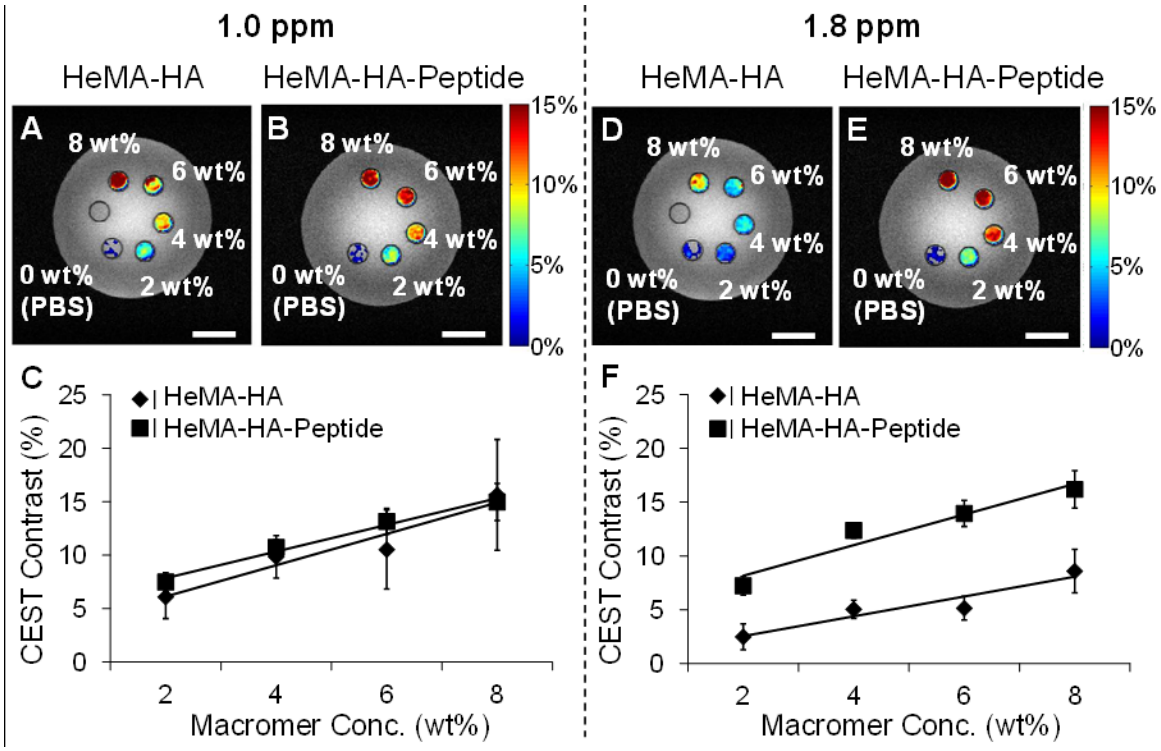

Figure 6.18. Altering the CEST effect by changing the chemistry and saturation frequency. CEST maps at 1.0 ppm (left) and 1.8 ppm (right) of HeMA-HA (A, D) and HeMA-HA-Peptide (B, E) hydrogel phantoms at 7 T and 37°C. CEST effect quantification at 1.0 ppm (C) and 1.8 ppm (F). Protons saturated using 400 Hz for 300 ms. Data presented as mean ± SD. Scale bars = 2 cm.

6.4. Discussion

Initial CEST imaging studies of a HeMA-HA hydrogel at 7 T demonstrated that the exchangeable protons present on the HA backbone could be manipulated using CEST MRI. More specifically, the hydroxyl protons were targeted over the amide protons on HA due to their higher concentration. Since CEST asymmetry analysis is based on the subtraction of images at corresponding but opposite chemical shifts around the water resonance, a peak in the plot indicates a decrease in the $+\Delta\omega$ signal due to saturation of the exchangeable protons resonating at that frequency (**Figure 6.4B**). Since the peak in the asymmetry plot occurred around 1 ppm, it confirmed that these exchangeable protons reside in the hydroxyl groups on HA (**Figure 6.2**),

which is consistent with previous studies.[19,30] Even though both the hydroxyl protons and amide protons on GAGs have been identified as suitable CEST agents, the high concentration and the fast exchange rate of hydroxyl protons make them a favorable option.[26] To further confirm the ability to visualize HA hydrogels using CEST imaging, saturation at the hydroxyl proton resonance frequency resulted in a CEST effect >10% (**Figure 6.4C**).

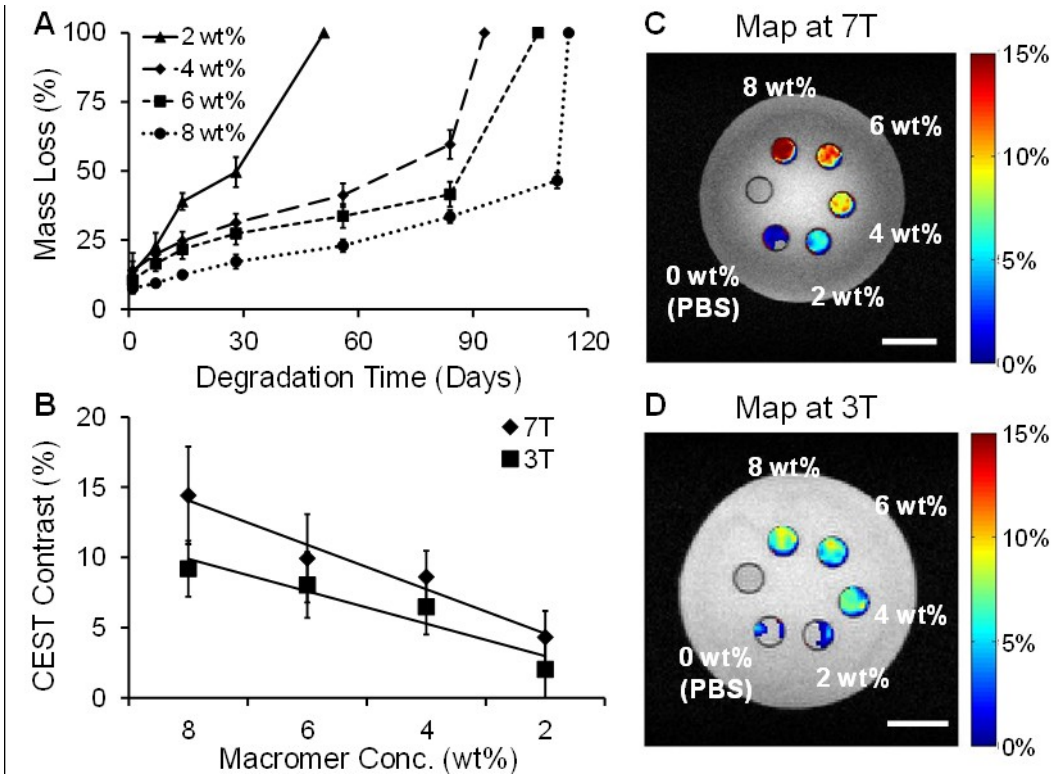

Figure 6.19. CEST effect of HeMA-HA hydrogels tracks with degradation at both field strengths. *In vitro* degradation of HeMA-HA hydrogels at varying macromer concentrations (A). CEST effect quantification of hydrogels at decreasing macromer concentrations (B). CEST maps at 1.0 ppm of hydrogels at varying concentration at 37°C using a field strength of 7T (C) or 3T (D). Protons saturated using a B_1 of 300 Hz for 300 ms. Data presented as mean ± SD. Scale bars = 2 cm.

Towards the goal of understanding injectable hydrogels *in vivo*, the ability to detect differences in material properties (i.e., macromer concentration) based on altering the CEST contrast is of great importance. As the concentration of the exchangeable proton pool increased

(due to the increase in macromer concentration), a larger extent of saturated magnetization could be transferred to the bulk water protons, leading to a greater decrease in the water signal. This trend was observed in the characterization study at 7T through the asymmetry analysis (**Figure 6.5B**) and visualization of the CEST effect in overlaid maps (**Figure 6.5C**). Furthermore, at both 7 T and 3 T, the CEST effect increased linearly with increasing macromer concentration (**Figure 6.8**) and therefore, a diminishing macromer concentration would be reflected by a smaller CEST effect. This decrease in macromer concentration could be used for future applications to mimic diminished hydrogel crosslinking or hydrogel degradation *in vitro* (**Figure 6.19**). Previous studies using injectable HA hydrogels demonstrated that their impact *in vivo* was dependent on both their degree of crosslinking (i.e., mechanics) and degradation profile.[28] Thus, the ability to visualize hydrogel crosslinking and/or degradation using CEST MRI could be used to predict hydrogel outcomes *in vivo* and provide insight into identifying optimal material properties.

To enable future *in vivo* applications of this technique, CEST was used to image HA hydrogels using clinically relevant scan parameters and in tissue explants. When initially determining if CEST could be a viable tool for hydrogel imaging, a long B_1 pulse duration was used to maximize the CEST signal by ensuring the protons have sufficient time to relax back to their steady state after manipulation.[19] After validating the use of CEST imaging, the pulse duration was decreased for all subsequent scans due to increased SAR concerns for *in vivo* injectable hydrogel applications[18] and hardware limitations at clinical field strength scanners. The relationship between long pulse durations leading to increased signal outputs accounts for the difference in CEST contrast generated between the initial characterization of a low macromer concentration hydrogel using a long duration (**Figure 6.4**) and the subsequent characterization of hydrogels at higher macromer concentrations using a shorter pulse duration (**Figure 6.5**). It is also advantageous to have the ability to restrict the pulse duration but maintain generation of a CEST contrast because the specific biological application may dictate time restraints, such as the case for cardiac CEST imaging.[35] Finally, shorter pulse durations are suitable for CEST imaging specific to hydroxyl protons due to their relatively rapid exchange rate.[19,41]

To further the translational value of CEST for biomaterial imaging, *ex vivo* scans were performed to distinguish injectable HA hydrogels from surrounding tissue (**Figures 6.6, 6.7**). Despite the decreased signal when transitioning from 7 T to 3 T (**Figures 6.5, 6.6**), the impact on the *ex vivo* hydrogel CEST effect was minimal when background corrected with the myocardial CEST signal (**Figure 6.12C**). Moreover, the large increase in power deposition at 7 T limits clinical use.[18] In the subsequent 3 T *ex vivo* scans, comparison of CEST maps at 1.0 ppm of myocardial samples with and without the hydrogel injections showed increased CEST contrast at the hydrogel location (**Figure 6.13A,B**). Conventional MRI using of T_1, $T_{1\rho}$, and T_2 mapping further confirmed the site of the injected hydrogel coincided with the location of increased CEST contrast (**Figure 6.14**).

In contrast to conventional MRI contrast, such as T_1- and T_2-weighting, CEST probes specific functional groups in biomaterials based on their exchangeable protons in a frequency-specific manner.[42] This was evident in this study because the greatest difference in the hydrogel to myocardial CEST contrast occurred at the HA hydrogel hydroxyl proton resonance frequency (**Figure 6.13A**). As $\Delta\omega$ increased such that saturation occurred further from the resonance frequency of the hydroxyl protons, the background myocardial CEST effect increased (**Figure 6.13**). This endogenous myocardial CEST contrast was likely due to saturation of native exchangeable protons, such as those present in extracellular matrix (ECM) molecules or in cardiac metabolites. One such metabolite is creatine, which is involved in the production of energy to power myocardial contraction.[35] The labile amine protons in creatine are known to resonate at ~1.8 ppm downfield of bulk water,[34,35] which was confirmed in this work by the increased CEST contrast when saturation occurred at 2.0 ppm (**Figure 6.13E,F**) relative to 1.5 ppm (**Figure 6.13C,D**) or 1.0 ppm (**Figure 6.13A,B**). Due to this chemical shift dependence, injectable materials with different functional groups possessing exchangeable protons with distinct chemical shifts could be designed such that CEST imaging could simultaneously visualize and discriminate between these materials.[30,31,43]

To demonstrate the ability of CEST imaging to differentiate injectable hydrogels based on the resonance frequency of their exchangeable protons, a peptide was coupled to HeMA-HA. The peptide was chosen to contain three arginines because the amine protons in arginine are known to resonate at 1.8 ppm downfield from the bulk water protons, which differs from the hydroxyl proton resonance at 1.0 ppm.[30,31,34,35] Amine protons not only offer the advantage of being at a chemical shift farther from water, which decreases direct water saturation and hence increases CEST sensitivity, but they also exchange at a relatively slower rate than hydroxyl protons, allowing more time for selective saturation before exchange, thus resulting in a larger CEST effect.[19,41] In addition, amine-based CEST has recently been used to image endogenous metabolites *in vivo* for cardiac and calf muscle applications.[35]

Non-water suppressed spectroscopy was used to confirm the presence of additional exchangeable protons in the HeMA-HA-Peptide macromer relative to HeMA-HA alone (**Figure 6.16A**) and highlight the potential for the arginine-based amine protons to generate a CEST effect (**Figure 6.16B**). To do so, the HeMA-HA-Peptide solution was exposed to varying temperatures since changes in temperature and pH are known to alter the exchange rate, and hence CEST effect.[22,44] As the temperature or pH increase, the proton exchange rate increases, leading to less time available for saturation and an overall decrease in the generated CEST contrast (**Figures 6.7, 6.11**). Similarly, as the temperature the HeMA-HA-Peptide solution was increased from 280 K to 295 K in the spectrometer, the exchange rate of the amine protons increased, resulting in formation of a single broad peak at 295 K from two separate, resolved peaks at 280 K at ~6.5 ppm with respect to TMS. The two peaks evident at the lower temperature represent the two equivalent amines in the guanidine group at the distal end of each arginine in the peptide where the delocalization of the positive charge between the double bond and the nitrogen lone pair facilitates exchange (**Figure 6.15C**).

The exchangeable proton and saturation frequency specificity of the CEST effect was further confirmed by phantom studies comparing HeMA-HA and HeMA-HA-Peptide hydrogels

(**Figure 6.18**). Since both macromers contain the same concentration of hydroxyl protons, they generated a similar CEST effect when saturated at the hydroxyl resonance frequency of 1.0 ppm (**Figure 6.18A-C**). In contrast, only the HeMA-HA-Peptide macromer contains the exchangeable arginine-based amine protons shown to resonate ~1.8 ppm downfield of water protons (**Figure 6.16B**). Therefore, application of the saturation pulse at 1.8 ppm led to generation of a CEST effect specific to the amine protons in the peptide. The two hydrogels were distinguished from one another at the resonance frequency of the amine protons because HeMA-HA-Peptide hydrogel generated a strong CEST effect whereas the HeMA-HA hydrogel did not (**Figure 6.18D-F**). The ability to visualize differences in hydrogels based on modulation of the exchangeable proton pool and chemical shift of saturation highlights the novelty of CEST as an imaging tool that can be tuned to the properties of the injectable material of interest.

6.5. Conclusions

In summary, this chapter demonstrated that a new MRI technique based on saturation transfer of specific exchangeable protons was successfully used to visualize injectable HA hydrogels *in vitro* and *ex vivo*. Alteration of hydrogel properties (i.e., macromer concentration) led to differences in the CEST contrast, indicating that this imaging approach could be used to identify different compositions or to track dynamic changes in biomaterial properties. In addition, the CEST effect was altered by changing the exchangeable proton group and saturation frequency, demonstrating the ability of CEST imaging to specifically image and discriminate between different injectable materials based on their chemistry. Moreover, the use of CEST MRI to accurately detect injectable hydrogels in tissue explants using clinically relevant scan parameters and magnetic field strengths highlights the potential for CEST imaging to be used as tool to simultaneously visualize and assess material properties of injectable materials *in vivo* for future biomaterial optimization. The next chapter will focus on applying injectable, degradable HA hydrogels to an *in vivo* infarct model and assessing outcomes using MRI.

6.6. References

1. Nguyen MK, Lee DS. Injectable biodegradable hydrogels. Macromol Biosci 2010;10(6):563-579.

2. Yu L, Ding J. Injectable hydrogels as unique biomedical materials. Chem Soc Rev 2008;37(8):1473-1481.

3. Burdick JA, Mauck RL, Gorman JH,III, Gorman RC. Acellular biomaterials: An evolving alternative to cell-based therapies. Science Translational Medicine 2013;5(176):176ps4.

4. Burdick JA. Injectable gels for tissue/organ repair. Biomed Mater 2012;7(2):020201.

5. Artzi N, Oliva N, Puron C, Shitreet S, Artzi S, Ramos AB, et al. In vivo and in vitro tracking of erosion in biodegradable materials using non-invasive fluorescence imaging. Nature Materials 2011;10(9):704-709.

6. MacArthur JW,Jr., Purcell BP, Shudo Y, Cohen JE, Fairman A, Trubelja A, et al. Sustained release of engineered stromal cell-derived factor 1-alpha from injectable hydrogels effectively recruits endothelial progenitor cells and preserves ventricular function after myocardial infarction. Circulation 2013;128(11):S79-S86.

7. Soranno DE, Lu HD, Weber HM, Rai R, Burdick JA. Immunotherapy with injectable hydrogels to treat obstructive nephropathy. Journal of Biomedical Materials Research Part a 2014;102(7):2173-2180.

8. Yuan Z, Zakhaleva J, Ren H, Liu J, Chen W, Pan Y. Noninvasive and high-resolution optical monitoring of healing of diabetic dermal excisional wounds implanted with biodegradable in situ gelable hydrogels. Tissue Engineering Part C-Methods 2010;16(2):237-247.

9. Kovar JL, Simpson MA, Schutz-Geschwender A, Olive DM. A systematic approach to the development agents for optical imaging of mouse of fluorescent contrast cancer models. Anal Biochem 2007;367(1):1-12.

10. Weissleder R, Ntziachristos V. Shedding light onto live molecular targets. Nat Med 2003;9(1):123-128.

11. Mottu F, Rufenacht DA, Doelker E. Radiopaque polymeric materials for medical applications - Current aspects of biomaterial research. Invest Radiol 1999;34(5):323-335.

12. Blakely B, Lee BH, Riley C, McLemore R, Pathak CP, Vernon BL. Formulation and characterization of radio-opaque conjugated in situ gelling materials. Journal of Biomedical Materials Research Part B-Applied Biomaterials 2010;93B(1):9-17.

13. Yu SB, Watson AD. Metal-based x-ray contrast media. Chem Rev 1999;99(9):2353-2377.

14. Leon CM, Lee BH, Preul M, McLemore R, Vernon BL. Synthesis and characterization of radio-opaque thermosensitive poly[N-isopropylacrylamide-2,2 '-(ethylenedioxy)bis(ethylamine)-2,3,5-triiodobenzamide]. Polym Int 2009;58(8):847-850.

15. Dixon JA, Spinale FG. Large animal models of heart failure: A critical link in the translation of basic science to clinical practice. Circ Heart Fail 2009;2(3):262-271.

16. Zhang Y, Sun Y, Yang X, Hilborn J, Heerschap A, Ossipov DA. Injectable in situ forming hybrid iron oxide-hyaluronic acid hydrogel for magnetic resonance imaging and drug delivery. Macromol Biosci 2014;14(9):1249-1259.

17. Karfeld-Sulzer LS, Waters EA, Kohlmeir EK, Kissler H, Zhang X, Kaufman DB, et al. Protein polymer MRI contrast agents: Longitudinal analysis of biomaterials in vivo. Magn Reson Med 2011;65(1):220-228.

18. van Zijl PCM, Yadav NN. Chemical Exchange Saturation Transfer (CEST): What is in a name and what isn't? Magn Reson Med 2011;65(4):927-948.

19. Kogan F, Hariharan H, Reddy R. Chemical exchange saturation transfer (CEST) imaging: Description of technique and potential clinical applications. Curr Radiol Rep 2013;1(2):102-114.

20. Sun P, van Zijl P, Zhou J. Optimization of the irradiation power in chemical exchange dependent saturation transfer experiments. J Magn Reson 2005;175(2):193-200.

21. Soesbe TC, Wu Y, Dean Sherry A. Advantages of paramagnetic chemical exchange saturation transfer (CEST) complexes having slow to intermediate water exchange properties as responsive MRI agents. NMR Biomed 2013;26(7):829-838.

22. Ward K, Aletras A, Balaban R. A new class of contrast agents for MRI based on proton chemical exchange dependent saturation transfer (CEST). J Magn Reson 2000;143(1):79-87.

23. Woessner D, Zhang S, Merritt M, Sherry A. Numerical solution of the Bloch equations provides insights into the optimum design of PARACEST agents for MRI. Magn Reson Med 2005;53(4):790-799.

24. Burdick JA, Chung C, Jia X, Randolph MA, Langer R. Controlled degradation and mechanical behavior of photopolymerized hyaluronic acid networks. Biomacromolecules 2005;6(1):386-391.

25. Burdick JA, Prestwich GD. Hyaluronic acid hydrogels for biomedical applications. Adv Mater 2011;23(12):H41-H56.

26. Ling W, Regatte RR, Navon G, Jerschow A. Assessment of glycosaminoglycan concentration in vivo by chemical exchange-dependent saturation transfer (gagCEST). Proc Natl Acad Sci U S A 2008;105(7):2266-2270.

27. Singh A, Haris M, Cai K, Kassey VB, Kogan F, Reddy D, et al. Chemical exchange saturation transfer magnetic resonance imaging of human knee cartilage at 3 T and 7 T. Magn Reson Med 2012;68(2):588-594.

28. Tous E, Ifkovits JL, Koomalsingh KJ, Shuto T, Soeda T, Kondo N, et al. Influence of injectable hyaluronic acid hydrogel degradation behavior on infarction-induced ventricular remodeling. Biomacromolecules 2011;12(11):4127-4135.

29. Sahoo S, Chung C, Khetan S, Burdick JA. Hydrolytically degradable hyaluronic acid hydrogels with controlled temporal structures. Biomacromolecules 2008;9(4):1088-1092.

30. Liu G, Moake M, Har-el Y, Long CM, Chan KWY, Cardona A, et al. In vivo multicolor molecular MR imaging using diamagnetic chemical exchange saturation transfer liposomes. Magn Reson Med 2012;67(4):1106-1113.

31. McMahon MT, Gilad AA, DeLiso MA, Berman SDC, Bulte JWM, van Zijl PCM. New "multicolor" polypeptide diamagnetic chemical exchange saturation transfer (DIACEST) contrast agents for MRI. Magn Reson Med 2008;60(4):803-812.

32. Purcell BP, Kim IL, Chuo V, Guenin T, Dorsey SM, Burdick JA. Incorporation of sulfated hyaluronic acid macromers into degradable hydrogel scaffolds for sustained molecule delivery. Biomater Sci 2014;2(5):693-702.

33. Cai K, Haris M, Singh A, Kogan F, Greenberg JH, Hariharan H, et al. Magnetic resonance imaging of glutamate. Nat Med 2012;18(2):302-306.

34. Haris M, Nanga RPR, Singh A, Cai K, Kogan F, Hariharan H, et al. Exchange rates of creatine kinase metabolites: Feasibility of imaging creatine by chemical exchange saturation transfer MRI. NMR Biomed 2012;25(11):1305-1309.

35. Haris M, Singh A, Cai K, Kogan F, McGarvey J, DeBrosse C, et al. A technique for in vivo mapping of myocardial creatine kinase metabolism. Nat Med 2014;20(2):209-214.

36. Bryant R. The dynamics of water-protein interactions. Annu Rev Biophys Biomol Struct 1996;25:29-53.

37. Liu G, Gilad AA, Bulte JWM, van Zijl PCM, McMahon MT. High-throughput screening of chemical exchange saturation transfer MR contrast agents. Contrast Media Mol Imaging 2010;5(3):162-170.

38. Kim M, Gillen J, Landman BA, Zhou J, van Zijl PCM. Water saturation shift referencing (WASSR) for chemical exchange saturation transfer (CEST) experiments. Magn Reson Med 2009;61(6):1441-1450.

39. Singh A, Cai K, Haris M, Hariharan H, Reddy R. On B1 inhomogeneity correction of in vivo human brain glutamate chemical exchange saturation transfer contrast at 7T. Magn Reson Med 2013;69(3):818-824.

40. Hoffman R. Standardization of chemical shifts of TMS and solvent signals in NMR solvents. Magn Reson Chem 2006;44(6):606-616.

41. Liepinsh E, Otting G. Proton exchange rates from amino acid side chains - Implications for image contrast. Magnetic Resonance in Medicine 1996;35(1):30-42.

42. Liu G, Song X, Chan KWY, McMahon MT. Nuts and bolts of chemical exchange saturation transfer MRI. NMR Biomed 2013;26(7):810-828.

43. Liu G, Gilad AA, Bulte JWM, van Zijl PCM, McMahon MT. High-throughput screening of chemical exchange saturation transfer MR contrast agents. Contrast Media Mol Imaging 2010;5(3):162-170.

44. Guivel-Scharen V, Sinnwell T, Wolff S, Balaban R. Detection of proton chemical exchange between metabolites and water in biological tissues. J Magn Reson 1998;133(1):36-45.

CHAPTER 7

Investigation of Injectable Hyaluronic Acid Hydrogel Therapy to Alter Myocardial Tissue Properties for Infarct Repair using MRI and FE Modeling

(Adapted from: Dorsey SM, McGarvey JR, Wang H, Nikou A, Arama L, Koomalsingh KJ, Kondo N, Pilla JJ, Gorman JH III, Gorman RC, Wenk JF, Burdick JA. Biomaterials, in preparation.)

7.1. Introduction

Heart failure is a leading cause of morbidity and mortality, affecting almost 23 million individuals worldwide and 6 million in the US alone.[1,2] Of these cases, nearly 70% are due to left ventricular (LV) remodeling initiated by myocardial infarction (MI).[3] LV remodeling is manifest by progressive LV dilation which results in thinning of the LV wall and a change in heart shape that can alter function.[4] The mechanical phenomenon that both initiates and sustains the adverse LV remodeling process is the initial infarct expansion. Infarct expansion is a progressive pathologic process that results from abnormal loading of the noncontractile infarcted myocardium, leading to increased mechanical stress in the perfused borderzone regions surrounding the infarct, altered systolic contractile properties, and eventual progression to heart failure.[5-8] Limiting infarct expansion has thus been identified as a potential therapy to reduce the morbidity associated with LV remodeling. Previous strategies to limit infarct expansion include surgical reconstruction of the dilated LV and physical LV restraint with polymeric meshes to prevent dilation.[9-13]

In contrast to passive restraint devices, injectable biomaterials offer the potential for minimally invasive delivery, which may limit tissue damage and enable rapid clinical translation. As discussed in Section 3.2.2, injectable acellular hydrogels have been used to mechanically stabilize the infarcted myocardial wall to prevent initial infarct thinning and attenuate remodeling

post-MI.[14,15] Several natural and synthetic injectable materials have been successful in maintaining cardiac structure and function in animal models,[16] but further information is needed to understand the impact of injectable materials on myocardial tissue properties.[17] Recent studies using injectable hyaluronic acid (HA) hydrogels were the first to investigate the importance of material mechanics[18] and degradation[19] in attenuating remodeling. However, the specific hydrogel properties for optimal *in vivo* outcomes are not clear.

To further elucidate how injectable hydrogels alter LV remodeling, tools are needed to assess the effects of these therapies on the infarcted myocardium. However, traditional histological analysis is invasive, thereby limiting temporal assessment, as it can ultimately only be performed in an excised heart. Imaging modalities, such as magnetic resonance imaging (MRI), can noninvasively provide information about the infarcted heart following treatment with injectable hydrogels. Unlike other well-established cardiac imaging modalities, advances in cardiac MRI offer the ability to not only assess standard geometrics but also depict myocardial wall motion with high image contrast and spatial resolution without using ionizing radiation.[20-25] Cine MRI continues to be the most accurate modality for evaluating LV structure and function with high spatial and temporal resolution.[26,27] MRI with the use of gadolinium contrast agents enables visualization of infarcted regions due to differences in tissue perfusion using late-gadolinium enhancement (LGE) MRI.[28] Myocardial (SPAMM) tagging with MRI can be used to visualize regional heart motion at high spatial resolution and quantify regional myocardial displacement (strain) as a measure of LV contractility.[29,30] Thus, within a single scan period, MRI can monitor changes in global LV structure and function, infarct properties, and regional wall motion to provide insight into the impact of injectable hydrogels on myocardial tissue parameters post-MI.

Theoretical finite element (FE) models can also be used to provide information on how injectable hydrogels attenuate LV remodeling. Previous FE models have shown that injectable materials decrease myocardial stresses after remodeling with levels that depend on hydrogel properties, such as mechanics and volume.[31-33] A FE model of injections into the borderzone

region with mechanical properties 20% greater than the stiffness of the native myocardium led to a concomitant 20% decrease in myocardial fiber stress relative to controls.[31] In a subsequent study, it was shown that this decreased stress depended on both the injection pattern and the volume of material dispersion, with larger numbers of injections and larger injection volumes having the greatest effects on myocardial fiber stress.[32] Despite these findings, the models used simulated injections[31,32] or three-dimensional echocardiographic data from large animal studies.[33] In contrast, MRI myocardial tagging enables a highly detailed assessment of myocardial motion as a measure of myocardial strain.[34] FE models using MRI tagging strains as input parameters have been examined in large animals[33,35-37] and humans[34,38] post-MI, but none have done so in the context of assessing the ability of injectable biomaterials to decrease myocardial stress.

The goal of this chapter was to better understand the role that injectable hydrogels have on positive structural and functional outcomes post-MI using cardiac MRI and FE modeling. As discussed in Section 4.1, hydrogels were formed by crosslinking HA, a linear polysaccharide found in native cardiac extracellular matrix (ECM) that plays a role in cardiac embryogenesis, scar reduction, cell migration and angiogenesis.[39-42] *In vivo* function was assessed in a well-established porcine infarct model at 1, 4, 8, and 12 weeks post-MI to determine the temporal effect of HA hydrogels on global LV remodeling, infarct expansion, myocardial wall motion, and myocardial stiffness. This study was the first to examine the efficacy of hydrogel therapies for MI repair using MRI-derived measures of regional myocardial systolic strain and FE-model derived measures of passive myocardial stiffness based on *in vivo* inputs. Ultimately, these results can broaden our understanding of hydrogel therapies to prevent progression to heart failure.

7.2. Materials and methods

7.2.1. Synthesis of HeMA-HA Macromer

As discussed previously in Section 4.2.1, HA was modified to include a hydrolytically degradable group, hydroxyethyl methacrylate (HeMA). Briefly, HeMA-HA was made by coupling

HA-tetrabutyl-ammonium salt (HA-TBA) to 2-hydroxyethyl-methacryl-succinate (HeMA-COOH) using 4-dimethylaminopyridine (DMAP, Sigma) and the coupling agent di-tert-butyl dicarbonate (BOC_2O, Sigma) for 20 hours at 45°C.[19] The macromer was purified by dialyzing against deionized (DI) water at 4°C, acetone precipitating, and dialyzing again. The macromer was then frozen and lyophilized. The extent of HA modification with HeMA was assessed with ^{1}H-NMR (Bruker, 360 MHz) and found to be ~25% of the HA repeat units, as in Section 4.2.1.

7.2.2. Hydrogel Formation and Characterization

Hydrogels were formed by crosslinking the methacrylate groups of HeMA-HA using a redox initiator system of ammonium persulfate (APS, 5 mM, Sigma) and N,N,N,N',N'-tetramethylenediamine (TEMED, 5 mM, Sigma),[43] as discussed in Section 4.2.3. Gel onset was quantified using an AR2000ex Rheometer (TA Instruments) by monitoring the storage (G') and loss (G") moduli over time at 37°C under 1% strain and 1 Hz frequency in a cone-plate geometry (1°, 20 mm diameter). For *in vitro* characterization of mechanics and degradation, hydrogels were formed between two glass slides in a Teflon mold sealed with vacuum grease. Compression testing was performed on gels using a Dynamic Mechanical Analyzer (DMA) (Q800 TA Instruments) at a strain rate of 10%/min and compressive moduli were calculated from 10 to 20% strain.[44] Degradation was monitored in PBS at 37°C and mass loss quantified using an uronic acid assay.[45,46] Mechanics and degradation were assessed immediately after gelation (day 0) and at desired time points throughout degradation (i.e., days 1, 7, 14, 28, 56 and 84 after gelation).

7.2.3. *In Vivo* Evaluation in Porcine Infarct Model

Fourteen male Yorkshire swine weighing 40-50 kg were enrolled in this study (*n=8* hydrogel treatment, *n=6* saline control). All animals received care in compliance with protocols approved by the University of Pennsylvania's Institutional Animal Care and Use Committee in accordance with the National Institutes of Health's "Guide for the Care and Use of Laboratory

Animals" (NIH Publication 85-23, revised 1996). All animals received a baseline MRI scan to evaluate LV volumes and regional strains 5-7 days prior to MI.

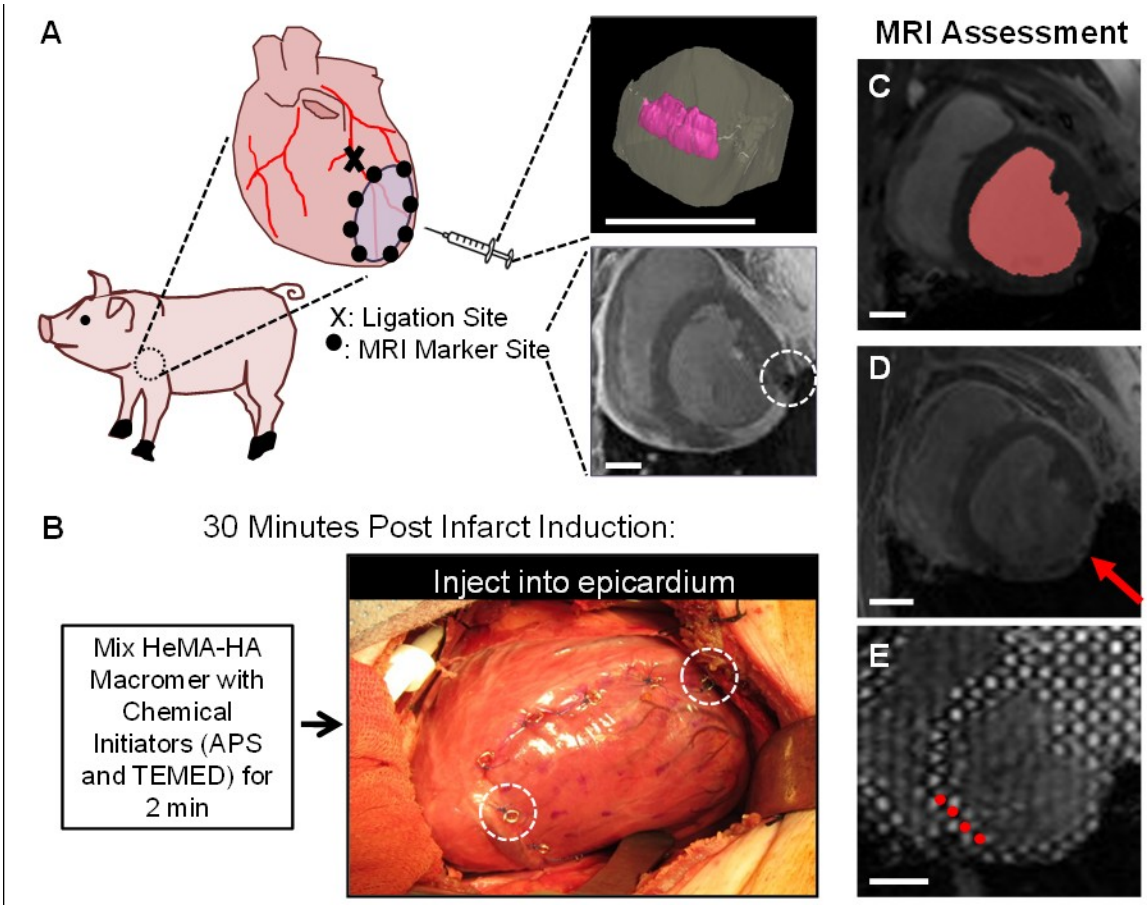

Figure 7.1. MRI analysis of *in vivo* porcine infarct model. *In vivo* function (*n=3-6/group*) was assessed in a porcine MI model (A). Inserts in panel A show a 3D MRI reconstruction of a hydrogel in a myocardial explant (top) and visibility of a MRI marker (white, dashed circle) placed post-MI for tracking infarct expansion (bottom). Thirty minutes post-MI, animals underwent an array of twenty 0.3 mL injections of either prepolymer solution or saline in the infarct (B). MRI compatible markers (white, dashed circles) are visible. MRI scans were performed at baseline (i.e., prior to infarction) and at 1, 4, 8 and 12 weeks post-MI. MRI data was analyzed to assess global LV structure and function from segmentation of the blood volume (red shape) in cine MRI

(C), infarct (red arrow) expansion from LGE MRI (D), and myocardial wall function from tracking grid displacement (red circles highlight select tags) in SPAMM tagged MRI (E). Scale bar = 2 cm.

For infarct induction, pigs were anesthetized and the LV free wall exposed through a left thoracotomy. Throughout the procedure, pigs were monitored with electrocardiography and aseptic technique was maintained. Animals were first sedated with intramuscular ketamine injection (25-30 mg/kg), intubated, and mechanically ventilated. General anesthesia was maintained on mixed isoflurane (1.5-3.0%) and oxygen, which was delivered by volume-controlled ventilation (tidal volume 10-15 mg/kg).[47] A posterolateral infarction was induced by ligation with nonabsorbable polypropylene suture of the left circumflex artery (LCX) and select obtuse marginal (OM) branches. In nearly all cases, this pattern of coronary ligations produced an infarct comprising 20-25% of the left ventricle.[48] Akinesis of the infarcted myocardium was confirmed using intraoperative echocardiography. Following infarct induction, thin MRI compatible, platinum wire markers were sutured to the epicardium to outline the infarct. These markers were tracked for quantitative assessment of infarct expansion over time (**Figure 7.1A**).[47]

Thirty minutes after infarction, animals received twenty evenly distributed 0.3 mL injections of either 0.9% normal saline (control) or HeMA-HA pre-hydrogel solution (treatment) in the infarct (**Figure 7.1B**). Real time 3D echocardiographs and hemodynamic data were obtained at baseline, immediately prior to MI, 30 minutes after MI, and 30 minutes post injection. After ensuring hemodynamic and electrophysiologic stability, all animals were recovered. MRI scans were performed at 1, 4, 8, and 12 weeks after injection. Animals were sacrificed at 12 weeks and histological evaluation of Masson's Trichrome and H&E staining was performed. Morphometric analysis was performed to assess infarct wall thickness using planimetry.[47]

7.2.4. MRI Acquisition

Serial cardiac MRI was used to noninvasively assess global and regional cardiac structure and function in each animal through a series of three scans: 1) cine imaging to assess

global LV morphology and function (**Figure 7.1C**), 2) late-gadolinium enhancement (LGE) imaging to assess infarct area thinning and expansion (**Figure 7.1D**), and 3) SPAMM (SPAtial Modulation of Magnetization) tagging to assess regional wall motion and function (**Figure 7.1E**). MR images were acquired using a 3T Tim Magnetom Trio Scanner (Seimens, Inc.; Malvern, PA). General anesthesia was maintained throughout all imaging procedures, as described above. For each MRI scan, a high-fidelity pressure transducer (Millar Instruments; Houston, TX) was guided into the LV for cardiac gating; the measured pressure was later used as an input for a finite element (FE) model to assess *in vivo* myocardial stress-strain relationships.

LV volume imaging was performed using prospectively-gated 3D steady-state free precession (SSFP) cine MRI with the following imaging parameters: field of view = 300 x 244 mm^2, matrix size = 192 x 156, repetition time = 3.11 ms, echo time = 1.53 ms, bandwidth = 1184 Hz/pixel, slice thickness = 4 mm, averages = 2.[47] Assessment of infarct location and wall thickness occurred fifteen minutes following intravenous injection of 0.1 mmol/kg gadobenatedimeglumine (MultiHance; Bracco Diagnostics, Princeton, NJ) using a 3D LGE spoiled gradient echo sequence with the following parameters: field of view = 350 x 350 mm^2, matrix size = 256 x 256, repetition time = 591.28 ms, echo time = 2.96 ms, inversion time = 200-300 ms, flip angle = 25˚, averages = 2.[47] Finally, regional LV strain was assessed using a 3D SPAMM tagged sequence with the following parameters: field of view = 260 x 260 mm^2, matrix size = 256 x 128, repetition time = 34.4 ms, tag spacing = 6 mm, bandwidth = 330 Hz/pixel, slice thickness = 2 mm, averages = 4.[47] Separate scans were performed for systolic and diastolic strain assessment. Images were archived and stored off-line for post-processing.

7.2.5. MR Image Post-Processing

7.2.5.1. LV Volume Measurement

Global LV structure and function was assessed from prospective SSFP cine MRI (**Figure 7.1C**). Raw short-axis images were automatically sorted, cropped, and contrast-normalized in a

custom MATLAB (Natick, MA) program to ensure homogenous LV coverage and image quality, respectively. Segmentation was subsequently performed throughout all cardiac phases using a semi-automated 3D active contour segmentation program (ITK-SNAP, open access/source)[49] using edge-based snakes to identify the LV blood volume. LV end-diastolic volume (EDV), end-systolic volume (ESV), and ejection fraction (EF) were calculated throughout the entire cardiac cycle from segmented images using inputs of in-plane and through-plane spatial resolution.

7.2.5.2. Infarct Assessment

Myocardial wall thickness was measured over the course of the study from cine MRI images at end diastole. For infarct thickness assessment, thirty radially-oriented spokes were randomly positioned throughout each 3D infarct area in fifteen mid-ventricular slices using ImageJ software (NIH; Bethesda, MD). Platinum markers placed immediately post-MI and LGE images were used to confirm infarct boundaries. Infarct thickness was computed at each time point from the average spoke length. Similarly, remote wall thickness was also measured as a comparison.

Infarct surface area and volume were assessed at end diastole from the LGE images at each imaging time point using MIPAV software (NIH; Bethesda, MD; **Figure 7.1D**). Both infarct surface area and volume were normalized to total LV surface area and volume for each data set, respectively. The epicardium, endocardium, and infarct regions were manually contoured in fifteen slices from base to apex. The infarct was identified from the enhanced region in the LGE images and confirmed by comparing to platinum marker locations in the cine and SPAMM images. Surface area was calculated by multiplying contour perimeters by the slice thickness (4 mm) and number of analyzed slices. Volume was calculated by converting LGE image contours to binary masks to sum the voxels and computing a volume based on the spatial resolution (1.37x1.37x4.00 mm^3). It should be noted that the epicardial, endocardial, and infarct contours were the same for both the surface area and volume calculations.

7.2.5.3. Myocardial Strain Analysis

Regional wall function was assessed in terms of contractility and passive properties using systolic and diastolic strains, respectively. Regional strain measurements were calculated from 3D SPAMM acquisitions using an optical flow technique (**Figure 7.1E**).[50] Raw short-axis SPAMM images were first manually cropped to include only the left ventricle from the apex to the mitral annulus using ImageJ. Epicardial and endocardial contours were manually segmented at the early systolic or early diastolic reference state for the systolic and diastolic SPAMM data sets, respectively. Image masks were created from the segmented contours at the reference state to isolate the LV myocardium. A custom optical flow mapping algorithm integrated into ImageJ was used to derive high resolution, 3D displacement flow fields and strain tensors from the SPAMM images tracking from the reference state through end systole or end diastole for the systolic and diastolic SPAMM data, respectively.[50] In both data sets, the endocardial and epicardial infarct boundaries were identified using the previously placed platinum markers and confirmed by comparison with the enhanced region in the LGE images.

A custom MATLAB program was used for subsequent regional systolic strain analysis. First, a centroid was placed within the LV for each short-axis slice. The borderzone myocardium was then automatically defined to be the region extending 20 degrees beyond the infarct boundaries on each side.[7] Remote regions were automatically defined as extending 60 degrees beyond the borderzone boundaries on each side. The endocardial and epicardial edges were excluded to reduce noise from blood and lung movement, respectively. Maximum (ε_{max}) principal strains were then calculated from the strain tensors for each myocardial region (i.e., borderzone, remote), where ε_{max} represents the maximum systolic thickening as an estimate of myocardial contractility. Three-dimensional strain maps were generated to pictorially represent transmural differences in regional systolic strain.

7.2.6. *In Vivo* Diastolic Material Property Estimation

The details of the diastolic material property estimation scheme, which employs a combination of MRI data, finite element (FE) simulations, and numerical optimization, have been described previously.[37] Briefly, early diastole was taken to be the reference state for the animal-specific ventricular FE models since it represents a relatively stress-free state due to minimal LV pressure. LV volume was calculated at early and end diastole using endocardial contours performed at those respective time points multiplied by the spatial resolution *(area x in-plane resolution x through-plane resolution*). Synchronous LV pressure was recorded throughout diastole and used as a pressure boundary condition in the model.

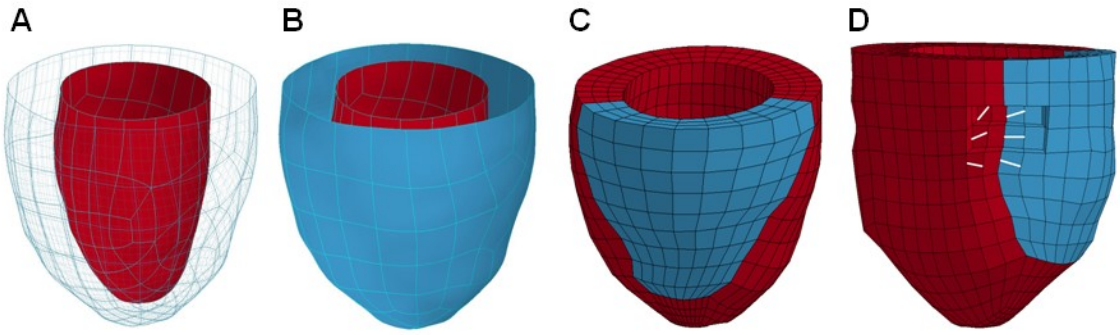

Figure 7.2. Development of finite element models from MRI-based animal specific data. FE models were generated by fitting MRI-derived endocardial and epicardial contours with 3D surfaces to represent the animal-specific geometry (A, B) and filling the myocardial space with hexahedral brick elements (C). The boundary between the infarct (blue) and remote (red) region was defined using 3D spline curves created from MRI-derived infarct contours projected onto the endocardial and epicardial surfaces (C). Myofiber angles were fixed for the remote region and assigned via optimization for the infarct region with respect to the circumferential direction (D).

As previously described,[37] FE models were generated by fitting the MRI-derived endocardial and epicardial contours at early diastole with 3D surfaces (Rapidform; INUS

Technology, Inc., Sunnyvale, CA; **Figure 7.2A,B**) and filling the myocardial space with hexahedral trilinear elements (TrueGrid; XYZ Scientific, Inc., Livermore, CA, USA; **Figure 7.2C**). The boundary between the infarct and remote region was defined using 3D spline curves created from MRI-derived infarct contours projected onto the endocardial and epicardial surfaces (**Figure 7.2C**). Myofiber angles were assigned for each hexahedral element using a custom MATLAB code. Remote angles were fixed to be 83° at the endocardial surface and -37° at the epicardial surface, with respect to the circumferential direction[51-53] whereas the infarct angles were assigned via an optimization algorithm (**Figure 7.2D**), which will be discussed later. For both the remote and infarct regions, the fiber angles were assumed to vary linearly in the transmural direction.

The diastolic material properties of both the control myocardial data and hydrogel-injected myocardial data were described by a nearly incompressible, transversely isotropic hyperelastic constitutive model given by:

$$W = \frac{1}{2}C(e^{Q} - 1) \tag{7.1}$$

where

$$Q = b_f E_{11}^2 + b_t(E_{22}^2 + E_{33}^2 + E_{23}^2 + E_{32}^2) + b_{fs}(E_{12}^2 + E_{21}^2 + E_{13}^2 + E_{31}^2) \tag{7.2}$$

The parameters C, b_f, b_t, b_{fs}, are constants that describe diastolic myocardial material properties and E_{ii} are the components of the Green–Lagrange strain tensor relative to the myofiber coordinate system (E_{11} = fiber direction, E_{22} = cross-fiber in-plane direction, E_{33} = transverse-fiber direction) and the remaining E_{ij} parameters are shear strains.[37] After splitting the strain energy function into dilatational and deviatoric components, near incompressibility was enforced using a penalty method on the dilatational part. Similar to Kichula et al.,[53] the same constitutive law was used to describe both the saline- and hydrogel-treated infarcts so that differences in myocardial stiffness could be attributed to altered material parameters with hydrogel delivery. The strain

energy function (**Equation 7.1**) was implemented using LS-DYNA software (Livermore Software Technology Corporation; Livermore, CA, USA).

Subsequently, LS-OPT software (Livermore Software Technology Corporation; Livermore, CA, USA) was used to determine the optimal set of material parameters by minimizing the error between the FE model predicted strain and the *in vivo* MRI measured strain. The parameters optimized included the diastolic material parameters (**Equation 7.1**) for the remote and infarct regions as well as the endocardial and epicardial fiber angles in the infarct. The mean standard error (MSE)[37] was the objective function minimized during the optimization to enable a direct comparison of the fit between the FE model- and MRI-derived strains. This was possible because the LV contours used to generate the model and the MRI-derived diastolic strains were from the same SPAMM data. In addition to the diastolic strain, constraints on LV cavity volume were incorporated into the MSE calculation to ensure better agreement, as described earlier. The parameters obtained from the optimization were then input into an equi-biaxial extension simulation to obtain representative stress-strain curves of the saline control and hydrogel treated regions.[37] To do so, it was assumed that the fiber and cross-fiber directions aligned with the two loading directions and that the simulated sample was a thin, incompressible tissue with uniform fiber orientation transmurally. Using a custom MATLAB code, stress was calculated for a range of strain values to facilitate a clearer interpretation of differences in myocardial properties.

7.2.7. Statistical Analysis

Data is presented as mean ± standard deviation (SD) or mean ± standard error of the mean (SEM), as indicated in each figure legend. Comparisons in LV volumes and function, wall thickness, infarct surface area, infarct volume, regional systolic strain, and diastolic material property estimations were performed using a one-way ANOVA with Tukey's post hoc evaluation. A $p<0.05$ was considered statistically significant.

7.3. Results

7.3.1. *In Vitro* Characterization of Selected Hydrogel Formulation

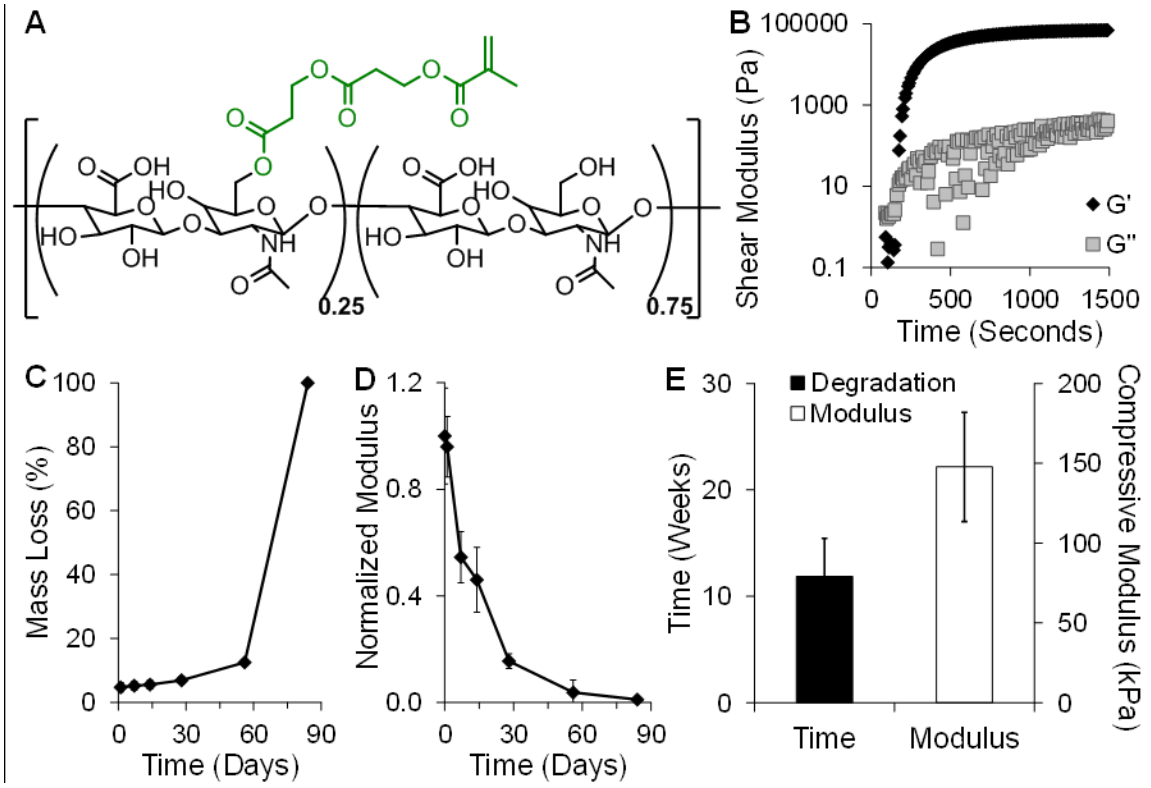

Figure 7.3. *In vitro* characterization of hydrogel selected for use *in vivo*. Chemical structure of HeMA-HA, where 25% of the HA repeat units were modified with HeMA (A). Representative rheological time sweep after mixing HeMA-HA with APS and TEMED, where the intersection of the storage (G') and loss (G") moduli is defined as gel onset (B). Representative temporal degradation, *n=1*, (C) and compressive mechanical, *n=4*, (D) profiles. Degradation and initial mechanics of selected HeMA-HA formulation, *n=4* (E). Data presented as mean ± SD.

Based on previous HeMA-HA hydrogel characterization studies (Section 4.3.2), a single HeMA-HA formulation was selected for *in vivo* assessment: 25% modified HeMA-HA (**Figure 7.3A**) at 8 wt% and gelled using 5 mM APS and 5 mM TEMED. Prior to its application *in vivo*, the properties of this selected formulation were characterized *in vitro*. Gelation onset occurred at 2.1

± 0.5 min and the crosslinking reaction reached a plateau within 20 minutes (gel completion: 15.9 ± 2.9 min) after introducing the dissolved macromer to the initiators (**Figure 7.3B**). As discussed in Section 5.2.6, the timing of gelation onset dictated the timing for injection *in vivo*. The temporal degradation (**Figure 7.3C**) and compressive mechanical (**Figure 7.3D**) profiles demonstrated hydrogels of this formulation gradually degraded and lost their mechanics over 12 weeks, which was the intended duration of the *in vivo* study. In addition, hydrogels were formed with an initial compressive modulus of 147.7 ± 34.2 kPa and degraded at 11.9 ± 3.6 weeks (**Figure 7.3E**).

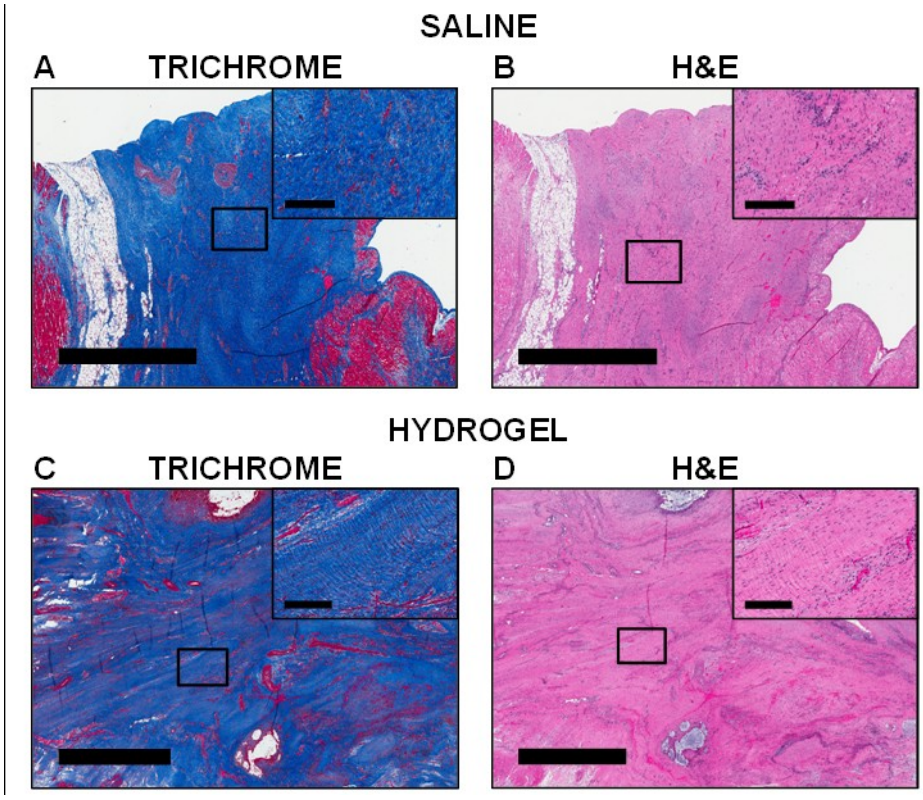

Figure 7.4. Histological assessment of infarcts. Histological evaluation using Masson's Trichrome (A, C) and H&E (B, D) stains of saline treated (A, B) and hydrogel treated (C, D) animals at 12 weeks post-MI. Inset indicated by black square. Scale bar = 2 mm; scale bar for inset = 200 μm.

7.3.2. Histological Evaluation and *Ex Vivo* Infarct Thickness

Histological assessment of the infarct region at the terminal time point revealed similar stages of remodeling (i.e., extensive collagen staining, lack of functional myocytes, etc.) in both the hydrogel treated and saline control animals (**Figure 7.4**). Hydrogel was not observed at 12 weeks following injection in the treatment animals, which is consistent with the previous *in vitro* degradation (**Figure 7.3C,E**). Regional myocardial wall thickness measured *ex vivo* at 12 weeks using planimetry showed greater thicknesses in the infarct, borderzone, and remote regions in the hydrogel treated animals relative to saline control animals (**Figure 7.6A,B**). In both the hydrogel and saline treated animals, the myocardial wall was most thin in the infarct region and became increasingly thicker moving outward to the borderzone and then the remote regions.

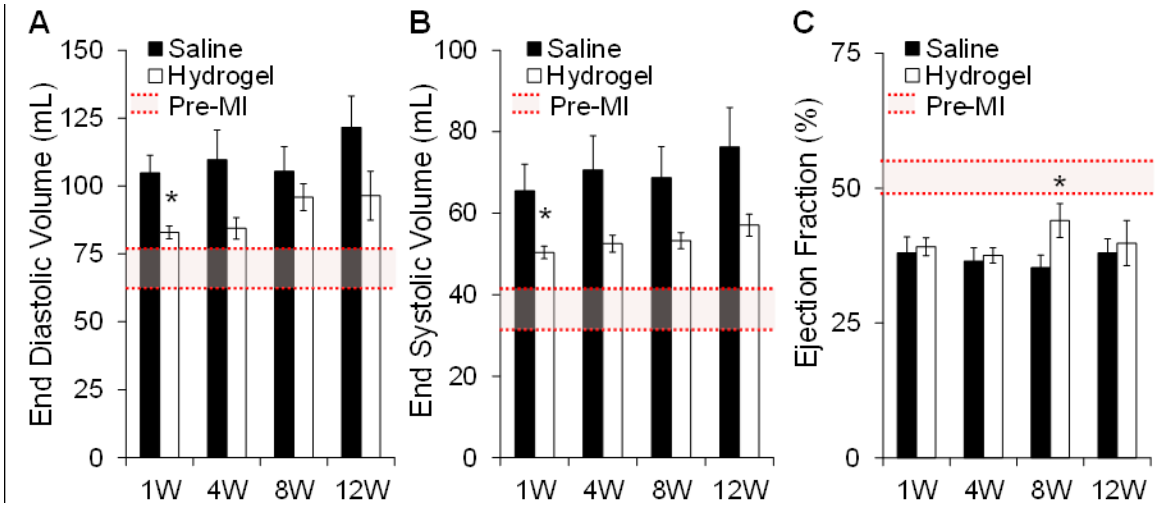

Figure 7.5. Global cardiac structural and functional outcomes. LV volume and function assessed by segmenting cine MRI images throughout all cardiac phases, *n=3-6/group*. Hydrogel treatment led to decreased LV volumes (A, B) and improved cardiac function in terms of ejection fraction (D). Data presented as mean ± SEM. **p<0.05* vs. saline controls.

7.3.3. Global LV Structure and Function

Analysis of the cine MRI data revealed that delivery of the injectable HeMA-HA hydrogel system to an *in vivo* porcine infarct model led to smaller LV end systolic volumes (ESV) and end diastolic volumes (EDV) at all time points relative to control animals that received saline injections (**Figure 7.5A,B**). Moreover, the LV volumes in the hydrogel treated animals were significantly smaller than the volumes of the saline control animals at 1 week post-MI (EDV, $p=0.005$; ESV, $p=0.03$). Overall, a trend towards progressively increasing LV volumes over time was observed in both the saline control and hydrogel treatment animals. Comparison of the saline treated volumes relative to the baseline (pre-MI) volumes (EDV, 69.4 ± 7.9 mL; ESV, 35.5 ± 5.7 mL) indicated that the majority of the ventricular expansion occurred within the first week post-MI. For the saline control group, all volumes were statistically greater ($p<0.05$) than the baseline volumes. For the hydrogel treatment group, all ESV were statistically greater than baseline whereas the EDV were not statistically different ($p>0.05$) from baseline values aside from at 8 weeks ($p=0.04$).

Ventricular function measured in terms of ejection fraction (EF) was greater with hydrogel therapy than saline at all time points (**Figure 7.5C**). At 8 weeks, the average EF of the hydrogel animals was significantly different ($p<0.05$) than controls. Relative to baseline (51.2 ± 3.5%), EF's were statistically different in the saline group at all time points and in the hydrogel group at 1 and 4 weeks post-MI. At 8 and 12 weeks post-MI, the EF of the hydrogel animals was not significantly different ($p>0.05$) than the baseline.

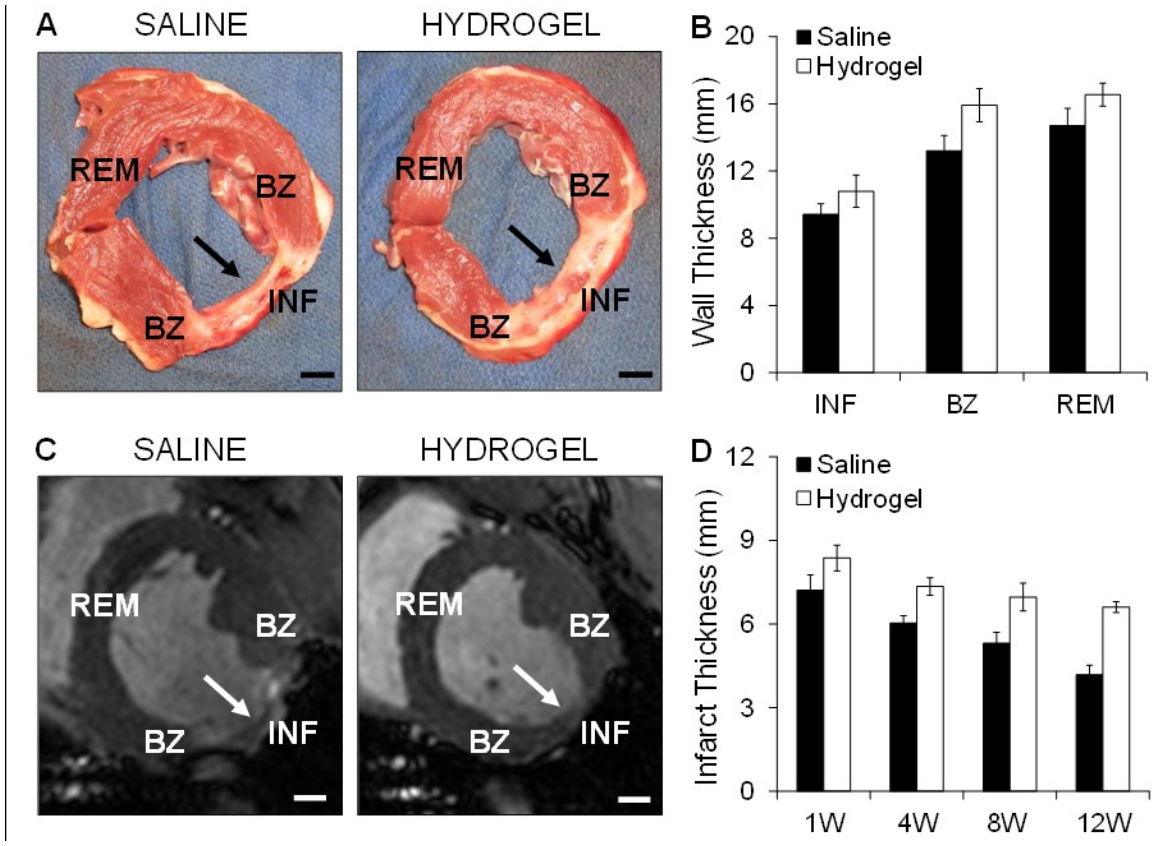

Figure 7.6. Myocardial wall thicknesses measured *ex vivo* and *in vivo*. Wall thickness was measured *ex vivo* at different locations (INF: infarct; BZ: borderzone; REM: remote) at 12 weeks using planimetry (A, B) and *in vivo* in the infarct (white arrows) throughout the study by analyzing cine MRI at end diastole (C, D). Representative MRI at 12 weeks indicating infarct region (arrows) are given for saline and hydrogel animals (A, C). Quantification both *ex vivo, n=5-6/group* (B) and *in vivo, n=3-6/group* (D) showed increased myocardial wall thickness with hydrogel therapy. Data presented as mean ± SEM. *$p<0.05$ vs. saline controls. Scale bars = 1 cm.

7.3.4. *In Vivo* Infarct Thickness and Expansion over Time

Infarct wall thickness measured *in vivo* throughout the duration of the study from cine MRI demonstrated increased thickness with hydrogel therapy as compared to controls that was statistically significant past one week (**Figure 7.6C,D**). Progressive infarct wall thinning occurred

in both groups over time. This trend was confirmed qualitatively in the LGE MRI, where regions of enhanced signal were localized to the infarct (**Figure 7.7**). All infarct thicknesses in both groups were statistically significant from the baseline posterolateral wall thickness (9.6 ± 0.4 mm) aside from the hydrogel group at 1 week post-MI (8.4 ± 0.5 mm, *p=0.07*). As a comparison, the remote wall thickness remained unchanged over the 12 week study for both groups (average over time points: hydrogel, 9.5 ± 0.1 mm; saline, 9.6 ± 0.1 mm) and there was no statistically significant difference as compared to the baseline value at each time point (baseline, 9.6 ± 0.2 mm).

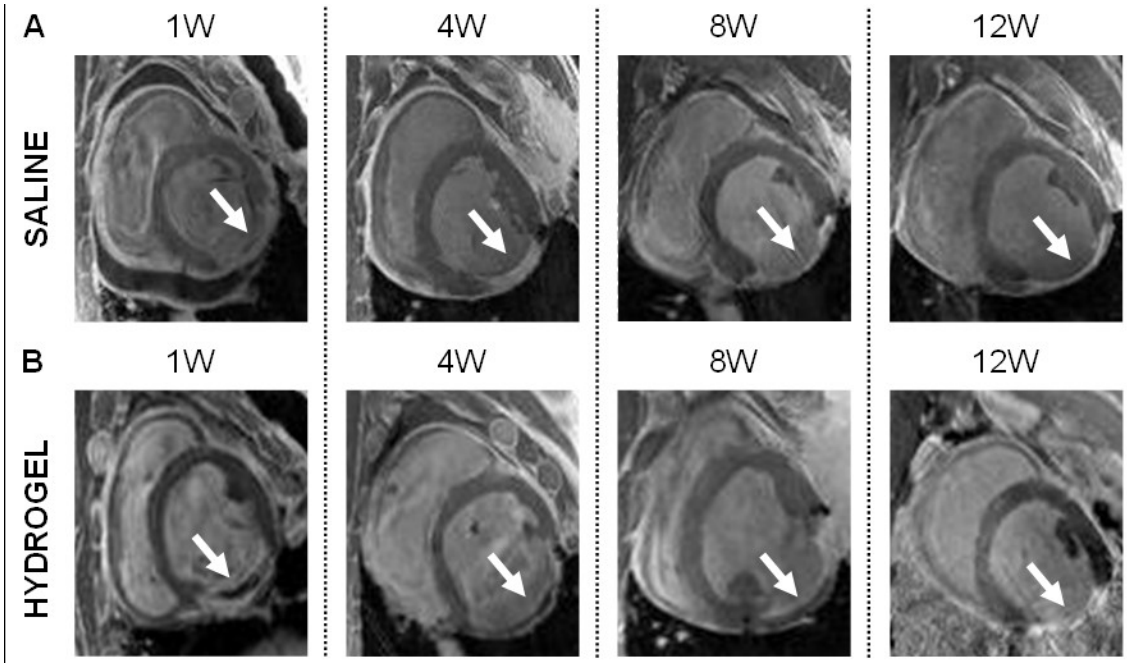

Figure 7.7. Infarct area assessment from late-gadolinium enhancement (LGE) MRI. Representative images from saline (A) and hydrogel (B) treated animals demonstrate thinning of the infarct (enhanced region) without therapy and hydrogel presence (dark regions) out to 8 weeks with treatment (arrows).

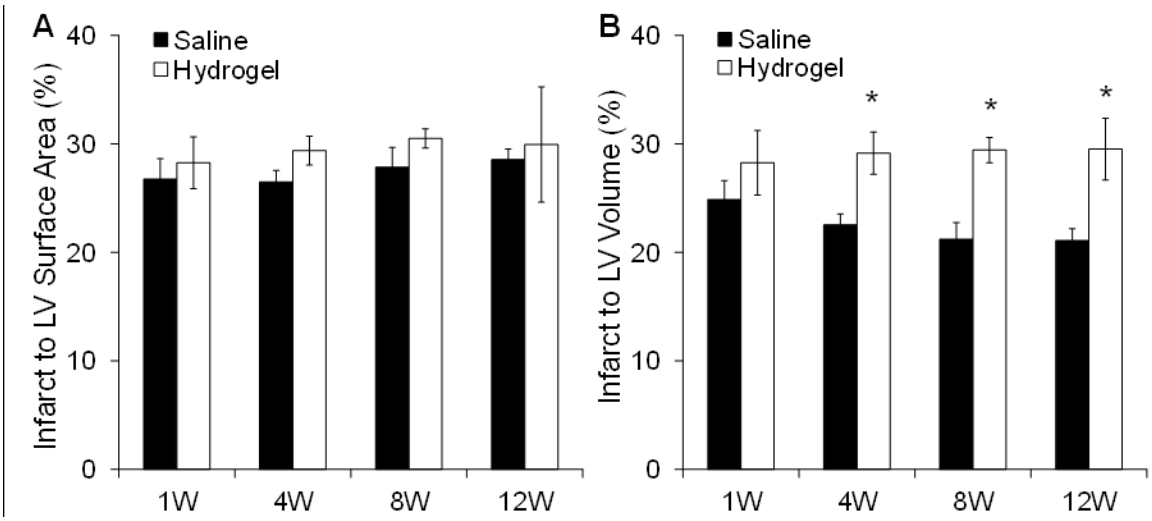

Figure 7.8. Contributions of infarct thinning and expansion from *in vivo* assessment. Infarct surface area and volume were quantified by contouring the infarct and LV in LGE images in MIPAV. Infarct surface area was similar between saline and hydrogel animals (A). Infarct volume was consistent in hydrogel animals due to bulking but decreased with saline due to thinning (B), *n=3-6/group*. Data presented as mean ± SEM. **p<0.05* vs. saline.

Changes in infarct expansion were assessed by analyzing the LGE MR images to measure infarct surface area and infarct volume. Infarct surface areas normalized to the total LV surface area were maintained throughout the duration of the study in both the hydrogel and saline groups without significant differences between the two groups (**Figure 7.8A**). Thus, the infarct surface area expanded at the same rate as the LV surface area over the course of the study. In contrast, infarct volumes normalized to the total LV volumes were maintained in the animals with hydrogel injections but decreased in saline treated animals over the four time points (**Figure 7.8B**). Beyond 1 week post-MI, the infarct volume in the hydrogel animals was significantly different (*p<0.05*) than the control animals.

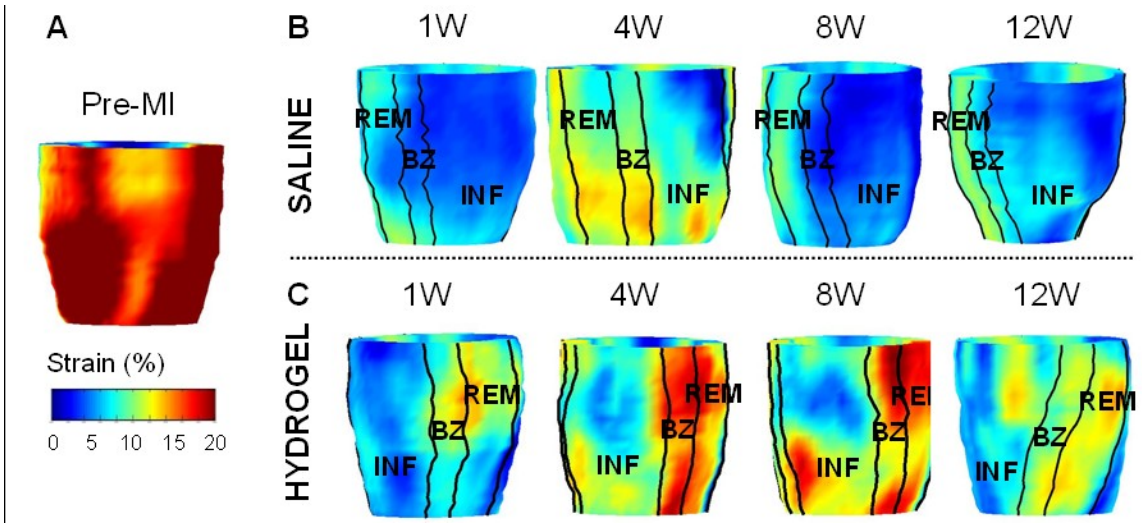

Figure 7.9. Regional wall function assessed in terms of contractility using systolic strain. Three-dimensional models of regional maximum principal strain (ε_{max}) from a representative baseline animal (A) and saline (B) and hydrogel (C) treated animals generated from SPAMM images using an optical flow method to track tag displacement. Strain was calculated for different myocardial locations (INF: infarct; BZ: borderzone; REM: remote) at 1, 4, 8, and 12 weeks post-MI.

7.3.5. Myocardial Systolic Strain as an Estimate of Contractility

Regional principal strain analysis of the systolic SPAMM data demonstrated increased maximum principal strain (ε_{max}) magnitude moving from the borderzone to the remote regions at each time point in both the hydrogel treatment and saline control groups. This trend was reflected both qualitatively through 3D strain models (**Figure 7.9**) and quantitatively (**Figure 7.10**). Beyond one week, the systolic borderzone strain magnitudes were higher with hydrogel therapy than saline delivery (**Figure 7.10B**), whereas remote systolic strain magnitude remained similar between the two conditions (**Figure 7.10C**). However, no statistical differences were observed in systolic strain magnitudes between the hydrogel and saline groups at each time point or between the different time points within each group for the borderzone and remote regions. In all regions at all time points and for both conditions, the systolic strain magnitude was significantly reduced ($p<0.05$) relative to the baseline systolic strain magnitude (15.5 ± 1.5%).

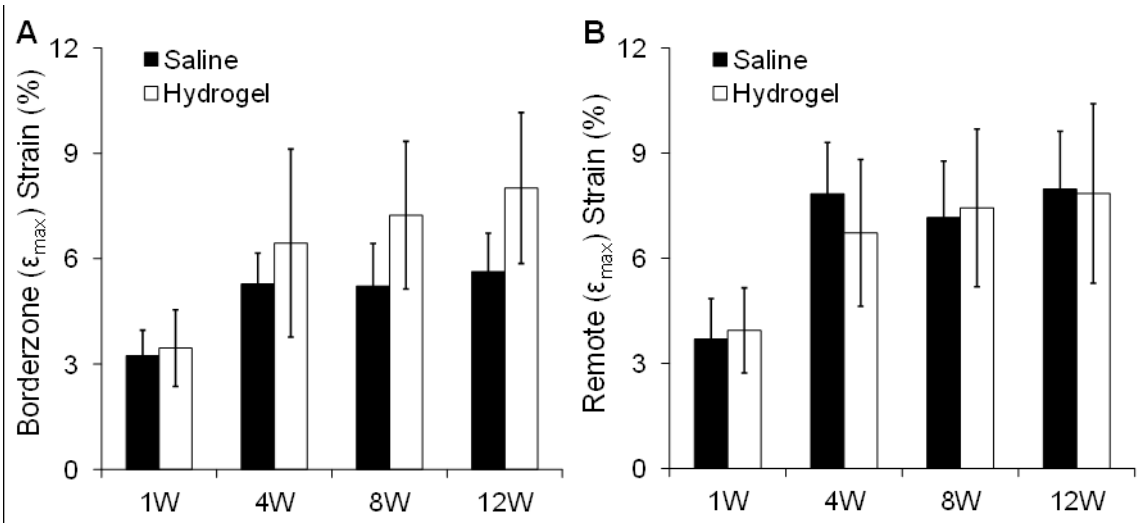

Figure 7.10. Quantification of regional systolic strain as an estimate of myocardial contractility. Regional radial maximum principal strain (ε_{max}) was calculated from systolic SPAMM images for the borderzone (A) and remote (B) regions. Beyond one week, systolic borderzone strain was higher with hydrogel therapy than saline, implying preserved contractility (A), whereas remote systolic strain remained similar between conditions (B), *n=3-6/group*. In all regions, systolic strain was significantly decreased (*p<0.05*) relative to the baseline (pre-MI) systolic strain of 15.5 ± 1.5%. Data presented as mean ± SEM.

7.3.6. Estimation of *In Vivo* Diastolic Myocardial Properties using FE Modeling

Animal-specific FE models were used to predict diastolic principal strains, for a given applied pressure, as a measure of passive myocardial properties (**Figure 7.11**). The constitutive model parameters (*C,* b_f, b_t, b_{fs}) and infarct fiber angles were determined via optimization to represent the diastolic myocardial properties for each treatment and control animal (**Tables 7.1**, **7.2**). The MSE values, which describe the degree of error between the MRI-derived and FE-model predicted strains, range from 6.1 ± 1.5 to 11.3 ± 9.5. The average MSE values are consistent with previous studies[36,54] and imply good agreement between the data and models. Also, the values were comparable over the different time points and similar but slightly less for the hydrogel data sets as compared to the saline data.

Table 7.1. FE model optimization results for infarct region.

		Time Point				
		Pre-MI	**1 Week**	**4 Week**	**8 Week**	**12 Week**
Saline	**C (kPa)**	0.39 ± 0.10	1.48 ± 1.40	6.08 ± 4.03	9.38 ± 5.10	4.01 ± 2.34
	b_f	72.03 ± 29.63	171.53 ± 39.78	13.77 ± 12.54	15.28 ± 19.71	19.01 ± 31.15
	b_t	5.08 ± 4.53	24.22 ± 19.62	6.58 ± 5.96	8.32 ± 4.59	8.07 ± 5.64
	b_{fs}	36.69 ± 18.23	22.25 ± 17.55	8.64 ± 2.51	25.27 ± 27.41	17.19 ± 18.13
	epi-angle (deg)		-14.89 ± 21.30	-23.00 ± 25.01	-18.15 ±21.81	-33.54 ± 25.73
	endo-angle (deg)		43.56 ± 2.50	35.66 ± 21.41	26.69 ± 14.61	9.18 ± 15.42
	MSE	8.64 ± 1.53	7.43 ± 4.02	7.62 ± 2.08	11.31 ± 9.46	8.14 ± 3.63
Hydrogel	**C (kPa)**		4.05 ± 2.86	4.38 ± 5.00	1.47 ± 1.54	5.36 ± 6.28
	b_f		137.67 ± 102.75	122.59 ± 94.49	139.26 ± 99.94	41.27 ± 67.66
	b_t		11.38 ± 6.95	9.21 ± 6.31	18.55 ± 23.25	14.46 ± 14.47
	b_{fs}		25.63 ± 21.05	30.02 ± 25.12	25.74 ± 20.63	23.54 ± 29.29
	epi-angle (deg)		-8.88 ± 15.60	-10.07 ± 17.17	-2.16 ± 3.07	-24.28 ± 20.95
	endo-angle (deg)		56.84 ± 16.75	32.07 ± 18.96	25.63 ± 17.16	28.83 ± 24.93
	MSE		6.14 ± 1.53	7.08 ± 2.16	9.81 ± 4.25	8.87 ± 3.55

Table 7.2. FE model optimization results for remote region.

		Time Point				
		Pre-MI	**1 Week**	**4 Week**	**8 Week**	**12 Week**
Saline	**C (kPa)**	0.39 ± 0.10	2.59 ± 2.13	1.85 ± 2.66	0.52 ± 0.18	0.41 ± 0.24
	b_f	72.03 ± 29.63	29.44 ± 39.21	30.15 ± 39.21	37.67 ± 28.94	29.52 ± 11.15
	b_t	5.08 ± 4.53	11.04 ± 15.64	9.28 ± 4.21	17.39 ± 15.75	11.14 ± 7.92
	b_{fs}	36.69 ± 18.23	19.35 ± 16.46	28.45 ± 18.67	23.12 ± 15.77	30.86 ± 15.45
Hydrogel	**C (kPa)**		0.75 ± 0.62	0.52 ± 0.43	0.69 ± 0.36	1.19 ± 1.37
	b_f		31.77 ± 26.07	56.01 ± 33.62	40.55 ± 28.70	42.29 ± 34.98
	b_t		22.11 ± 16.87	25.14 ± 14.68	19.62 ± 15.13	17.39 ± 18.33
	b_{fs}		33.84 ± 13.89	45.49 ± 6.55	43.07 ± 11.50	46.02 ± 4.31

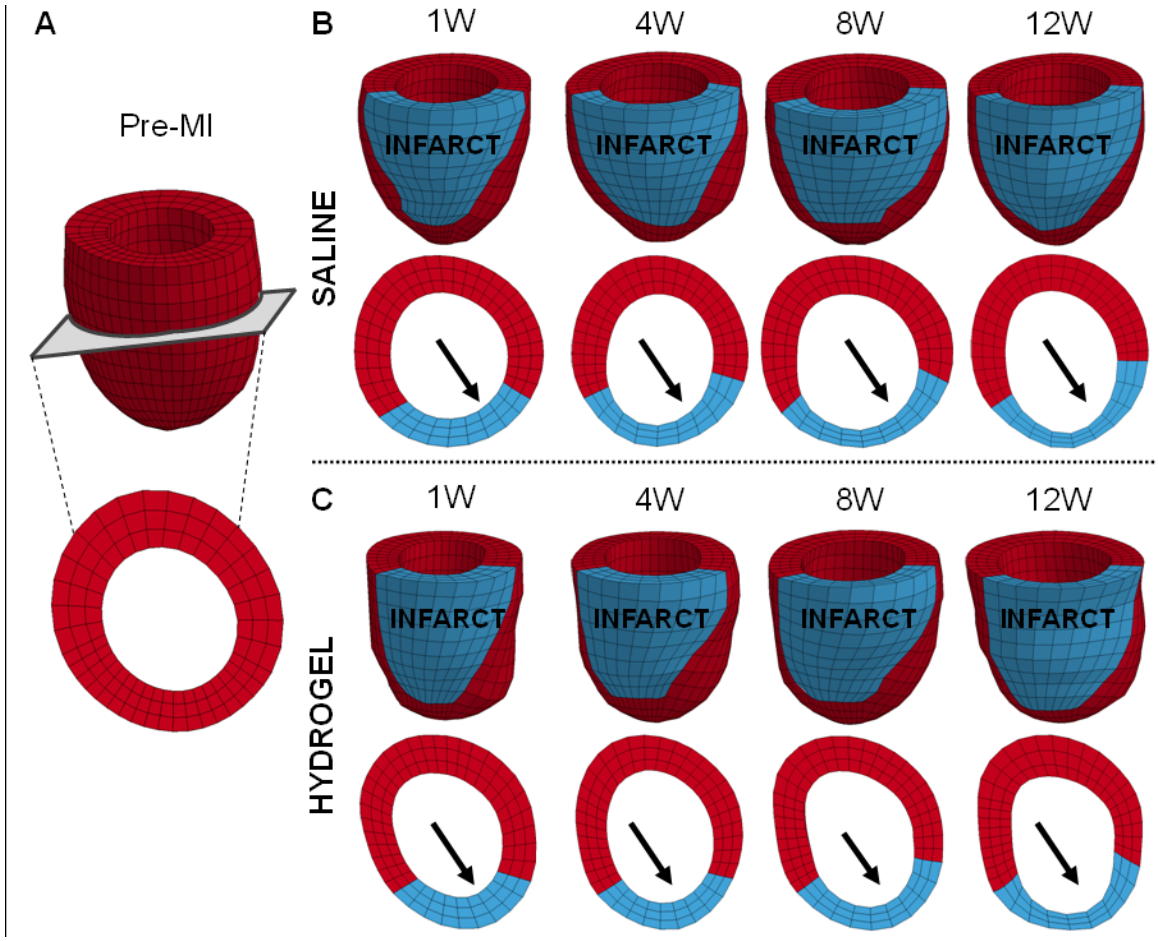

Figure 7.11. Finite element model to assess passive myocardial properties. Representative finite element models of a baseline animal (A) and saline (B) and hydrogel (C) treated animals at 1, 4 and 8, and 12 weeks. The infarct (red) and remote (blue) regions were assigned different myocardial tissue properties. Short axis views taken from roughly the same position at mid-ventricle demonstrate thinning of the infarct region over time (arrows).

The optimized infarct fiber angles ranged from -33.5 ± 25.7° to -2.2 ± 3.1° at the epicardial surface and 9.2 ± 15.4° to 56.8 ± 16.8° at the endocardial surface. In both animal conditions, the fiber angles were closer to 0° at the epicardial than endocardial surface, where proximity to 0° dictates the degree of circumferential fiber orientation. Comparison of the fiber angles between the hydrogel and saline data sets revealed that the epicardial fiber angles were

closer to 0° in the hydrogel data but the endocardial angles were closer to 0° in the saline data. Over time, the epicardial angles increased to be further away from 0° whereas the endocardial angles decreased closer to 0° in both conditions. Using the optimized parameters, FE models showed small strains in the infarct that increased outward to the surrounding remote regions in both groups (**Figure 7.12**). Also, both the remote and infarct strains increased over the study.

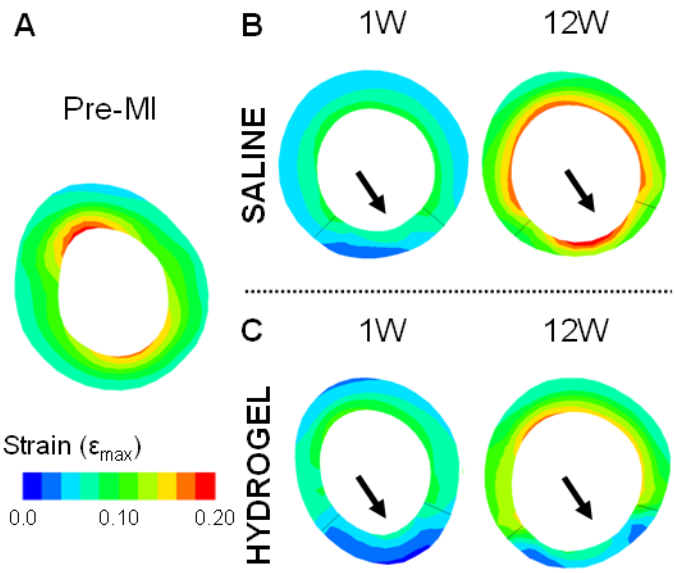

Figure 7.12. Short-axis view of the diastolic principal strain generated from FE model simulations. Representative short-axis strain maps of a baseline animal (A) and saline (B) and hydrogel (C) treated animals at 1 and 12 weeks. The end-diastolic pressure was set to be a constant 10 mmHg to ensure all data sets experienced the same load.

To better understand differences in passive myocardial properties, simulated equi-biaxial tests were used to estimate stress over a given range of strain values and generate stress-strain curves in the fiber and cross-fiber direction. The Green–Lagrange strain ranges were selected from the FE model predicted diastolic strains (**Figure 7.12**). Examination of the stress-strain curves revealed stiffening of the infarct in both the hydrogel and saline animals at 1 week following infarct induction as compared to baseline (**Figure 7.13**). With each subsequent time

point, the infarct became progressively less stiff in both animal groups, yet remained stiffer than at baseline even out to 12 week post-MI. These trends were consistent between the fiber and cross-fiber direction but the stiffness in the fiber direction was greater than the cross-fiber direction at each time point when comparing within each animal condition. Most importantly, at each time point, the stiffness of the infarct in the hydrogel treated animals was greater than that of saline injected animals in both the fiber and cross-fiber direction.

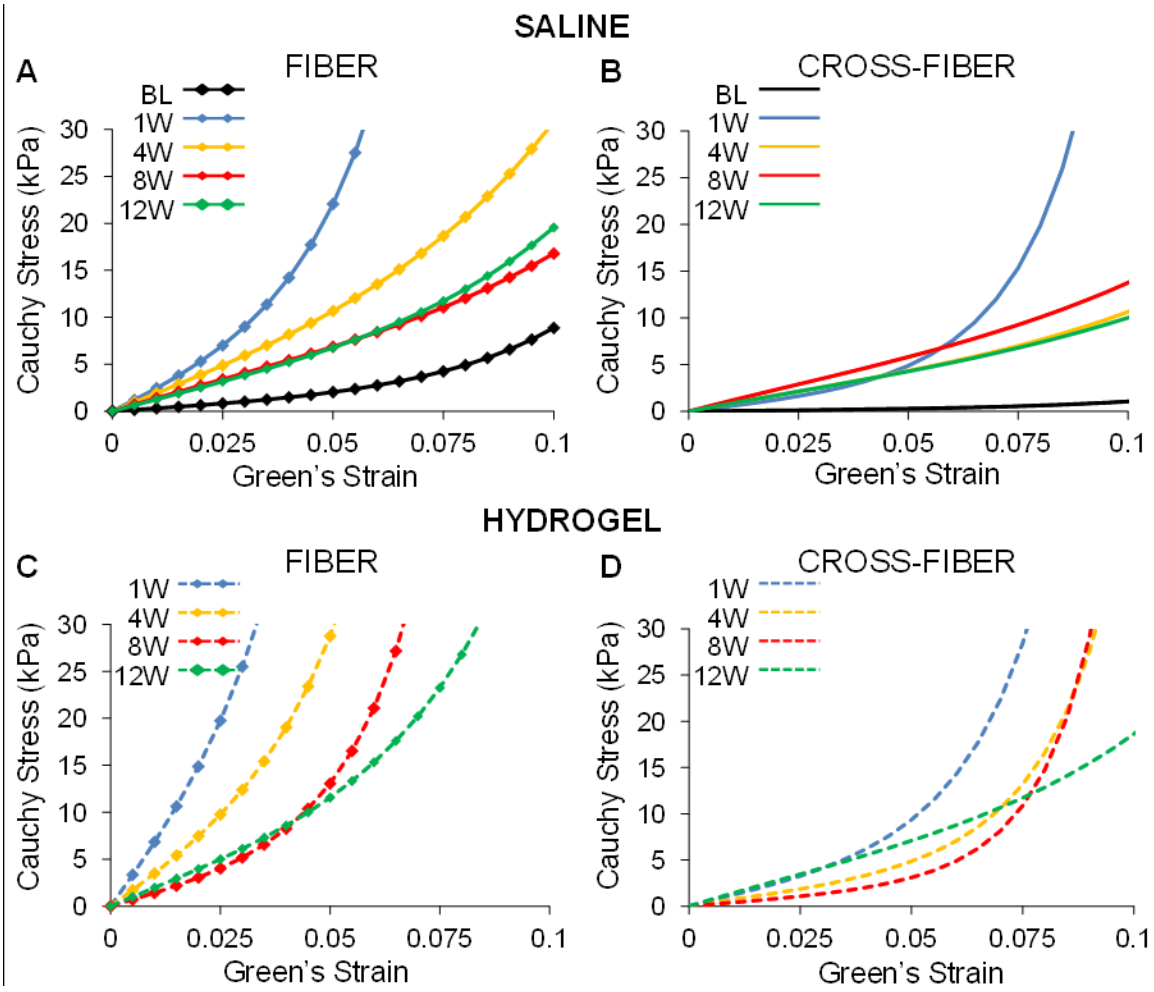

Figure 7.13. Simulated equi-biaxial extension tests using FE model optimization parameters. Stress-strain equations were implemented to calculate stress at the same set of strain points for each case. Average stress-strain plots for the infarct region of saline (top) and hydrogel (bottom) animals in the fiber (A, C) and cross-fiber (B, D) direction in saline treated animals over time.

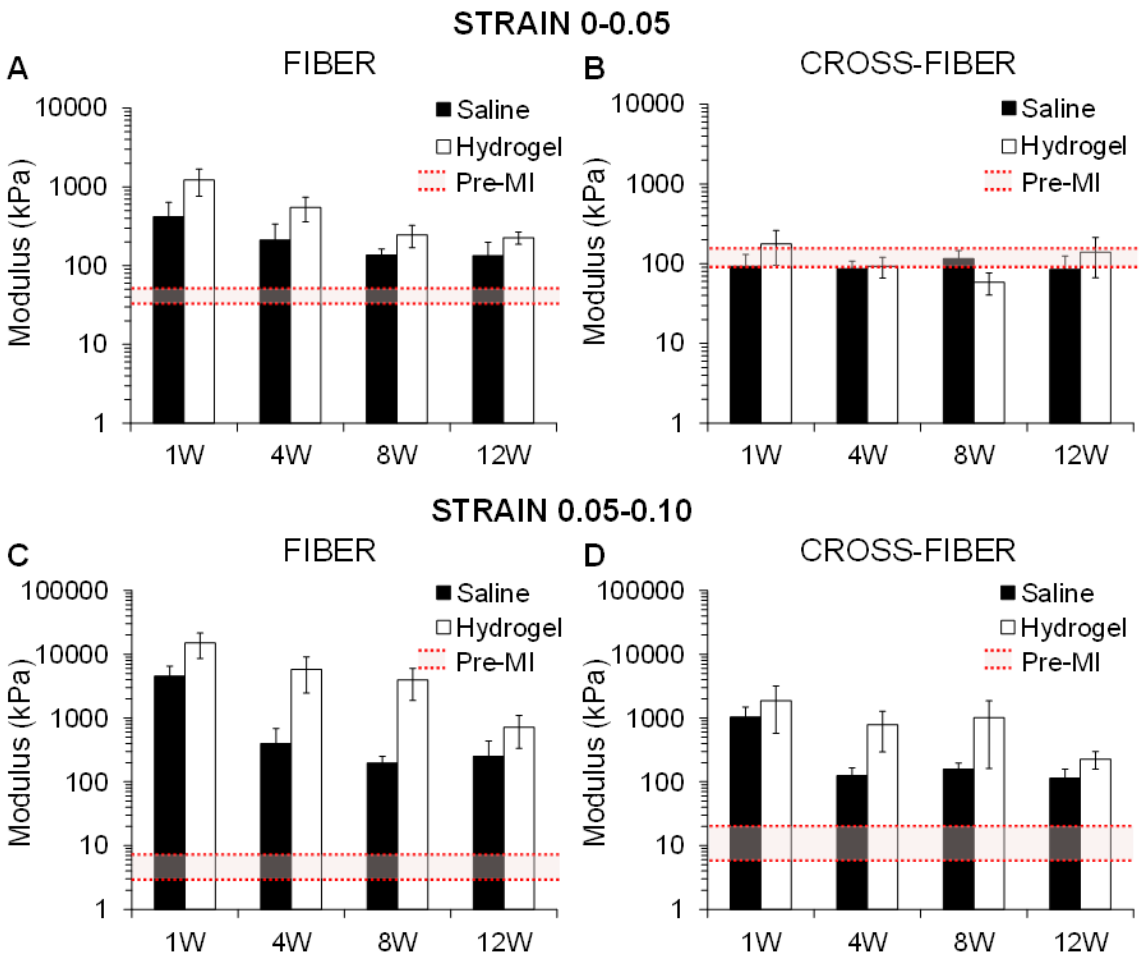

Figure 7.14. Quantification of moduli in the infarct region from simulated equi-biaxial tests. Moduli were calculated at different strain ranges for extension in both the fiber (A, C) and cross-fiber (B, D) direction in saline and hydrogel treated animals over time. Data presented as mean ± SEM.

Quantification of the moduli from the stress-strain plots over different strain ranges (0-0.05 and 0.05-0.10) further confirmed greater infarct stiffness in the hydrogel animals as compared to the saline control animals at each time point out to 12 weeks, particularly in the fiber direction (**Figure 7.14**). In addition, infarct stiffness was greater with extension simulated in the fiber direction relative to the cross-fiber direction and this stiffening response progressively declined as time from infarct induction increased. Despite the trends, there were no statistical differences between the hydrogel and control moduli. For the 0-0.05 strain range, all moduli were

statistically greater than baseline aside from the hydrogel group at 12 weeks in the fiber direction ($p=0.01$) and the saline group at 8 weeks in the fiber direction ($p=0.03$) and at 4 and 8 weeks in the cross-fiber direction (4 weeks, $p=0.03$; 8 weeks, $p=0.04$). For the 0.05-0.10 strain range, all moduli were significantly different than baseline aside from the moduli in the cross-fiber direction for the hydrogel group at 12 weeks ($p=0.03$) and the saline group at 8 weeks ($p=0.03$).

7.4. Discussion

Over the past decade, it has become evident that the regional mechanical changes in the myocardium must be considered when designing biomaterial approaches for MI repair.[4,17,55] Previous biomaterial studies designed to alter myocardial mechanics post-MI have demonstrated that delivery of injectable materials leads to thicker, stiffer infarcts with limited infarct expansion and preserved LV geometry.[18,19,56,57] Although promising, increased myocardial wall thickness[58-62] and/or decreased infarct size[58] alone do not directly correlate with improved cardiac function. Thus, a better understanding of the correlations between myocardial tissue properties and improved outcomes is needed to identify optimal biomaterial properties and improve therapy design. Towards this goal, this work used MRI and FE modeling as tools to examine the impact of an injectable hydrogel system on myocardial tissue properties in terms of regional thickness and expansion, contractility, and stiffening.

In this chapter, a HA hydrogel with high initial mechanics was used to investigate the ability of injectable hydrogels to alter myocardial tissue properties as a means to attenuate LV remodeling. Previous *in vivo* studies using HA hydrogels demonstrated that gels that were present for over eight weeks with initial mechanics greater than that of the normal myocardium (compressive modulus ~7-10 kPa) were more effective at maintaining LV structure post-MI than hydrogels with lower mechanics in an ovine infarct model.[18,19] Moreover, FE modeling using experimentally derived biaxial inputs from HA hydrogel-myocardial composites indicated that a stiffer hydrogel formulation will further reduce wall stress to attenuate remodeling.[53] Therefore, a single hydrogel formulation was selected for *in vivo* application with the following anticipated

optimal properties: an *in vitro* degradation profile greater than eight weeks and an initial compressive modulus greater than ten times that of the normal myocardium. LGE MR images throughout the 12 week study correlated with the *in vitro* degradation profile (**Figure 7.3C,E**) of this formulation in that the material appeared to be present in the infarct region at the 8 week time point but was no longer present at 12 weeks (**Figure 7.7**). This was further confirmed by histology where gel was not observed at the terminal time point (**Figure 7.4**). Even though one hydrogel formulation was applied, the use of *in vivo*-derived MRI data and FE modeling as tools to better understand impact of hydrogels on LV remodeling can be applied to any injectable system.

Remodeling post-MI was evaluated using MRI at 1, 4, 8, and 12 weeks following injection of either hydrogel for the treatment animals or saline for the control animals. Outcomes were assessed into the chronic remodeling period to contrast with the majority of previous cardiac biomaterial studies which focus on acute remodeling out to 4 or 8 weeks post-MI.[63] The impact of hydrogel delivery on LV remodeling was first examined in terms of global ventricular structure and function. As expected, intramyocardial hydrogel injection resulted in preserved LV geometry and improved cardiac function as compared to saline delivery at all time points (**Figure 7.5**). Although both groups demonstrated signs of adverse remodeling relative to baseline conditions, the ability of hydrogel therapy to minimize LV dilation was maintained throughout the 12 week study, in contrast to previous work where structural LV benefits observed at 4 weeks were lost by the 2 month terminal time point.[61] These findings correlated with our previous echocardiographic studies which demonstrated better maintenance of LV structure with HA hydrogel injection compared to infarct controls in an ovine anteroapical infarct model.[18,19] To expand upon our previous work, this chapter used MRI to serially examine the impact of hydrogel delivery on *in vivo* infarct thinning and expansion, myocardial contractility, and passive myocardial stiffening to better understand how hydrogel therapy led to these positive structural and functional outcomes.

Thinning of the myocardium post-MI has been identified to be an important contributor to increased wall stress, both in the infarct and surrounding borderzone regions. Thus, myocardial

thickness was measured to assess the ability of hydrogel therapy to bulk and stabilize the heart wall to attenuate remodeling. As anticipated, *ex vivo* assessment at the terminal time point revealed increased thickness in the infarct, borderzone, and remote myocardium with hydrogel therapy, and *in vivo* assessment over the course of the 12 week study demonstrated increased infarct thickness in the infarct at each time point due to hydrogel bulking (**Figure 7.6A,B**). Many studies have demonstrated similar increases in *ex vivo* infarct thickness with material delivery[18,19,63], but few have quantified parameters of infarct thinning noninvasively over time similar to this study.[47] Moreover, the progressive decrease in infarct wall thickness observed over time in both groups is consistent with the global LV outcomes and provides insight into the biological consequence of remodeling. A contributing factor to remodeling is the increase is the activation of matrix metalloproteinases (MMPs) in the myocardium which leads to extracellular matrix (ECM) breakdown;[60,64,65] this offers a biological explanation for the global LV dilation and associated infarct thinning and expansion.

The infarct expansion into the surrounding borderzone regions that occurs as the heart dilates and myocardial walls thin has been shown to both precipitate and sustain the entire remodeling process.[6,66-68] Thus, the impact of hydrogel injection on infarct expansion (i.e., stretching) was assessed by measuring the infarct surface area and volume and normalizing to total LV surface area and volume, respectively. Infarct surface area is primarily a measure of infarct expansion whereas infarct volume accounts for both infarct thinning and expansion. From the global ventricular assessment of EDV and ESV (**Figure 7.5A,B**), it was known that the LV was dilating outward in both groups over the 12 weeks. The minimal change in infarct surface area over time and between the two groups suggests that the rate of infarct expansion was similar to the rate of LV dilation in both hydrogel and saline treated animals (**Figure 7.8A**). However, since there was less overall LV dilation with hydrogel delivery at each time point (**Figure 7.5A,B**), the infarct in the hydrogel treated animals expanded less than in the saline animals. Furthermore, since the infarct at the time of induction comprised 20-25% of the LV

surface area by the surgeon's visual assessment,[48] infarct surface areas on the order of ~30% at 1 week indicate that the majority of the infarct expansion occurred within the first week after MI.

In contrast to infarct surface area, assessment of infarct volume resulted in differences between the hydrogel and saline groups. Since infarct volume accounts for both infarct thinning and expansion, the maintained infarct volume relative to the total LV volume over the four time points with hydrogel therapy (**Figure 7.8B**) is consistent with the minimal changes in infarct thickness (**Figure 7.6C,D**) and infarct surface area as a measure of expansion (**Figure 7.8A**). Similarly, the decrease in infarct volume over time with saline delivery correlates with the extreme thinning observed over time due to matrix degradation in the infarct (**Figure 7.6**), since minimal changes were observed in rate of infarct expansion (**Figure 7.8B**). Thus, assessment of infarct surface area demonstrated less infarct expansion with hydrogel therapy due to less LV dilation as compared to controls whereas assessment of infarct volume over time further confirmed the trends in infarct thickness in that injectable hydrogels function by bulking the myocardial wall.

Abnormal stress distributions in the borderzone myocardium which result from infarct thinning and expansion may lead to global contractile dysfunction and heart failure.[5,6,8,66,69] Thus, regional myocardial systolic strain was measured as an estimate of myocardial contractility and regional wall function. The low principal strain magnitudes at 1 week seen in all regions and in both groups can be explained by myocardial stunning in the acute post-MI period.[71] Past 1 week, hydrogel delivery was shown to improve borderzone myocardial contractility throughout the duration of the study relative to saline injections (**Figure 7.10B**). By bulking the myocardial wall in the region of infarction (**Figure 7.6**), the injectable HA hydrogels facilitated an environment where normally perfused myocardium could continue to contract. Combined with a limitation in outward infarct extension (**Figure 7.8B**), this suggests that hydrogel therapy prevented the expansion of contractile dysfunction to progressively larger regions of perfused borderzone myocardium, which in turn led to improved global cardiac outcomes (**Figure 7.5**). The increased systolic borderzone strain in the hydrogel treated animals as compared to controls supports the theory that LV

remodeling is driven by thinning of the myocardial wall in the region of infarction leading to increased wall compliance. However, systolic myocardial wall strain and global LV function are indirect measures of *in vivo* myocardial compliance and wall stress, parameters that are traditionally assessed using *ex vivo* biaxial testing. To circumvent the need for *ex vivo* assessment, *in vivo* strain data was subsequently input into a FE model to simulate LV diastolic filling and measure forces in the myocardial wall.

Due to the role of increased infarct compliance in sustaining adverse remodeling,[70,72] MRI-derived diastolic strains were input into a FE model to directly quantify *in vivo* passive mechanical properties in the myocardium and provide an understanding of the impact of hydrogel delivery on *in vivo* wall compliance (**Figure 7.11**). Assessment of regional stress-strain relationships using simulated equi-biaxial extension tests demonstrated that hydrogel injection led to increased myocardial stiffness in the infarct region relative to controls, with a larger impact on mechanics in the fiber direction as compared to the cross-fiber direction (**Figures 7.13**, **7.14**). In both animal groups, extensive stiffening of the infarct was seen at 1 week post-MI compared to baseline and the stiffening response progressively decreased over time. This initial stiffening response can be attributed to the collagen deposition occurs in the infarct region during remodeling as the infarct attempts unsuccessfully to repair itself[73,74] whereas the gradual decrease in infarct stiffness could result from a combination of matrix degradation due to MMP activation[60,64,65] and extensive loss of type I collagen post-MI,[75] leaving the myocardium at a mechanical disadvantage. Furthermore, the increased stiffening with hydrogel injection indicates that hydrogel delivery successfully altered the material properties of the infarct at a time point prior to when the body had compensated for remodeling and highlights the importance of appropriately timing hydrogel delivery in the remodeling process to maximize benefit. In combination with the systolic strain assessment of contractility, this suggests that the stiffening of the infarct with hydrogel injections led to stabilization of the borderzone myocardium, which in turn preserved the contractile function in this region (**Figure 7.10B**).

7.5. Conclusions

An injectable, degradable hydrogel system was successfully applied to an *in vivo* porcine infarct model to examine its effect on global LV remodeling, infarct thinning and expansion, and regional myocardial wall function using MRI and FE modeling. MRI analysis demonstrated that injectable HA hydrogels can improve LV structure and function, preserve infarct thickness, limit infarct dilatation, and preserve borderzone contractility. Input of MRI-derived diastolic strain parameters into a FE model showed hydrogel delivery led to increased myocardial stiffness in the infarct that was better maintained throughout the 12 week study as compared to saline-treated controls. Overall, evaluation of myocardial properties using MRI and FE modeling provides additional insight into the mechanism by which injectable materials improve long-term structural and functional outcomes post-MI and ultimately, can serve as a tool to determine optimal biomaterial properties for MI repair.

7.6. References

1. Bui AL, Horwich TB, Fonarow GC. Epidemiology and risk profile of heart failure. Nat Rev Cardiol 2011;8(1):30-41.

2. Go AS, Mozaffarian D, Roger VL, Benjamin EJ, Berry JD, Blaha MJ, et al. Heart disease and stroke statistics-2014 update: A report from the American Heart Association. Circulation 2014;129(3):e28-e292.

3. Gheorghiade M, Bonow RO. Chronic heart failure in the United States: A manifestation of coronary artery disease. Circulation 1998;97(3):282-289.

4. Buckberg GD. Architecture must document functional evidence to explain the living rhythm. Eur J Cardiothorac Surg 2005;27(2):202-209.

5. Jackson BM, Gorman JH,3rd, Salgo IS, Moainie SL, Plappert T, St John-Sutton M, et al. Border zone geometry increases wall stress after myocardial infarction: Contrast echocardiographic assessment. Am J Physiol Heart Circ Physiol 2003;284(2):H475-H479.

6. Kramer CM, Lima JA, Reichek N, Ferrari VA, Llaneras MR, Palmon LC, et al. Regional differences in function within noninfarcted myocardium during left ventricular remodeling. Circulation 1993;88(3):1279-1288.

7. Pilla JJ, Blom AS, Gorman JH,3rd, Brockman DJ, Affuso J, Parish LM, et al. Early postinfarction ventricular restraint improves borderzone wall thickening dynamics during remodeling. Ann Thorac Surg 2005;80(6):2257-2262.

8. Epstein FH, Yang Z, Gilson WD, Berr SS, Kramer CM, French BA. MR tagging early after myocardial infarction in mice demonstrates contractile dysfunction in adjacent and remote regions. Magn Reson Med 2002;48(2):399-403.

9. Kelley ST, Malekan R, Gorman JH,3rd, Jackson BM, Gorman RC, Suzuki Y, et al. Restraining infarct expansion preserves left ventricular geometry and function after acute anteroapical infarction. Circulation 1999;99(1):135-142.

10. Klodell CT,Jr, Aranda JM,Jr, McGiffin DC, Rayburn BK, Sun B, Abraham WT, et al. Worldwide surgical experience with the Paracor HeartNet cardiac restraint device. J Thorac Cardiovasc Surg 2008;135(1):188-195.

11. Sartipy U, Albage A, Lindblom D. The Dor procedure for left ventricular reconstruction. Ten-year clinical experience. Eur J Cardiothorac Surg 2005;27(6):1005-1010.

12. Starling RC, Jessup M, Oh JK, Sabbah HN, Acker MA, Mann DL, et al. Sustained benefits of the CorCap Cardiac Support Device on left ventricular remodeling: Three year follow-up results from the Acorn clinical trial. Ann Thorac Surg 2007;84(4):1236-1242.

13. Batista R. Partial left ventriculectomy--the Batista procedure. Eur J Cardiothorac Surg 1999;15 Suppl 1:S12-9; discussion S39-43.

14. Shapira K, Dikovsky D, Habib M, Gepstein L, Seliktar D. Hydrogels for cardiac tissue regeneration. Biomed Mater Eng 2008;18(4-5):309-314.

15. Nelson DM, Ma Z, Fujimoto KL, Hashizume R, Wagner WR. Intra-myocardial biomaterial injection therapy in the treatment of heart failure: Materials, outcomes and challenges. Acta Biomater 2011;7(1):1-15.

16. Tous E, Purcell B, Ifkovits JL, Burdick JA. Injectable acellular hydrogels for cardiac repair. J Cardiovasc Transl Res 2011;4(5):528-542.

17. Holmes JW, Borg TK, Covell JW. Structure and mechanics of healing myocardial infarcts. Annu Rev Biomed Eng 2005;7:223-253.

18. Ifkovits JL, Tous E, Minakawa M, Morita M, Robb JD, Koomalsingh KJ, et al. Injectable hydrogel properties influence infarct expansion and extent of postinfarction left ventricular remodeling in an ovine model. Proc Natl Acad Sci U S A 2010;107(25):11507-11512.

19. Tous E, Ifkovits JL, Koomalsingh KJ, Shuto T, Soeda T, Kondo N, et al. Influence of injectable hyaluronic acid hydrogel degradation behavior on infarction-induced ventricular remodeling. Biomacromolecules 2011;12(11):4127-4135.

20. Reeder SB, Du YP, Lima JA, Bluemke DA. Advanced cardiac MR imaging of ischemic heart disease. Radiographics 2001;21(4):1047-1074.

21. Steffans JC, Sakuma H, Bourne MW, Higgins CB. Magnetic resonance imaging in ischemic heart disease. Am Heart J 1996;132(1 Pt 1):156-173.

22. Unlu M, Anik Y, Demirci A, Ural D, Kahraman G, Komsuoglu B. Cardiac MRI in ischemic heart disease with severe coronary artery stenosis. Acad Radiol 2006;13(11):1387-1393.

23. Viswamitra S, Higgins CB, Meacham DF, Mehta JL. Magnetic resonance imaging in myocardial ischemia. Curr Opin Cardiol 2004;19(5):510-516.

24. Rerkpattanapipat P, Link KM, Hamilton CA, Hundley WG. Detecting left ventricular myocardial ischemia during intravenous dobutamine with cardiovascular magnetic resonance imaging (MRI). J Cardiovasc Magn Reson 2001;3(1):21-25.

25. Sakuma H. Magnetic resonance imaging for ischemic heart disease. J Magn Reson Imaging 2007;26(1):3-13.

26. Ishida M, Kato S, Sakuma H. Cardiac MRI in ischemic heart disease. Circ J 2009;73(9):1577-1588.

27. Watzinger N, Maier R, Reiter U, Reiter G, Fuernau G, Wonisch M, et al. Clinical applications of cardiovascular magnetic resonance. Curr Pharm Des 2005;11(4):457-475.

28. Ligabue G, Fiocchi F, Ferraresi S, Barbieri A, Romagnoli R, Torricelli P. How to quantify infarct size on delayed-enhancement MR images: A comparison between visual and quantitative approach. Radiol Med 2007;112(7):959-968.

29. Axel L, Dougherty L. Heart wall motion: Improved method of spatial modulation of magnetization for MR imaging. Radiology 1989;172(2):349-350.

30. Zerhouni EA, Parish DM, Rogers WJ, Yang A, Shapiro EP. Human heart: tagging with MR imaging - A method for noninvasive assessment of myocardial motion. Radiology 1988;169(1):59-63.

31. Wall ST, Walker JC, Healy KE, Ratcliffe MB, Guccione JM. Theoretical impact of the injection of material into the myocardium: A finite element model simulation. Circulation 2006;114(24):2627-2635.

32. Wenk JF, Wall ST, Peterson RC, Helgerson SL, Sabbah HN, Burger M, et al. A method for automatically optimizing medical devices for treating heart failure: Designing polymeric injection patterns. J Biomech Eng 2009;131(12):121011.

33. Wenk JF, Eslami P, Zhang Z, Xu C, Kuhl E, Gorman,Joseph H.,,III, et al. A novel method for quantifying the in-vivo mechanical effect of material injected into a myocardial infarction. Ann Thorac Surg 2011;92(3):935-941.

34. Wenk JF, Klepach D, Lee LC, Zhang Z, Ge L, Tseng EE, et al. First evidence of depressed contractility in the border zone of a human myocardial infarction. Ann Thorac Surg 2012;93(4):1188-1194.

35. Walker JC, Ratcliffe MB, Zhang P, Wallace AW, Fata B, Hsu EW, et al. MRI-based finite-element analysis of left ventricular aneurysm. Am J Physiol Heart Circ Physiol 2005;289(2):H692-700.

36. Sun K, Stander N, Jhun C, Zhang Z, Suzuki T, Wang G, et al. A computationally efficient formal optimization of regional myocardial contractility in a sheep with left ventricular aneurysm. J Biomech Eng -Trans ASME 2009;131(11):111001.

37. Mojsejenko D, McGarvey JR, Dorsey SM, Gorman JH,3rd, Burdick JA, Pilla JJ, et al. Estimating passive mechanical properties in a myocardial infarction using MRI and finite element simulations. Biomech Model Mechanobiol 2014.

38. Xi J, Lamata P, Niederer S, Land S, Shi W, Zhuang X, et al. The estimation of patient-specific cardiac diastolic functions from clinical measurements. Med Image Anal 2013;17(2):133-146.

39. Burdick JA, Prestwich GD. Hyaluronic acid hydrogels for biomedical applications. Adv Mater 2011;23(12):H41-H56.

40. Li Y, Toole BP, Dealy CN, Kosher RA. Hyaluronan in limb morphogenesis. Dev Biol 2007;305(2):411-420.

41. Toole BP. Hyaluronan: From extracellular glue to pericellular cue. Nat Rev Cancer 2004;4(7):528-539.

42. Toole BP. Hyaluronan in morphogenesis. J Intern Med 1997;242(1):35-40.

43. Temenoff JS, Kasper FK, Mikos AG. Fumarate-based macromers as scaffolds for tissue engineering applications. In: Ashammakhi N, Reis R, Chiellini E, editors. Topics in Tissue Engineering. 3rd ed. Oulu, Finland: University of Oulu; 2007. p. 6.1-6.16.

44. Anseth KS, Bowman CN, Brannon-Peppas L. Mechanical properties of hydrogels and their experimental determination. Biomaterials 1996;17(17):1647-1657.

45. Bitter T, Muir HM. A modified uronic acid carbazole reaction. Anal Biochem 1962;4:330-334.

46. Platzer M, Ozegowski JH, Neubert RH. Quantification of hyaluronan in pharmaceutical formulations using high performance capillary electrophoresis and the modified uronic acid carbazole reaction. J Pharm Biomed Anal 1999;21(3):491-496.

47. McGarvey JM, Kondo N, Witschey WRT, Takebe M, Aoki C, Burdick JA, et al. Injectable microsphere gel progressively improves global ventricular function, regional contractile strain, and mitral regurgitation after myocardial infarction. in review .

48. Witschey WRT, Pilla JJ, Ferrari G, Koomalsingh K, Haris M, Hinmon R, et al. Rotating frame spin lattice relaxation in a swine model of chronic, left ventricular myocardial infarction. Magn Reson Med 2010;64(5):1454-1461.

49. Yushkevich PA, Piven J, Hazlett HC, Smith RG, Ho S, Gee JC, et al. User-guided 3D active contour segmentation of anatomical structures: Significantly improved efficiency and reliability. Neuroimage 2006;31(3):1116-1128.

50. Xu C, Pilla JJ, Isaac G, Gorman JH,3rd, Blom AS, Gorman RC, et al. Deformation analysis of 3D tagged cardiac images using an optical flow method. J Cardiovasc Magn Reson 2010;12:19.

51. Lee W, Pernot M, Couade M, Messas E, Bruneval P, Bel A, et al. Mapping myocardial fiber orientation using echocardiography-based shear wave imaging. IEEE Trans Med Imaging 2012;31(3):554-562.

52. Hooks DA, Trew ML, Caldwell BJ, Sands GB, LeGrice IJ, Smaill BH. Laminar arrangement of ventricular myocytes influences electrical behavior of the heart. Circ Res 2007;101(10):E103-E112.

53. Kichula ET, Wang H, Dorsey SM, Szczesny SE, Elliott DM, Burdick JA, et al. Experimental and computational investigation of altered mechanical properties in myocardium after hydrogel injection. Ann Biomed Eng 2014;42(7):1546-1556.

54. Wenk JF, Sun K, Zhang Z, Soleimani M, Ge L, Saloner D, et al. Regional left ventricular myocardial contractility and stress in a finite element model of posterobasal myocardial infarction. J Biomech Eng -Trans ASME 2011;133(4):044501.

55. Gupta KB, Ratcliffe MB, Fallert MA, Edmunds LH,Jr, Bogen DK. Changes in passive mechanical stiffness of myocardial tissue with aneurysm formation. Circulation 1994;89(5):2315-2326.

56. Morita M, Eckert CE, Matsuzaki K, Noma M, Ryan LP, Burdick JA, et al. Modification of Infarct Material Properties Limits Adverse Ventricular Remodeling. Ann Thorac Surg 2011;92(2):617-625.

57. Ryan LP, Matsuzaki K, Noma M, Jackson BM, Eperjesi TJ, Plappert TJ, et al. Dermal filler injection: A novel approach for limiting infarct expansion. Ann Thorac Surg 2009;87(1):148-155.

58. Yu J, Christman KL, Chin E, Sievers RE, Saeed M, Lee RJ. Restoration of left ventricular geometry and improvement of left ventricular function in a rodent model of chronic ischemic cardiomyopathy. J Thorac Cardiovasc Surg 2009;137(1):180-187.

59. Landa N, Miller L, Feinberg MS, Holbova R, Shachar M, Freeman I, et al. Effect of injectable alginate implant on cardiac remodeling and function after recent and old infarcts in rat. Circulation 2008;117(11):1388-1396.

60. Mukherjee R, Zavadzkas JA, Saunders SM, McLean JE, Jeffords LB, Beck C, et al. Targeted myocardial microinjections of a biocomposite material reduces infarct expansion in pigs. Ann Thorac Surg 2008;86(4):1268-1276.

61. Dobner S, Bezuidenhout D, Govender P, Zilla P, Davies N. A synthetic non-degradable polyethylene glycol hydrogel retards adverse post-infarct left ventricular remodeling. J Card Fail 2009;15(7):629-636.

62. Rane AA, Christman KL. Biomaterials for the treatment of myocardial infarction: A 5-year update. J Am Coll Cardiol 2011;58(25):2615-2629.

63. Dorsey SM, Burdick JA. Hydrogels for cardiac repair. In: Khademhosseini A, Demirci U, editors. Applications of Hydrogels in Regenerative Medicine; in press.

64. Mukherjee R, Brinsa TA, Dowdy KB, Scott AA, Baskin JM, Deschamps AM, et al. Myocardial infarct expansion and matrix metalloproteinase inhibition. Circulation 2003;107(4):618-625.

65. Mukherjee S, Venugopal JR, Ravichandran R, Ramakrishna S, Raghunath M. Multimodal biomaterial strategies for regeneration of infarcted myocardium. Journal of Materials Chemistry 2010;20(40):8819-8831.

66. Jackson BM, Gorman JH,3rd, Moainie SL, Guy TS, Narula N, Narula J, et al. Extension of borderzone myocardium in postinfarction dilated cardiomyopathy. J Am Coll Cardiol 2002;40(6):1160-7; discussion 1168-71.

67. Weisman HF, Healy B. Myocardial infarct expansion, infarct extension, and reinfarction - Pathophysiologic concepts. Prog Cardiovasc Dis 1987;30(2):73-110.

68. Erlebacher JA, Weiss JL, Weisfeldt ML, Bulkley BH. Early Dilation of the Infarcted Segment in Acute Transmural Myocardial-Infarction - Role of Infarct Expansion in Acute Left-Ventricular Enlargement. J Am Coll Cardiol 1984;4(2):201-208.

69. Weisman HF, Bush DE, Mannisi JA, Bulkley BH. Global cardiac remodeling after acute myocardial-infarction - A study in the rat model. J Am Coll Cardiol 1985;5(6):1355-1362.

70. Pilla JJ, Koomalsingh KJ, McGarvey JM, Witschey WRT, Dougherty L, Gorman JH,3rd, et al. Regional myocardial three-dimensional principal strains during post-infarction left ventricular remodeling. in review .

71. Camici PG, Prasad SK, Rimoldi OE. Stunning, hibernation, and assessment of myocardial viability. Circulation 2008;117(1):103-114.

72. Pilla JJ, Gorman JH,3rd, Gorman RC. Theoretic impact of infarct compliance on left ventricular function. Ann Thorac Surg 2009;87(3):803-811.

73. Holmes JW, Nunez JA, Covell JW. Functional implications of myocardial scar structure. American Journal of Physiology-Heart and Circulatory Physiology 1997;272(5):H2123-H2130.

74. Fomovsky GM, Rouillard AD, Holmes JW. Regional mechanics determine collagen fiber structure in healing myocardial infarcts. J Mol Cell Cardiol 2012;52(5):1083-1090.

75. Herpel E, Pritsch M, Koch A, Dengler T, Schirmacher P, Schnabel P. Interstitial fibrosis in the heart: differences in extracellular matrix proteins and matrix metalloproteinases in end-stage dilated, ischaemic and valvular cardiomyopathy. Histopathology 2006;48(6):736-747.

CHAPTER 8

Conclusions, Limitations, and Future Directions

8.1. Conclusions

Left ventricular (LV) remodeling initiated by a myocardial infarction (MI) continues to be a large clinical burden due to the high rate of progression to heart failure. Current treatment approaches focus on pharmacological and/or surgical therapies which are either insufficient to limit remodeling or highly invasive to deploy, respectively. Therefore, as described in Chapter 1, both noninvasive therapies and noninvasive techniques to assess the effects of therapies are needed to address the clinical burden of MI induced heart failure.

As discussed in Chapter 3, injectable hydrogels offer a noninvasive approach to target LV remodeling by simultaneously mechanically stabilizing the myocardial wall and modulating maladaptive biological processes as a delivery vehicle for therapies, such as cells and growth factors. Even though injectable materials have shown success in locally delivering cells and molecules to the heart, concerns with retention, engraftment, and dosage motivate the use of acellular materials as bulking agents to counteract the geometric changes post-MI in this dissertation. In addition, various natural and synthetic injectable materials have been investigated to attenuate remodeling, but the mechanism by which these injectable systems lead to positive structural and functional outcomes post-MI remains unclear. One step towards understanding this mechanism is the application of noninvasive imaging techniques to evaluate the reciprocal interaction between the injected material and the surrounding myocardial tissue. Of the imaging modalities, magnetic resonance imaging (MRI) is particularly well suited for material assessment and temporal evaluation of myocardial properties due to its high spatial and temporal resolution.

To assess differences in material properties once delivered to the myocardium, injectable systems with tunable properties are needed. Thus, Chapter 4 focused on the *in vitro* characterization of tunable, injectable hyaluronic acid (HA) hydrogels. Macromers were synthesized with a range of modifications by coupling either hydroxyethyl methacrylate (HeMA) or methacrylate (Me) to HA to generate the gel precursors HeMA-HA and MeHA, respectively. Hydrogels were formed by covalently crosslinking the methacrylate groups using a two component redox initiator system of APS and TEMED. In HeMA-HA homopolymer hydrogels, the initiator concentration, macromer modification, and macromer concentration were altered to investigate their effect on hydrogel gelation, degradation, and mechanics. Increased initiator concentration, macromer modification, or macromer concentration led to accelerated gelation, prolonged degradation, and higher initial mechanics that were maintained over longer durations. Altering a combination of the macromer modification and concentration was used to tailor HeMA-HA hydrogel degradation while maintaining similar initial mechanics. For hydrogels with approximately the same initial mechanics (30 kPa, 60 kPa, or 90 kPa), formulations with a higher modification but lower macromer concentration maintained their mechanics for longer and degraded slower (on the order of 6 weeks or more) than formulations with a lower modification but higher macromer concentration. Another approach to tuning hydrogel degradation was to form copolymer hydrogels of HeMA-HA and MeHA, where increased incorporation of non-hydrolytically susceptible MeHA led to slower degradation. The tunability of HA hydrogel properties was then applied to investigate the ability of MRI to detect these differences *ex vivo* in myocardial explants (Chapters 5 and 6) and to select a single hydrogel formulation with anticipated positive outcomes[1,2] for use in an *in vivo* infarct model (Chapter 7).

Two MRI approaches were then explored to visualize and characterize the properties of HA hydrogels in myocardial tissue explants. Theoretical models have demonstrated that hydrogel dispersion in tissue directly correlates with their ability to attenuate LV remodeling.[3] Thus, in Chapter 5, conventional MRI was used to quantify differences in three-dimensional hydrogel distribution in tissue based on varied gelation properties. Gelation onset was altered in MeHA

hydrogels such that an increased initiator concentration or macromer modification led to accelerated gelation, with initiator concentration having a greater impact on the time to gelation. Differences in the time to gelation led to differences in the distribution of the crosslinked (MRI detectable) portion of each hydrogel, with higher initiator concentration and higher macromer modification (at low initiator concentration) leading to a larger crosslinked volume. To investigate differences in the mechanism of gelation, hydrogel volumes were also assessed for self-assembling guest-host hydrogels. Unlike covalently crosslinked HA hydrogels which distributed along the myocardial fibers and formed a composite with the surrounding myocardial tissue, physically crosslinked guest-host HA hydrogels formed distinct plugs with calculated volumes comparable to the injected volume. Thus, MRI was successfully shown to characterize differences in hydrogel distribution based on gelation timing and mechanism of formation.

In Chapter 6, CEST MRI was used to visualize injectable HeMA-HA hydrogels either alone or after injection into tissue based on manipulation of the exchangeable hydroxyl (–OH) protons on the HA backbone. The CEST effect was shown to track with changes in material properties such that as hydrogel macromer concentration increased, the CEST contrast increased linearly. Furthermore, CEST MRI was used to detect HA hydrogels injected once into cardiac explants with an increase in signal at the hydrogel site relative to the surrounding myocardial signal. Unlike conventional MRI, CEST was shown to simultaneously visualize and discriminate between different injectable materials based on their specific chemical composition. More specifically, the CEST signal was tuned to detect differences in two hydrogel systems based on their dominant functional groups. The covalent addition of an arginine-based peptide to HeMA-HA hydrogels led to a two-fold increase in signal when the exchangeable amine ($–NH_2$) protons in the peptide were targeted. Therefore, CEST MRI was demonstrated to be a valuable tool for studying injectable hydrogel properties and could enable further optimization of biomaterial therapies aimed at clinical translation.

After examining the use of MRI to characterize the properties of injectable hydrogels once delivered to myocardial tissue, the focus of this dissertation shifted to using MRI to evaluate the effects of HA hydrogels on myocardial tissue properties as a means to understand their role in attenuating adverse remodeling following infarction. In Chapter 7, we investigated the long-term effects of degradable HeMA-HA hydrogels on global LV remodeling, infarct thinning and expansion, myocardial wall motion, and myocardial stiffness in a porcine infarct model out to 12 weeks post-MI using MRI and finite element (FE) modeling. Hydrogel treatment generally led to decreased LV volumes, improved ejection fractions, and increased wall thicknesses as compared to saline injected controls. Beyond 1 week post-MI, systolic borderzone strain was higher with hydrogel therapy than saline, implying preserved borderzone contractility. Furthermore, FE model simulations with diastolic strain inputs demonstrated that hydrogel therapy increased infarct stiffness out to 12 weeks post-MI. Hence, evaluation of myocardial tissue properties through MRI and FE modeling provided insight into the effect of injectable HA hydrogels therapies on myocardial structure and function post-MI and more universally, could serve as tools to investigate the impact of any injectable system on myocardial tissue properties.

8.2. Limitations

Specific Aim 1: Synthesize and characterize degradable HA hydrogels with a range of properties, particularly gelation, degradation, and mechanics.

8.2.1. Limitations in *In Vitro* Characterization Studies

A limitation in the *in vitro* characterization studies performed for Aim 1 was that degradation and mechanics were coupled in the HA hydrogel systems used (i.e., HeMA-HA and MeHA). In pure HeMA-HA hydrogels, even though a wide range of degradation profiles (1.7 to 22.5 weeks) and initial mechanics (2.6 to 457.6 kPa) were achieved by altering the macromer modification and concentration, the system was limited in that the degradation could only be tuned within a narrow range without altering the mechanics. To achieve similar initial mechanics,

the time to hydrogel degradation had to be relatively long (i.e., greater than 7 weeks). Similarly, to achieve large differences in degradation (i.e., 6 weeks or more), the initial mechanics had to be high relative to normal myocardial mechanics (i.e., 30 kPa or greater). Thus, it was not possible to form hydrogels with different rates of degradation but similar initial mechanics that matched those of the native myocardium (compressive modulus ~7-10 kPa). As will be discussed in Section 8.3.2, to achieve HeMA-HA hydrogels with degradation profiles that fit different stages of LV remodeling (i.e., ~2-3 weeks for acute remodeling and ~10-12 weeks for chronic remodeling),[4] the desire to have similar initial mechanics had to be sacrificed. Moreover, the incorporation of MeHA to form HeMA-HA/MeHA copolymer hydrogels further prolonged the degradation, where gels were stable over the span of several months, which was not physiologically relevant for a degradable system for MI repair. To decouple degradation and mechanics, other HA hydrogel systems should be explored with different mechanisms of crosslinking.[5,6]

Specific Aim 2: Visualize HA hydrogels using MRI as a means to examine hydrogel dispersion and detect differences in hydrogel chemical composition *ex vivo*.

8.2.2. Limitations in T_2-Weighted Imaging

In Aim 2 of this dissertation, the T_2-weighted imaging of HA hydrogels was limited to *ex vivo* studies and did not progress to *in vivo* studies. An *in vivo* study at 3 T was attempted where HeMA-HA hydrogels were injected into the posterolateral wall of a healthy sheep but magnetic field inhomogeneities, particularly in the free wall at the injection locations, severely limited material detection. Magnetic field inhomogeneity in the heart is primarily due to differences in magnetic field susceptibility[7,8] between the myocardium, blood, lung parenchyma and, in the case of animals that have undergone a recent thoracotomy, air spaces in the chest wall. Delivery of injectable materials via catheter may decrease magnetic field susceptibility differences to improve homogeneity by eliminating air in the chest cavity. However, since the magnetic susceptibility of cardiac tissue is spatially varying and unique to each animal (i.e., dependent on the animal's size and organ distribution), it is not possible to eliminate these effects completely. Shimming, or

mapping the magnetic field inhomogeneity to compensate for it, does help improve magnetic field homogeneity but is particularly challenging in the posterolateral heart wall due to the proximity to the lung parenchyma, which leads to a significant magnetic field gradient.[9] Moreover, maintaining field homogeneity is more difficult at higher field strengths because, from an engineering perspective, it is more challenging to induce a strong homogeneous magnetic field than a weak one.[7] This not only impacts the main B_0 field but also the homogeneity of the RF (B_1) field, which scales linearly with the main field. Thus, moving to lower but still clinically relevant magnetic field strength, such as 1.5 T, would decrease the inhomogeneity effects. Finally, certain pulse sequences are more susceptible to field inhomogeneity. As opposed to cardiac sequences such as those used for cine, perfusion, or SPAMM-tagging MRI, T_2 sequences are especially sensitive to field inhomogeneity because the RF refocusing pulses depend on precise B_1 homogeneity and the signal readout depends on excellent B_0 homogeneity.[9]

Another limitation of the T_2-weighted MRI of HA hydrogels in myocardial explants was that hydrogel visualization and quantification was only possible using normal, non-infarcted myocardial tissue. Whereas hydrogel distribution was easily quantified in explants following *in vivo* injection then sacrifice in a normal animal (Section 5.3.3), it was barely detectable in infarcted myocardial tissue where HA hydrogels were injected into mini-pigs immediately following MI and sacrificed at various time points out to two weeks post-MI. The adverse physiologic state of the infarcted myocardium, consisting of disordered collagen and myofiber architecture, fibrosis, and inflammation leading to iron deposition,[10-13] prevented quantification of hydrogel volumes in infarcted explants, potentially due to similarities in T_2 relaxation properties between the injected hydrogel and the surrounding damaged myocardial tissue.

8.2.3. Limitations in CEST Imaging

There were also several limitations and challenges encountered for the second non-contrast MRI technique explored in Aim 2. CEST imaging of HeMA-HA hydrogels phantoms at both 7 T and 3 T demonstrated that the CEST effect was not uniform within the hydrogels,

perhaps due to inhomogeneous crosslinking. Furthermore, *ex vivo* studies showed that the CEST effect from HeMA-HA hydrogels was fairly small (i.e., less than 3%) and also variable within the injection site, as may be expected due to crosslinking variations as the material dispersed between the myocardial fibers. This made translation to *in vivo* studies challenging. Moving to high field strength (i.e., 7 T) may help due to the improved signal-to-noise ratio (SNR) and spatial resolution, as demonstrated in Section 6.3.2. However, as discussed previously, magnetic field inhomogeneities scale with increased field strength, so increased inhomogeneity would make *in vivo* material detection more challenging. In addition, the large increase in power deposition at 7 T limits its clinical use,[14] as opposed to 3 T MR scanners which are utilized clinically.

Moreover, despite the higher concentration of hydroxyl (–OH) protons on the HA backbone, hydroxyl CEST is generally challenging due to the proximity of the –OH proton resonance to that of bulk water protons, leading to a higher potential for direct water saturation. Partial direct water saturation leads to a decrease in the water signal due to the RF pulse application and not from proton exchange, misconstruing the true CEST effect and thus decreasing CEST sensitivity.[15,16] As seen in the non-water suppressed spectroscopy studies (Section 6.3.3), where direct saturation effects should be smaller than at 3 T due to the higher magnetic field strength of the spectrometer (9.4 T), the –OH proton peak could not be resolved from the bulk water proton peak. Furthermore, it is possible that partial direct saturation could explain the positive CEST contrast seen in the phantom and explant studies.

Finally, similar to the T_2-weighted hydrogel imaging, CEST MRI was also limited to myocardial explants. Whereas *ex vivo* 3 T studies targeting the –OH protons on HA were promising, an *in vivo* study of HeMA-HA hydrogel injections attempted at 3 T in a normal sheep was unsuccessful. The injection site of the material in the posterolateral free wall made detection challenging due to substantial motion, particularly at higher saturation frequencies further from the bulk water resonance, despite both respiratory and cardiac gating. This motion led to large magnetic field inhomogeneities that were not able to be perfectly corrected for using the standard

WASSR techniques,[17,18] and thus prevented accurate z-spectral fitting of the CEST effect as a function of chemical shift to extract a reliable CEST contrast. To address the motion concerns of cardiac CEST *in vivo*, our collaborators in the Reddy lab developed a more accurate z-spectral fitting technique based on a probabilistic combination of Lorentzian functions to account for the direct saturation, magnetization transfer and CEST effects impacting the myocardial tissue.[19,20] When applied to the–OH CEST data from the *in vivo* injection study, there was substantial overlap in the proton resonance peaks between the bulk water protons and nearby –OH protons preventing resolution of the separate peaks for accurate fitting.

The partial direct saturation effect concerns with manipulating the –OH protons on HA motivated the switch to targeting amine (–NH) protons in an arginine-dominate peptide coupled to HA since they resonate further downfield from the bulk water protons.[20-23] Even though phantom studies demonstrated the ability to generate a CEST effect specific to the exchangeable proton group of interest (Section 6.3.3), this was unsuccessful in attempted explant studies. This limitation was most likely due to the high background myocardial CEST effect from endogenous amines that prevented detection of the arginine-based amines in the HA coupled peptide. More specifically, the labile amines in endogenous myocardial creatine, which is involved in energy production to power contraction, are known to resonate ~1.8 ppm downfield of bulk water,[20,23] which is identical to the resonance of the amines in the peptide as identified from spectroscopy. Future work should focus on the coupling of peptides with exchangeable protons whose resonance differs from that of endogenous myocardial metabolites. HeMA-HA-peptide hydrogels were also delivered *in vivo* to a healthy sheep and *in vivo* CEST imaging attempted. However, despite the decrease in direct water saturation, the same motion and inhomogeneity concerns as previously described with the HeMA-HA injections were encountered.

Specific Aim 3: Assess the temporal effects of degradable HA hydrogel therapy on long-term myocardial tissue remodeling post-MI using cardiac MRI and FE modeling in an *in vivo* porcine infarct model.

8.2.4. Limitations in *In Vivo* Study

A limitation of the *in vivo* work performed in Aim 3 was that only a single hydrogel formulation was assessed. Even though it was selected based on previous studies from our group[1,2] to have optimal properties (i.e., an *in vitro* degradation profile greater than eight weeks and an initial compressive modulus greater than ten times that of the normal myocardium), delivery of only one formulation prevented assessment of the correlation between material properties and positive *in vivo* outcomes. Based on the study design, it could not investigate the optimal degree and duration of mechanical stabilization needed to attenuate remodeling, and thus, the specific hydrogel properties for optimal *in vivo* outcomes remains unclear.

The animal model also involved injecting the hydrogel therapy into the infarct at thirty minutes following infarction. Even though this timing for delivery has been used by our group[1,2,24] and others[25-27] to evaluate the efficacy of injectable materials in animal MI studies, it is not clinically relevant[28,29] as MI patients would not receive therapy for at least several hours after the onset of MI. In addition, patients may be unstable during the initial period following MI trauma due to the upregulation of MMPs, which may cause the ventricle to be vulnerable to rupture.[30-34] Delivery at one week post-MI would be more clinically practical as it would give patients a period to recover and stabilize before undergoing an injection procedure.

The mode of material delivery directly into the myocardium through the epicardial surface with the need for a thoracotomy was also not clinically translatable. As discussed in Chapter 1, the primary advantage of injectable biomaterials over other tissue engineering strategies for cardiac repair, such as LV restraints or cardiac patches, is the potential for minimally invasive delivery, which decreases damage to the target tissue and other surrounding tissues and enables more rapid translation. Catheter-based approaches are ideal for a clinical setting to decrease procedure and recovery times for patients. Recent studies have shown the ability for injectable biomaterials to be delivered to large animal MI models using catheters.[35] However, the hydrogel

system utilized in this dissertation was unable to be delivered *in vivo* via catheter due to its rapid gelation time over the course of a few minutes.

Furthermore, the *in vivo* work in Aim 3 focused on the mechanical benefits of injectable HA hydrogels and their impact on myocardial tissue mechanics. However, biological processes, such as the activation of MMPs, play an important contributing factor in the progression to global LV remodeling and thus should be evaluated. In this work, temporal assessment with MRI prevented examination of the biological aspects of remodeling, aside from at the terminal time point. In addition, previous studies have demonstrated that HA itself has biological benefits with the ability to increase angiogenesis and potentially aid in cardiac regeneration in a MI model.[36,37] In the injectable system utilized in Aim 3, the biological benefits of HA delivery could not be evaluated separately from the mechanical benefits of the hydrogel because degradation and mechanics were coupled. Comparison to a non-bioactive material with similar hydrogel degradation and mechanics would demonstrate the biological significance of HA.

8.2.5. Limitations in FE Model

Even though the FE model developed in Aim 3 was novel in that it incorporated *in vivo*-derived parameters to describe the LV geometry and myocardial tissue properties in terms of regional strains, it was also limited. Myocardial fiber architecture was not incorporated, as the average myofiber angles were assigned to the myocardium and assumed to vary linearly in the transmural direction. To generate a more anatomically representative FE model, the spatially varying myofiber architecture should have been assessed using diffusion tensor MRI as another input for the model.[38] In addition, the model only examines the LV, which is directly impacted by the infarct, but does not incorporate pressures and deformations caused by the adjacent RV. Finally, early diastole was selected to be the reference state on which the FE model was built since pressure is at a minimum. However, the LV is still partially loaded at this phase and there may be residual active tension in the myocardial fibers that, if not adequately accounted for, would alter the mechanical properties of the myocardium. Recent studies have incorporated

techniques for determining the unloaded LV geometry[39] that should be utilized in the future to make the model more physiologically relevant.

8.3. Future Directions

8.3.1. *In Vivo* Hydrogel Imaging

Based on the limitations of the studies performed throughout this dissertation, there are several avenues for future exploration related to the assessment of injectable HA hydrogels using MRI. First of all, future studies should involve the translation of the T_2-weighted and CEST MRI techniques investigated in Aim 2 to imaging injectable hydrogels *in vivo*. As discussed previously in Section 8.2.2, a major challenge of the *in vivo* T_2-weighted imaging was the presence of magnetic field inhomogeneities at 3 T.[7] If remaining at 3 T, injection via catheter to prevent air spaces in the chest cavity or injection into a location farther from the lung parenchyma (i.e., septum) may decrease the magnetic field susceptibility differences to improve homogeneity, but an ideal imaging technique would enable material detection regardless of delivery method or injection site. Preliminary work from the explanted heart following *in vivo* HeMA-HA injection suggests that the T_2 relaxation times of the material and surrounding myocardium are different enough to enable *in vivo* detection of the hydrogel if the magnetic field inhomogeneity is decreased by moving to a lower field strength of 1.5 T; thus, this is the most promising approach.

Due to the specificity of CEST imaging for the specific functional groups in the hydrogel, it would be highly beneficial to progress to *in vivo* work as well. Unlike T_2-weighted imaging, CEST MRI may provide the opportunity to image hydrogels *in vivo* after infarction if the exchangeable proton group manipulated is selected appropriately. Recent work from our collaborators demonstrated that amine protons in creatine can be manipulated by CEST to distinguish between healthy and infarcted myocardium in large animals.[20] A decrease in creatine-based CEST contrast was observed in infarcted relative to healthy tissue, suggesting a decrease in creatine levels in the akinetic, ischemic tissue as contractile function becomes limited.[20] Due to the known

background myocardial signal from predominately amine protons resonating at about 1.8 ppm away from bulk water, selection of a functional group or peptide sequence to couple to HA with an exchangeable proton group that resonates away from the endogenous amines, preferably further downfield from bulk water protons, would enable detection of HA hydrogels within the infarct. In addition, the functional group or peptide sequence should have a single, uniform peak for the exchangeable protons, unlike the peptide sequence chosen for this study which had multiple exchangeable protons peaks, as demonstrated by high-resolution, non-water suppressed spectroscopy. A single resolved peak will not only lead to enhanced CEST contrast but also enable application of the new fitting technique based on a probabilistic model to better compensate for magnetic field inhomogeneity *in vivo*, as previously described.[20]

The ability to specifically visualize injectable hydrogels *in vivo* using CEST MRI would provide the opportunity to track changes in hydrogel properties over time. One material property of particular interest is the rate of *in vivo* degradation since previous MI studies in large animals have demonstrated that the therapeutic impact of hydrogels depends on their duration of mechanical stabilization and thus, degradation.[1] To determine the optimal rate of degradation for positive *in vivo* outcomes, different hydrogel formulations could be directly compared and tracked over the chronic remodeling process. Furthermore, previous studies from our lab have shown that encapsulated small molecule release tracks with HA hydrogel degradation.[5,40] Thus, the ability to track hydrogel degradation *in vivo* would provide an indirect assessment of therapeutic molecule release, as will be discussed further in Section 8.3.2. Ultimately, the use of a single, clinically relevant imaging modality (i.e., MRI) to simultaneously track hydrogel properties over time *in vivo* and investigate their impact on myocardial tissue properties (as described in Aim 3) would enable direct correlation between specific material properties and their positive effects on tissue remodeling post-MI within a single scan period. This would provide insight for the future development of biomaterial systems with optimal properties to attenuate infarct remodeling.

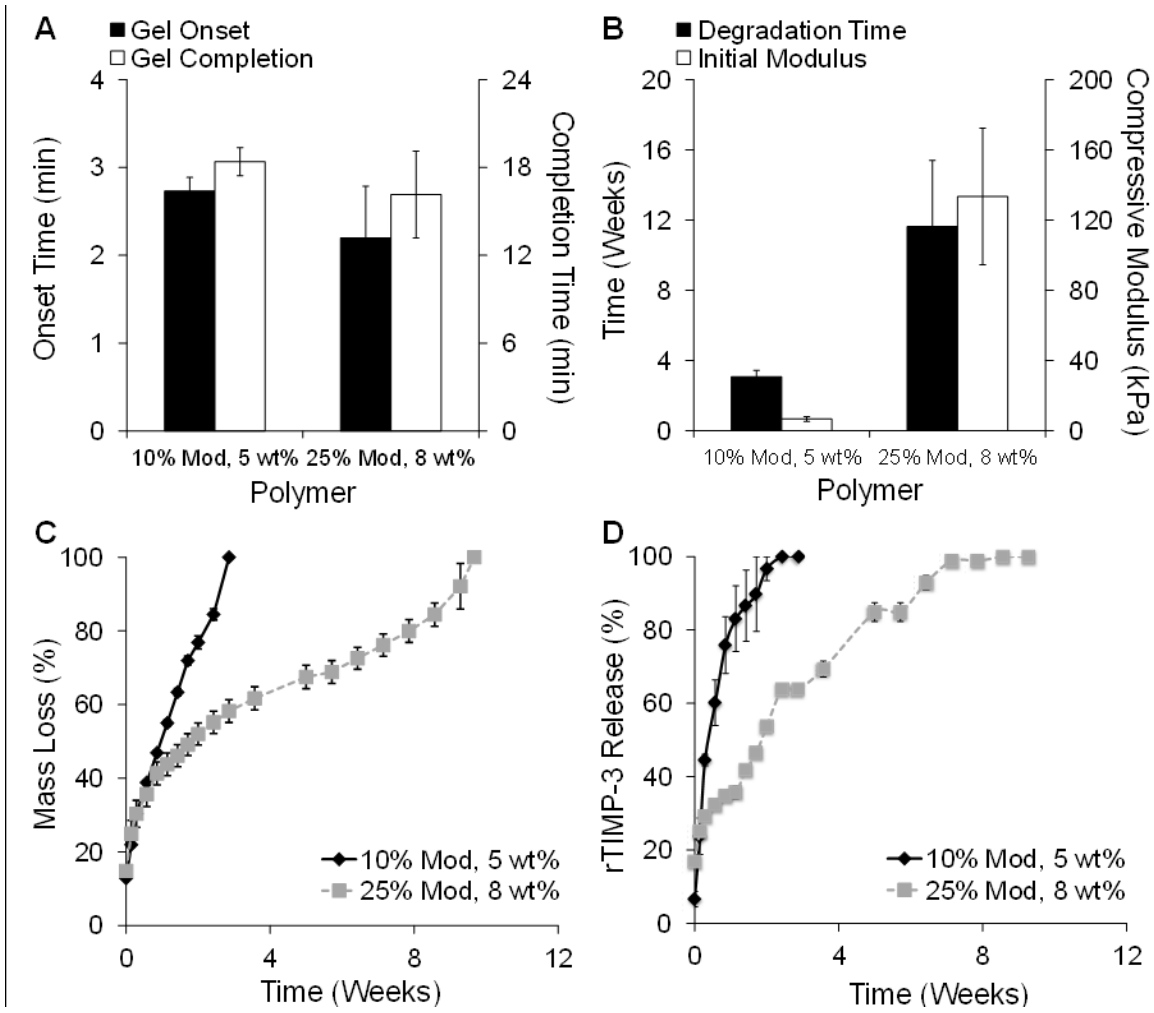

Figure 8.1. Tuning HeMA-HA hydrogel properties to alter degradation and small molecule release. Gel onset and completion, *n=3-4/group*, for selected formulations (A). Degradation time and initial compressive moduli, *n=3-4/group* (B). Degradation (C) of both formulations correlated with release of r-TIMP-3 (D), *n=3-4/group*. Degradation and release performed in PBS with 1% reagent diluent BSA. Data presented as mean ± SEM. All comparisons between polymers were statistically significant ($p<0.05$) in panels A and B. Differences between formulations were statistically significant ($p<0.05$) in panel C aside from at days 1 and 12 and in panel D past day 2.

8.3.2. Small Molecule Release from Injectable HA Hydrogels

To further apply the temporal control of HA hydrogel degradation discussed in Aim 1 and expand the *in vivo* application investigated in Aim 3 to biological process post-MI, HA hydrogels could be used to deliver encapsulated small molecules; as the hydrogel degrades, the molecule is released.[5,40,41] A model small molecule that has recently been explored by our group for MI repair is tissue inhibitor of metalloproteinase-3 (TIMP-3).[5] As previously discussed in Chapter 1, following MI, there is an increase in the activation of matrix metalloproteinases (MMPs) in the myocardium, which contributes to breakdown of extracellular matrix (ECM) and consequently infarct expansion and associated LV dilation.[42-45] Whereas MMPs are upregulated post-MI, their endogenous tissue inhibitors (TIMPs) are not.[46-48] More specifically, TIMP-3 is a critical regulator of MMP activity; all four TIMPs inhibit MMPs but TIMP-3 has the broadest inhibition spectrum.[49] In addition, unlike the other TIMPs, TIMP-3 is tightly bound to the ECM due to interactions with GAGs,[49-51] suggesting there is a native affinity between HA and TIMP-3.[5] Thus, HA hydrogels can serve as a platform for TIMP-3 release as a model small molecule both *in vitro* and *in vivo*.

To demonstrate the feasibility of tuning small molecule release based on differences in degradation, release of rTIMP-3 was examined from two HeMA-HA hydrogels formulations with anticipated differences in degradation based on previous studies (Section 4.3.2): 10% modified HeMA-HA at 5 wt% and 25% modified HeMA-HA at 8 wt%, both gelled using 5 mM APS/TEMED. As predicted, gel onset and completion times were slightly slower in the 10% than 25% modified gels (**Figure 8.1A**) and the initial compressive moduli slightly lower (**Figure 8.1B**). More importantly, degradation of the 25% modified gels (11.6 ± 3.8 weeks) was significantly ($p<0.05$) slower than the 10% modified gels (3.1 ± 0.4 weeks, **Figure 8.1B**). Quantification of mass loss over time further highlighted these degradation differences, with significantly less HA loss from the 25% modified gels at all time points aside from days 1 and 12 (**Figure 8.1C**). Correspondingly, release of rTIMP-3 as a model small molecule was slower in the 25% than 10% modified gels and significantly so past day 2 (**Figure 8.1D**). Due to the native affinity between HA

and TIMP-3,[49-51] as the HA-based hydrogels degraded, TIMP-3 was released through both diffusion and bound with HA fragments.

For future *in vivo* applications similar to the study design of Aim 3, the hydrogel degradation profiles selected for rTIMP-3 release targeted different phases of the LV remodeling process, as discussed in Chapter 3.[4] This is particularly beneficial for TIMP release since the activation of MMPs post-MI is time-dependent.[48,51] The degradation of the 10% modified hydrogel at about 3 weeks correlates well with the acute LV remodeling stage, whereas the degradation of the 25% modified hydrogel at slightly before 12 weeks corresponds well to the chronic remodeling stage. In addition, previous studies from our group examined the *in vivo* benefit of rTIMP-3 release from HA hydrogels post-MI.[5] However, these studies were performed using a single hydrogel formulation and outcome assessment primarily occurred during the acute period out to 2 weeks post-MI with minor assessment of LV volumes at 4 weeks post-MI.[5] Therefore, comparing *in vivo* outcomes between hydrogels with different release profiles (**Figure 8.1**) would elucidate the optimal rate of TIMP-3 delivery. Furthermore, future studies assessing the therapeutic benefit of TIMP-3 delivery out to 12 weeks post-MI with an emphasis on the myocardial tissue properties (as utilized in Aim 3) would provide insight as to if early MMP inhibition delays the progression of global LV remodeling or permanently interrupts maladaptive myocardial remodeling. Ultimately, delivery of small, physiologically relevant molecules using the degradable HA hydrogels explored in Aim 1 would enable HA hydrogel therapy to address the biological implications of post-MI remodeling in addition to the mechanical benefits discussed in Aim 3 of this dissertation.

8.3.3. Improved *In Vivo* Study Design

In Aim 3 of this dissertation, a single hydrogel formulation was delivered *in vivo* as a platform to develop tools to assess the impact of hydrogel therapy on myocardial tissue properties. Future *in vivo* work should focus on applying the combination of MRI and FE modeling assessment to evaluate a range of hydrogels with varying properties. To make the material system more clinically applicable, hydrogel injection should occur farther past the onset of MI

(i.e., 1 week post-MI). Delivering hydrogels at even later times into the chronic remodeling stages (i.e., weeks to months following MI) would also lead to a better understanding of the therapeutic window during which injectable materials need to be delivered to optimize their therapeutic benefit. Finally, the percutaneous delivery of the hydrogels through catheters would facilitate clinical translation and allow for therapeutic hydrogel application in a wider population of patients where a thoracotomy is not part of their standard clinical care.

8.4. Summary

Myocardial tissue remodeling following infarction is considered the main contributing factor in the progression to heart failure, yet current therapies do little to address these alterations in tissue properties over time. Injectable materials offer a minimally invasive strategy to attenuate myocardial remodeling, but noninvasive tools are also needed to assess the effects of these therapies. The goal of this dissertation was to use MRI to investigate injectable HA hydrogel properties and their therapeutic effect on myocardial properties for infarct repair. The data presented in this dissertation demonstrates that differences in hydrogel properties can be noninvasively assessed after delivery to the myocardium and that injectable hydrogels positively impact myocardial mechanical properties (e.g., thickness, strain, stiffness) into the chronic remodeling stages. The findings of this dissertation represent advancements in imaging technology and provide insight into biomaterial design criteria for better therapies to target myocardial infarct remodeling and prevent progression to heart failure.

8.5. References

1. Tous E, Ifkovits JL, Koomalsingh KJ, Shuto T, Soeda T, Kondo N, et al. Influence of injectable hyaluronic acid hydrogel degradation behavior on infarction-induced ventricular remodeling. Biomacromolecules 2011;12(11):4127-4135.

2. Ifkovits JL, Tous E, Minakawa M, Morita M, Robb JD, Koomalsingh KJ, et al. Injectable hydrogel properties influence infarct expansion and extent of postinfarction left ventricular remodeling in an ovine model. Proc Natl Acad Sci U S A 2010;107(25):11507-11512.

3. Wenk JF, Wall ST, Peterson RC, Helgerson SL, Sabbah HN, Burger M, et al. A method for automatically optimizing medical devices for treating heart failure: Designing polymeric injection patterns. J Biomech Eng 2009;131(12):121011.

4. Sutton M, Sharpe N. Left ventricular remodeling after myocardial infarction - Pathophysiology and therapy. Circulation 2000;101(25):2981-2988.

5. Purcell BP, Lobb D, Charati MB, Dorsey SM, Wade RJ, Zellars KN, et al. Injectable and bioresponsive hydrogels for on-demand matrix metalloproteinase inhibition. Nat Mater 2014;13(6):653-661.

6. Rodell CB, Kaminski AL, Burdick JA. Rational design of network properties in guest-host assembled and shear-thinning hyaluronic acid hydrogels. Biomacromolecules 2013;14(11):4125-4134.

7. Oshinski JN, Delfino JG, Sharma P, Gharib AM, Pettigrew RI. Cardiovascular magnetic resonance at 3.0T: Current state of the art. J Cardiovasc Magn Reson 2010;12:55.

8. Krishnamurthy R, Pednekar A, Kouwenhoven M, Cheong B, Muthupillai R. Evaluation of a subject specific dual-transmit approach for improving B-1 field homogeneity in cardiovascular magnetic resonance at 3T. J Cardiovasc Magn Reson 2013;15:68.

9. Han Q, Han Y, Gorman RC, Witschey WR. The influence of static and RF field heterogeneity on T1rho cardiovascular MRI. J Cardiovasc Magn Reson 2014;16(Suppl 1):P70.

10. Holmes JW, Nunez JA, Covell JW. Functional implications of myocardial scar structure. American Journal of Physiology-Heart and Circulatory Physiology 1997;272(5):H2123-H2130.

11. Gupta KB, Ratcliffe MB, Fallert MA, Edmunds LH,Jr, Bogen DK. Changes in passive mechanical stiffness of myocardial tissue with aneurysm formation. Circulation 1994;89(5):2315-2326.

12. Fomovsky GM, Rouillard AD, Holmes JW. Regional mechanics determine collagen fiber structure in healing myocardial infarcts. J Mol Cell Cardiol 2012;52(5):1083-1090.

13. Fomovsky GM, Holmes JW. Evolution of scar structure, mechanics, and ventricular function after myocardial infarction in the rat. Am J Physiol -Heart Circul Physiol 2010;298(1):H221-H228.

14. van Zijl PCM, Yadav NN. Chemical Exchange Saturation Transfer (CEST): What is in a Name and What Isn't? Magn Reson Med 2011;65(4):927-948.

15. Kogan F, Hariharan H, Reddy R. Chemical Exchange Saturation Transfer (CEST) Imaging: Description of Technique and Potential Clinical Applications. Curr Radiol Rep 2013;1(2):102-114.

16. Liepinsh E, Otting G. Proton exchange rates from amino acid side chains - Implications for image contrast. Magnetic Resonance in Medicine 1996;35(1):30-42.

17. Kim M, Gillen J, Landman BA, Zhou J, van Zijl PCM. Water saturation shift referencing (WASSR) for chemical exchange saturation transfer (CEST) experiments. Magn Reson Med 2009;61(6):1441-1450.

18. Singh A, Cai K, Haris M, Hariharan H, Reddy R. On B1 inhomogeneity correction of in vivo human brain glutamate chemical exchange saturation transfer contrast at 7T. Magn Reson Med 2013;69(3):818-824.

19. Zaiss M, Schmitt B, Bachert P. Quantitative separation of CEST effect from magnetization transfer and spillover effects by Lorentzian-line-fit analysis of z-spectra. Journal of Magnetic Resonance 2011;211(2):149-155.

20. Haris M, Singh A, Cai K, Kogan F, McGarvey J, DeBrosse C, et al. A technique for in vivo mapping of myocardial creatine kinase metabolism. Nat Med 2014;20(2):209-214.

21. Liu G, Moake M, Har-el Y, Long CM, Chan KWY, Cardona A, et al. In vivo multicolor molecular MR imaging using diamagnetic chemical exchange saturation transfer liposomes. Magn Reson Med 2012;67(4):1106-1113.

22. McMahon MT, Gilad AA, DeLiso MA, Berman SDC, Bulte JWM, van Zijl PCM. New "multicolor" polypeptide diamagnetic chemical exchange saturation transfer (DIACEST) contrast agents for MRI. Magn Reson Med 2008;60(4):803-812.

23. Haris M, Nanga RPR, Singh A, Cai K, Kogan F, Hariharan H, et al. Exchange rates of creatine kinase metabolites: Feasibility of imaging creatine by chemical exchange saturation transfer MRI. NMR Biomed 2012;25(11):1305-1309.

24. Morita M, Eckert CE, Matsuzaki K, Noma M, Ryan LP, Burdick JA, et al. Modification of infarct material properties limits adverse ventricular remodeling. Ann Thorac Surg 2011;92(2):617-625.

25. Shen D, Wang X, Zhang L, Zhao X, Li J, Cheng K, et al. The amelioration of cardiac dysfunction after myocardial infarction by the injection of keratin biomaterials derived from human hair. Biomaterials 2011;32(35):9290-9299.

26. Okada M, Payne TR, Oshima H, Momoi N, Tobita K, Huard J. Differential efficacy of gels derived from small intestinal submucosa as an injectable biomaterial for myocardial infarct repair. Biomaterials 2010;31(30):7678-7683.

27. Kofidis T, Lebl DR, Martinez EC, Hoyt G, Tanaka M, Robbins RC. Novel injectable bioartificial tissue facilitates targeted, less invasive, large-scale tissue restoration on the beating heart after myocardial injury. Circulation 2005;112(9 Suppl):I173-7.

28. Jneid H, Fonarow GC, Cannon CP, Palacios IF, Kilic T, Moukarbel GV, et al. Impact of time of presentation on the care and outcomes of acute myocardial infarction. Circulation 2008;117(19):2502-2509.

29. Miura T, Miki T. Limitation of myocardial infarct size in the clinical setting: current status and challenges in translating animal experiments into clinical therapy. Basic Res Cardiol 2008;103(6):501-513.

30. Birnbaum Y, Fishbein M, Blanche C, Siegel R. Current concepts - Ventricular septal rupture after acute myocardial infarction. N Engl J Med 2002;347(18):1426-1432.

31. Menon V, Webb J, Hillis L, Sleeper L, Abboud R, Dzavik V, et al. Outcome and profile of ventricular septal rupture with cardiogenic shock after myocardial infarction: A report from the SHOCK Trial Registry. J Am Coll Cardiol 2000;36(3):1110-1116.

32. Lemery R, Smith HC, Giuliani ER, Gersh BJ. Prognosis in rupture of the ventricular septum after Acute myocardial-infarction and role of early surgical intervention. Am J Cardiol 1992;70(2):147-151.

33. Edwards BS, Edwards WD, Edwards JE. Ventricular septal rupture complicating acute myocardial-infarction - Identification of simple and complex types in 53 autopsied hearts. Am J Cardiol 1984;54(10):1201-1205.

34. Pohjola-Sintonen S, Muller JE, Stone PH, Willich SN, Antman EM, Davis VG, et al. Ventricular septal and free wall rupture complicating acute myocardial-infarction - Experience in the multicenter investigation of limitation of infarct size. Am Heart J 1989;117(4):809-818.

35. Seif-Naraghi SB, Singelyn JM, Salvatore MA, Osborn KG, Wang JJ, Sampat U, et al. Safety and efficacy of an injectable extracellular matrix hydrogel for treating myocardial infarction. Sci Transl Med 2013;5(173):173ra25.

36. Yoon SJ, Fang YH, Lim CH, Kim BS, Son HS, Park Y, et al. Regeneration of ischemic heart using hyaluronic acid-based injectable hydrogel. J Biomed Mater Res B Appl Biomater 2009;91(1):163-171.

37. Kang S, Cho E, Kim B. PLGA microspheres in hyaluronic acid gel as a potential bulking agent for urologic and dermatologic injection therapies. J Microbiol Biotechnol 2005;15(3):510-518.

38. Wang VY, Lam HI, Ennis DB, Cowan BR, Young AA, Nash MP. Modelling passive diastolic mechanics with quantitative MRI of cardiac structure and function. Med Image Anal 2009;13(5):773-784.

39. Krishnamurthy A, Villongco CT, Chuang J, Frank LR, Nigam V, Belezzuoli E, et al. Patient-specific models of cardiac biomechanics. J Comput Phys 2013;244:4-21.

40. MacArthur JW,Jr., Purcell BP, Shudo Y, Cohen JE, Fairman A, Trubelja A, et al. Sustained release of engineered stromal cell-derived factor 1-alpha from injectable hydrogels

effectively recruits endothelial progenitor cells and preserves ventricular function after myocardial infarction. Circulation 2013;128(11):S79-S86.

41. Purcell BP, Kim IL, Chuo V, Guenin T, Dorsey SM, Burdick JA. Incorporation of sulfated hyaluronic acid macromers into degradable hydrogel scaffolds for sustained molecule delivery. Biomater Sci 2014;2(5):693-702.

42. Gao X, Xu Q, Kiriazis H, Dart A, Du X. Mouse model of post-infarct ventricular rupture: time course, strain- and gender-dependency, tensile strength, and histopathology. Cardiovasc Res 2005;65(2):469-477.

43. Mukherjee R, Brinsa TA, Dowdy KB, Scott AA, Baskin JM, Deschamps AM, et al. Myocardial infarct expansion and matrix metalloproteinase inhibition. Circulation 2003;107(4):618-625.

44. Mukherjee R, Zavadzkas JA, Saunders SM, McLean JE, Jeffords LB, Beck C, et al. Targeted myocardial microinjections of a biocomposite material reduces infarct expansion in pigs. Ann Thorac Surg 2008;86(4):1268-1276.

45. Nahrendorf M. Imaging of infarct healing predicts left ventricular remodeling and evolution of heart failure: Focus on protease activity. Circ Cardiovasc Imaging 2011;4(4):351-353.

46. Spinale FG, Coker ML, Heung LJ, Bond BR, Gunasinghe HR, Etoh T, et al. A matrix metalloproteinase induction/activation system exists in the human left ventricular myocardium and is upregulated in heart failure. Circulation 2000;102(16):1944-1949.

47. Spinale FG, Coker ML, Krombach SR, Mukherjee R, Hallak H, Houck WV, et al. Matrix metalloproteinase inhibition during the development of congestive heart failure: Effects on left ventricular dimensions and function. Circ Res 1999;85(4):364-376.

48. Wilson E, Moainie S, Baskin J, Lowry A, Deschamps A, Mukherjee R, et al. Region- and type-specific induction of matrix metalloproteinases in post-myocardial infarction remodeling. Circulation 2003;107(22):2857-2863.

49. Brew K, Nagase H. The tissue inhibitors of metalloproteinases (TIMPs): An ancient family with structural and functional diversity. Biochim Biophys Acta-Mol Cell Res 2010;1803(1):55-71.

50. Yu W, Yu S, Meng Q, Brew K, Woessner J. TIMP-3 binds to sulfated glycosaminoglycans of the extracellular matrix. J Biol Chem 2000;275(40):31226-31232.

51. Lee M, Atkinson S, Murphy G. Identification of the extracellular matrix (ECM) binding motifs of tissue inhibitor of metalloproteinases (TIMP)-3 and effective transfer to TIMP-1. J Biol Chem 2007;282(9):6887-6898.